



THE HONG KONG
POLYTECHNIC UNIVERSITY

香港理工大學

Pao Yue-kong Library

包玉剛圖書館

Copyright Undertaking

This thesis is protected by copyright, with all rights reserved.

By reading and using the thesis, the reader understands and agrees to the following terms:

1. The reader will abide by the rules and legal ordinances governing copyright regarding the use of the thesis.
2. The reader will use the thesis for the purpose of research or private study only and not for distribution or further reproduction or any other purpose.
3. The reader agrees to indemnify and hold the University harmless from and against any loss, damage, cost, liability or expenses arising from copyright infringement or unauthorized usage.

IMPORTANT

If you have reasons to believe that any materials in this thesis are deemed not suitable to be distributed in this form, or a copyright owner having difficulty with the material being included in our database, please contact lbsys@polyu.edu.hk providing details. The Library will look into your claim and consider taking remedial action upon receipt of the written requests.

**MATERIAL CHARACTERISATION AND
STRUCTURAL BEHAVIOUR OF COLD-FORMED
POLYGONAL HOLLOW SECTION STEEL COLUMNS**

LIU HAIXIN

PhD

The Hong Kong Polytechnic University

2023

The Hong Kong Polytechnic University

Department of Civil and Environmental Engineering

**Material Characterisation and
Structural Behaviour of
Cold-Formed Polygonal Hollow Section Steel Columns**

LIU Haixin

A thesis submitted in partial fulfilment of the requirements for the

Degree of Doctor of Philosophy

March 2023

CERTIFICATE OF ORIGINALITY

I hereby declare that this thesis is my own work and that, to the best of my knowledge and belief, it reproduces no material previously published or written nor material that has been accepted for the award of any other degree or diploma, except where due acknowledgement has been made in the text.

_____ (Signed)

LIU Haixin (Name of student)

Abstract

Cold-formed structural steel members are widely adopted in structural engineering owing to their merits of ease of fabrication, high-customised cross-section, and high strength-to-weight ratios. Two commonly used manufacturing methods for cold-formed steel are cold-rolling and press-braking, in which a steel sheet is continuously fed into a successive set of rollers, or predetermined bends are punched along the length of the steel sheet, to produce required cold-formed steel sections. Both of the two methods introduce different levels of plastic deformation into the cold-formed regions of the cross-section. As a result, material properties of steel in the deformed regions vary from those of the parent materials due to the pronounced strain-hardening. A more rounded stress-strain response with an enhanced yield strength, an enhanced ultimate tensile strength and reduced ductility can be observed among those metallic materials that experienced cold-forming. This thesis provides a consistent and thorough investigation into effects of cold-forming on normal strength and high strength steel. Based on the generated test results and collected test data from the global literature, a series of semi-empirical models are proposed to predict the material properties of structural steel after cold-forming, and a material constitutive model which incorporates the proposed predictive expressions is developed to accurately represent the stress-strain response of cold-formed steel.

As for structural behaviour of cold-formed steel structures, extensive researches reveal that their structural behaviour was manufacturing method-dependant, which means differences in structural behaviour not only exist among different types of cross-sections, but also among identical cross-sections fabricated from different manufacturing methods. Hence, this thesis conducts a comprehensive investigation into the structural behaviour of cold-formed polygonal hollow section steel columns,

including columns made from rectangular hollow sections and octagonal hollow sections. Material tests, residual stress measurements, stub column tests, and long column tests are conducted, and test results are presented in this thesis. Finite element models are developed and validated against experimental results. Effects of material properties, residual stresses, global and local initial geometric imperfections and other parameters are studied. Following the validation of the developed finite element models, extensive parametric studies are carried out to supplement and broaden the test database. Then current design methods for cold-formed steel structures from Australia, China, Europe, and the United States are reviewed. Assessments and modifications to the codified design rules are made based on the test and numerical results. Subsequently, reliability analyses are performed to verify the applicability of the proposed design recommendations.

Publications

1. Junbo Chen, **Haixin Liu**, Tak-Ming Chan. Material properties and residual stresses of cold-formed octagonal hollow sections. *Journal of Constructional Steel Research*, 2020, 170: 106078.
2. **Haixin Liu**, Han Fang, Jiong-Yi Zhu, Tak-Ming Chan. Numerical investigation on the structural performance of octagonal hollow section columns. *Structures*, 2021, 34: 3257–3267.
3. **Haixin Liu**, Hao Jiang, Yi-Fei Hu, Tak-Ming Chan, Kwok-Fai Chung. Structural behaviour of Q355 and Q460 press-braked rectangular hollow section stub columns. *Journal of Constructional Steel Research*, 2022, 197: 107497.
4. **Haixin Liu**, Junbo Chen, Tak-Ming Chan. Predictive models for material properties of cold-formed conventional steels in the corner region. *Thin-Walled Structures*, 2023, 187: 110740.
5. **Haixin Liu**, Junbo Chen, Tak-Ming Chan. Mechanical properties of corner material in cold-formed steel structure: from normal strength to high strength. *Journal of Building Engineering* (under review).
6. **Haixin Liu**, Junbo Chen, Tak-Ming Chan. Material constitutive model for cold-formed steels. *Construction and Building Materials* (under preparation).
7. **Haixin Liu**, Jiong-Yi Zhu, Tak-Ming Chan. Structural behaviour and design of cold-formed regular octagonal hollow section pin-ended columns. *Engineering Structures* (under preparation).
8. **Haixin Liu**, Jiong-Yi Zhu, Tak-Ming Chan. Cold-formed irregular octagonal hollow section columns subjected to local-flexure interactive buckling. *Engineering Structures* (under preparation).

Acknowledgement

First and most importantly, I would like to express my sincere appreciation to my supervisor, Dr. CHAN Tak-Ming, for his invaluable advice, useful guidance and continuous supports throughout my PhD study. His rigorous attitude towards academic and his lovely odd joke will always inspire me and guide me. I would also like to thank my big brothers Dr. CHEN Junbo and Dr. ZHU Jiongyi, for their coordination of the experimental programme conducted in Huazhong University of Science and Technology and Shanghai University, tremendous suggestions and advice throughout the period of my PhD study. Without their support, I would never complete my PhD study so smoothly.

I wish to acknowledge the financial supports and facilities from The Hong Kong Polytechnic University and the Chinese National Engineering Research Centre for Steel Construction (Hong Kong Branch) for my PhD study.

Sincere thanks also go to the technicians in Structural Lab and Concrete Lab, Mr. King-Hee Wong, Mr. Man-Chuen Ng, and Mr. Henry Cheung, for their supports during my experimental works.

I will always have a special place in my heart for my friends and colleagues, Dr. ZHANG Yuze, Dr. XIAO Meng, Dr. HU Yifei, Dr. JIN Hao, Dr. FANG Han, Dr. XU Fei, Dr. LAN Xiaoyi, Dr. Paola Pannuzzo, Dr. Partha Debnath, Dr. LIU Junzhi, Dr. LI Shuai, Dr. CHEN Shuxian, Dr. GUO Jiachen, Dr. WANG Chen, Dr. XUE Zhihang, Dr. HUANG Junchao, Dr. SU Bing, Dr. ZHUANG Zhuoxuan, Dr. ZHANG Zhuozhi, Mr. HAN Xiaozhou, Mr. MA Qi, Mr. ZHAO Shentao, Mr. Aswin Jeyabalan, Ms. NING Weijie, Mr. CHEN Wei, Mrs. GAN Lihong, and Ms. WANG Manli. The moments we spent together are unforgettable and irreplaceable.

Finally, I would also like to express my deepest thanks to my beloved parents LIU Weichong and HUANG Xianqin, and my cutest wife WU Xiaoyun, who have provided me with their everlasting love and countless support.

Content

Chapter 1	Introduction	1
1.1	Background.....	1
1.2	Objectives and scope	3
1.3	Outline of this thesis	5
Chapter 2	Literature review.....	7
2.1	Introduction	7
2.2	Strength enhancement due to cold-forming process	7
2.3	Material constitutive models for structural steels	16
2.3.1	Structural steel with sharply defined yield point and distinct yield plateau	16
2.3.2	Cold-formed steel.....	20
2.4	Cold-formed polygonal hollow sections.....	31
2.4.1	Rectangular hollow sections	31
2.4.2	Hexagonal and octagonal hollow sections.....	33
2.5	Concluding remarks.....	36
Chapter 3	Cold-forming effect and material constitutive model of cold-formed steels.....	37
3.1	Introduction	37
3.2	Manufacturing and preparations of specimens for the tensile coupon test	38
3.2.1	General.....	38
3.2.2	Specimen details of flat coupons	38

3.2.3	Specimen details of corner coupons	39
3.3	Material tests and results.....	42
3.3.1	Tensile test procedures	42
3.3.2	Material test results	44
3.4	Establishment of the cold–formed steel database.....	56
3.5	Analysis of results and development of predictive expressions.....	61
3.5.1	Recalibration of material parameters of parent materials.....	61
3.5.2	Young’s moduli of cold–formed steels	63
3.5.3	Strength enhancement.....	65
3.5.4	Loss in ultimate strain.....	71
3.5.5	Loss in elongation at fracture	73
3.6	Proposed material constitutive model	74
3.6.1	One–stage model	75
3.6.2	Two–stage Ramberg–Osgood model	77
3.6.3	Evaluation of proposed models	79
3.7	Concluding remarks.....	90
Chapter 4	Behaviour and design of rectangular hollow section steel columns under pure compression.....	91
4.1	Introduction	91
4.2	Press–braked RHS stub columns.....	92
4.2.1	General.....	92
4.2.2	Material properties	94
4.2.3	Residual stress patterns	97
4.2.4	Local imperfection measurement	101

4.2.5	Stub column tests	102
4.2.6	Finite element modelling and parametric study.....	106
4.2.7	Assessment and modification of current design methods.....	112
4.3	Press-braked RHS long columns.....	118
4.3.1	General.....	118
4.3.2	Long column tests.....	118
4.3.3	Finite element modelling and parametric study.....	123
4.3.4	Assessment and modification of current design methods.....	128
4.3.5	Reliability analysis.....	136
4.4	Concluding remarks.....	139
Chapter 5	Structural behaviour and design of pin-ended octagonal hollow section columns	141
5.1	Introduction	141
5.2	Experimental investigation of OctHS columns.....	142
5.2.1	Specimen details of OctHS columns	142
5.2.2	Material properties.....	145
5.2.3	Initial global geometric imperfection	148
5.2.4	Test set-up and loading eccentricity.....	148
5.2.5	Column test results	150
5.3	Numerical investigations and parametric study.....	162
5.3.1	Finite element modelling validation	162
5.3.2	Parametric study	169
5.4	Analysis of results and design of OctHS long columns	171
5.4.1	Analysis of numerical results.....	171

5.4.2	Cross–section classifications of the OctHS	175
5.4.3	Column buckling strengths of the OctHS	176
5.5	Reliability analysis	188
5.5.1	EN 1990 method	188
5.5.2	AISI S100 method.....	190
5.6	Concluding remarks.....	191
Chapter 6	Conclusions and future works.....	193
6.1	Introduction	193
6.2	Material characterisation of cold–formed steels	193
6.3	Behaviour and design of rectangular hollow section steel columns under pure compression	194
6.4	Structural behaviour and design of pin–ended octagonal hollow section columns.....	195
6.5	Future works.....	197
References	198

List of Figures

Figure 2.1 Manufacturing process of indirect forming RHS tubes (Tayyebi <i>et al.</i> , 2020).	8
Figure 2.2 Manufacturing process of direct forming RHS tubes (Tayyebi <i>et al.</i> , 2020).	9
Figure 2.3 Manufacturing process of press-braking RHS tubes.	9
Figure 2.4 Effects of strain hardening and strain aging.	10
Figure 2.5 Illustration of the simplified corner model.	12
Figure 2.6 Material constitutive models of the hot-rolled steel.	17
Figure 2.7 Typical stress-strain response of the cold-formed steel.	20
Figure 2.8 The comparison between the original Ramberg-Osgood model and Mirambell model (Mirambell and Real, 2000).	23
Figure 2.9 The comparison between the two-stage Ramberg-Osgood model and Ma model (Ma <i>et al.</i> , 2015).	31
Figure 3.1 Illustration of locations of flat coupons and different directions.	38
Figure 3.2 Water-jet cutting of flat tensile coupons.	39
Figure 3.3 Geometrical dimensions of tensile coupons.	39
Figure 3.4 Fabrication process and press-braked specimens.	40
Figure 3.5 Punches with different bending radii ($r_p = 3\text{mm}$, 5mm , and 10mm).	40
Figure 3.6 Processing example of scanned corner coupon.	41
Figure 3.7 Test setup for the normal strength part of coupons.	42
Figure 3.8 Test setup for the high strength part of coupons.	43
Figure 3.9 Information about the specially designed pin grip.	43

Figure 3.10 Stress–strain curves of tested coupons.	46
Figure 3.11 Trends of the yield strengths $f_{y,c}$ and ultimate tensile strengths $f_{u,c}$ against various punch radii R_p and included angles θ for normal strength steels.	47
Figure 3.12 Trends of the yield strengths $f_{y,c}$ and ultimate tensile strengths $f_{u,c}$ against various punch radii R_p and included angles θ for high strength steels.....	48
Figure 3.13 Distributions of parent material yield strengths and r_i/t ratios after cold–forming in the database.	58
Figure 3.14 Processing examples to obtain material coefficient k and strain–hardening exponent n_{se}	61
Figure 3.15 Work example of obtainment of k and n_{se} values.	62
Figure 3.16 Assessment of the material coefficients and strain hardening exponents.	63
Figure 3.17 Change of Young’s modulus before and after cold–forming.....	64
Figure 3.18 Relationships of the f_u/f_y with f_y for normal and high strength steels before and after cold–forming.....	65
Figure 3.19 Trends of enhanced strengths against r_i/t ratio.	67
Figure 3.20 Prediction accuracy for enhanced strengths.	70
Figure 3.21 Trend between the change of ultimate strain and related parameters.....	72
Figure 3.22 Trend between the change of elongation at fracture and strength enhancement level.....	74
Figure 3.23 Trend between the fitted value of m_o and $(r_i/t)*\ln(f_{u,f}/f_{y,f})$	77
Figure 3.24 Comparison between the predicted m_o values and measured m_o values. .	77
Figure 3.25 Comparison of the stress–strain curves predicted from one–stage model based on measured or predicted material parameters with test stress–strain curves.	83
Figure 3.26 Comparison of the stress–strain curves predicted from modified two–stage	

Ramberg–Osgood model based on measured or predicted material parameters with test stress–strain curves.....	87
Figure 4.1 Definition of dimensions for the press–braked RHS.....	93
Figure 4.2 Test setup for tensile coupon tests.	95
Figure 4.3 Typical stress–strain curves obtained from coupon tests.....	97
Figure 4.4 Sectioning of press–braked RHS H250×150×6.	98
Figure 4.5 Residual stress distributions of press–braked RHSs.	99
Figure 4.6 The simplified predictive residual stress pattern of press–braked RHS...	100
Figure 4.7 Instrumentation of the local imperfection measurement.	101
Figure 4.8 The local imperfection profile of specimen H250×150×6.	102
Figure 4.9 Press–braked RHS stub column test setups.....	103
Figure 4.10 Typical failure modes of press–braked RHS stub columns.....	104
Figure 4.11 Normalised axial strength versus axial strain curves of press–braked RHS stub columns.	105
Figure 4.12 Mesh convergency study of specimen N150×100×6.	107
Figure 4.13 Input membrane residual stress distribution for H250×150×6 FE model.	108
Figure 4.14 Comparisons of local buckling failure modes obtained from the experiment and numerical model.....	109
Figure 4.15 Comparisons of axial load versus end shortening curves between experimental and numerical results.	110
Figure 4.16 Evaluation of the cross–section classification for press–braked RHSs..	113
Figure 4.17 Comparison of test and FE results with effective width method–based design approaches.	114

Figure 4.18 Comparison of test and FE results with original and modified direct strength methods.	117
Figure 4.19 Comparison of test and FE results normalised by original and modified direct strength methods.	117
Figure 4.20 Instrumentation of long column test.	119
Figure 4.21 Failure modes of long column specimens.	121
Figure 4.22 Axial load versus mid–height deflection curves of long column tests. ..	122
Figure 4.23 Comparisons of the axial load–lateral displacement curves for specimen L250×150×10–f–R.	125
Figure 4.24 Comparisons of the axial load–end rotation curves for specimen L250×150×10–f–R.	125
Figure 4.25 Comparisons of the failure modes for specimen L250×150×10–d.	126
Figure 4.26 Comparisons of Test and numerical results with codified design curves.	128
Figure 4.27 Comparisons of test and numerical results with the design values calculated from different design methods.	131
Figure 4.28 Comparisons of results with the design values calculated from GB 50017.	133
Figure 4.29 Comparison of results with the design values from ANSI/AISC 360–16.	134
Figure 4.30 Comparison of test and numerical results with the design values calculated from AS 4100:2020.	136
Figure 5.1 Half section of irregular octagonal hollow section ($H/W = 2$).	142
Figure 5.2 Arrangement of spot welds and ceramic backing plates of specimen.	143
Figure 5.3 Definition of symbols and locations of tensile coupons for the regular octagonal hollow section.	144

Figure 5.4 Definition of symbols and locations of tensile coupons for the irregular octagonal hollow section.....	144
Figure 5.5 Measured stress–strain curves of Q460 – 3 mm and Q690 – 3 mm flat and corner coupons.....	145
Figure 5.6 Measured stress–strain curves of Q460 – 6 mm and Q690 – 6 mm flat and corner coupons.....	146
Figure 5.7 Isometric view of testing machine.....	148
Figure 5.8 Flexural buckling test setup of OctHS columns.....	149
Figure 5.9 Axial load–mid–height lateral deflection curves of regular OctHS column specimens.....	151
Figure 5.10 Axial load–mid–height lateral deflection curves of irregular OctHS column specimens.....	152
Figure 5.11 Axial load–axial strain curves of regular OctHS specimens.....	156
Figure 5.12 Axial load–axial strain curves of irregular OctHS specimens.....	157
Figure 5.13 Failure modes of regular OctHS columns.....	159
Figure 5.14 Failure modes of irregular OctHS columns.....	161
Figure 5.15 The assigned residual stress distribution on the modelled specimen.....	164
Figure 5.16 The effect of membrane residual stress on the load–bearing capacities.....	165
Figure 5.17 Comparisons of experimental and numerical load–mid–height lateral deflection curves of regular OctHS specimens.....	165
Figure 5.18 Comparisons of experimental and numerical load–mid–height lateral deflection curves of irregular OctHS specimens.....	166
Figure 5.19 Comparisons of global flexural buckling failure mode of regular OctHS column specimens.....	168
Figure 5.20 Comparisons of global flexural buckling failure mode of irregular OctHS	

column specimens.....	168
Figure 5.21 Comparison of local deformation failure mode for regular OctHS columns.	169
Figure 5.22 Comparison of local deformation failure mode for irregular OctHS columns.	169
Figure 5.23 Representative stress–strain curves of input materials.....	171
Figure 5.24 Effects of steel grades on the strengths of regular OctHS columns.	172
Figure 5.25 Effects of steel grades on the strengths of irregular OctHS columns.....	173
Figure 5.26 Effects of aspect ratios (H/W) on the strengths of irregular OctHS columns.	174
Figure 5.27 Comparisons of experimental and numerical results with codified design curves for regular OctHS columns.....	177
Figure 5.28 Comparisons of experimental and numerical results with codified design curves for irregular OctHS columns.	177
Figure 5.29 Comparisons of experimental and numerical results with design values from different methods for regular OctHS columns.	179
Figure 5.30 Comparisons of experimental and numerical results with design values from different methods for irregular OctHS columns.....	180
Figure 5.31 Comparisons of experimental and numerical results with design values from GB 50017–2017 for regular OctHS.	182
Figure 5.32 Comparisons of experimental and numerical results with design values from GB 50017–2017 for irregular OctHS columns.	183
Figure 5.33 Comparisons of experimental and numerical results with design values from American specifications for regular OctHS columns.....	185
Figure 5.34 Comparisons of experimental and numerical results with design values from American specifications for irregular OctHS columns.	185

Figure 5.35 Comparisons of experimental and numerical results with design values from AS 4100:2020 for regular OctHS columns.	187
Figure 5.36 Comparisons of experimental and numerical results with design values from AS 4100:2020 for irregular OctHS columns.	187
Figure 5.37 Values of $k_1 - k_3$ adopted in EN 1990 method for regular OctHS columns.	189
Figure 5.38 Values of $k_1 - k_3$ adopted in EN 1990 method for irregular OctHS columns.	189

List of Tables

Table 3.1 Key parameters obtained from flat coupon tests of normal strength steels.	48
Table 3.2 Key parameters of the normal strength steel corner coupon tests.....	50
Table 3.3 Key parameters obtained from flat coupon tests of high strength steels.....	54
Table 3.4 Key parameters of the high strength steel corner coupon tests.....	54
Table 3.5 Key information of collected cold–formed steel database.....	59
Table 3.6 Young’s moduli for normal and high strength steels.....	64
Table 3.7 Statistical evaluations between different predictive expressions.	71
Table 3.8 Assessment of prediction accuracy for $\varepsilon_{u,c}$ and $\varepsilon_{f,c}$	73
Table 3.9 Measured and predicted material properties of cold–formed steels used for comparison.....	88
Table 3.10 Quantitative evaluation results between proposed material models.	89
Table 4.1 Welding parameters for the Gas–shield metal arc welding.....	93
Table 4.2 Measured material properties of N series press–braked RHSs.....	95
Table 4.3 Measured material properties of H series press–braked RHSs.....	96
Table 4.4 Key parameters and results of press–braked RHS stub column tests.	104
Table 4.5 Comparisons of test results to different FE models.	110
Table 4.6 Adopted parameters in parametric studies.	111
Table 4.7 Inputted material properties in parametric studies.....	112
Table 4.8 Comparisons between test and FEM results and design methods.	115
Table 4.9 Key parameters and results of press–braked RHS long column test.	120
Table 4.10 Comparisons between different adopted values of global imperfection..	124

Table 4.11 Input material properties adopted in the parametric study.	127
Table 4.12 Comparison of experimental and numerical results with design values..	132
Table 4.13 Summary of statistical parameters in reliability analysis.....	137
Table 4.14 Results of reliability analysis for different design methods.....	138
Table 5.1 Welding parameters for the Gas–shield metal arc welding.....	143
Table 5.2 Obtained material properties of Q460 steel plates.	147
Table 5.3 Obtained material properties of Q690 steel plates.	147
Table 5.4 Dimensions and test results of regular OctHS columns.....	153
Table 5.5 Dimensions and test results of irregular OctHS columns.	154
Table 5.6 Comparisons between different global imperfection for regular OctHSs..	167
Table 5.7 Comparisons between different global imperfection for irregular OctHSs.	167
Table 5.8 Input material properties adopted in the parametric study.	170
Table 5.9 Assessments of different design methods.	181
Table 5.10 Results of reliability analysis for different design methods.....	190

Chapter 1 Introduction

1.1 Background

With the advancement of steel manufacturing methods like thermal mechanical control processing (TMCP) and quenching and tempering (QT), and the developing cognition on the welding technique, use of high strength structural steels (with nominal yield strength ≥ 460 MPa) is gradually becoming the mainstream in the construction markets. The high strength steel members typically offer larger resistance and higher strength-to-weight ratio than their normal strength counterparts, which further result in reduced component sizes and increased floor area. Meanwhile, the decrease in resource consumption and transportation time can reduce the carbon footprint and support the sustainability agenda. Due to the advantages of ease of fabrication, less energy consumption, and cost-effectiveness, cold-formed high strength steel members have been widely employed in a variety of structural engineering projects.

Two commonly used cold-formed manufacturing methods are cold-rolling and press-braking, in which the steel sheet is continuously fed into a successive set of rollers, or predetermined bends are punched along the length of the steel sheet, to produce required cold-formed steel sections. Different levels of cold-work (plastic deformation) are generated during the manufacturing process of cold-formed cross-sections, resulting in changes to the stress-strain characteristics of the material. Generally, cold-work results in a more rounded stress-strain response with an increased yield strength and, to a lesser extent, an increased ultimate strength, but reduced ductility. Strength enhancement and material constitutive models are an essential part of structural engineering and a key component of analytical, numerical and design models. A number of material models have been developed to represent the strength

enhancement level and stress–strain response of cold–formed steels. However, those models are mainly established on the experimental results of conventional strength steels with nominal yield strengths of 235 MPa to 355 MPa, and there is lack of test data on high strength steel with nominal yield strengths equal to or larger than 460 MPa. Hence, to obtain precise strength enhancement and material constitutive models for cold–formed steels, more cold–formed steels fabricated from normal to high strength steels should be tested to provide fundamental test data.

Cold–formed structural hollow sections have been widely applied in steel construction worldwide due to their high resistance against torsion and desirable architectural appearance. Typical profiles of structural polygonal hollow sections usually include rectangular hollow sections (RHS), hexagonal hollow sections (HexHS), octagonal hollow sections (OctHS), etc. Numerous research studies have been carried out over the last decades on the structural performance of rectangular, circular and elliptical steel hollow sections, covering the structures made of conventional strength steel and high strength steel with nominal yield strength up to 1100 MPa. However, limited research has been conducted on the polygonal hollow sections. Octagonal hollow section (OctHS), as a member of the polygonal hollow section family, has been extensively adopted in transmission structures, substation structures, and steel pole structures. The multi–sided feature of OctHSs allows the cross–section to have the capabilities to provide a better local buckling resistance and more effective confining stress to the concrete core in CFST than its rectangular hollow section counterpart with the same outer perimeter. What is more important, it can also offer a more convenient accessible construction platform for welding and bolting of beam–to–column connection, as compared with its circular hollow section counterpart. Despite the fact that extensive research has been performed on OctHS and octagonal concrete–filled stub columns, no experimental investigation on OctHS long columns was conducted to

understand their global buckling (also known as flexural buckling) behaviour, though the most common applications of OctHSs can be found as the bracing in tubular transmission structures and the compression member in steel pole structures where columns were designed to withstand the gravity load of overhead power lines and other affiliated facilities. Hence, an investigation into the global buckling behaviour of these slender components is necessary to further guarantee the precise and safe structural design of civil infrastructures.

1.2 Objectives and scope

The key objectives of this project are shown below:

(1) To propose predictive expressions for material properties of cold-formed steel.

Cold-forming effects lead to changes to mechanical properties within the cold-formed corner region. To examine the cold-forming effect and strength enhancement level within the corner region, cold-formed angle sections with various desired degrees of angles are fabricated through the press-braking process. Different degree of angle indicates a different level of plastic deformation and a different degree of change in mechanical properties. The material properties obtained from the cold-formed corner region are compared with those obtained from the virgin steel sheet. Predictive expressions are proposed to predict the changes of material properties within the cold-formed corner region.

(2) To establish the stress-strain relationship incorporating strength enhancement models of cold-formed steel.

The stress-strain characterisation of cold-formed steels is investigated based on

the extensive measured and collected experimental data. A material constitutive model for cold-formed steel is proposed to reproduce the stress-strain relationship incorporating the strength enhancement model. The applicability and accuracy of the proposed constitutive model are evaluated by comparing the reproduced stress-strain curve with the measured one.

(3) To investigate the structural behaviour of cold-formed polygonal hollow section steel columns.

The structural behaviours of cold-formed polygonal hollow sections are investigated through a series of column tests on rectangular hollow sections (RHS) and octagonal hollow sections (OctHS). Different steel grades, various cross-sectional slenderness and different non-dimensional slenderness are covered. Finite element models (FEM) are developed to replicate the test observations and conduct parametric studies, which are aimed to generate a wider range of databases.

(4) To propose a design approach for cold-formed polygonal hollow section steel structures.

The experimental and numerical results of cold-formed polygonal hollow section steel columns are obtained to examine the applicability of current codes of practice in the American Specifications ANSI/AISC 360-16, and ASCE SEI 48-19, the European codes EN 1993-1-1, EN 1993-1-5, EN 1993-1-12, Chinese code GB 50017-2017, and Australian code AS 4100-2020. Design recommendations for polygonal hollow section structures are proposed. The predicted design strengths from different methods are compared to the test and numerical results, and the reliability analysis is also

performed to verify the applicability of the proposed design approaches.

1.3 Outline of this thesis

This thesis focuses on the material characterisation and structural behaviour of cold-formed polygonal hollow section columns. The layout of this thesis is summarised as follows:

Chapter 1 briefly introduces the content of this thesis, describing the background, objectives and scope of this research project.

Chapter 2 reports a comprehensive review of the strength enhancement models, material constitutive models for hot-rolled steels and cold-formed steels, and the structural behaviour of polygonal hollow sections under compression.

Chapter 3 presents the experimental investigation of the mechanical properties of cold-formed steels through the standard tensile coupon test. Predictive expressions for the change of material properties and material constitutive models are proposed based on the generated test results and collected test data.

Chapter 4 presents an experimental investigation programme on the press-braked rectangular hollow section columns, including material properties, residual stress measurements, local imperfection measurements, stub columns tests and long column tests. Finite element models are developed and validated against the test results and used to generate a wider spectrum of database. Existing design rules are assessed, and design recommendations are proposed for press-braked RHS columns.

Chapter 5 presents an experimental investigation programme on the cold-formed OctHS columns. Specimen design details, material properties, measurement of initial global imperfection, pin-ended column test setup, and test results are reported. Finite

element models are developed and validated against the test results and used to generate a wider spectrum of database. Existing design rules are assessed, and design recommendations are proposed for cold-formed OctHS columns.

Chapter 6 draws the conclusion of the current findings of this thesis. The important findings are summarised in this chapter. Future research works are also presented.

Chapter 2 Literature review

2.1 Introduction

This chapter presents a comprehensive review of previous research on strength enhancement due to the cold-forming process and material constitutive models for hot-rolled and cold-formed structural steels. Following the review on the material level, a review of the cross-section and member behaviour of cold-formed polygonal hollow sections including rectangular hollow sections and polygonal hollow sections was conducted. Further details of the review work will be presented in the following sub-chapters.

2.2 Strength enhancement due to cold-forming process

In the manufacturing of steel products, manufacturing methods may lead to significant changes to the mechanical properties of steel. For instance, rectangular hollow section (RHS) tube products can be generally classified into two sets based on their manufacturing methods, namely hot-finished tubes and cold-formed tubes. Hot-finished RHS tubes may be more favourable because of the uniform distribution of material properties and neglectable residual stresses after heat treatment. However, cold-formed RHS tubes still gain their positions in the market due to the merits of comparatively easier fabrication methods and high economic efficiencies. For the RHS tube undergoes cold-working but without post-production heat treatment during their fabrication process, they can be regarded as cold-formed RHS tubes. There are various cold-working methods to produce RHS tubes, including indirect-forming, direct-forming and a less common method by tip-to-tip welding of two press-braked channel sections.

For the indirect-forming process, the steel strip was firstly roll-formed into a circular shape, then the open circular shape was merged by longitudinal welding and subsequently flattened to the desired rectangular hollow section, as illustrated in Figure 2.1. With respect to the direct-forming process illustrated in Figure 2.2, the steel strip was directly formed into an open rectangular shape by a set of rollers, and then the opening was closed by the longitudinal welding, typically Submerged-arc welding. Similar to the direct-forming, such as the tube undergoes only one-time cold-working, the cold-formed RHS tubes can also be manufactured by tip-to-tip welding two press-braked channel sections together, as shown in Figure 2.3.

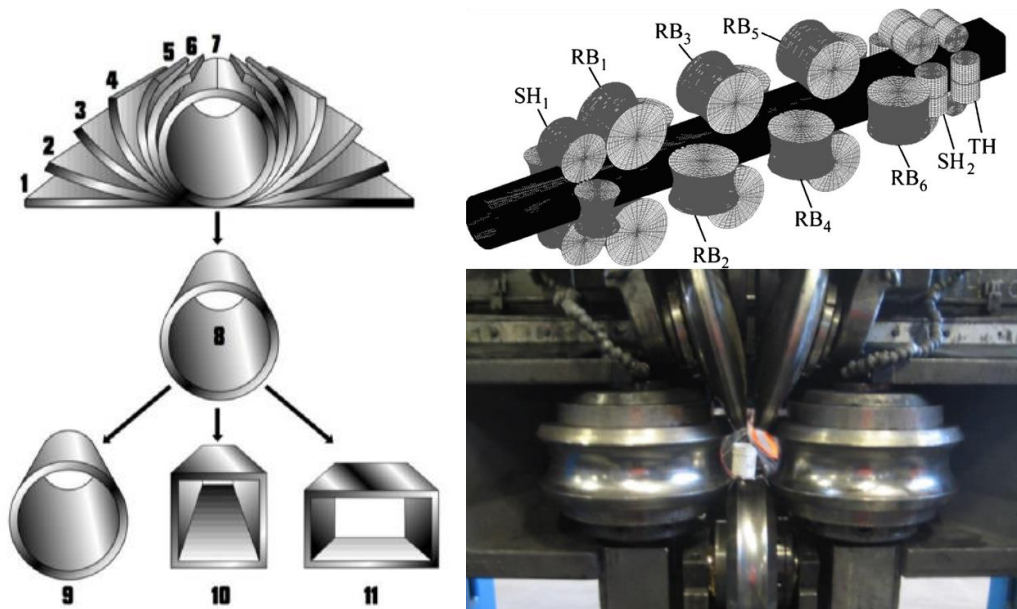


Figure 2.1 Manufacturing process of indirect forming RHS tubes (Tayyebi *et al.*, 2020).

Generally, these cold-forming manufacturing processes introduce different levels of plastic deformation into the deformed regions of cross-sections. As a result, the material properties of steels in the deformed region vary from those of parent materials. A more rounded stress-strain response with reduced Young's modulus, enhanced yield strength and ultimate tensile strength, and loss in ductility can be observed among those metallic materials experienced cold-forming.

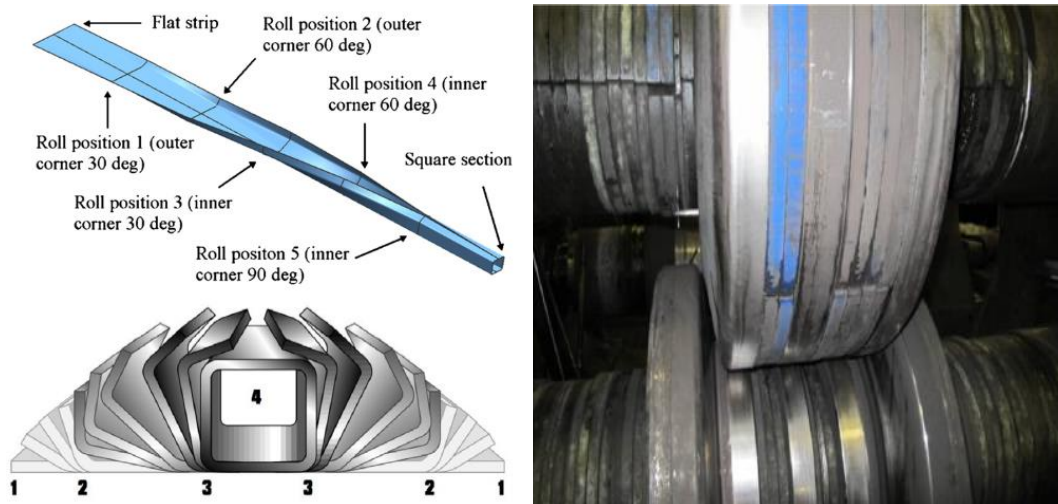


Figure 2.2 Manufacturing process of direct forming RHS tubes (Tayyebi *et al.*, 2020).



Figure 2.3 Manufacturing process of press-braking RHS tubes.

As illustrated in Figure 2.4, during the yielding process of a steel specimen subjected to an external load, slip occurs between two adjacent planes of atoms, and the slip further generates a permanent deformation and random dislocation regions in the crystal structure. With the increase of deformation, the steel specimen gradually deforms into strain hardening range, in which more dislocations are generated and piled up between crystal boundaries and interactions between adjacent dislocations becomes more complicated, in turn restraining the slip and thus adding additional obstacles to the yielding process. At this moment, if the steel specimen is unloaded and reloaded immediately, reduced Young's modulus (Kim *et al.*, 2013; Yang *et al.*, 2004) and increased proportional limit strength may be obtained (Chajes *et al.*, 1963), and the original ultimate tensile strength and remaining ductility will be conserved (shown as

the green dash line in Figure 2.4). This instantaneous effect of plastic deformation (except for the decrease in Young's modulus), known as strain hardening, leads to an increase in the proportional limit strength, but does not affect the ultimate tensile strength and the ductility.

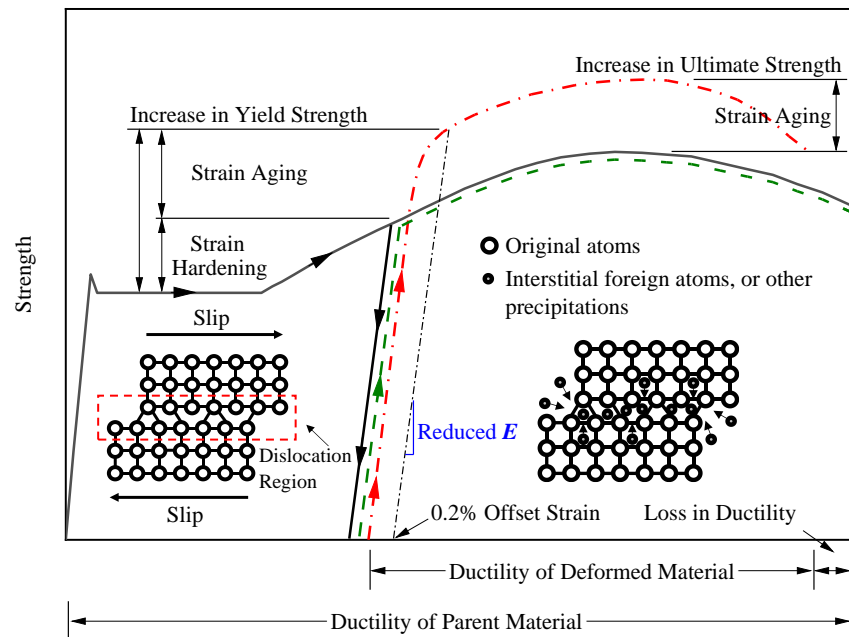


Figure 2.4 Effects of strain hardening and strain aging.

In the other case, if the deformed steel specimen is reloaded after sufficient time, the steel specimen behaves differently from the immediately reloaded counterpart. During the sufficient time before reloading, the foreign atoms, such as interstitial carbon and nitrogen atoms and other precipitations began to diffuse to the vicinity of dislocations, and subsequently fill the vacant space between dislocations. These impurities impede the movements and strengthen the interactions between dislocations (Hosford, 2012). This long-lasting effect is known as strain ageing, which leads to an increase in the yield strength and ultimate tensile strength, but deterioration of ductility. Thereafter, increases in yield strength and ultimate tensile strength, but a loss in ductility can be observed in the test (shown as the red dash-dot line in Figure 2.4). In general, the most significant part of strain aging effect happens in the first 14 days at

ambient temperature or 30 mins at 100 °C (Chajes *et al.*, 1963; Yang *et al.*, 2022). It should be noted that in this study enough elapsed time was allowed before material tests.

In the 1960s, a comprehensive research project on the effects of cold-forming with a specific emphasis on cold-formed light-gauge steel members began at Cornell University under the direction of Professor George Winter. The progress report of this project (Karren, 1965) summarised the experimental investigations and findings on the effects of cold-forming on the yield strength of flat and corner portions of sections, full section compression and tension tests and column buckling tests. Discussions on this research item can be found in Britvec *et al.* (1970). A semi-empirical model has been proposed and calibrated on the basis of Karren's experimental data. To derive the final form of this semi-empirical predictive model, several simplifications and assumptions should be made as follows. A power equation was adopted to represent the strain hardening behaviour of the plastic region in true stress-strain response ($\bar{\sigma} - \bar{\varepsilon}$), as expressed in Eq. (2.1).

$$\bar{\sigma} = k (\bar{\varepsilon})^{n_{se}} \quad \text{Eq. (2.1)}$$

where k and n_{se} are material coefficient and strain-hardening exponent, respectively, given by

$$k = 2.80 f_{u,f} - 1.55 f_{y,f} \quad \text{Eq. (2.2)}$$

$$n_{se} = 0.225 f_{u,f} / f_{y,f} - 0.120 \quad \text{Eq. (2.3)}$$

A simplified corner model was established to analyse the plastic strain caused by cold-works in the corner region, as shown in Figure 2.5, in which t is the thickness of steel sheet, θ is the included angle, r_i , r_n , r_o are the inner corner radius, radius at the neutral surface, and outer corner radius, respectively. To theoretically compute the

average corner yield strength $f_{y,c}$ in the corner area, the effective stress was integrated over the entire area of the corner A_c using Eq. (2.4). The effective stress can then be integrated analytically, and the enhanced corner yield strength can be calculated by Eq. Eq. (2.4).

$$l_0 f_{y,c} = k \int_A |\bar{\epsilon}|^{n_{se}} dA \quad \text{Eq. (2.4)}$$

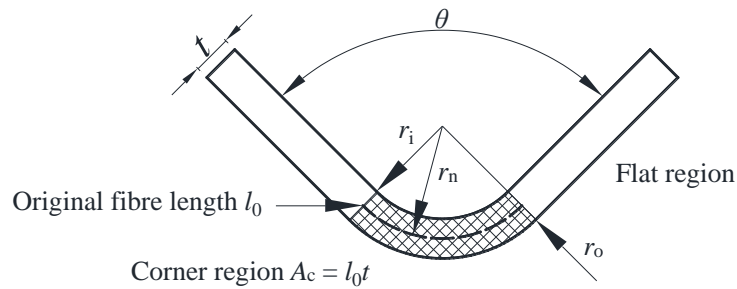


Figure 2.5 Illustration of the simplified corner model.

Utilising the assumptions of von Mises yield criteria under uniaxial tension and invariable volume strain of element, Eq. (2.4) can be subsequently converted to Eq. (2.5).

$$\frac{f_{y,c}}{k} = \frac{1}{t} \int_{r_i}^{r_o} \left| \frac{2}{\sqrt{3}} \ln \frac{r}{(r_i + r_o)/2} \right|^{n_{se}} \frac{r}{(r_i + r_o)/2} dr \quad \text{Eq. (2.5)}$$

If the ratio of r_i/t is less than 10, linear relationships can be found between $f_{y,c}/k$ and r_i/t on the log–log paper, then Eq. (2.5) can be further simplified and approximated. The final form of Karren’s predictive model can thus be obtained, as given by

$$f_{y,c} = \frac{kb}{(r_i/t)^m} \quad \text{Eq. (2.6)}$$

where $b = 1.0-1.3n_{se}$ and $m = 0.035+0.855n_{se}$.

Karren’s theory and model to predict the strength enhancement for sections formed by both cold–rolling and press–braking is currently adopted in the North American

Specification for the Design of Cold-Formed Steel Structural Members (AISI, 2016), as the basis for computing the design yield stress of cold-formed sections. The predictive expression for increased corner strength is formulated as Eq. (2.7), where key parameters B_c , and m can be determined through Eq. (2.8) to Eq. (2.9). According to this model, the ratio of the virgin steel material's ultimate tensile strength $f_{u,f}$ to yield strength $f_{y,f}$, the inner bending radius of the corner r_i , and the thickness t of the flat steel sheet all influence the increase in yield strength at the corners.

$$f_{y,c} = \frac{B_c f_{y,f}}{\left(\frac{r_i}{t}\right)^m} \quad \text{Eq. (2.7)}$$

$$B_c = 3.69 \left(\frac{f_{u,f}}{f_{y,f}}\right) - 0.819 \left(\frac{f_{u,f}}{f_{y,f}}\right)^2 - 1.79 \quad \text{Eq. (2.8)}$$

$$m = 0.192 \left(\frac{f_{u,f}}{f_{y,f}}\right) - 0.068 \quad \text{Eq. (2.9)}$$

Lind and Schroff (1971) suggested that the Karren's model is complicated, impossible to understand without recourse to Karren (1967), and difficult to manually execute without referring to the specification or standard for details. Hence, based on Karren's experimental data and without further testing, Lind and Schroff (1971) developed a new and less complicated theory to predict the corner yield strength. The proposed linear model permits a very simple application for calculating the yield force for a corner as given by Eq. (2.10), where ΔP is the increase in yield force, t is the tube thickness, and θ is the corner angle. Then the enhanced corner yield strength can be determined by Eq. (2.11), in which A is the area of the corner. However, according to the evaluation results, this model tends to overestimate the corner yield strength for cold-formed sections with relatively small bending radii.

$$\Delta P = 5t^2 (f_u - f_y) (\theta / 90^\circ) \quad \text{Eq. (2.10)}$$

$$f_{y,c} = f_{y,f} + \Delta P / A \quad \text{Eq. (2.11)}$$

Based on two series of experimental investigations on cold-formed steel channel sections, Abdel-Rahman and Sivakumaran (1997) suggested that there is also an additional strength enhancement region $1/2\pi r$ existed in the adjacent area of the corner, though the increase of yield strength in the adjacent area was not as significant as that in corner portion. Hence, Abdel-Rahman and Sivakumaran (1997) revised the original Karren's model to predict the average increase in yield strength of the corner zone (Quadrant+ $1/2\pi r$), and the modified model is given by Eq. (2.12).

$$\text{Average } \Delta f_y = 0.6 \left(\frac{B_c}{\left(\frac{r}{t}\right)^m} - 1.0 \right) f_{y,f} \quad \text{Eq. (2.12)}$$

Similarly, on the basis of experimental results on extracted corner coupons from cold-rolled steel rectangular hollow sections, Gardner *et al.* (2010) modified the predictive model given in AISI S100-16 (AISI, 2016) by adopting the original form of the AISI model but with a revised predictive expression for coefficients B_c and m , as given by Eq. (2.13) and Eq. (2.14). The modified predictive model was found to have a better performance in predicting the strength enhancement in the corners of cold-rolled RHS.

$$B_c = 2.90 \left(\frac{f_{u,f}}{f_{y,f}} \right) - 0.752 \left(\frac{f_{u,f}}{f_{y,f}} \right)^2 - 1.09 \quad \text{Eq. (2.13)}$$

$$m = 0.230 \left(\frac{f_{u,f}}{f_{y,f}} \right) - 0.041 \quad \text{Eq. (2.14)}$$

Since Karren (1967) proposed their model, taking into account the effects of the

ratio of the virgin steel material's ultimate tensile strength $f_{u,f}$ to yield strength $f_{y,f}$, the inner bending radius of the corner r_i , and the thickness t of the flat steel sheet, it provides a reasonable model for predicting the strength enhancement of nonlinear metallic material due to the cold-forming effects. The development of the Karren's model into stainless steel can also be found in the literature (Ashraf *et al.*, 2005; Coetsee *et al.*, 1990; Van den Berg and Van der Merwe, 1992).

Rossi *et al.* (2013) proposed an alternative model to predict the strength enhancement in the corner regions of cold-formed sections based on determining the plastic strains associated with the dominant stages in the fabrication process and using an inverted compound Ramberg–Osgood stress–strain relationship for the unformed material. The Rossi models for predicting the increased yield strength of the flat portions $f_{y,f}$ of cold-rolled sections and the corner portions $f_{y,c}$ of cold-rolled and press-braked sections, are given by Eq. (2.15) and Eq. (2.16), respectively, in which $\varepsilon_{f,av}$ and $\varepsilon_{c,av}$ are the induced averaged plastic strain during the cold-forming process, as defined by Eq. (2.17) and Eq. (2.18), and p and q refer to the material parameters that can be directly computed from Eq. (2.19) and Eq. (2.20).

$$f_{y,f} = p(\varepsilon_{f,av} + \varepsilon_{0.2})^q, \text{ but } \leq f_u \quad \text{Eq. (2.15)}$$

$$f_{y,c} = p(\varepsilon_{c,av} + \varepsilon_{0.2})^q, \text{ but } \leq f_u \quad \text{Eq. (2.16)}$$

$$\varepsilon_{f,av} = \left[\frac{t}{900} \right] + \left[\frac{\pi t}{2(b+h-2t)} \right] \quad \text{Eq. (2.17)}$$

$$\varepsilon_{c,av} = \frac{t}{2(2r_i + t)} \quad \text{Eq. (2.18)}$$

$$p = \frac{f_y}{\varepsilon_{0.2}^q} \quad \text{Eq. (2.19)}$$

$$q = \frac{\ln(f_y / f_u)}{\ln(\varepsilon_{0.2} / \varepsilon_u)} \quad \text{Eq. (2.20)}$$

2.3 Material constitutive models for structural steels

Since the rapid development of advanced analytical and numerical modelling techniques of structural engineering, finite element modelling software such as ANSYS and ABAQUS are able to mimic steel structures undergoing different working conditions. One of the most significant features to establish an accurate structural model is how to precisely depict the material stress–strain relationship. Precise material stress–strain relationships make it possible to accurately simulate the behaviour of steel structures under different workloads and expected scenarios. In this section, a brief developing history overview of existing material constitutive models for hot–rolled steel and cold–formed steel is presented.

2.3.1 Structural steel with sharply defined yield point and distinct yield plateau

Normal strength structural steels and part of high strength steels generally exhibit a patterned stress–strain response due to their specific fabrication. The typical stress–strain response of hot–rolled steel generally consists of three parts: (1) In the linear elastic stage, the curve is defined by a constant modulus of elasticity E_s and the yield strength f_y , (Upper and lower yield strength) (2) In the plastic yield plateau, the zone of the plastic flow in the yield plateau is restricted from the yield strain ε_y until the strain–hardening strain ε_{sh} , and (almost constant yield stress) (3) In the strain–hardening range, the stress starts to increase again with a reducing rate up to the ultimate tensile strength f_u and the corresponding ultimate tensile strain ε_u .

To facilitate the description of material behaviour, several simplified material constitutive models have been proposed to describe the stress–strain response of this

type of steel with a sharply defined yield point and distinct yield plateau. According to their degree of simplification, those constitutive models can be divided into 5 groups as illustrated in Figure 2.6:

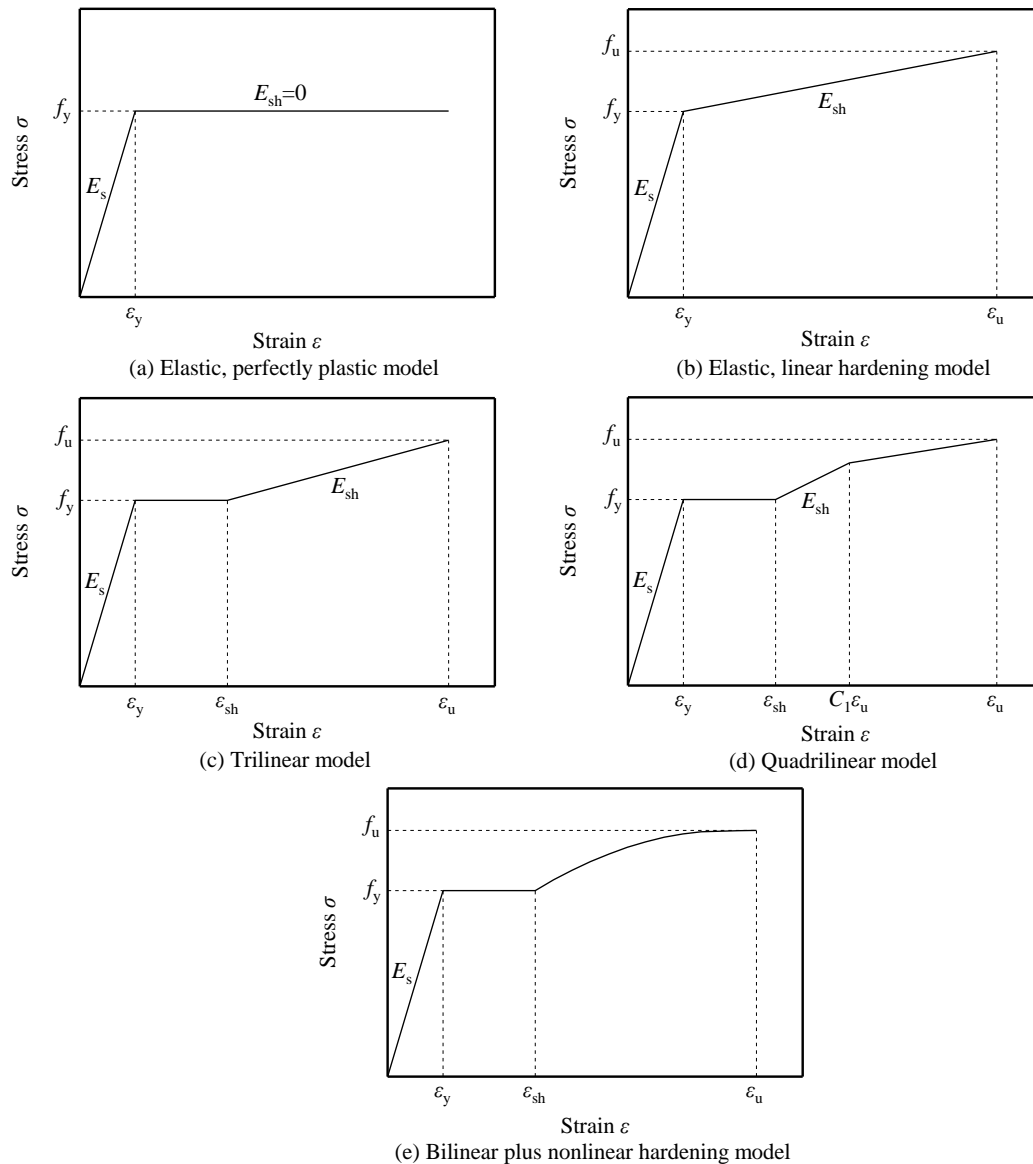


Figure 2.6 Material constitutive models of the hot-rolled steel.

(a) Elastic, perfectly plastic model: This model is the most simplified model in which the strain-hardening is ignored and this model is the fundamental assumption of EN 1993-1-1 (CEN, 2005) design methods. This model is a good choice for situations when strain hardening isn't expected to happen in the modelling of structural elements whose failure mode is dominated by instability or if strain hardening is simply ignored

for simplified calculation. The elastic, perfectly plastic model can be expressed as Eq. (2.21).

$$\sigma = \begin{cases} E\varepsilon & \text{for } \varepsilon \leq \varepsilon_y \\ f_y & \text{for } \varepsilon > \varepsilon_y \end{cases} \quad \text{Eq. (2.21)}$$

(b) Elastic, linear hardening model: The simplest consideration of strain–hardening is taken into consideration in this model to permit structural steels to develop their beneficial features of strain–hardening and allow for a more cost–effective design in the current steel structure design methods, for instance, EN 1993–1–5 (CEN, 2009) and continuous strength method (Buchanan *et al.*, 2016; Yun *et al.*, 2018). The elastic, linear hardening model can be expressed as Eq. (2.22).

$$\sigma = \begin{cases} E\varepsilon & \text{for } \varepsilon \leq \varepsilon_y \\ f_y + E_{sh}(\varepsilon - \varepsilon_y) & \text{for } \varepsilon_y < \varepsilon \leq \varepsilon_u \end{cases} \quad \text{Eq. (2.22)}$$

(c) Trilinear model: Though the elastic, linear hardening model simply takes into account the strain–hardening behaviour, it neglects the most noteworthy characteristic of hot–rolled steel, the yield plateau in which the yield stress remains approximately constant. Hence, a trilinear model is proposed to represent the characteristics of materials that have the yield plateau and the following strain–hardening behaviour. Similar to the elastic, linear hardening model, a constant strain–hardening modulus E_{sh} is adopted in the trilinear model, as shown in Eq. (2.23).

$$\sigma = \begin{cases} E\varepsilon & \text{for } \varepsilon \leq \varepsilon_y \\ f_y & \text{for } \varepsilon_y < \varepsilon \leq \varepsilon_{sh} \\ f_y + E_{sh}(\varepsilon - \varepsilon_{sh}) & \text{for } \varepsilon_{sh} < \varepsilon \leq \varepsilon_u \end{cases} \quad \text{Eq. (2.23)}$$

(d) Quadrilinear model: The quadrilinear model proposed by Yun and Gardner (2017) is established on the improvement of the trilinear model in which the linear

strain-hardening behaviour is divided into two segments. This modified two-stage strain-hardening behaviour can simply represent the material behaviour of reduced stiffness in the actual stress-strain response. The quadrilinear model is given by Eq. (2.24), in which the strain-hardening strain ε_{sh} , the strain-hardening modulus E_{sh} , the ultimate tensile strain ε_u , and the control parameters C_1 and C_2 can find their empirical solution in Yun and Gardner (2017).

$$\sigma = \begin{cases} E\varepsilon & \text{for } \varepsilon \leq \varepsilon_y \\ f_y & \text{for } \varepsilon_y < \varepsilon \leq \varepsilon_{sh} \\ f_y + E_{sh}(\varepsilon - \varepsilon_{sh}) & \text{for } \varepsilon_{sh} < \varepsilon \leq C_1\varepsilon_u \\ f_{C_1\varepsilon_u} + \frac{f_u - f_{C_1\varepsilon_u}}{\varepsilon_u - C_1\varepsilon_u}(\varepsilon - C_1\varepsilon_u) & \text{for } C_1\varepsilon_u < \varepsilon \leq \varepsilon_u \end{cases} \quad \text{Eq. (2.24)}$$

(e) Bilinear plus nonlinear hardening model: Serving for the mimic of the gradual loss of material stiffness in advanced numerical simulation, Mander (1983) proposed bilinear plus nonlinear hardening models to represent the progressive loss of stiffness up to the ultimate tensile strength f_u . Recently, this bilinear plus nonlinear hardening model was modified by Yun and Gardner (2017) based on the calibration against over 500 collected actual stress-strain curves from the literature and was presented in Eq. (2.25). The proposed constitutive model for both normal and high strength hot-rolled structural steels were demonstrated to be more accurate than the frequently used ECCS (ECCS, 1986) model and to be in good agreement with actual stress-strain responses throughout the whole range of tensile strains.

$$\sigma = \begin{cases} E\varepsilon & \text{for } \varepsilon \leq \varepsilon_y \\ f_y & \text{for } \varepsilon_y < \varepsilon \leq \varepsilon_{sh} \\ f_y + (f_u - f_y) \left\{ 0.4 \left(\frac{\varepsilon - \varepsilon_{sh}}{\varepsilon_u - \varepsilon_{sh}} \right) + 2 \left(\frac{\varepsilon - \varepsilon_{sh}}{\varepsilon_u - \varepsilon_{sh}} \right) / \left[1 + 400 \left(\frac{\varepsilon - \varepsilon_{sh}}{\varepsilon_u - \varepsilon_{sh}} \right)^5 \right]^{1/5} \right\} & \text{for } \varepsilon_{sh} < \varepsilon \leq \varepsilon_u \end{cases} \quad \text{Eq. (2.25)}$$

2.3.2 Cold-formed steel

As compared with steel with a sharply defined yield point and distinct yield plateau, cold-formed steels and part of high strength steels are similar to the stainless steels and aluminium that have a relatively rounded stress–strain response with no sharply defined yield point. This phenomenon can be attributed to the cold-forming process in which steel undergoes enormous plastic deformation and then the yield plateau has been erased. Due to the rounded stress–strain response and lack of the yield plateau, it is not as easy as hot-rolled steel to define the yield strength for cold-formed steels and part of the high strength steels. Subsequently, the 0.2% proof strength $f_{0.2}$ (Defined as the stress resulting in 0.2% plastic strain) was selected to replace the yield strength for those steels. A typical stress–strain response for cold-formed steel and the key parameters of the material model are depicted in Figure 2.7.

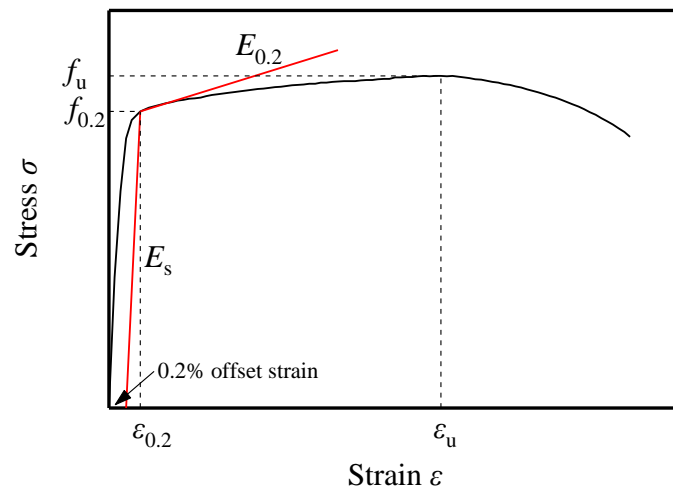


Figure 2.7 Typical stress–strain response of the cold-formed steel.

Holmquist and Nadai (1939) firstly proposed a polynomial formula (Eq. (2.26)) to depict the material response beyond the proportional limit which forms the basis of predicting the buckling resistance of metallic tubes.

$$\varepsilon = \begin{cases} \frac{\sigma}{E} & \text{for } \sigma \leq f_P \\ \frac{\sigma}{E} + \varepsilon_y \left(\frac{\sigma - f_P}{f_y - f_P} \right)^n & \text{for } \sigma > f_P \end{cases} \quad \text{Eq. (2.26)}$$

Later, Ramberg and Osgood (1943) proposed an expression to describe the stress–strain relationship for stainless steel, aluminium alloy, and carbon steel sheet, as shown in Eq. (2.27). In this formula which is well known as Ramberg and Osgood model, three basic parameters modulus of elasticity E , constants K and n can be derived from a given material stress–strain curve.

$$\varepsilon = \frac{\sigma}{E} + K \left(\frac{\sigma}{E} \right)^n \quad \text{Eq. (2.27)}$$

Hill (1944) modified the original Ramberg–Osgood model to achieve a simple application by adopting two offset strengths $f_{0.2}$ (0.2% proof strength) and $f_{0.01}$ (0.01% proof strength). The simplified Ramberg–Osgood model is shown in Eq. (2.28), in which n is the strain hardening exponent (Rasmussen and Hancock, 1993) and can be determined from Eq. (2.29), which is adopted in the current design code EN 1993–1–4 (CEN, 2006a).

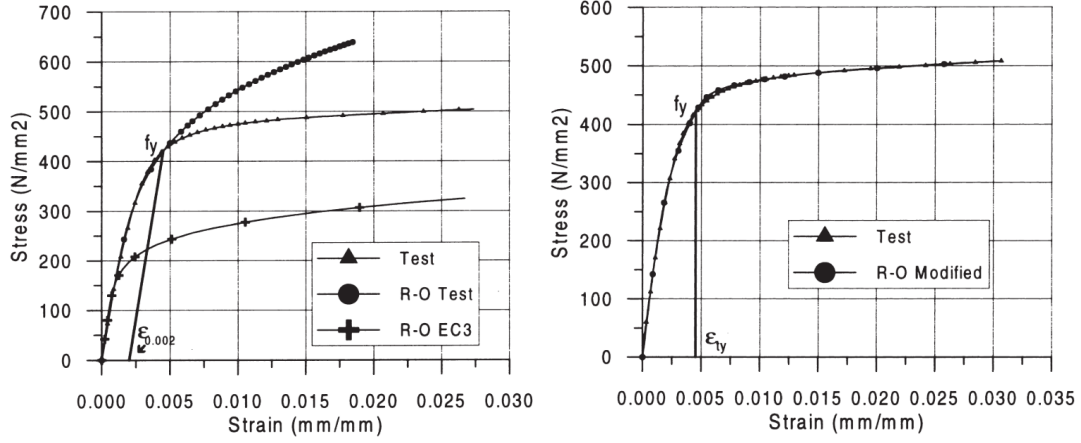
$$\varepsilon = \frac{\sigma}{E} + 0.002 \left(\frac{\sigma}{f_{0.2}} \right)^n \quad \text{Eq. (2.28)}$$

$$n = \frac{\ln(20)}{\ln(f_{0.2} / f_{0.01})} \quad \text{Eq. (2.29)}$$

Though original and modified Ramberg–Osgood models were found to yield a satisfactory agreement with the measured material stress–strain curves before the equivalent yield point ($\varepsilon_{0.2}$, $f_{0.2}$) by selecting appropriate strain hardening exponent n , these one–stage Ramberg–Osgood models generally cannot accurately capture the

stress–strain behaviour in higher stress level (Between the yield point $(\varepsilon_{0.2}, f_{0.2})$ and the ultimate tensile point (ε_u, f_u)), overestimating the material behaviour, as shown in Figure 2.8 (a). Based on this observation, Mirambell and Real (2000) proposed a two–stage material stress–strain model for stainless steels, establishing on the original Ramberg–Osgood formula, as given by Eq. (2.30), in which the strain hardening exponents n and m were obtained through trial and error. They deemed that the shape of the stress–strain curve in the range of the yield point $(\varepsilon_{0.2}, f_{0.2})$ to the ultimate tensile point (ε_u, f_u) is similar to the shape of the curve between the origin point $(0,0)$ up to the yield point $(\varepsilon_{0.2}, f_{0.2})$. Hence, the second stage of the Mirambell and Real’s model was established by moving both vertical and horizontal axes from the origin point $(0,0)$ to the yield point $(\varepsilon_{0.2}, f_{0.2})$, substituting the $\sigma - f_{0.2}$ for σ , $E_{0.2}$ for E , plastic strain at the ultimate strength $\varepsilon_u - \varepsilon_{0.2} - \frac{f_u - f_{0.2}}{E_{0.2}}$ for 0.002 (0.2%) strain, and $f_u - f_{0.2}$ for $f_{0.2}$. At the transition point (i.e., the yield point $(\varepsilon_{0.2}, f_{0.2})$) between the two stages, continuity of slope and position can still be maintained. As shown in Figure 2.8 (b), the modified two–stage Ramberg–Osgood model yield a better agreement in the range of the yield point $(\varepsilon_{0.2}, f_{0.2})$ to the ultimate tensile point (ε_u, f_u) .

$$\varepsilon = \begin{cases} \frac{\sigma}{E} + 0.002 \left(\frac{\sigma}{f_{0.2}} \right)^n & \text{for } \sigma \leq f_{0.2} \\ \frac{\sigma - f_{0.2}}{E_{0.2}} + \left(\varepsilon_u - \varepsilon_{0.2} - \frac{f_u - f_{0.2}}{E_{0.2}} \right) \left(\frac{\sigma - f_{0.2}}{f_u - f_{0.2}} \right)^m + \varepsilon_{0.2} & \text{for } f_{0.2} < \sigma \leq f_u \end{cases} \quad \text{Eq. (2.30)}$$



(a) The original Ramberg–Osgood model.

(b) Mirambell model

Figure 2.8 The comparison between the original Ramberg–Osgood model and Mirambell model (Mirambell and Real, 2000).

Due to the fact that relatively large tensile strain can be obtained in stainless steel alloys, Rasmussen (2003) simplified Mirambell and Real’s model by approximating the transformed ultimate plastic strain $\varepsilon_u - \varepsilon_{0.2} - \frac{f_u - f_{0.2}}{E_{0.2}}$ by total ultimate plastic strain ε_u , as shown in Eq. (2.31), where the tangential modulus of elasticity at the yield point $(\varepsilon_{0.2}, f_{0.2}) E_{0.2}$, the second strain hardening exponent m , the ultimate tensile strain ε_u , the ultimate tensile strength f_u are given by Eq. (2.32) to Eq. (2.35). The Rasmussen model is nowadays adopted in Annex C of EN1993–1–4 (CEN, 2006a).

$$\varepsilon = \begin{cases} \frac{\sigma}{E} + 0.002 \left(\frac{\sigma}{f_{0.2}} \right)^n & \text{for } \sigma \leq f_{0.2} \\ \frac{\sigma - f_{0.2}}{E_{0.2}} + \varepsilon_u \left(\frac{\sigma - f_{0.2}}{f_u - f_{0.2}} \right)^m + \varepsilon_{0.2} & \text{for } f_{0.2} < \sigma \leq f_u \end{cases} \quad \text{Eq. (2.31)}$$

$$E_{0.2} = \frac{E}{1 + 0.002n \frac{E}{f_{0.2}}} \quad \text{Eq. (2.32)}$$

$$\frac{f_{0.2}}{f_u} = \begin{cases} 0.2 + 185 \frac{f_{0.2}}{E} & \text{for austenitic and duplex} \\ \frac{0.2 + 185 \frac{f_{0.2}}{E}}{1 - 0.0375(n-5)} & \text{for all stainless steel alloys} \end{cases} \quad \text{Eq. (2.33)}$$

$$\varepsilon_u = 1 - \frac{f_{0.2}}{f_u} \quad \text{Eq. (2.34)}$$

$$m = 1 + 3.5 \frac{f_{0.2}}{f_u} \quad \text{Eq. (2.35)}$$

Regarding the similar rounded stress–strain response of various stainless steel alloys, it is necessary to clarify accurate representations of the key parameters in material constitutive models to represent different material behaviours. Hence, on the basis of a comprehensive material database in which there are more than 600 collected measured stress–strain curves, Arrayago *et al.* (2015) proposed calibrated predictive expressions for those key parameters which affect the degree of roundedness, the level of strain hardening, and the ultimate tensile strain of stress–strain curves, as concluded in Eq. (2.36) to Eq. (2.39). Those predictive formulae were obtained through a curve fitting process based on least–squares adjustment techniques and the suitability and accuracy of those predictive parameters were further confirmed by performing validations against an additional 400 collected experimental results.

$$n = \frac{\ln(4)}{\ln(f_{0.2} / f_{0.05})} \quad \text{for all grades} \quad \text{Eq. (2.36)}$$

$$\frac{f_{0.2}}{f_u} = \begin{cases} 0.2 + 185 \frac{f_{0.2}}{E} & \text{for austenitic, duplex and lean duplex} \\ 0.46 + 145 \frac{f_{0.2}}{E} & \text{for ferritic stainless steel alloys} \end{cases} \quad \text{Eq. (2.37)}$$

$$\varepsilon_u = \begin{cases} 1 - \frac{f_{0.2}}{f_u} & \text{for austenitic, duplex and lean duplex} \\ 0.6 \left(1 - \frac{f_{0.2}}{f_u} \right) & \text{for ferritic stainless steel alloys} \end{cases} \quad \text{Eq. (2.38)}$$

$$m = 1 + 2.8 \frac{f_{0.2}}{f_u} \quad \text{for all grades} \quad \text{Eq. (2.39)}$$

For certain scenarios of advanced modelling, such as modelling the cold-forming process under very large strain and structural connection behaviour under extreme loading and deformation, a precise description of material stress-strain response up to very high strains is necessary. Following the need for more accurate material stress-strain relationships, three-stage Ramberg-Osgood expressions were developed by Quach *et al.* (2008) and Hradil *et al.* (2013).

To precisely represent material stress-strain relationships under both tensile and compressive conditions for both small to intermediate strains in the field of structural elements under the desired loading and large strains in the field of cold-forming processes, Quach *et al.* (2008) proposed a full range three-stage material constitutive model Eq. (2.40) that uses the basic Ramberg-Osgood expression for the first stage covering the strain range up to $\varepsilon_{0.2}$, the modified Gardner and Nethercot (2004) model for the second stage covering the strain range of $\varepsilon_{0.2} < \varepsilon < \varepsilon_{2.0}$. In the third stage of the Quach model, a straight line passing through the 2.0% proof strength point $(\varepsilon_{2.0}, f_{2.0})$ and ultimate tensile point (ε_u, f_u) is adopted, based on the observation of Olsson (2001) that the true stress-nominal strain relationship can be regarded as a straight line for stress beyond $f_{2.0}$ and the resulting inaccuracy can be compromised in such regime of high strains. In this material model, the empirical predictive formulae of key parameters for various materials under different working conditions can be found from Eq. (2.41) to Eq. (2.45).

$$\varepsilon = \begin{cases} \frac{\sigma}{E} + 0.002 \left(\frac{\sigma}{f_{0.2}} \right)^n & \sigma \leq f_{0.2} \\ \frac{\sigma - f_{0.2}}{E_{0.2}} + \left[0.008 + (f_{1.0} - f_{0.2}) \left(\frac{1}{E} - \frac{1}{E_{0.2}} \right) \right] \left(\frac{\sigma - f_{0.2}}{f_{1.0} - f_{0.2}} \right)^{n'_{0.2,1.0}} + \varepsilon_{0.2} & f_{0.2} < \sigma \leq f_{2.0} \\ \frac{\sigma - a}{b \mp \sigma} & f_{2.0} < \sigma \leq f_u \end{cases}$$

Eq. (2.40)

$$f_{2.0} \cong \frac{1 + (f_{1.0} / f_{0.2} - 1) A^{1/n'_{0.2,1.0}}}{1 + e(E / E_{0.2} - 1)(f_{1.0} / f_{0.2} - 1) \frac{A^{1/n'_{0.2,1.0}}}{n'_{0.2,1.0} B}} f_{0.2}$$

Eq. (2.41)

$$\frac{f_{1.0}}{f_{0.2}} = \begin{cases} 0.542 / n + 1.072 & \text{for tension coupons} \\ 0.662 / n + 1.085 & \text{for compression coupons} \end{cases}$$

Eq. (2.42)

$$n'_{0.2,1.0} = \begin{cases} 12.255 \left(\frac{E_{0.2}}{E} \right) \left(\frac{f_{1.0}}{f_{0.2}} \right) + 1.037 & \text{for tension coupons} \\ 6.399 \left(\frac{E_{0.2}}{E} \right) \left(\frac{f_{1.0}}{f_{0.2}} \right) + 1.145 & \text{for compression coupons} \end{cases}$$

Eq. (2.43)

$$f_u = \begin{cases} \frac{f_{0.2}^{\text{ten}}}{0.2 + 185 \frac{f_{0.2}^{\text{ten}}}{E}} & \text{for austenitic and duplex under tension} \\ \frac{1 - 0.0375(n - 5)}{0.2 + 185 \frac{f_{0.2}^{\text{ten}}}{E}} f_{0.2}^{\text{ten}} & \text{for all stainless steels under tension} \\ f_u^{\text{ten}} (1 + \varepsilon_u^{\text{ten}})^2 & \text{for all stainless steels under compression} \end{cases}$$

Eq. (2.44)

$$\varepsilon_u = \begin{cases} 1 - \frac{f_{0.2}^{\text{ten}}}{f_u^{\text{ten}}} & \text{for tension coupons} \\ 1 - \frac{1}{1 + \varepsilon_u^{\text{ten}}} & \text{for compression coupons} \end{cases}$$

Eq. (2.45)

Based on the fundamental concept of the Mirambell and Real model and the

Gardner and Nethercott model, Hradil *et al.* (2013) proposed a generalised three-stage material model which utilises three basic Ramberg–Osgood expressions with different reference systems for three corresponding stages. The complete form of this generalised three-stage model is formulated in Eq. (2.46), where the tangent moduli of elasticity and equivalent plastic strains of the second and third stages can be computed through Eq. (2.47) to Eq. (2.50). In additional, the inversion of the stress–strain relationship is also provided in Eq. (2.51) for the purpose of direct numerical iteration, while the model parameters and tangential moduli at each stage can be calculated according to details described in Hradil *et al.* (2013).

$$\varepsilon = \begin{cases} \frac{\sigma}{E} + 0.002 \left(\frac{\sigma}{f_{0.2}} \right)^{n^{0-0.2}} & \sigma \leq f_{0.2} \\ \frac{\sigma - f_{0.2}}{E_{0.2}} + \varepsilon_{0.2}^* \left(\frac{\sigma - f_{0.2}}{f_{1.0} - f_{0.2}} \right)^{n^{0.2-1.0}} + 0.002 + \frac{f_{0.2}}{E} & f_{0.2} < \sigma \leq f_{1.0} \\ \frac{\sigma - f_{1.0}}{E_{1.0}} + \varepsilon_{1.0}^* \left(\frac{\sigma - f_{1.0}}{f_u - f_{1.0}} \right)^{n^{1.0-u}} + 0.01 + \frac{f_{1.0}}{E} & f_{1.0} < \sigma \leq f_u \end{cases} \quad \text{Eq. (2.46)}$$

$$E_{0.2} = \frac{E}{1 + 0.002n \frac{E}{f_{0.2}}} \quad \text{Eq. (2.47)}$$

$$E_{1.0} = \frac{E_{0.2}}{1 + \varepsilon_{0.2}^* \times n_{0.2-1.0} \left(E_{0.2} / (f_{1.0} - f_{0.2}) \right)} \quad \text{Eq. (2.48)}$$

$$\varepsilon_{0.2}^* = 0.008 - (f_{1.0} - f_{0.2}) \left(\frac{1}{E_{0.2}} - \frac{1}{E} \right) \quad \text{Eq. (2.49)}$$

$$\varepsilon_{1.0}^* = (\varepsilon_u^{pl} - 0.01) - (f_u - f_{1.0}) \left(\frac{1}{E_{1.0}} - \frac{1}{E} \right) \quad \text{Eq. (2.50)}$$

$$\sigma = \begin{cases} \frac{E\varepsilon}{1 + (r_0 - 1)(\varepsilon / \varepsilon_{0.2})^{p_0}} & \varepsilon \leq \varepsilon_{0.2} \\ f_{0.2} + \frac{E_{0.2}(\varepsilon - \varepsilon_{0.2})}{1 + (r_{0.2} - 1)\left(\frac{\varepsilon - \varepsilon_{0.2}}{\varepsilon_{1.0} - \varepsilon_{0.2}}\right)^{p_{0.2}}} & \varepsilon_{0.2} < \varepsilon \leq \varepsilon_{1.0} \\ f_{1.0} + \frac{E_{1.0}(\varepsilon - \varepsilon_{1.0})}{1 + (r_{1.0} - 1)\left(\frac{\varepsilon - \varepsilon_{1.0}}{\varepsilon_u - \varepsilon_{0.2}}\right)^{p_{1.0}}} & \varepsilon_{1.0} < \varepsilon \leq \varepsilon_u \end{cases} \quad \text{Eq. (2.51)}$$

Since cold-formed steels have similar rounded stress–strain responses as compared to stainless steels, Quach and Huang (2011) extended the application range of Eq. (2.30) from stainless steels to light gauge carbon steels for advanced numerical modelling of cold-formed steel structures. In Eq. (2.30), the second strain hardening exponent m that ensures the modelled stress–strain curve passes through the yield point $(\varepsilon_{0.2}, f_{0.2})$, ultimate tensile point (ε_u, f_u) , and intermediate point (ε_r, f_r) can be determined by Eq. (2.52). Also, the predictive formulae of ultimate tensile strength f_u , the strain at ultimate tensile strength ε_u , 1.0% proof strength $f_{1.0}$ and 2.0% proof strength $f_{2.0}$ are given from Eq. (2.53) to Eq. (2.56). Those empirical formulae were developed and validated against a total of 133 tensile coupon test results, showing generally close agreement with the experimental stress–strain curves.

$$m = \begin{cases} \frac{\ln\left(0.008 + \frac{f_{1.0} - f_{0.2}}{E} - \frac{f_{1.0} - f_{0.2}}{E_{0.2}}\right) - \ln\left(\varepsilon_u - \varepsilon_{0.2} - \frac{f_u - f_{0.2}}{E_{0.2}}\right)}{\ln(f_{1.0} - f_{0.2}) - \ln(f_u - f_{0.2})} \geq 1 & \text{for } f_r = f_{1.0} \\ \frac{\ln\left(0.018 + \frac{f_{2.0} - f_{0.2}}{E} - \frac{f_{2.0} - f_{0.2}}{E_{0.2}}\right) - \ln\left(\varepsilon_u - \varepsilon_{0.2} - \frac{f_u - f_{0.2}}{E_{0.2}}\right)}{\ln(f_{2.0} - f_{0.2}) - \ln(f_u - f_{0.2})} \geq 1 & \text{for } f_r = f_{2.0} \end{cases} \quad \text{Eq. (2.52)}$$

$$\frac{f_{0.2}}{f_u} = 112.94 \frac{f_{0.2}}{E} + 0.61 \quad \text{Eq. (2.53)}$$

$$\frac{\varepsilon_u}{\varepsilon_{0.2}} = \begin{cases} 0.253 \frac{E}{f_{0.2}} - 91.86 & \text{for } n \leq 8 \\ 32.6 & \text{for } 8 < n < 16 \text{ and } f_{0.01} < 320 \text{MPa} \\ 0.0834 \frac{E}{f_{0.2}} - 23.51 & \text{for } 8 < n < 16 \text{ and } f_{0.01} \geq 320 \text{MPa} \\ 0.181 \exp\left(\frac{0.01E}{f_{0.2}}\right) & \text{for } n \geq 16 \end{cases} \quad \text{Eq. (2.54)}$$

$$\frac{f_{1.0}}{f_{0.2}} = 0.000644n \frac{E}{f_{0.2}} + 1.017 \quad \text{Eq. (2.55)}$$

$$\frac{f_{2.0}}{f_{0.2}} = 0.000709n \frac{E}{f_{0.2}} + 1.053 \quad \text{Eq. (2.56)}$$

The most recent proposal of a modified two-stage Ramberg–Osgood model (Eq. (2.30)) was developed by Gardner and Yun (2018) to describe stress–strain relationships of cold–formed steels with yield strengths ranging from 235 MPa to 1100 MPa. Predictive formulae of key parameters to be inputted into the material model are derived on the basis of a comprehensive stress–strain curves database which comprises more than 700 tensile coupon results collected from the literature. With the aid of those predictive expressions (Eq. (2.57) to Eq. (2.60)), that make it possible to depict a full range of stress–strain curve for cold–formed steels through limited information, for instance, yield strength f_y and 0.2% proof strength $f_{0.2}$. Furthermore, better agreement with the experimental stress–strain curve can be achieved if more input information such as ultimate tensile strength f_u and the strain at ultimate tensile strength ε_u , are provided.

$$f_u / f_{0.2} = 1 + (130 / f_{0.2})^{1.4} \quad \text{Eq. (2.57)}$$

$$\varepsilon_u = 0.6 \left(1 - \frac{f_{0.2}}{f_u} \right) \quad \text{Eq. (2.58)}$$

$$m = 1 + 3.3 \frac{f_{0.2}}{f_u} \quad \text{Eq. (2.59)}$$

$$m = \frac{\ln\left(0.008 + \frac{f_{1.0} - f_{0.2}}{E} - \frac{f_{1.0} - f_{0.2}}{E_{0.2}}\right) - \ln\left(\varepsilon_u - \varepsilon_{0.2} - \frac{f_u - f_{0.2}}{E_{0.2}}\right)}{\ln(f_{1.0} - f_{0.2}) - \ln(f_u - f_{0.2})}, \text{ for } \varepsilon_u > \max\left(\varepsilon_{0.2} + \frac{f_u - f_{0.2}}{E_{0.2}}, \varepsilon_{1.0}\right) \quad \text{Eq. (2.60)}$$

Ma *et al.* (2015) found that the most widely used two-stage Ramberg–Osgood models cannot capture the stress–strain behaviour well at the transition position near the yield point, as shown in Figure 2.9 (a). This mismatching between modelled and measured stress–strain curves can be attributed to the fact that the strain hardening exponent n is increasing with the growth of plastic strain ε_p , so a fixed value of n leads to inaccuracy in predicting the material response. Therefore, innovative predictive formula for the new strain hardening exponent n_{Ma} was proposed, and the original Ramberg–Osgood model was revised as Eq. (2.61), where n_{Ma} is the modified strain hardening exponent that can be determined from Eq. (2.62), the coefficient K can be determined using material parameters by Eq. (2.63), and the exponent m is determined by trial and error to fit the model to measured stress–strain curves.

$$\varepsilon_p = \varepsilon - \frac{\sigma}{E} = 0.002 \left(\frac{\sigma}{f_{0.2}} \right)^{n_{\text{Ma}}} \quad \text{Eq. (2.61)}$$

$$n_{\text{Ma}} = f(\varepsilon_p) = n + K \varepsilon_p^m \quad \text{Eq. (2.62)}$$

$$K = \frac{\log\left(\frac{f_u}{f_{0.2}}\right) \left(\frac{\varepsilon_{\text{pu}}}{0.002}\right) - n}{\left(\varepsilon_{\text{pu}}\right)^m} \quad \text{Eq. (2.63)}$$

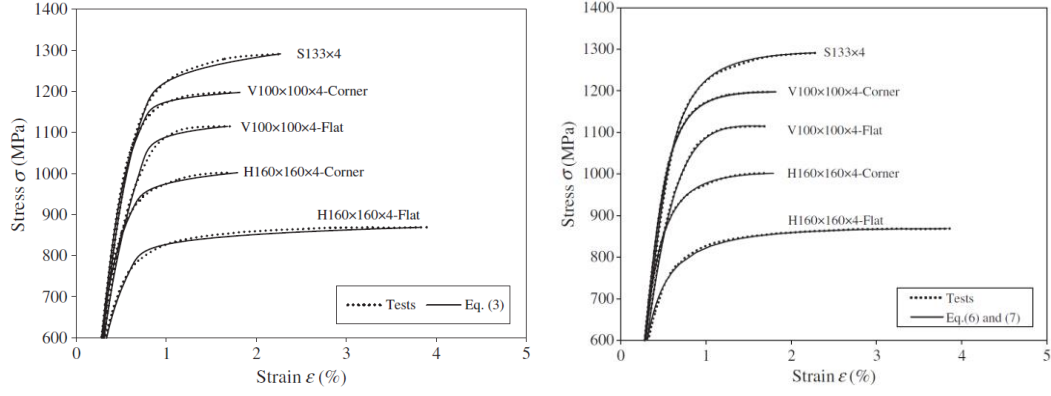


Figure 2.9 The comparison between the two–stage Ramberg–Osgood model and Ma model (Ma *et al.*, 2015).

The explicit form of this innovative material constitutive model (Eq. (2.64) and Eq. (2.65)) can be obtained by substituting Eq. (2.63) into Eq. (2.62) and Eq. (2.61), showing great agreement with the measured stress–strain curves, as shown in Figure 2.9 (b).

$$\sigma = \left(\frac{\varepsilon_p}{0.002} \right)^{\left(\frac{1}{n+K\varepsilon_p^m} \right)} f_{0.2} \quad \text{Eq. (2.64)}$$

$$\varepsilon = \varepsilon_p + \frac{\sigma}{E} = \varepsilon_p + \frac{f_{0.2}}{E} \left(\frac{\varepsilon_p}{0.002} \right)^{\left(\frac{1}{n+K\varepsilon_p^m} \right)} \quad \text{Eq. (2.65)}$$

Further discussion on the abovementioned material constitutive models will be conducted in Chapter 3.

2.4 Cold–formed polygonal hollow sections

2.4.1 Rectangular hollow sections

There are various cold–working methods to produce cold–formed RHS tubes, including indirect–forming, direct–forming, and tip–to–tip welding of two press–braked channel sections. For indirect–forming, the steel strip was firstly roll–formed

into a circular shape, then the open circular shape was merged by longitudinal welding and subsequently flattened to the desired rectangular hollow section. The magnitude and effect of residual stresses contained in this kind of indirect-formed RHS tube were experimentally and numerically studied by Zhang *et al.* (2016). Gardner *et al.* (2010) investigated effects of various manufacturing methods on material properties and structural responses on the S355 hot-rolled and S235 cold-rolled RHSs, revealing that the current cross-section slenderness limits may be manufacturing method-dependant based on the compression test results and the plastic design for continuous beam can be equally applied to hot-rolled and cold-rolled RHSs. Research on S500 to S960 cold-rolled RHSs conducted by Wang *et al.* (2017) indicated the partial safety factors of current Eurocode 3 (CEN, 2005) for the design of Class 3 and 4 cross-sections should be greater than unity to yield a required reliability level. Somodi and Kövesdi (2017) and Meng and Gardner (2020b) performed experimental and numerical investigations into the flexural buckling behaviour of cold-rolled high strength RHSs, proposing that a steel grade-dependant imperfection factor α can be incorporated in computing the reduction factor to account for the effects due to different material properties. Moreover, a comprehensive experimental programme on S700 to S1100 cold-rolled RHS structural members was performed by Ma *et al.* (2015, 2016a, 2016b, 2019, 2021), and those investigations include material properties, residual stress patterns, stub column tests, beam tests, stub column under compression and bending tests and beam-column tests. Complemented with further parametric studies, corresponding design methods for high strength cold-rolled tubes were subsequently proposed.

With respect to the direct-forming process, the steel strip was directly formed into an open rectangular shape by a set of rollers, and then the opening was closed by the longitudinal welding, typically submerged-arc welding (SAW). The differences in static properties of cold-formed RHSs fabricated by direct-forming and indirect-

forming were studied by Sun and Packer (2014). As the section width to plate thickness ratio increases, variations in the full section tensile behaviour between those types of sections are found to become greater. Conversely, the difference in full section compressive behaviour becomes smaller with the increase of the ratio. Galvanised cold-formed steel structures are often applied in bridges, marine structures, and transmission towers because of their superior anti-corrosion ability. Tayyebi *et al.* (2020), Tayyebi and Sun (2020, 2021) experimentally investigated the effects of hot-dip galvanizing on the direct-formed RHSs with nominal yield strengths of 355 MPa and 690 MPa. Post-galvanizing treatment is found to be similar to post-production heat treatment, which can effectively decrease the residual stress level which was introduced during the direct-forming process and greatly delay the initiation of the local buckling, improving the stub column behaviour.

2.4.2 Hexagonal and octagonal hollow sections

Hexagonal hollow section (HexHS) and Octagonal hollow section (OctHS), as members of the polygonal hollow section family, have been extensively adopted in transmission structures, substation structures, and steel pole structures (CENELEC, 2012; Kalaga and Yenumula, 2016; Slocum, 2015). Over the last decade, researchers tried to tap the full potential of HexHSs and OctHSs in the structural engineering discipline, for instance, the OctHS acting as the confining jacket to provide confinement to the concrete core (Zhu and Chan, 2019), the concrete-filled steel tubes (CFST) bending member (Chen and Chan, 2019), and the concrete-filled beam-column members (Chen *et al.*, 2019). The reason why polygonal hollow sections have been widely used can be attributed to their multi-sided feature. This feature allows the cross-section to have the capabilities to provide a better local buckling resistance (Naohiro *et al.*, 2017) and more effective confining stress to the concrete core in CFST (Fang *et al.*,

2021b; Zhu and Chan, 2018) than its rectangular hollow section (RHS) counterpart with the same outer perimeter, and also offer a more convenient accessible construction platform for welding and bolting (Xu *et al.*, 2023) of beam-to-column connection, as compared with its circular hollow section counterpart. All these mentioned advantages of polygonal hollow sections prompt the research into investigating the behaviour and design of polygonal hollow section steel columns.

Regarding the effect of different manufacturing process, the welding heat-input generated around weld seams and their vicinal heat affected zones and the plastic deformation introduced around the cold-formed corners, both influence properties of the base material and the initial internal stress state of the structure. The strength variations and residual stress distributions within the OctHS made of S355 (Zhu *et al.*, 2019), S460 (Chen *et al.*, 2020), and S690 (Fang *et al.*, 2018a) grade steels were experimentally investigated. These properties HexHSs have been systematically investigated in experiments by Liu *et al.*, (2022), and Liu *et al.*, (2022a). Based on the measured test results, predictive patterns for strength variations and residual stress distribution were proposed correspondingly, which make it possible to establish accurate models in the advanced numerical analysis without preliminarily complicated experimental works.

The thin-walled hollow section structures are susceptible to the occurrence of local buckling, owing to the fact that slender plate elements tend to buckle locally before reaching their yield capacity. A proper determination of the cross-section classification limit is the crucial step to achieve a safe and economical structural design at the cross-sectional resistance level. Hence, a great deal of research was conducted to study the local buckling behaviour of OctHSs under different loading conditions, such as uniaxial compression (Fang *et al.*, 2019; Godat *et al.*, 2012; Naohiro *et al.*, 2017; Zhu *et al.*,

2019), bending subjected to constant moment and moment gradient (Dalia *et al.*, 2021), and combined compression and bending (Fang *et al.*, 2021a). The experimental and numerical results of these studies demonstrate that the current codified cross-section classification limits developed for rectangular hollow sections are somewhat optimistic and overpredict the cross-sectional capacity of OctHSs in various degrees. Corresponding design recommendations were proposed to tighten the plate slenderness limits codified in different design methods, as the 135° corners existed in OctHSs tend to provide a weaker restraint to their adjacent plate elements compared to the restraint provided by 90° corners in RHSs. Liu *et al.*, (2022a) and Liu *et al.*, (2022b) conducted experimental and numerical investigations on the high strength steel HexHS stub columns, and draw a similar conclusion. Moreover, the behaviour of octagonal CFST structures under axial loading (Ayough *et al.*, 2021; Ding *et al.*, 2016; Fang *et al.*, 2021b; Zhang *et al.*, 2018; Zhu and Chan, 2018), combined compression and bending (Fang *et al.*, 2023), and seismic action (Lu and Zhao, 2022) were also experimentally and numerically investigated.

Despite the fact that extensive research has been performed on HexHS, OctHS and octagonal concrete-filled stub columns, no experimental investigation on OctHS long columns was conducted to understand their global buckling (also known as flexural buckling) behaviour, though the most common applications of OctHSs can be found as the bracing in tubular transmission structures and the compression member in steel pole structures where columns were designed to withstand the gravity load of overhead power lines and other affiliated facilities.

2.5 Concluding remarks

This chapter presents a comprehensive review on the strength enhancement models of cold-formed corner yield strength, material constitutive models of metals with nonlinear stress–strain response, and investigation on rectangular and octagonal hollow section columns. After reviewing the literature, it is found that although there are many works focused on the cold-formed steels and cold-formed steel structures, these works still have their disadvantages and shortcomings. For instance, the Karren model for predicting the enhanced yield strength of cold-formed corner was developed based on tensile tests of conventional strength steels, and cannot be directly applied on the high strength steel. The widely used Ramberg–Osgood model for describing nonlinear stress–strain responses of metal cannot capture well the material behaviour in the transition region. And there are still lack of systematic design rules for predicting the column buckling resistance for polygonal hollow section columns. Hence, the research needs of this PhD thesis are identified by revealing those shortcomings existed in the current works. Systematic research to characterise the material properties of cold-formed steels from normal to high strength, and to investigate the structural compressive behaviour of cold-formed polygonal hollow section steel columns is performed, and corresponding methodology and results are presented in the following chapter.

Chapter 3 Cold-forming effect and material constitutive model of cold-formed steels

3.1 Introduction

Cold-formed structural steel members have been broadly used in a range of structural engineering projects as they offer merits of ease of fabrication, high strength-to-weight ratio, and economic efficiency. Different levels of plastic deformation were introduced into the deformed regions of cross-sections during the cold-forming process. As a result, the material properties of steels in the deformed region vary from those of parent materials due to the pronounced strain-hardening. A more rounded stress-strain response with enhanced yield strength and ultimate tensile strength and loss in ductility can be observed among those metallic materials experienced cold-work.

This chapter therefore presents an extensive material test programme on the cold-forming effect of normal and high strength structural steels. In this material test programme, flat tensile coupon tests to determine the basic key parameters of parent materials, and corner tensile coupon tests to obtain the material properties of cold-formed corner materials were conducted. The obtained material test results were further combined with the data collected from the global literature to develop an extensive experimental database. Based on this large database, corresponding predictive expressions were proposed to predict the enhanced strengths, loss in ultimate strain and elongation at fracture of cold-formed structural steels, respectively. A material constitutive model was then proposed to accurately describe the stress-strain response of cold-formed steel in the corner region, while the key parameters used in this model can be determined from the abovementioned predictive expressions.

3.2 Manufacturing and preparations of specimens for the tensile coupon test

3.2.1 General

In this chapter, a total of 13 types of structural steel plates with various nominal steel grades and thicknesses, including Q235 2 mm, Q235 3 mm, Q235 5 mm, Q275 2 mm, Q275 3 mm, Q275 5 mm, Q355 5mm a, Q355 5 mm b, Q355 5 mm c, Q460 3 mm, Q460 6 mm, Q550 6 mm, and Q690 3mm steel plates, were selected as the parent materials. Flat tensile coupons were firstly extracted from parent steel plates and tested to obtain material properties of parent materials. A series of steel plates were then press-braked into cold-formed angle sections and corner coupons were sectioned afterwards to investigate the effect of cold-forming.

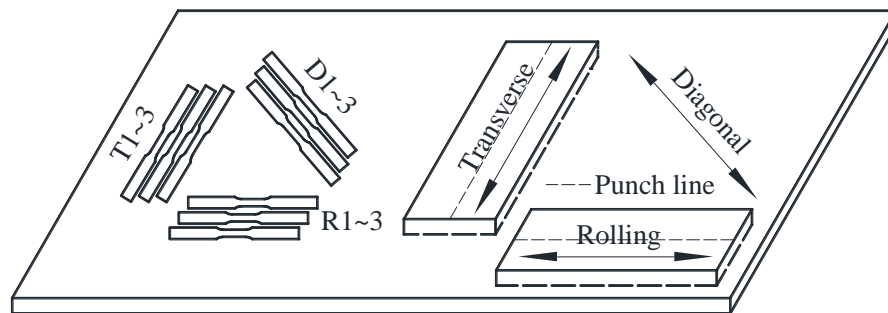


Figure 3.1 Illustration of locations of flat coupons and different directions.

3.2.2 Specimen details of flat coupons

Before the cold-forming process being performed on the parent materials, the flat steel plates have previously experienced the process of coiling to the steel coil, uncoiling of steel coil, and final flattening. The mechanical properties of steel coils in rolling and transverse directions may be varied because of the plastic deformation induced in the previous processes. Hence, to investigate the variations on material properties in different directions of normal strength steels, three flat tensile coupons

were extracted from rolling, diagonal (45 degrees), and transverse directions of parent steel plates, respectively, while the arrangement of flat coupon was shown in Figure 3.1. The flat coupon specimens were sectioned through water-cutting machine, as shown in Figure 3.2. and their dimensions were conformed to the requirements of EN ISO 6892–1: 2019 (CEN, 2019), as shown in Figure 3.3 (a).

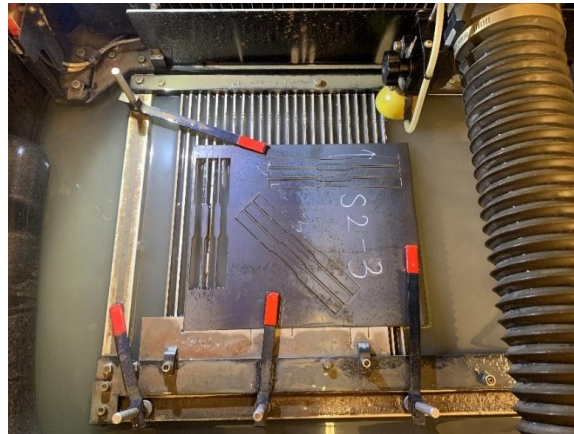


Figure 3.2 Water-jet cutting of flat tensile coupons.

In total, 93 pieces of flat coupons were fabricated in the experimental program. The flat coupon specimens were labelled by their nominal steel grades, thicknesses, and extraction directions. For instance, 275–3–D1 indicates that the first flat coupon extracted from the diagonal direction of 3mm Q275 plate.

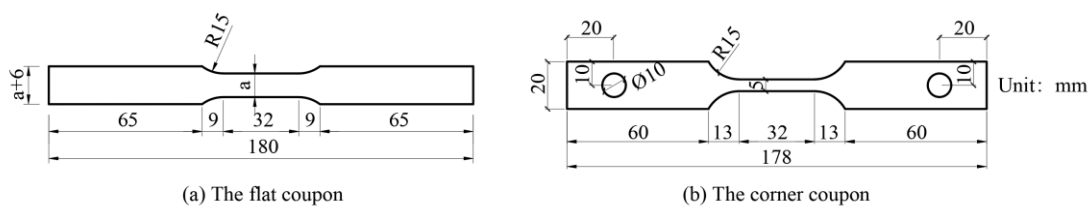


Figure 3.3 Geometrical dimensions of tensile coupons.

3.2.3 Specimen details of corner coupons

All corner coupons were extracted from press-braked angle sections. To fabricate the press-braked angle sections, parent steel parent plates were firstly cut into small pieces with width by length of 120 mm × 400 mm, as shown in Figure 3.1. Each small

piece was subsequently press-braked into angle sections using a CNC press-braking machine. As the plastic deformation is associated with inner radius to thickness ratio r_i/t , punches with various punch radii ($R_p = 3$ mm, 5 mm, 10 mm, and 15 mm) were adopted and different included angles ($\theta = 90^\circ$, 120° , 135° , and 150°) were considered in the press-braking process, as shown in Figure 3.4 and Figure 3.5.

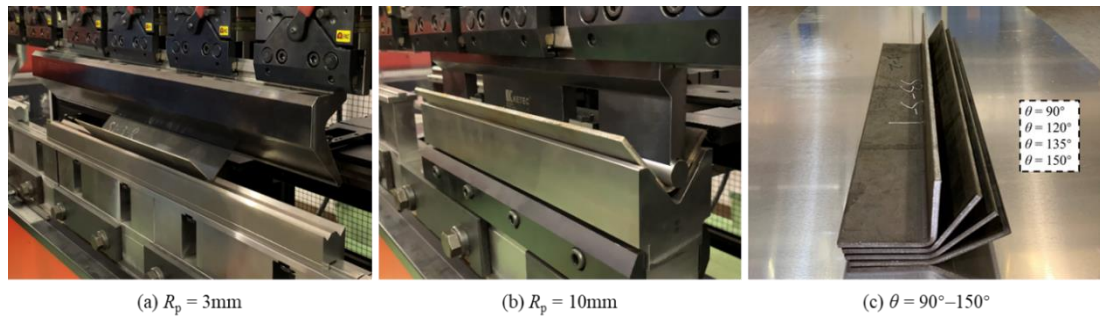


Figure 3.4 Fabrication process and press-braked specimens.

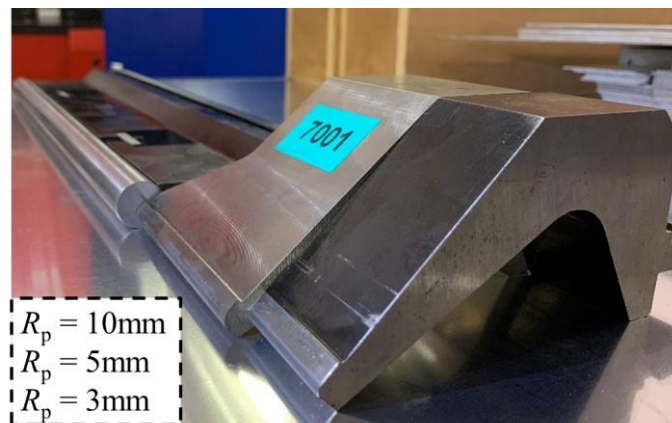


Figure 3.5 Punches with different bending radii ($r_p = 3$ mm, 5 mm, and 10 mm).

Majority of steel plates were press-braked along the rolling direction, except for one batch of specimens on 5 mm Q355 plate, which was designed to be press-braked on the transverse direction, to consider the effect of directions of cold-forming on the change of material properties. After press-braking, the included angle of the angle sections was carefully measured by a digital protractor and the tolerance of the included angle was within $\pm 1^\circ$. It should be noted that geometric dimensions of press-braked angle sections in this study broadly covers the scope of application in North American

Specification AISI S100–16 (AISI, 2016) ($r_i/t \leq 7$ and included angle $\theta \leq 120^\circ$), and no visible micro crack was observed in cold–formed regions after press–braking. Then two identical corner coupons were machined along the centreline of the corner in each press–braked angle section using a wire cutting machine under the protection of coolants. To ensure the repeatability and reliability of the test program, some repeated specimens were included. In this case, a total of four identical corner coupons were prepared.

To accurately measure the inner bending radius and area of curved coupons, the cross–section of the curved coupon was scanned and transferred into AutoCAD software to obtain corresponding inner curved radius and cross–sectional area, as shown in Figure 3.6.

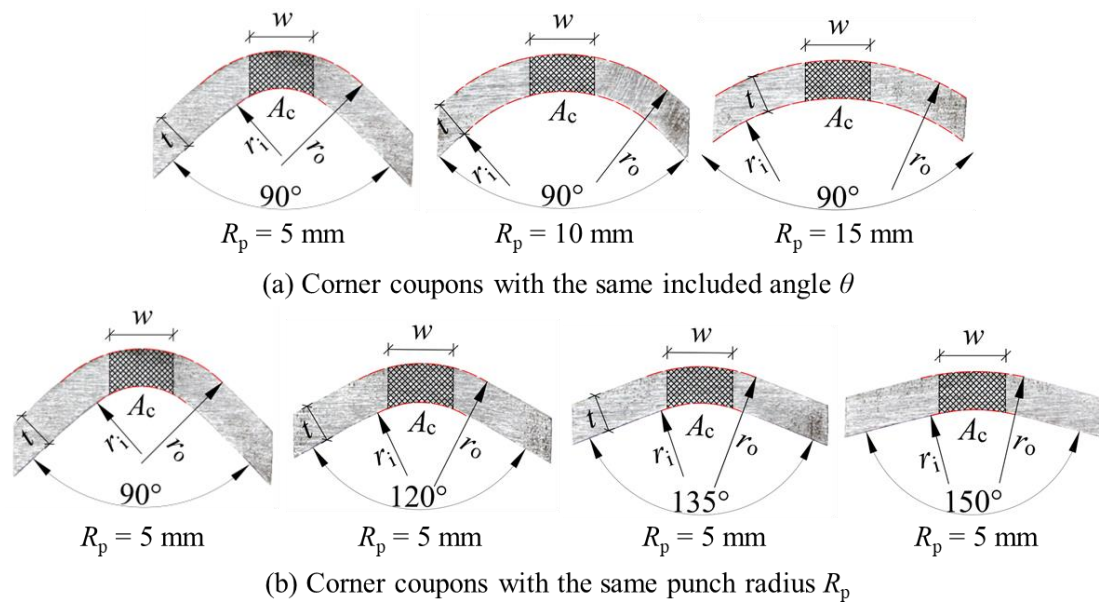


Figure 3.6 Processing example of scanned corner coupon.

In total, 212 pieces of corner coupons were fabricated in the experimental program. The nomenclature of corner coupons identifies the nominal steel grade, plate thickness, included angle and adopted punch radius. For example, 550–6–135–P15 indicates a corner coupon machined from a 135° angle section fabricated from a 6 mm Q550 parent

steel plate using a punch with 15 mm punch radius.

3.3 Material tests and results

3.3.1 Tensile test procedures

All tensile coupons were tested in accordance with EN ISO 6892–1:2019, while the normal strength part of coupon tests were conducted using an Instron 100kN electromechanical testing machine, and the high strength part of coupon tests were performed using a LABSANS tension machine, as shown in Figure 3.7 and Figure 3.8, respectively. A pair of uniaxial strain gauges with the extensometer (50 mm gauge length for flat coupons and 25 mm gauge length for corner coupons) were mounted on the tensile coupons to record the longitudinal strain development. Prior to the tensile coupon test, several fine lines were marked perpendicular to the parallel length of coupons prior to the tensile tests following the approach adopted in Chen *et al.* (2020). After the completion of tensile tests, failed tensile coupons were matched together and the elongation at fracture was subsequently obtained by comparing the length after fracture to the original length.

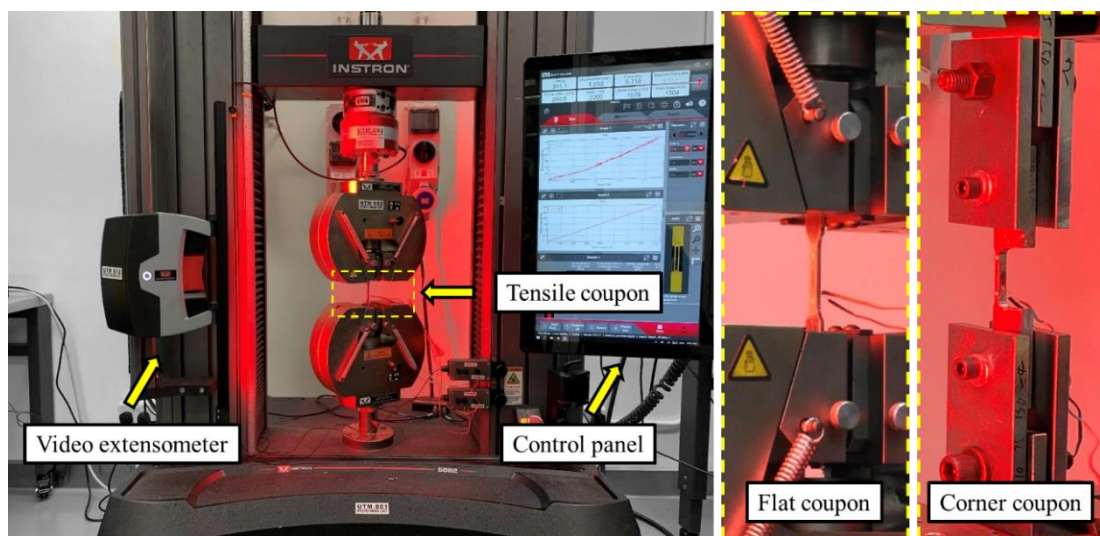


Figure 3.7 Test setup for the normal strength part of coupons.

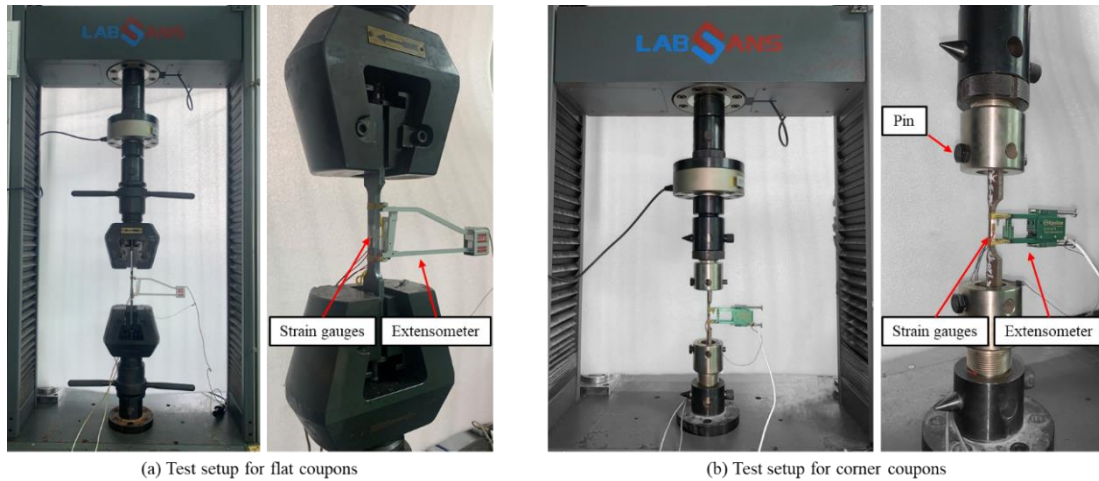


Figure 3.8 Test setup for the high strength part of coupons.

For each tensile coupon test, the loading strain rate can be divided into 3 stages, initially 0.3 mm/min from beginning to the end of the yield plateau (or after 0.2% proof strength for corner coupons that have no yield plateau), 0.8 mm/min up to ultimate tensile strength, and 2 mm/min from ultimate tensile strength to the fracture of specimen. It is worth noting that the corner coupons were carefully aligned and tested using a specially designed pin grip to minimise the effect of eccentricity. Information about the specially designed pin grip are illustrated in Figure 3.9.

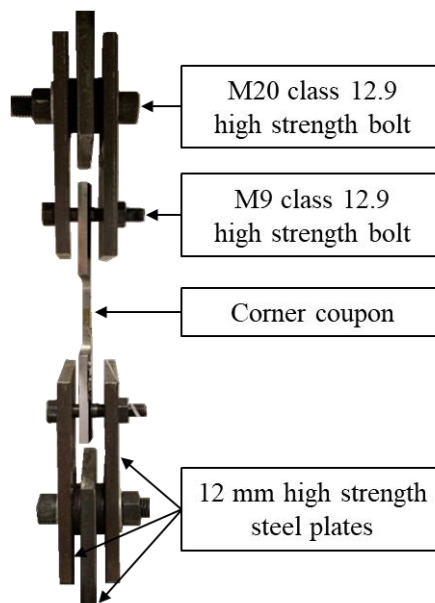
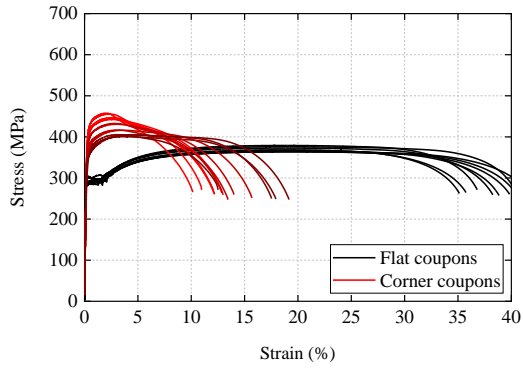


Figure 3.9 Information about the specially designed pin grip.

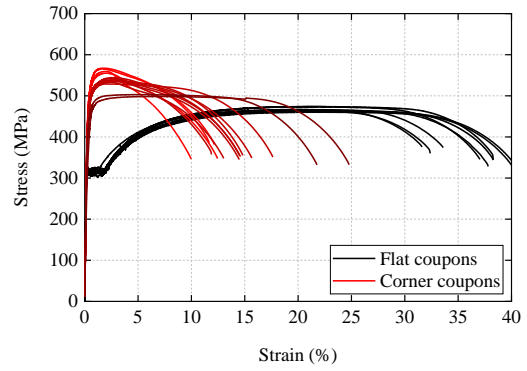
3.3.2 Material test results

Key material parameters were obtained through the material test, including the elastic modulus E , the yield strength f_y (taken as the lower yield strength for coupons with yield plateau or 0.2% proof strength for coupons without yield plateau), the ultimate tensile strength f_u , the ultimate strain ε_u (strain corresponding to f_u), and the elongation at fracture ε_f . Test results of normal strength steel specimens are tabulated in Table 3.1 and Table 3.2, and the results of high strength steel specimens are reported in Table 3.3 and Table 3.4. Subscripts ‘f’ and ‘c’ are used to distinguish material properties of flat coupons and corner coupons, respectively. It can be found from Table 3.1 that material properties of flat coupons extracted from rolling, diagonal, and transverse directions of parent metals show little difference, indicating that the materials are isotropic.

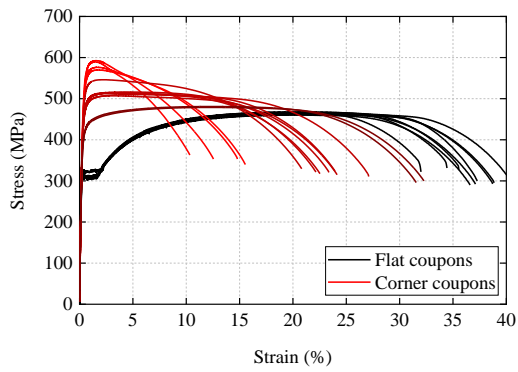
Apparent strength enhancements in not only the yield strength but also the ultimate tensile strength can be found among corner coupons. Stress–strain curves of all specimens are presented in Figure 3.10, in which colours of these curves are transitioning from black to red with the increase level of strength enhancement. The level of strength enhancement for cold–formed steels is significantly associated with the level of permanent plastic deformation. In this study, the level of plastic deformation that specimens experienced directly relates to the adopted punch radius R_p and included angle θ during the press–braking process, and the level of cold–forming can be reflected by the measured r_i/t value of the corresponding corner coupon.



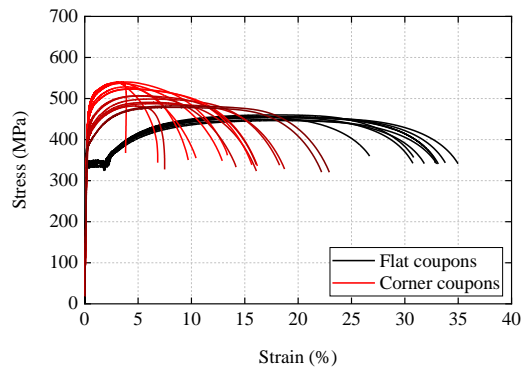
(a) 235 – 2 mm



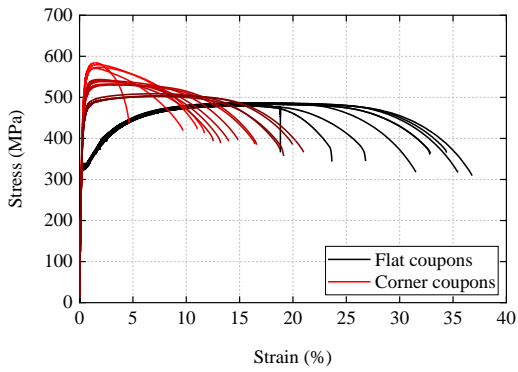
(b) 235 – 3 mm



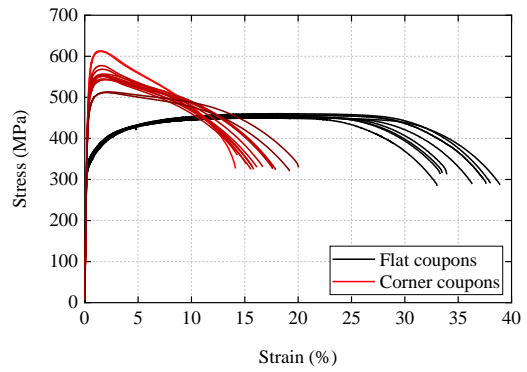
(c) 235 – 5 mm



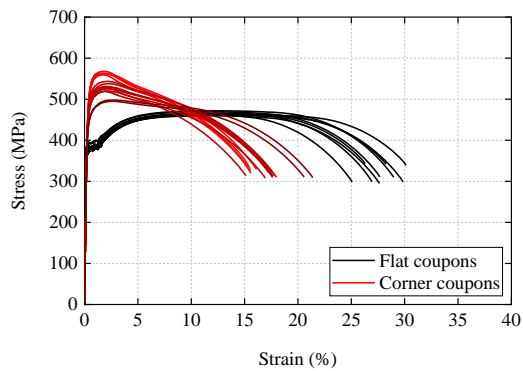
(d) 275 – 2 mm



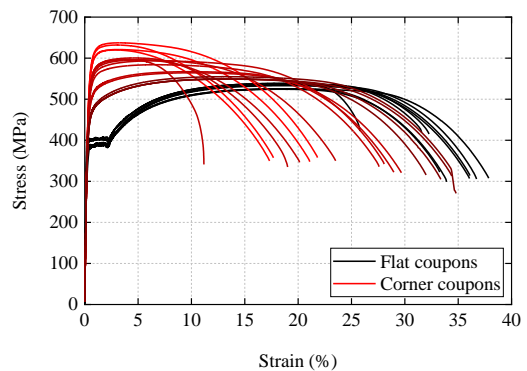
(e) 275 – 3 mm



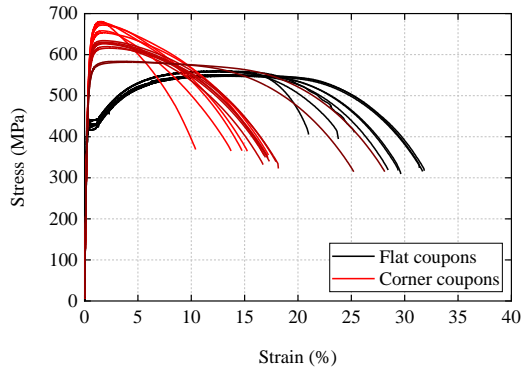
(f) 275 – 5 mm



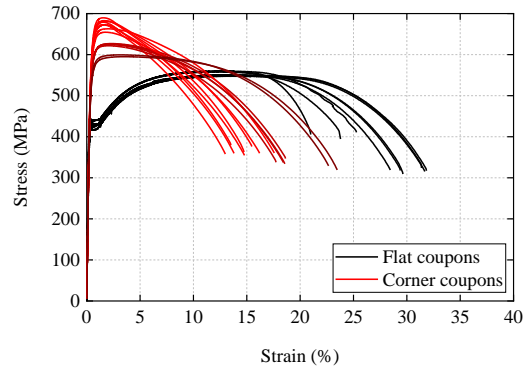
(g) 355 – 5 mm a



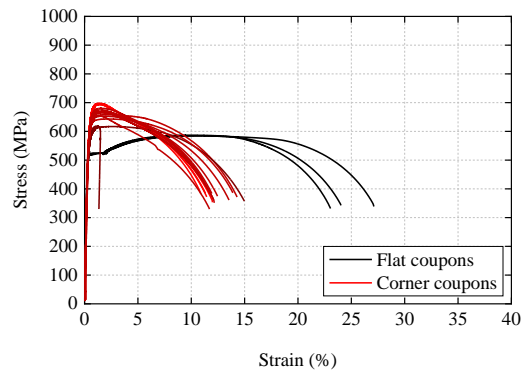
(h) 355 – 5 mm b



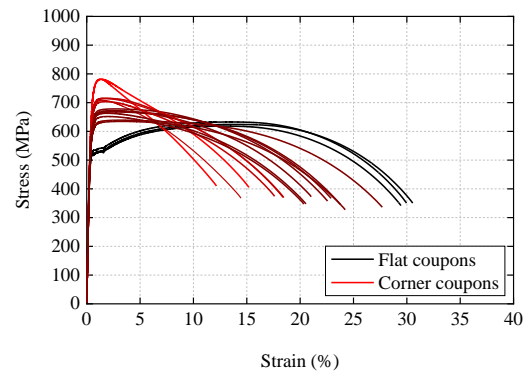
(i) 355 – 5 mm c Rolling



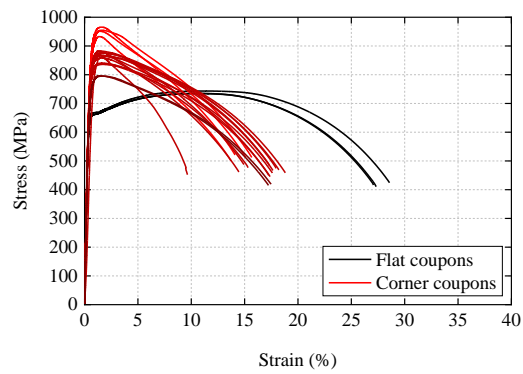
(j) 355 – 5 mm c Transverse



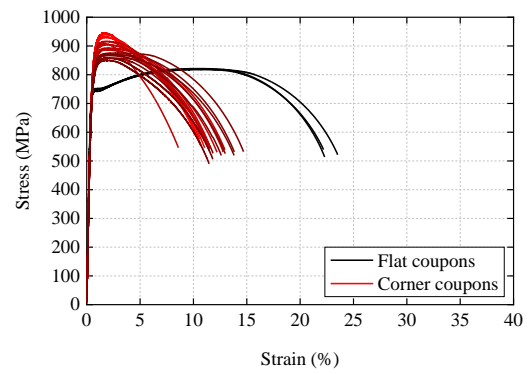
(k) 460 – 3 mm



(l) 460 – 6 mm



(m) 550 – 6 mm



(n) 690 – 3 mm

Figure 3.10 Stress–strain curves of tested coupons.

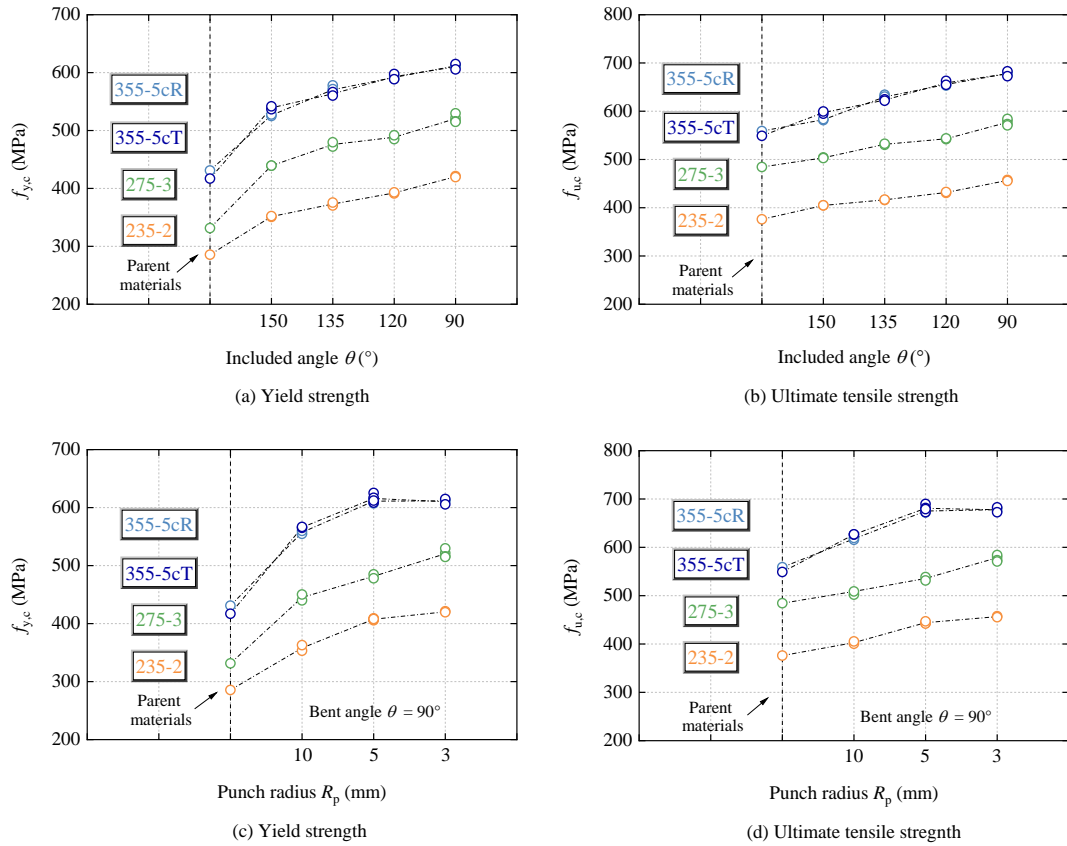


Figure 3.11 Trends of the yield strengths $f_{y,c}$ and ultimate tensile strengths $f_{u,c}$ against various punch radii R_p and included angles θ for normal strength steels.

The obtained $f_{y,c}$ and $f_{u,c}$ of four representative groups of specimens are plotted against the included angle and punch radius in Figure 3.11 and Figure 3.12. General increase trends of strengths with increasing levels of cold-forming can be observed. For specimens press-braked by the same punch, a smaller included angle results in a smaller inner corner radius, leading to a larger plastic deformation and therefore a larger strength enhancement. For specimens with the same included angle (take 90° as example) but press-braked by different punches, it is obvious that using a punch with smaller punch radius leads to a smaller inner corner radius, also resulting in a greater strength enhancement. It is also worth noting that the effects of different directions on the material properties of cold-formed steels are negligible, reflected by the test results of 355-5cR and 355-5cT specimens as displayed in Figure 3.11.

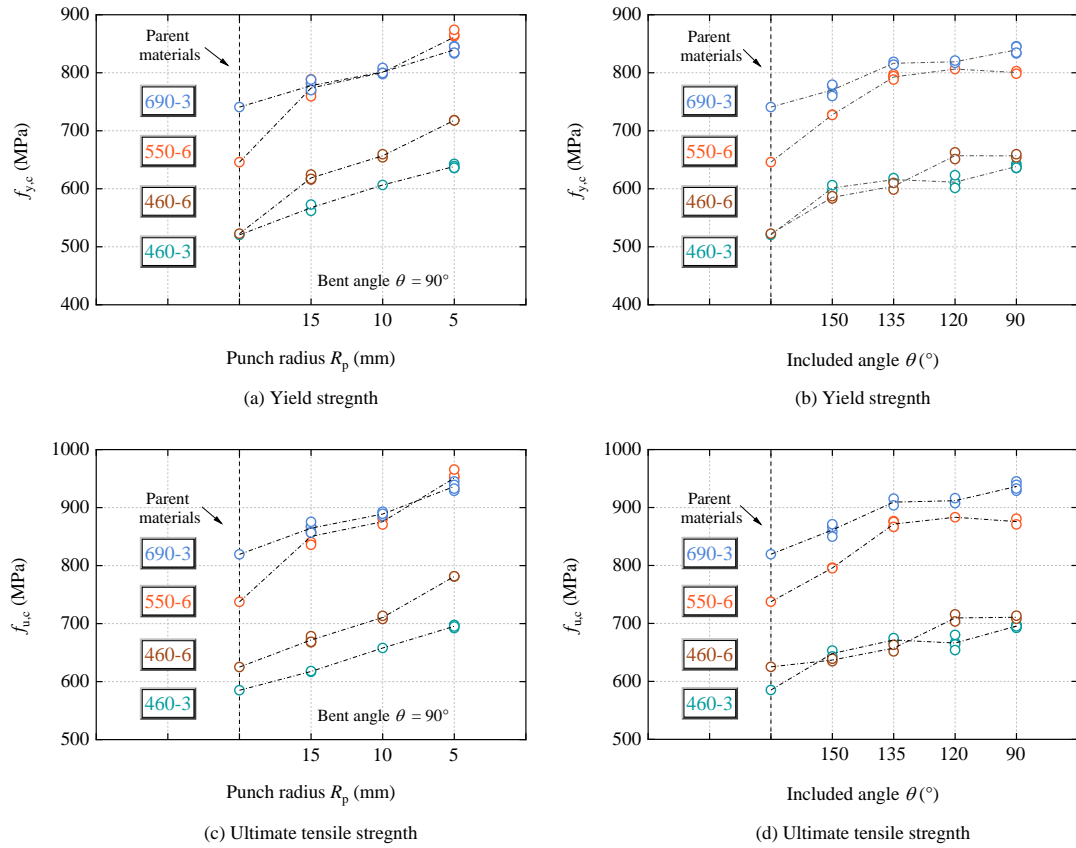


Figure 3.12 Trends of the yield strengths $f_{y,c}$ and ultimate tensile strengths $f_{u,c}$ against various punch radii R_p and included angles θ for high strength steels.

Table 3.1 Key parameters obtained from flat coupon tests of normal strength steels.

Specimen		E_f (GPa)	$f_{y,f}$ (MPa)	$f_{u,f}$ (MPa)	$\varepsilon_{u,f}$ (%)	$\varepsilon_{f,f}$ (%)	k	n_{se}
235-2	-R1	206.2	290	379	18.73	36.80	607	0.168
	-R2	208.0	284	376	18.58	40.50	592	0.160
	-R3	204.3	283	373	18.44	38.26	584	0.158
	-D1	202.6	287	365	18.89	40.53	576	0.160
	-D2	201.2	282	364	19.47	39.83	579	0.160
	-D3	202.9	282	364	19.31	41.86	577	0.158
	-T1	215.0	290	366	19.66	38.84	564	0.152
	-T2	212.5	299	368	18.80	35.73	563	0.152
	-T3	206.6	291	368	18.51	35.12	568	0.156
235-3	-R1	206.5	314	474	20.31	37.02	859	0.234
	-R2	212.1	303	465	21.57	38.27	850	0.240
	-R3	211.5	308	474	20.97	38.28	861	0.237
	-D1	210.8	313	463	21.75	40.50	838	0.234
	-D2	217.8	312	464	24.35	37.81	820	0.224
	-D3	214.6	312	460	22.30	40.32	823	0.229
	-T1	213.7	312	467	19.43	31.61	806	0.208

	-T2	216.2	316	466	21.00	33.60	831	0.226
	-T3	212.2	319	463	20.10	32.38	831	0.229
235-5	-R1	202.9	307	465	21.28	38.71	833	0.229
	-R2	199.0	304	463	21.14	40.55	831	0.229
	-R3	204.0	302	463	21.15	38.84	832	0.229
	-D1	202.9	308	462	19.93	37.27	827	0.227
	-D2	206.9	310	463	20.21	37.11	824	0.225
	-D3	206.5	305	460	20.15	36.61	824	0.227
	-T1	213.9	314	467	20.77	34.44	834	0.225
	-T2	211.9	317	465	19.75	32.00	831	0.226
	-T3	211.4	318	467	20.77	35.56	827	0.222
275-2	-R1	206.0	325	454	18.00	33.78	765	0.193
	-R2	178.5	334	455	18.08	34.98	753	0.185
	-R3	205.5	325	454	18.42	33.13	760	0.190
	-D1	199.3	335	446	18.30	32.99	738	0.185
	-D2	200.2	333	449	17.51	31.81	738	0.181
	-D3	204.9	336	454	17.45	30.75	760	0.190
	-T1	207.0	335	456	17.28	32.84	768	0.191
	-T2	207.2	342	457	16.22	26.70	765	0.189
	-T3	206.7	337	460	17.82	30.82	765	0.187
275-3	-R1	217.3	328	483	16.26	32.83	801	0.182
	-R2	220.9	333	484	15.82	32.89	792	0.176
	-R3	215.6	333	486	16.55	34.39	801	0.179
	-D1	204.9	327	486	16.94	36.78	790	0.178
	-D2	207.1	332	487	16.44	35.46	791	0.173
	-D3	208.7	331	486	16.32	31.52	792	0.173
	-T1	213.7	324	480	14.90	29.50	772	0.165
	-T2	210.1	327	479	14.90	23.65	789	0.177
	-T3	203.2	324	479	15.26	26.81	789	0.178
275-5	-R1	214.7	328	452	17.45	33.50	673	0.133
	-R2	212.9	331	452	17.49	33.94	670	0.131
	-R3	217.0	336	453	16.93	33.33	665	0.153
	-D1	205.6	346	450	16.69	33.02	648	0.117
	-D2	210.7	343	451	17.11	36.32	655	0.122
	-D3	212.2	342	450	17.03	38.93	654	0.121
	-T1	211.7	341	460	17.94	38.03	694	0.140
	-T2	212.5	345	452	17.40	41.58	663	0.126
	-T3	210.1	344	457	18.01	37.61	677	0.131
355-5a	-R1	204.0	381	464	11.71	28.23	694	0.129
	-R2	204.5	379	463	13.35	30.12	693	0.131
	-R3	205.3	373	463	12.30	26.28	698	0.133
	-D1	199.8	380	463	10.83	25.07	686	0.125

	-D2	200.7	380	461	11.97	29.84	677	0.122
	-D3	200.0	373	460	11.39	27.63	679	0.124
	-T1	205.0	383	466	11.68	26.93	684	0.122
	-T2	203.3	392	469	11.53	27.67	681	0.117
	-T3	207.0	391	472	11.49	28.97	693	0.122
355-5b	-R1	194.6	390	535	18.43	36.72	939	0.214
	-R2	195.8	384	535	18.37	36.06	947	0.218
	-R3	200.7	384	533	19.00	36.10	941	0.217
	-D1	193.5	387	525	18.62	37.86	911	0.209
	-D2	189.2	382	525	18.33	33.27	913	0.209
	-D3	186.5	385	524	18.06	33.90	920	0.214
	-T1	204.2	399	538	18.16	31.58	934	0.208
	-T2	205.9	396	538	18.10	32.25	941	0.211
	-T3	206.4	402	537	17.90	25.79	936	0.209
355-5c	-R1	214.3	433	560	12.17	25.28	889	0.157
	-R2	212.9	430	559	12.17	20.99	888	0.157
	-R3	216.8	429	558	11.88	23.78	892	0.159
	-D1	205.7	426	549	12.88	28.44	873	0.158
	-D2	207.8	430	549	12.97	29.64	879	0.161
	-D3	209.2	423	551	13.43	31.84	884	0.162
	-T1	198.4	415	549	14.18	31.38	876	0.161
	-T2	196.2	420	550	13.27	29.39	865	0.153
	-T3	199.9	416	547	13.37	31.67	871	0.159

Notes: “R”, “D”, and “T” indicate the rolling, diagonal, and transverse directions, respectively.

Table 3.2 Key parameters of the normal strength steel corner coupon tests.

Specimen	r_i/t	E_c (GPa)	$f_{0.01,c}$ (MPa)	$f_{0.05,c}$ (MPa)	$f_{y,c}$ (MPa)	$f_{u,c}$ (MPa)	$\epsilon_{u,c}$ (%)	$\epsilon_{f,c}$ (%)	
235-2-90-3	-1	2.10	209.8	299	329	421	458	1.97	11.16
	-2	2.11	208.0	317	332	420	455	2.33	12.07
235-2-90-5	-1	2.65	207.0	297	322	408	443	2.52	13.40
	-2	2.87	206.8	298	325	408	444	2.54	14.28
	-3	2.92	201.9	295	325	406	442	2.56	13.34
	-4	2.82	204.6	301	328	409	447	2.47	13.26
235-2-90-10	-1	5.27	178.5	208	248	353	401	3.52	19.72
	-2	5.44	205.7	284	305	363	405	3.10	13.76
235-2-120-5	-1	3.34	205.3	291	311	391	431	2.95	15.42
	-2	3.34	205.8	286	311	393	433	2.80	17.83
235-2-135-5	-1	3.86	203.9	281	305	371	416	3.63	19.83
	-2	3.65	208.3	277	301	376	417	3.06	18.44

235-2-150-5	-1	4.69	206.7	279	298	351	405	4.45	21.83
	-2	4.95	207.0	272	295	352	405	4.10	21.67
235-3-90-3	-1	1.19	202.6	316	355	507	567	1.69	11.23
	-2	1.20	200.2	320	356	504	565	1.68	11.77
235-3-90-5	-1	1.86	196.1	346	383	504	555	2.06	10.64
	-2	1.82	198.8	349	391	511	559	1.93	10.82
235-3-90-10	-1	3.59	202.6	350	381	486	542	2.72	13.36
	-2	3.50	202.5	341	377	482	537	2.76	13.45
	-3	3.54	204.1	334	371	483	539	2.68	14.36
	-4	3.44	203.8	344	380	487	544	2.55	12.91
235-3-120-3	-1	1.79	197.0	293	331	475	535	2.37	16.00
	-2	1.75	195.4	278	314	470	529	2.14	17.68
235-3-135-3	-1	2.68	201.3	344	380	480	535	2.66	15.32
	-2	2.58	201.3	347	379	481	533	2.34	15.05
235-3-150-3	-1	3.78	195.3	274	307	445	503	4.73	20.32
	-2	3.61	146.9	256	279	428	498	6.50	22.82
235-5-90-3	-1	0.92	184.6	342	381	546	589	1.41	14.67
	-2	0.93	174.9	317	363	537	592	1.50	12.75
235-5-90-5	-1	1.18	174.7	323	361	525	576	1.67	15.09
	-2	1.13	182.2	307	345	518	570	1.75	11.33
235-5-90-10	-1	2.46	190.1	279	320	463	515	2.97	22.35
	-2	2.13	188.6	280	317	456	507	3.09	21.89
	-3	2.31	189.9	271	312	460	513	3.55	19.51
	-4	2.28	191.5	277	319	460	514	3.23	21.66
235-5-120-5	-1	Test failed							
	-2	1.67	187.1	310	345	496	546	2.26	18.01
235-5-135-5	-1	2.14	186.1	281	316	466	516	4.26	19.81
	-2	2.14	186.9	277	313	457	510	4.86	25.08
235-5-150-5	-1	3.21	183.9	260	293	408	479	11.84	30.41
	-2	3.53	185.4	253	294	411	481	12.54	29.30
275-2-90-3	-1	2.20	203.1	354	386	479	540	3.21	11.89
	-2	2.36	205.0	357	387	480	538	2.93	11.28
275-2-90-5	-1	2.89	205.0	362	391	474	537	3.33	15.28
	-2	2.76	204.9	348	385	475	539	3.36	14.50
	-3	2.87	200.8	340	372	462	528	3.83	13.33
	-4	2.89	205.0	331	375	477	540	3.91	16.00
275-2-90-10	-1	5.57	198.7	240	276	412	482	4.61	1.83
	-2	5.51	199.4	328	348	407	487	6.08	19.06
	-3	5.37	199.1	311	341	417	499	6.16	18.61
	-4	5.44	199.0	329	353	413	491	5.88	17.89
275-2-120-3	-1	3.93	202.4	340	371	457	523	4.34	15.94
	-2	3.67	204.0	350	372	457	524	4.49	16.83

275-2-135-3	-1	4.75	202.5	345	370	431	506	5.13	18.00
	-2	4.80	203.0	344	364	433	506	5.03	19.78
275-2-150-3	-1	7.54	198.6	339	348	388	478	8.16	26.00
	-2	6.72	200.9	335	349	390	482	8.60	25.78
275-3-90-3	-1	1.09	197.8	311	353	522	580	1.72	12.14
	-2	1.05	196.3	336	372	530	584	1.47	12.41
	-3	1.02	191.2	307	349	516	573	1.86	12.68
	-4	1.06	189.2	304	346	515	571	1.45	12.82
275-3-90-5	-1	1.77	190.5	295	336	485	538	2.12	13.73
	-2	1.81	186.1	297	335	478	531	2.72	17.18
275-3-90-10	-1	3.60	188.8	265	308	440	502	7.04	21.23
	-2	3.57	186.2	270	313	450	509	6.96	21.41
275-3-120-3	-1	1.44	184.4	292	332	485	542	2.07	14.00
	-2	1.36	186.6	298	339	492	544	1.78	15.45
275-3-135-3	-1	1.61	190.8	279	321	472	530	2.97	16.82
	-2	1.60	187.0	275	318	480	533	3.13	17.45
275-3-150-3	-1	3.04	192.4	275	316	439	504	7.90	22.05
	-2	3.21	186.5	266	305	439	503	7.72	23.64
275-5-90-3	-1	0.61	190.8	354	393	558	612	1.52	13.71
	-2	0.60	195.7	359	399	560	613	1.46	14.14
275-5-90-5	-1	1.10	196.1	349	385	529	577	1.57	13.50
	-2	1.08	189.5	323	367	521	568	1.64	14.64
275-5-90-10	-1	2.01	202.1	312	358	500	552	1.89	16.75
	-2	2.05	195.5	308	354	492	543	1.96	16.29
275-5-120-5	-1	1.19	191.2	326	366	504	551	1.66	13.75
	-2	1.16	193.4	327	366	504	551	1.72	16.21
	-3	1.26	194.9	343	376	509	557	1.81	17.25
	-4	1.27	192.5	323	366	507	554	1.66	16.14
275-5-135-5	-1	1.40	194.9	314	355	506	553	1.67	15.82
	-2	1.34	198.2	316	358	498	545	1.78	17.25
275-5-150-5	-1	2.04	196.3	310	344	465	513	2.23	18.29
	-2	2.14	195.5	310	346	467	512	2.06	19.21
355-5a-90-3	-1	1.15	196.2	343	384	520	568	1.78	14.43
	-2	1.11	193.1	332	379	513	563	1.90	14.32
355-5a-90-5	-1	1.22	192.5	340	378	513	559	1.71	13.96
	-2	1.29	197.6	339	378	516	563	1.72	13.57
355-5a-90-10	-1	2.07	198.7	326	368	487	538	2.25	16.79
	-2	2.06	198.6	316	367	496	543	2.12	14.61
355-5a-120-5	-1	2.26	195.1	330	367	481	525	2.18	17.14
	-2	2.20	195.8	332	372	486	531	2.03	16.68
	-3	2.14	190.0	334	366	479	526	2.09	17.36
	-4	2.10	197.9	323	364	483	530	1.97	18.93

355-5a-135-5	-1	2.33	195.0	315	349	471	519	1.89	17.68
	-2	2.35	195.6	322	360	475	520	2.12	17.29
355-5a-150-5	-1	4.04	197.6	305	339	446	495	2.58	20.29
	-2	3.84	201.1	306	342	446	498	2.69	20.75
355-5b-90-3	-1	1.26	184.9	332	372	559	637	3.18	16.36
	-2	1.28	186.1	328	372	553	632	2.93	17.25
355-5b-90-5	-1	1.46	184.0	332	365	547	621	3.04	19.04
	-2	1.37	185.8	323	373	546	620	2.81	18.32
355-5b-90-10	-1	2.16	182.1	309	353	518	595	5.26	22.29
	-2	2.19	188.4	306	347	520	600	4.44	20.79
	-3	2.20	185.0	310	357	518	597	4.38	20.32
	-4	2.14	186.6	310	353	521	597	3.72	19.57
355-5b-120-5	-1	2.42	182.2	306	343	502	584	6.50	25.21
	-2	2.52	186.8	300	340	509	593	6.58	25.07
355-5b-135-5	-1	3.46	187.5	285	325	472	564	9.81	26.96
	-2	3.45	189.8	283	321	474	567	9.66	26.29
355-5b-150-5	-1	5.31	186.8	271	303	438	549	13.31	30.79
	-2	5.50	188.4	276	309	439	549	13.39	30.86
	-3	5.65	188.2	280	314	437	549	13.30	31.61
	-4	5.72	188.3	272	309	442	555	13.10	33.46
355-5cR-90-3	-1	0.96	184.8	385	433	613	681	1.50	12.94
	-2	0.90	183.3	378	419	610	675	1.66	13.82
355-5cR-90-5	-1	1.03	182.6	379	426	607	672	1.74	13.02
	-2	0.96	185.9	380	425	615	678	1.55	12.94
355-5cR-90-10	-1	2.04	186.4	381	423	555	616	2.25	16.17
	-2	2.04	184.1	370	417	560	619	2.16	17.36
355-5cR-120-5	-1	1.11	186.4	338	390	589	653	1.78	15.67
	-2	1.09	188.3	352	388	594	658	1.75	15.21
355-5cR-135-5	-1	1.17	192.9	359	403	566	628	1.89	17.66
	-2	1.24	184.9	349	392	567	626	1.80	17.78
	-3	1.29	189.4	343	388	578	634	1.83	18.93
	-4	1.30	186.4	338	379	571	630	1.91	17.66
355-5cR-150-5	-1	1.68	188.9	332	373	525	581	3.89	24.08
	-2	1.53	187.9	333	375	528	584	3.55	23.77
355-5cT-90-3	-1	1.19	185.7	373	421	615	683	1.63	15.36
	-2	1.12	184.8	380	421	606	673	1.70	15.40
355-5cT-90-5	-1	0.88	186.9	384	428	625	690	1.54	14.09
	-2	0.92	184.2	382	428	617	681	1.76	13.21
	-3	0.94	181.0	343	385	609	673	1.45	15.13
	-4	0.91	185.5	341	381	612	679	1.57	14.86
355-5cT-90-10	-1	2.02	187.9	347	399	565	626	2.09	17.16
	-2	1.99	189.3	357	405	567	627	2.32	18.09

355-5cT-120-5	-1	1.34	186.3	305	364	598	663	2.02	18.01
	-2	1.29	184.3	349	392	589	655	1.71	16.01
355-5cT-135-5	-1	1.45	190.9	361	400	566	624	1.93	18.43
	-2	1.44	186.2	358	396	560	622	2.11	19.08
355-5cT-150-5	-1	1.99	190.6	334	369	537	595	3.47	22.58
	-2	1.81	189.0	330	372	542	599	3.02	23.19

Notes: 355-5, -5b, and -5c are three different types of steel plates with the same nominal grade of 355 MPa and the same nominal thickness of 5 mm. 355-5cR and 355-5cT are the plates extracted from the rolling and transverse directions of 355-5c parent materials, respectively.

Table 3.3 Key parameters obtained from flat coupon tests of high strength steels.

Specimen		E_f (GPa)	$f_{y,f}$ (MPa)	$f_{u,f}$ (MPa)	$\epsilon_{u,f}$ (%)	$\epsilon_{f,f}$ (%)	k -	n_{se} -
460-3	-R1	204.1	521	587	9.79	23.05	843.2	0.112
	-R2	204.9	521	585	10.14	27.11	842.0	0.114
	-R3	203.5	519	584	10.41	24.02	847.7	0.117
	Mean	204.1	520	585	10.11	24.73	844.3	0.114
460-6	-R1	194.0	515	618	12.80	29.44	928.6	0.135
	-R2	193.1	531	633	13.64	29.96	949.2	0.135
	-R3	195.2	521	624	13.61	30.54	937.7	0.135
	Mean	194.1	523	625	13.35	29.98	938.5	0.135
550-6	-R1	198.1	643	734	10.78	27.32	1034.9	0.106
	-R2	198.5	643	735	10.49	27.66	1036.6	0.106
	-R3	209.8	652	743	11.36	29.29	1059.9	0.111
	Mean	202.1	646	737	10.88	28.09	1043.8	0.108
690-3	-R1	200.7	746	819	11.00	23.51	1147.4	0.103
	-R2	204.1	743	818	10.56	22.19	1147.5	0.104
	-R3	213.6	733	821	10.45	22.30	1152.7	0.104
	Mean	206.1	741	819	10.67	22.67	1149.2	0.104

Table 3.4 Key parameters of the high strength steel corner coupon tests.

Specimen		r_i/t -	E_c (GPa)	$f_{0.01,c}$ (MPa)	$f_{0.05,c}$ (MPa)	$f_{y,c}$ (MPa)	$f_{u,c}$ (MPa)	$\epsilon_{u,c}$ (%)	$\epsilon_{f,c}$ (%)
460-3-90-5	-1	1.74	193.3	399	454	636	692	1.41	13.91
	-2	1.78	189.8	385	444	643	697	1.25	14.82
	-3	1.83	198.5	386	440	639	698	1.41	14.05
	-4	1.77	183.3	390	437	636	695	1.41	13.50
460-3-90-10	-1	3.70	186.9	384	434	606	658	1.94	17.68

	-2	Test failed								
460-3-90-15	-1	5.43	186.1	338	389	562	617	2.59	18.82	
	-2	5.54	194.1	353	404	573	618	1.18	16.55	
460-3-120-5	-1	2.64	191.6	371	429	611	667	1.50	15.41	
	-2	2.39	187.1	376	426	610	664	1.56	15.18	
	-3	2.28	188.8	378	433	623	680	1.53	15.27	
	-4	2.23	189.8	366	414	601	654	1.36	15.36	
460-3-135-5	-1	2.55	194.1	361	415	613	668	1.46	17.50	
	-2	2.96	193.1	365	418	618	675	1.43	15.86	
460-3-150-5	-1	3.94	194.1	361	413	597	653	1.71	18.05	
	-2	4.09	191.4	512	529	606	643	2.23	18.36	
460-6-90-5	-1	0.82	192.1	426	488	718	781	1.40	17.50	
	-2	0.73	192.6	426	485	718	782	1.30	16.33	
460-6-90-10	-1	1.66	194.1	386	447	654	708	1.45	18.20	
	-2	1.66	194.0	391	452	660	713	1.72	19.40	
460-6-90-15	-1	2.58	193.8	368	425	618	672	2.55	20.17	
	-2	2.57	193.8	371	425	624	678	2.77	22.23	
	-3	2.55	192.8	375	427	616	668	2.51	22.00	
	-4	2.53	200.2	371	430	617	669	2.75	21.90	
460-6-120-10	-1	1.46	194.7	397	460	663	716	1.66	20.60	
	-2	1.45	191.8	393	450	651	703	1.73	19.00	
460-6-135-10	-1	2.00	189.5	356	410	599	652	2.02	20.33	
	-2	1.94	189.9	369	426	610	663	1.91	20.50	
460-6-150-10	-1	2.89	192.0	350	404	583	635	3.25	25.23	
	-2	2.96	195.2	354	409	587	639	3.22	24.17	
550-6-90-5	-1	0.82	195.1	509	582	863	951	1.42	16.53	
	-2	0.80	195.5	484	560	844	933	1.33	15.53	
	-3	0.75	196.5	502	579	865	955	1.63	15.97	
	-4	0.76	197.8	509	588	874	966	1.61	16.13	
550-6-90-10	-1	1.67	204.1	468	539	803	881	1.41	16.40	
	-2	1.67	201.4	470	543	798	871	1.19	16.33	
550-6-90-15	-1	2.33	199.5	463	531	781	858	1.60	18.03	
	-2	2.23	197.2	467	538	789	867	1.67	18.43	
	-3	2.48	200.9	451	520	767	841	1.63	17.23	
	-4	2.53	202.2	449	516	759	836	1.82	18.17	
550-6-120-10	-1	Test failed								
	-2	1.53	196.7	473	545	806	881	1.31	16.83	
550-6-135-10	-1	1.80	200.0	469	537	792	867	1.55	17.20	
	-2	1.98	200.7	478	546	797	877	1.60	17.83	
	-3	1.81	198.2	473	535	794	875	1.64	18.10	
	-4	2.03	197.6	454	527	788	867	1.68	19.30	
550-6-150-10	-1	3.18	194.2	434	493	728	795	1.38	18.53	

	-2	3.05	195.0	437	500	727	795	1.65	19.00
690-3-90-5	-1	1.91	193.0	496	573	846	942	1.44	15.77
	-2	1.90	193.5	498	574	845	939	1.74	14.82
	-3	1.83	195.0	493	564	833	929	1.75	15.95
	-4	1.89	195.3	508	572	835	933	1.74	16.00
690-3-90-10	-1	3.73	195.4	434	516	808	887	1.91	15.05
	-2	3.69	193.5	466	534	800	893	2.02	15.91
	-3	3.61	194.0	476	540	798	886	1.89	15.68
	-4	3.61	197.0	474	541	800	889	2.06	16.50
690-3-90-15	-1	5.60	193.7	468	540	783	868	2.61	19.41
	-2	5.50	197.4	459	535	788	875	2.67	18.36
	-3	5.63	193.4	439	511	771	858	2.53	17.27
	-4	5.62	195.2	446	514	770	857	2.21	16.86
690-3-120-5	-1	2.08	190.9	479	546	817	908	1.67	14.59
	-2	1.97	195.3	487	550	821	916	1.79	15.64
690-3-135-5	-1	2.57	199.6	472	543	819	915	1.94	15.55
	-2	2.74	200.3	471	543	814	904	1.91	15.45
690-3-150-5	-1	4.04	195.8	449	514	765	858	1.87	15.45
	-2	3.78	192.0	454	519	760	850	1.82	16.36
	-3	3.86	190.9	455	520	777	866	2.01	15.27
	-4	4.93	191.8	451	518	779	871	2.04	14.64

3.4 Establishment of the cold-formed steel database

To characterise the material properties of cold-formed steels in the corner region, more than 900 tensile test results including 341 flat coupons and 613 corner coupons of normal and high strength steels from 40 sources were collated to establish a comprehensive database. For the normal strength steel ($f_{y,f} < 460$ MPa), a large set of continuous test data reported in this thesis and scattered data extracted from different cold-formed cross-sections (Afshan *et al.*, 2013; Gardner *et al.*, 2010; Guo *et al.*, 2007; Hayeck, 2016; Hui, 2014; Kettler, 2008; Key *et al.*, 1988; Liu *et al.*, 2022; Singh and Singh, 2018; Tayyebi and Sun, 2020; Wilkinson and Hancock, 1998; Zhu *et al.*, 2019) were collected. In terms of high strength steel ($f_{y,f} \geq 460$ MPa), a spectrum of test data generated in this study and other high strength data on various structural cold-formed members from global literature (Chen *et al.*, 2020; Fang *et al.*, 2018a; Jiang and Zhao,

2022a, 2022b; Kyvelou *et al.*, 2017; Li and Young, 2022; Liu *et al.*, 2022; Liu *et al.*, 2022a, 2022b; Liu *et al.*, 2022; Ma *et al.*, 2015; Pandey and Young, 2019; Pham *et al.*, 2021; Somodi and Kövesdi, 2017; Tayyebi and Sun, 2020; Tran *et al.*, 2016; Wang *et al.*, 2019, 2020; Wang *et al.*, 2017; Xiao *et al.*, 2022; Yang *et al.*, 2022; Zhang *et al.*, 2019, 2020; Zhong *et al.*, 2021) were collected. The key information of collected material test data is summarised in Table 3.5, including source, nominal steel grade or yield strength, available material parameters (Young's modulus E , the yield strength f_y , the ultimate tensile strength f_u , the ultimate strain ϵ_u , the elongation at fraction ϵ_f , and inner corner radius to thickness ratio r_i/t), number of test data, and cross-section from which the coupons were extracted. It should be noted that some unpublished test data from authors' research group were also included in the database.

The assembled database covers nominal yield strength of parent structural steels ranging from 235 MPa to 960 MPa and measured yield strength of cold-formed corner materials varying from 343 MPa to 1324 MPa. Table 3.5 shows that the tensile test results were extracted from a wide range of cold-formed cross-sections, including angle sections, channel sections, built-up cold-formed sections, square and rectangular hollow sections, and polygonal hollow sections such as hexagonal and octagonal hollow sections. In terms of some data extracted from cold-rolled hollow sections, the tensile test results of flat coupon machined from the flat face were selected as the benchmark parameters instead of the unreported material properties of parent materials. This strategy was thought to be adequately acceptable since the average strength enhancement of flat materials in cold-rolled hollow sections was only around 4% (Gardner *et al.*, 2010).

Since the material parameters of tensile coupons in different literatures were reported in different degrees of completeness, the number of data used also varies

among different sub-groups for analysis. Among the total of 314 flat coupon test results, 209 test results were reported with their full range of stress–strain curves, which have been utilised to establish the relationships between $f_{u,t}/f_{y,t}$ ratio and material coefficient k and strain–hardening exponent n_{se} . These data combined with the remaining flat coupon data were also served as the benchmark parameters in the following analysis for cold–formed steels. Among the total of 613 corner coupon test results, 385 test results were used for deriving the predictive model for young’s modulus E_c of cold–formed steels, 236 for 0.01% proof strength $f_{0.01,c}$, 266 for 0.05% proof strength $f_{0.05,c}$, 482 for enhanced yield strength $f_{y,c}$, 472 for enhanced ultimate strength $f_{u,c}$, 516 for ultimate strain $\epsilon_{u,c}$, and 209 for elongation at fraction $\epsilon_{f,c}$, respectively. Distributions of parent material yield strengths and r_i/t ratios after cold–forming are plotted in Figure 3.13.

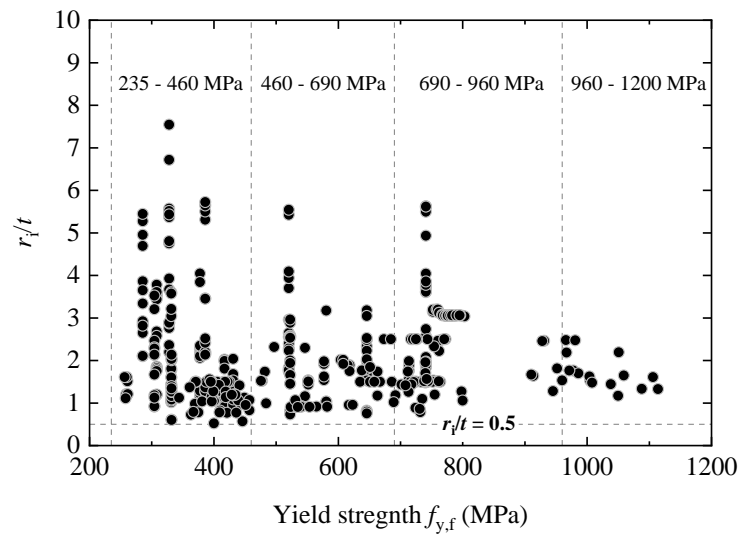


Figure 3.13 Distributions of parent material yield strengths and r_i/t ratios after cold–forming in the database.

Table 3.5 Key information of collected cold–formed steel database.

References	Steel grade or yield strength	Cross–sections from which coupons were extracted	Available parameters of flat coupons	Available parameters of corner coupons	Number of data
Normal strength steels					
This thesis	Q235/Q275/Q355	Angle sections	$E_f, f_{y,f}, f_{u,f}, \varepsilon_{u,f}, \varepsilon_{f,f}$	$E_c, f_{y,c}, f_{u,c}, \varepsilon_{u,c}, \varepsilon_{f,c}, r_i/t$	143
Gardner <i>et al.</i> (2010)	235 MPa	SHS/RHS	$E_f, f_{y,f}, f_{u,f}$	$E_c, f_{y,c}, f_{u,c}, r_i/t$	5
Guo <i>et al.</i> (2007)	235 MPa	SHS/RHS	$f_{y,f}, f_{u,f}$	$f_{y,c}, f_{u,c}, r_i/t$	6
Kettler (2008)	S275/S355	SHS/RHS	$E_f, f_{y,f}, f_{u,f}$	$f_{y,c}, f_{u,c}, \varepsilon_{u,c}$	2
Singh and Singh (2018)	Yst–310	SHS/RHS	$E_f, f_{y,f}, f_{u,f}$	$E_c, f_{y,c}, f_{u,c}, r_i/t$	5
Tayyebi and Sun (2020)	344–409 MPa	SHS/RHS	$E_f, f_{y,f}, f_{u,f}$	$E_c, f_{y,c}, f_{u,c}, r_i/t$	5
Key <i>et al.</i> (1988)	350 MPa	SHS/RHS	$f_{y,f}, f_{u,f}$	$f_{y,c}, f_{u,c}, \varepsilon_{u,c}, r_i/t$	11
Zhu <i>et al.</i> (2019)	355 MPa	SHS/RHS	$E_f, f_{y,f}, f_{u,f}, \varepsilon_{u,f}$	$E_c, f_{y,c}, f_{u,c}, \varepsilon_{u,c}, r_i/t$	2
Liu <i>et al.</i> (2022)	Q355	SHS/RHS	$E_f, f_{y,f}, f_{u,f}, \varepsilon_{u,f}$	$E_c, f_{y,c}, f_{u,c}, \varepsilon_{u,c}, r_i/t$	8
Afshan <i>et al.</i> (2013)	S355	SHS/RHS	$E_f, f_{y,f}, f_{u,f}$	$E_c, f_{y,c}, f_{u,c}, \varepsilon_{u,c}, r_i/t$	8
Hayeck (2016)	S355	RHS	$E_f, f_{y,f}, f_{u,f}$	$f_{y,c}, f_{u,c}, \varepsilon_{u,c}$	12
Hayeck (2015)	S355/S460	SHS/RHS	–	$f_{y,c}, f_{u,c}, \varepsilon_{u,c}$	95
Wilkinson and Hancock (1998)	C350/C450	SHS/RHS	$f_{y,f}, f_{u,f}$	$f_{y,c}, f_{u,c}, r_i/t$	51
Hui (2014)	390 MPa	Channel sections	–	$f_{y,c}, f_{u,c}, \varepsilon_{u,c}$	4
High strength steels					
This thesis	Q460/Q550/Q690	Angle sections	$E_f, f_{y,f}, f_{u,f}, \varepsilon_{u,f}, \varepsilon_{f,f}$	$E_c, f_{y,c}, f_{u,c}, \varepsilon_{u,c}, \varepsilon_{f,c}, r_i/t$	66
Unpublished data from authors	Q460/Q690	Octagonal hollow sections	$E_f, f_{y,f}, f_{u,f}, \varepsilon_{u,f}, \varepsilon_{f,f}$	$E_c, f_{y,c}, f_{u,c}, \varepsilon_{u,c}, \varepsilon_{f,c}, r_i/t$	23
Pham <i>et al.</i> (2021)	G450	Channel sections	$E_f, f_{y,f}, f_{u,f}$	$E_c, f_{y,c}, f_{u,c}, r_i/t$	2
Kyvelou <i>et al.</i> (2017)	S450	Channel sections	$f_{y,f}, f_{u,f}$	$f_{y,c}, r_i/t$	2

Liu <i>et al.</i> (2022)	Q460	SHS/RHS	$E_t, f_{y,f}, f_{u,f}, \varepsilon_{u,f}$	$E_c, f_{y,c}, f_{u,c}, \varepsilon_{u,c}, r_i/t$	8
Chen <i>et al.</i> (2020)	460 MPa	Octagonal hollow sections	$E_t, f_{y,f}, f_{u,f}, \varepsilon_{u,f}, \varepsilon_{f,f}$	$E_c, f_{y,c}, f_{u,c}, \varepsilon_{u,c}, \varepsilon_{f,c}, r_i/t$	8
Li and Young (2022)	500 MPa/550 MPa	Built-up cold-formed sections	$E_t, f_{y,f}, f_{u,f}$	$E_c, f_{y,c}, f_{u,c}, r_i/t$	6
Wang <i>et al.</i> (2017)	S500/S700/S960	SHS	$f_{y,f}, f_{u,f}$	$f_{y,c}, f_{u,c}, \varepsilon_{u,c}, r_i/t$	9
Tayyebi and Sun (2020)	638–730 MPa	SHS/RHS	$E_t, f_{y,f}, f_{u,f}$	$E_c, f_{y,c}, f_{u,c}, r_i/t$	5
Tran <i>et al.</i> (2016)	S650	Polygonal hollow sections	–	$f_{y,c}, f_{u,c}, \varepsilon_{u,c}$	6
Liu <i>et al.</i> (2022)	Q690	Hexagonal hollow sections	$E_t, f_{y,f}, f_{u,f}$	$E_c, f_{y,c}, f_{u,c}, \varepsilon_{u,c}, r_i/t$	7
Liu <i>et al.</i> (2022)	Q690	Irregular hexagonal hollow sections	$E_t, f_{y,f}, f_{u,f}$	$E_c, f_{y,c}, f_{u,c}, \varepsilon_{u,c}, r_i/t$	30
Liu <i>et al.</i> (2022)	Q690	Irregular octagonal hollow sections	$E_t, f_{y,f}, f_{u,f}$	$E_c, f_{y,c}, f_{u,c}, \varepsilon_{u,c}, r_i/t$	10
Fang <i>et al.</i> (2018)	S690	Octagonal hollow sections	$E_t, f_{y,f}, f_{u,f}$	$E_c, f_{y,c}, f_{u,c}, \varepsilon_{u,c}, r_i/t$	6
Jiang and Zhao (2022)	S690	Angle sections	$E_t, f_{y,f}, f_{u,f}$	$E_c, f_{y,c}, f_{u,c}, \varepsilon_{u,c}, r_i/t$	4
Jiang and Zhao (2022)	S690	Channel sections	$E_t, f_{y,f}, f_{u,f}$	$E_c, f_{y,c}, f_{u,c}, \varepsilon_{u,c}, r_i/t$	5
Xiao <i>et al.</i> (2022)	S690	SHS	$E_t, f_{y,f}, f_{u,f}$	$E_c, f_{y,c}, f_{u,c}, \varepsilon_{u,c}, r_i/t$	6
Zhang <i>et al.</i> (2019)	S690	Angle sections	$E_t, f_{y,f}, f_{u,f}$	$E_c, f_{y,c}, f_{u,c}, \varepsilon_{u,c}, r_i/t$	6
Zhang <i>et al.</i> (2020)	S690	Channel sections	$E_t, f_{y,f}, f_{u,f}$	$E_c, f_{y,c}, f_{u,c}, \varepsilon_{u,c}, r_i/t$	12
Zhong <i>et al.</i> (2021)	S700	SHS	$E_t, f_{y,f}, f_{u,f}$	$E_c, f_{y,c}, f_{u,c}, \varepsilon_{u,c}, r_i/t$	4
Ma <i>et al.</i> (2015)	S700/S900	SHS/RHS	$E_t, f_{y,f}, f_{u,f}$	$E_c, f_{y,c}, f_{u,c}, \varepsilon_{u,c}, r_i/t$	11
Yang <i>et al.</i> (2022)	S700/S900	SHS	$f_{y,f}, f_{u,f}$	$f_{y,c}, f_{u,c}, \varepsilon_{u,c}, r_i/t$	3
Somodi and Kovesdi (2017)	S700/S960	SHS	$f_{y,f}, f_{u,f}$	$f_{y,c}, f_{u,c}, \varepsilon_{u,c}, r_i/t$	3
Pandey and Young (2019)	900 MPa/960 MPa	SHS/RHS	$E_t, f_{y,f}, f_{u,f}$	$E_c, f_{y,c}, f_{u,c}, r_i/t$	10
Wang <i>et al.</i> (2020)	S960	Angle and channel sections	$E_t, f_{y,f}, f_{u,f}$	$E_c, f_{y,c}, f_{u,c}, \varepsilon_{u,c}, r_i/t$	2
Wang <i>et al.</i> (2019)	S960	Channel sections	$E_t, f_{y,f}, f_{u,f}$	$E_c, f_{y,c}, f_{u,c}, \varepsilon_{u,c}, r_i/t$	2
Total					613

3.5 Analysis of results and development of predictive expressions

3.5.1 Recalibration of material parameters of parent materials

Material coefficient k and strain–hardening exponent n_{se} are two key parameters linking the predictive model to the material properties of parent materials. The empirical relationships between these two parameters and values of $f_{y,f}$ and $f_{u,f}$ proposed by Karren (1967) were determined based on the material test results of normal strength parent plates. Hence, to further propose the new predictive expressions, a fundamental step is to re–evaluate their relationships including the test data of high strength steels. To obtain the k and n_{se} values, the engineering stress–engineering strain relations (σ_E – ϵ_E) of flat coupons were converted to true stress–true strain relations (σ_T – ϵ_T), and the true stress–true strain relations were then plotted on a log–log scale paper, as illustrated in Figure 3.14. The plots of the logarithm σ_T versus log ϵ_T appear as a straight line in the plastic region.

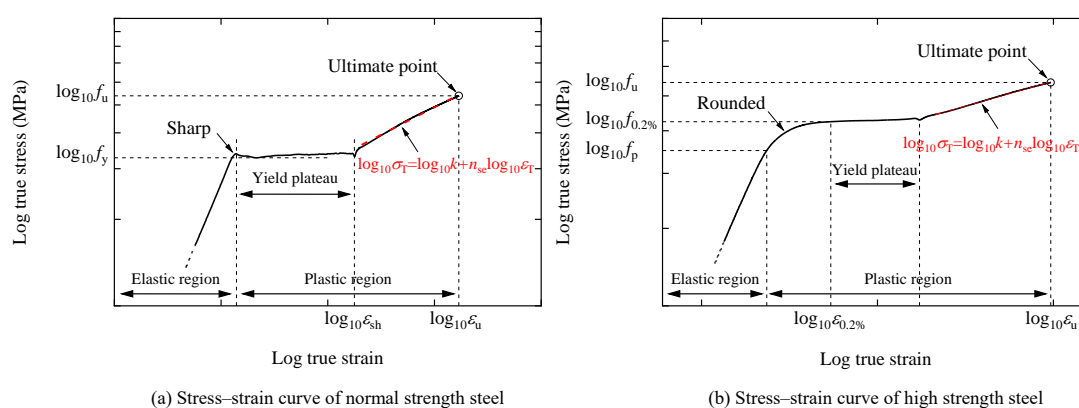


Figure 3.14 Processing examples to obtain material coefficient k and strain–hardening exponent n_{se} .

Linear regression analysis is subsequently performed on plastic region following the approach in Karren (1967), utilising a general regression equation of $\sigma_T = k \epsilon_T^{n_{se}}$. Work examples to obtain k and n_{se} values are given in Figure 3.15.

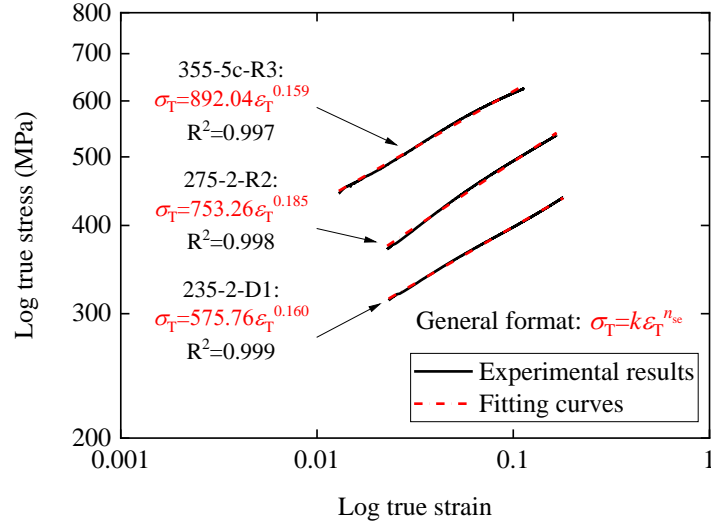


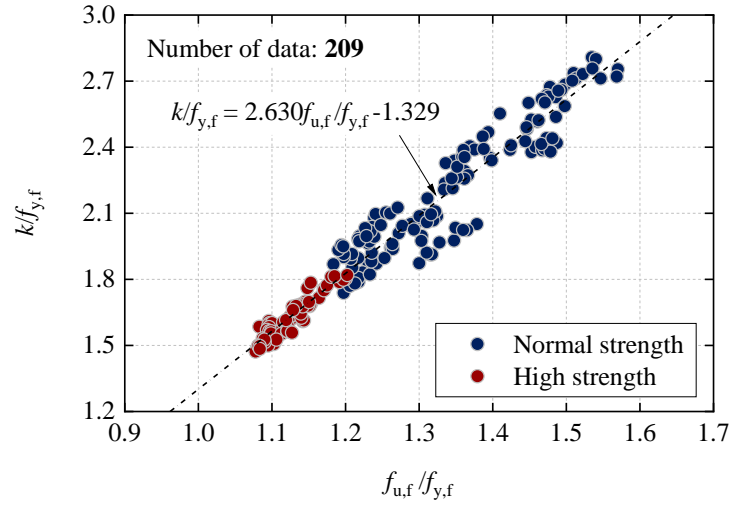
Figure 3.15 Work example of obtainment of k and n_{se} values.

The k and n_{se} values obtained from all flat coupon tests are tabulated in Table 3.1 and Table 3.3, and are plotted in Figure 3.16 for normal and high strength steels, respectively.

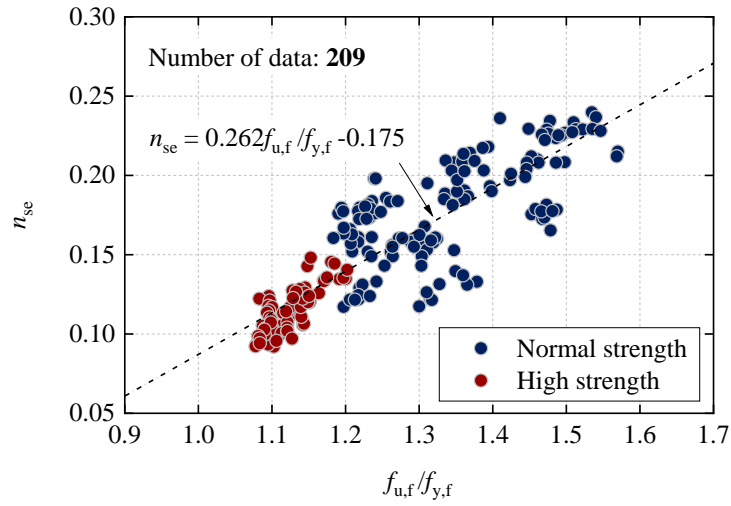
By performing linear regression analysis again, the relationship between material parameters and values of $f_{y,f}$ and $f_{u,f}$ were acquired, as expressed in Eq. (3.1) and Eq. (3.2). The proposed predictive expressions for k and n_{se} provide accurate predictions for normal and high strength steels, with mean values of 1.00 and 1.02, and corresponding coefficients of variation (COV) of 0.04 and 0.13, respectively.

$$k = 2.630 f_{u,f} - 1.329 f_{y,f} \quad \text{Eq. (3.1)}$$

$$n_{se} = 0.262 f_{u,f} / f_{y,f} - 0.175 \quad \text{Eq. (3.2)}$$



(a) Material coefficient k



(b) Strain hardening exponent n_{se}

Figure 3.16 Assessment of the material coefficients and strain hardening exponents.

3.5.2 Young's moduli of cold-formed steels

The average Young's moduli of flat coupon E_f and corner coupon E_c for normal and high strength steels are listed in Table 3.6. The average E_f of parent materials is 207,108 MPa, and the average E_c of cold-formed corner materials is 197,672 MPa, which is 4.4% slightly lower than that of parent materials.

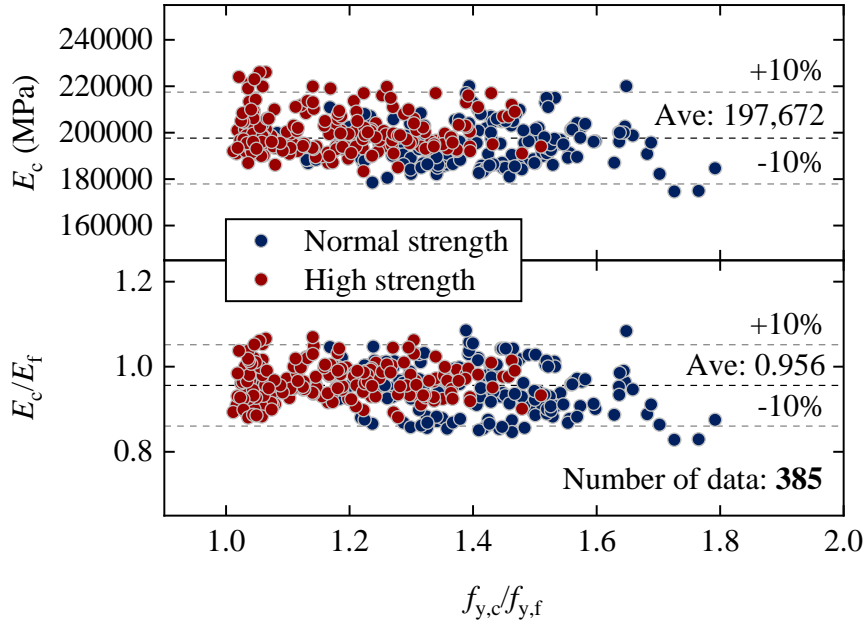


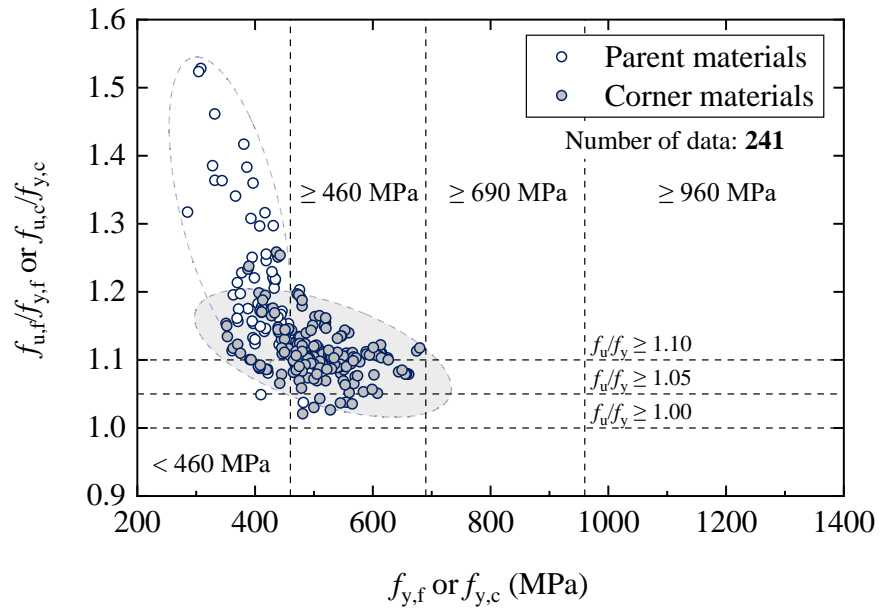
Figure 3.17 Change of Young's modulus before and after cold-forming.

In terms of normal and high strength steel, Figure 3.17 indicates that generally no apparent trend between the reduction of Young's modulus and strength enhancement level can be observed. Hence, given the consistent test result, a fixed Young's modulus value of 198,000 MPa is recommend for cold-formed steels in the corner region, since this value recommended in the European cold-formed members standard (CEN, 2006c), American cold-formed steel members design specification (AISI, 2016) and Australian cold-formed steel structures design standard (AS/NZS, 2018) is 210,000 MPa, 203,000 MPa, and 200,000 MPa, respectively.

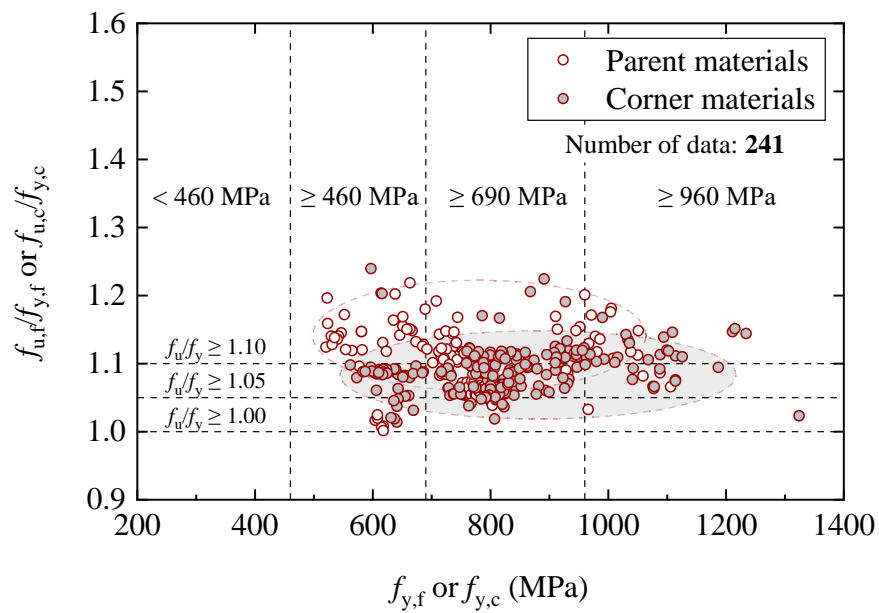
Table 3.6 Young's moduli for normal and high strength steels.

	Number of data	E_f	E_c	E_c/E_f
		Average value		
	–	MPa	MPa	–
Normal strength steels	170	206,646	194,783	0.945
High strength steels	215	207,475	199,969	0.964
All	385	207,108	197,672	0.956

3.5.3 Strength enhancement



(a) Normal strength steels

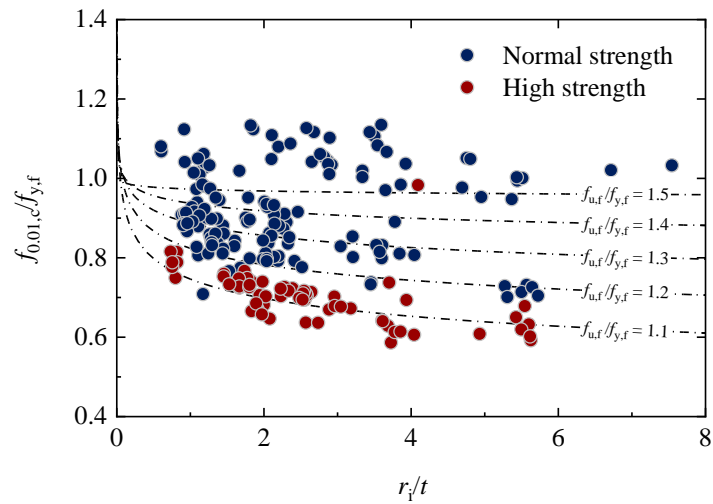


(b) High strength steels

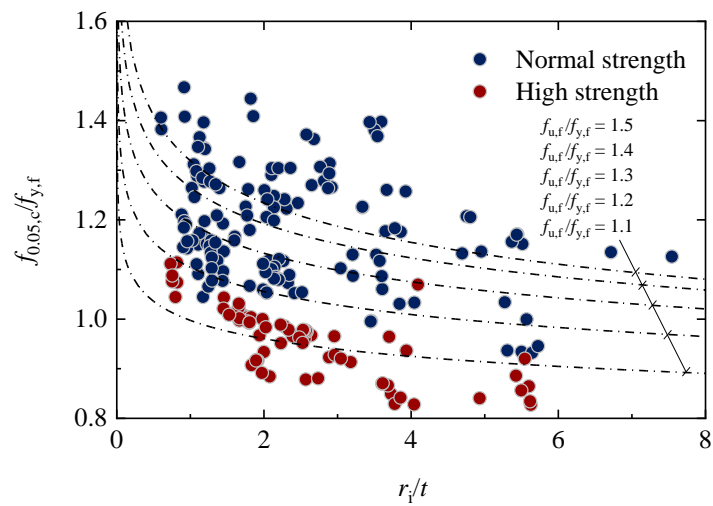
Figure 3.18 Relationships of the f_u/f_y with f_y for normal and high strength steels before and after cold-forming.

In Figure 3.18, the development of f_u/f_y ratios against yield strength f_y for structural steels before and after cold-forming was depicted and grouped according to their measured yield strength for comparison purposes. A general trend of reducing f_u/f_y ratio

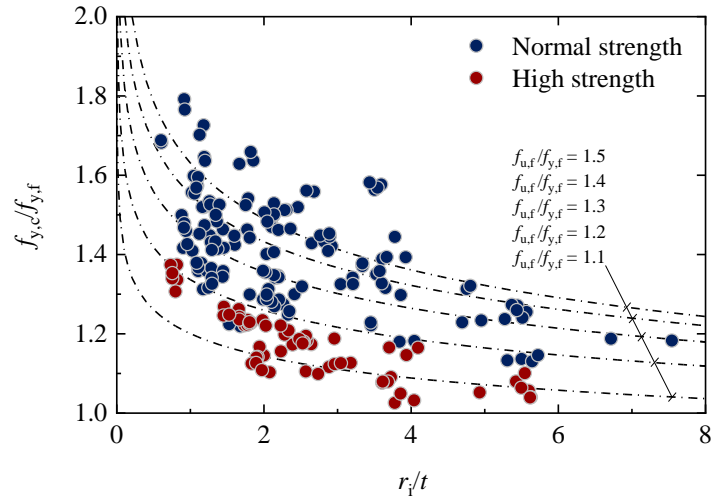
with the strength enhancement caused by cold-forming effects can be apparently observed. Moreover, the majority of flat and corner coupon results fulfil the strength ratio requirement ($f_u/f_y > 1.05$) of EN 1993-1-12 (CEN, 2007). It can be seen that high strength steel materials that possessed a relatively lower f_u/f_y ratio can develop a fewer strength enhancement as compared with normal strength steel materials, vice versa.



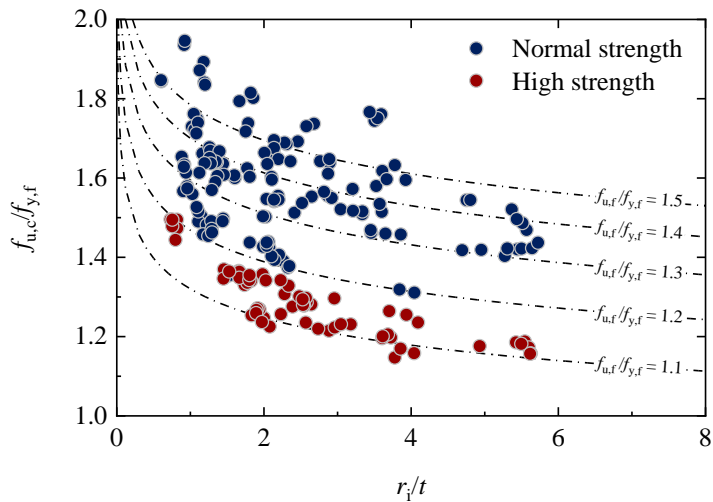
(a) $f_{0.01,c}$



(b) $f_{0.05,c}$



(c) Yield strength



(d) Ultimate tensile strength

Figure 3.19 Trends of enhanced strengths against r_i/t ratio.

This phenomenon can be more clearly revealed when the strength enhancement levels $f_{y,c}/f_{y,f}$ are plotted against r_i/t ratios in Figure 3.19, in which a tighter r_i/t ratios implies a larger permanent plastic deformation and cold-forming effect. This figure explicitly demonstrates that the trends of strength enhancement have no different developing mechanism, and there is no clear boundary between normal and high strength steels. The influencing parameters affecting the strength enhancement behaviour are only the $f_{u,t}/f_{y,f}$ ratio of parent materials and the indicator of plastic

deformation r_i/t ratio after cold-forming.

Also, as shown in Figure 3.19, it is worth noting that a similar conclusion can be drawn for the strength enhancement of the proof strengths $f_{0.01}$ and $f_{0.05}$, the ultimate tensile strength f_u for normal and high strength structural carbon steels, which means the relationship of $f_{u,c}/f_{y,f}$, r_i/t , and $f_{u,f}/f_{y,f}$ can also be potentially predicted.

Based on the abovementioned findings, to propose predictive expressions for those enhanced strengths after cold-forming, the collection of normal and high strength steel corner coupon data was fitted using the generalised predictive model which was derived based on Karren's model, as given in Eq. (3.3). On the basis of a series of least square regression analysis, the four model coefficients C_1 – C_4 used in the generalised predictive model were subsequently determined for the 0.01% proof strength $f_{0.01,c}$ ($C_1 = 0.591$, $C_2 = -1.004$, $C_3 = 0.194$, and $C_4 = -0.854$), the 0.05% proof strength $f_{0.05,c}$ ($C_1 = 0.782$, $C_2 = -1.274$, $C_3 = 0.010$, and $C_4 = 0.397$), the enhanced yield strength $f_{y,c}$ ($C_1 = 0.923$, $C_2 = -1.373$, $C_3 = 0.006$, and $C_4 = 0.570$) and the enhanced ultimate strength $f_{u,c}$ ($C_1 = 1.019$, $C_2 = -1.544$, $C_3 = 0.091$, and $C_4 = -0.078$). Substituting C_1 – C_4 into the generalised predictive model, the proposed strength enhancement models can be simplified and rewritten as Eq. (3.4) to Eq. (3.7), following the format of American and Australian standard.

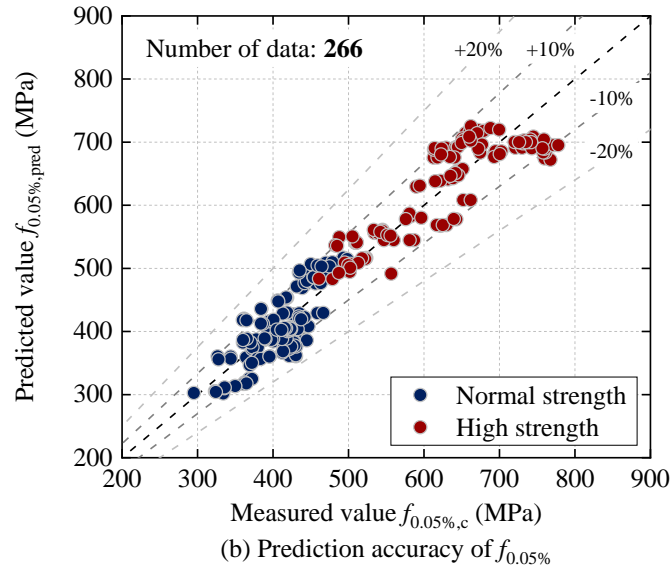
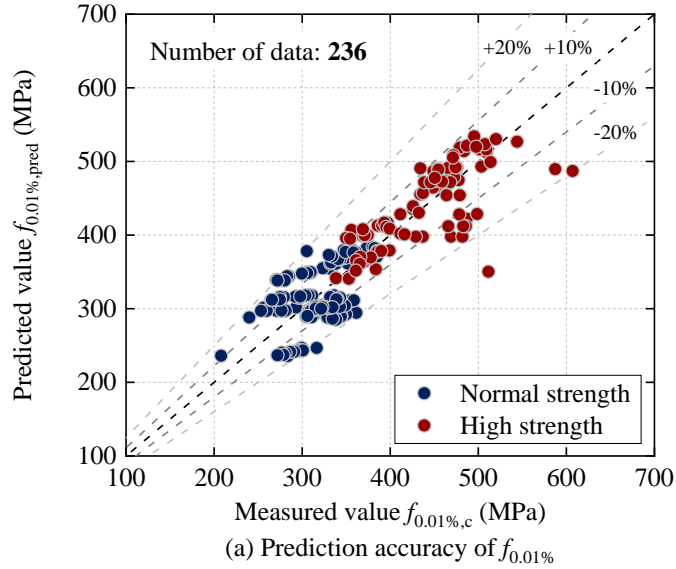
$$f_{y,c \text{ or } u,c} = \frac{k\alpha}{(r_i/t)^\beta} \text{ in which } \begin{cases} \alpha = C_1 + C_2 n_{se} \\ \beta = C_3 + C_4 n_{se} \end{cases} \quad \text{Eq. (3.3)}$$

$$f_{0.01,c} = \frac{B_c f_{y,f}}{(r_i/t)^\beta} \text{ in which } \begin{cases} B_c = 2.366(f_{u,f}/f_{y,f}) - 0.692(f_{u,f}/f_{y,f})^2 - 1.019 \\ \beta = -0.224(f_{u,f}/f_{y,f}) + 0.343 \end{cases} \quad \text{Eq. (3.4)}$$

$$f_{0.05,c} = \frac{B_c f_{y,f}}{(r_i/t)^\beta} \text{ in which } \begin{cases} B_c = 3.087(f_{u,f}/f_{y,f}) - 0.878(f_{u,f}/f_{y,f})^2 - 1.336 \\ \beta = 0.104(f_{u,f}/f_{y,f}) - 0.060 \end{cases} \quad \text{Eq. (3.5)}$$

$$f_{y,c} = \frac{B_c f_{y,f}}{(r_i/t)^\beta} \text{ in which } \begin{cases} B_c = 3.538(f_{u,f}/f_{y,f}) - 0.946(f_{u,f}/f_{y,f})^2 - 1.546 \\ \beta = 0.149(f_{u,f}/f_{y,f}) - 0.094 \end{cases} \quad \text{Eq. (3.6)}$$

$$f_{u,c} = \frac{B_c f_{y,f}}{(r_i/t)^\beta} \text{ in which } \begin{cases} B_c = 3.928(f_{u,f}/f_{y,f}) - 1.064(f_{u,f}/f_{y,f})^2 - 1.713 \\ \beta = -0.020(f_{u,f}/f_{y,f}) + 0.105 \end{cases} \quad \text{Eq. (3.7)}$$



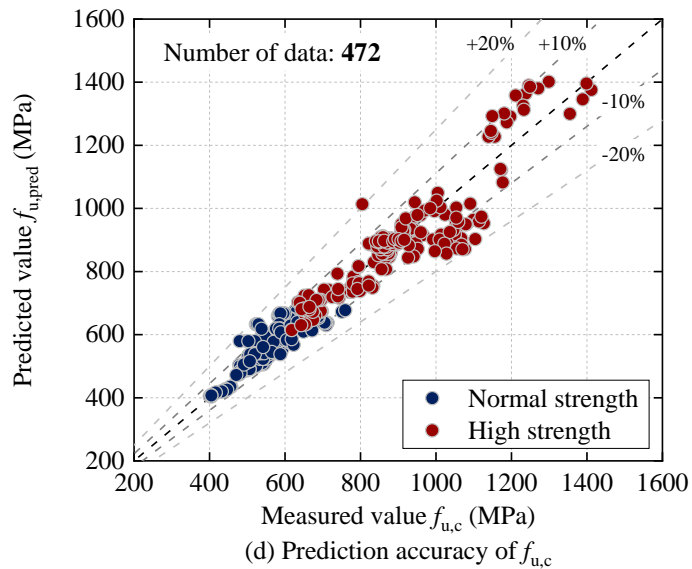
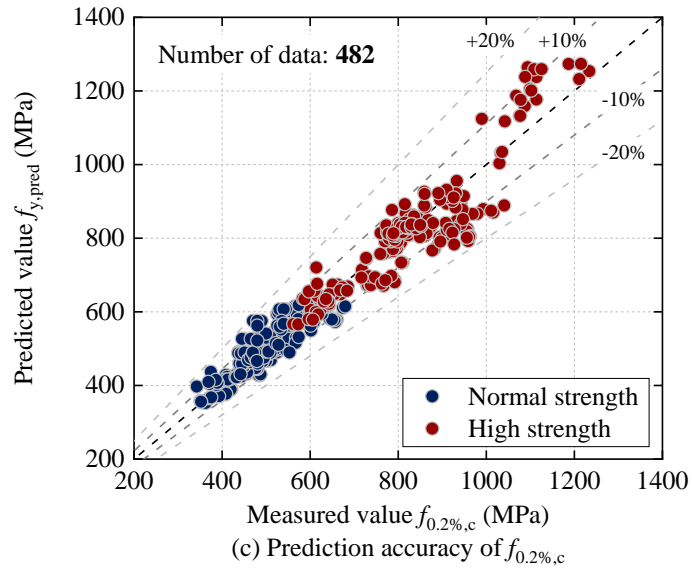


Figure 3.20 Prediction accuracy for enhanced strengths.

The accuracies of above strength enhancement models are graphically demonstrated in Figure 3.20, where the predicted values are plotted against the measured values. It can be seen from Figure 3.20 that the predicted values yield accurate prediction of the measured values, with the mean predicted to measured value being 1.00, 1.00, 1.00, and 1.00 and the corresponding COV being 0.105, 0.073, 0.066 and 0.063 for the 0.01% proof strength $f_{0.01,c}$, the 0.05% proof strength $f_{0.05,c}$, the enhanced yield strength $f_{y,c}$ and enhanced ultimate strength $f_{u,c}$, respectively. Moreover, the prediction accuracy of the proposed models was compared to those models

proposed Karren (1967), Gardner *et al.* (2010) and Rossi *et al.* (2013), and the comparison results are given in Table 3.7.

Table 3.7 Statistical evaluations between different predictive expressions.

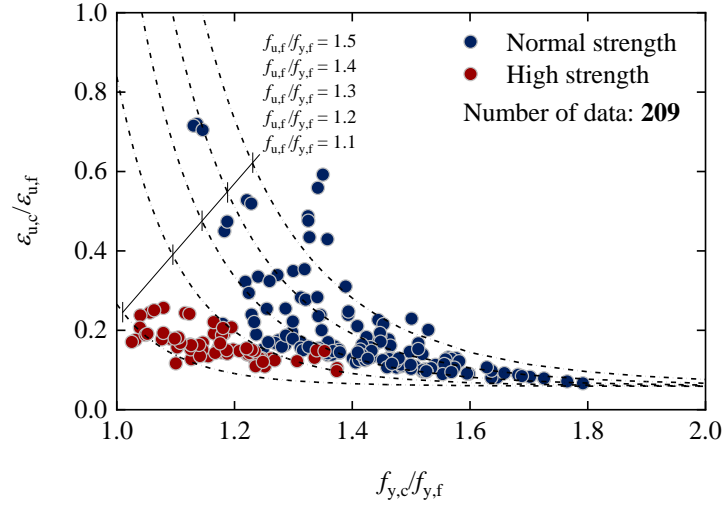
		Predicted-to-measured values			
		Proposed model	Karren's model	Gardner's model	Rossi's model
$f_{0.01,c}$	Mean	1.00	–	–	–
	COV	0.105	–	–	–
$f_{0.05,c}$	Mean	1.00	–	–	–
	COV	0.073	–	–	–
$f_{y,c}$	Mean	1.00	1.04	0.90	0.95
	COV	0.066	0.085	0.107	0.058
$f_{u,c}$	Mean	1.00	–	–	–
	COV	0.063	–	–	–

3.5.4 Loss in ultimate strain

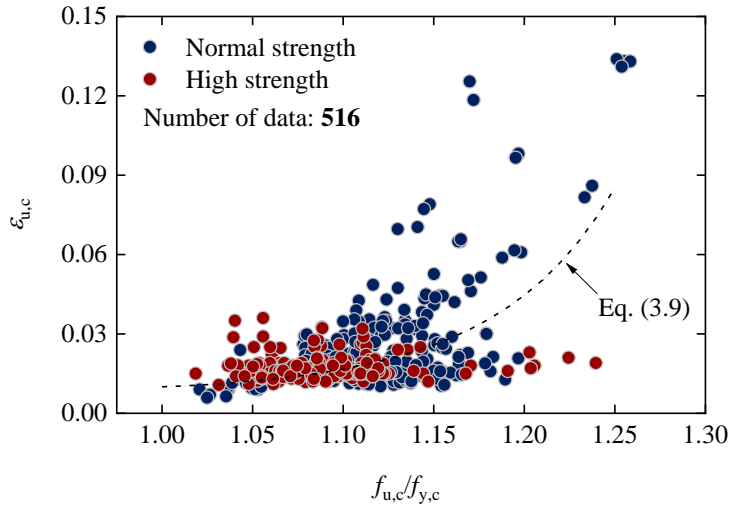
The ultimate strain of corner coupons was found to be gradually reducing with the increase of cold-works. To make a direct comparison, the corner coupon test results of normal strength steels and high strength steels generated in this study are presented in Figure 3.21 (a), in which the values of $\varepsilon_{u,c}/\varepsilon_{u,f}$ (the ultimate strains after and before cold-forming) are plotted against the strength enhancement level $f_{y,c}/f_{y,f}$. It can be seen from the figure that high strength steels may suffer severer deterioration on ultimate strain after cold-forming as compared with normal strength steels, which may be attributed to the lower $f_{u,f}/f_{y,f}$ ratio of parent materials. Based on a process of regression analysis, a predictive expression for $\varepsilon_{u,c}$ was proposed and expressed as Eq. (3.8), in which the effects of $f_{u,f}/f_{y,f}$ of parent materials was directly incorporated.

$$\varepsilon_{u,c} / \varepsilon_{u,f} = \frac{[-6.093 + 5.727(f_{u,f} / f_{y,f})]}{(f_{y,c} / f_{y,f})^{[18.594 - 7.602(f_{u,f} / f_{y,f})]}} + 0.059, \text{ but } \varepsilon_{u,c} / \varepsilon_{u,f} \leq 1.0 \text{ for } \varepsilon_{u,f} \text{ remains known}$$

Eq. (3.8)



(a) Ultimate strain $\varepsilon_{u,f}$ known



(b) Ultimate strain $\varepsilon_{u,f}$ unknown

Figure 3.21 Trend between the change of ultimate strain and related parameters.

Moreover, if the yield strength and ultimate strength of corner coupon is known (or can be predicted using Eq. (3.6) and Eq. (3.7)), but the original ultimate strain $\varepsilon_{u,f}$ of parent material remains unknown, a predictive expression for $\varepsilon_{u,c}$ without the variable of $\varepsilon_{u,f}$ is preferable. Hence, the collected 516 ultimate strain values in the developed database were also plotted against the correspond $f_{u,c}/f_{y,c}$ ratios in Figure 3.21 (b), and a predictive expression was proposed to reasonably capture the relationship between the values of $\varepsilon_{u,c}$ and the values of $f_{u,c}/f_{y,c}$, as given in Eq. (3.9). Table 3.8 provides the assessment results for these predictive expressions, with mean values of 1.05 and 1.00,

and corresponding COV of 0.25 and 0.42 for Eq. (3.8) and Eq. (3.9), respectively. It should be noted that the ultimate strain of cold-formed steels in the corner region is much lower than that in the flat region and hot-rolled steels, which is similar to the finding presented by Gardner and Yun (2018).

$$\varepsilon_{u,c} = 0.01(f_{u,c} / f_{y,c})^{(28f_{u,c}/f_{y,c}-25.4)}, \text{ for } \varepsilon_{u,f} \text{ remains unknown} \quad \text{Eq. (3.9)}$$

Table 3.8 Assessment of prediction accuracy for $\varepsilon_{u,c}$ and $\varepsilon_{f,c}$.

		Predicted-to-measured values		
		Eq. (3.8)	Eq. (3.9)	Eq. (3.10)
$\varepsilon_{u,c}$	Mean	1.05	1.00	–
	COV	0.25	0.42	–
$\varepsilon_{f,c}$	Mean	–	–	1.00
	COV	–	–	0.17

3.5.5 Loss in elongation at fracture

Elongation at fracture is indicative to the plastic deformation that steel can undergo before fracture. Since most of elongations at fracture $\varepsilon_{f,c}$ were not reported in the literature and not all of them were measured in the same manner presented in Section 2.3, only the normal strength steel data and the high strength steel data from this study were selected and used in the assessment to make a consistent comparison. The elongation at fracture of corner coupons $\varepsilon_{f,c}$ is normalised by the elongation at fracture of parent materials $\varepsilon_{f,f}$, and plotted against the strength enhancement level in Figure 3.22. On the basis of the least square regression analysis, the proposed predictive expression for $\varepsilon_{f,c}$ is given by Eq. (3.10). As reported in Table 3.8, the mean predicted-to-measured value is equal to 1.00, with a moderate COV of 0.17, indicating that the proposed model can provide accurate predictions.

$$\varepsilon_{f,c}/\varepsilon_{f,f} = 0.202 + 0.779(f_{y,c}/f_{y,f})^{-2.914} \quad \text{Eq. (3.10)}$$

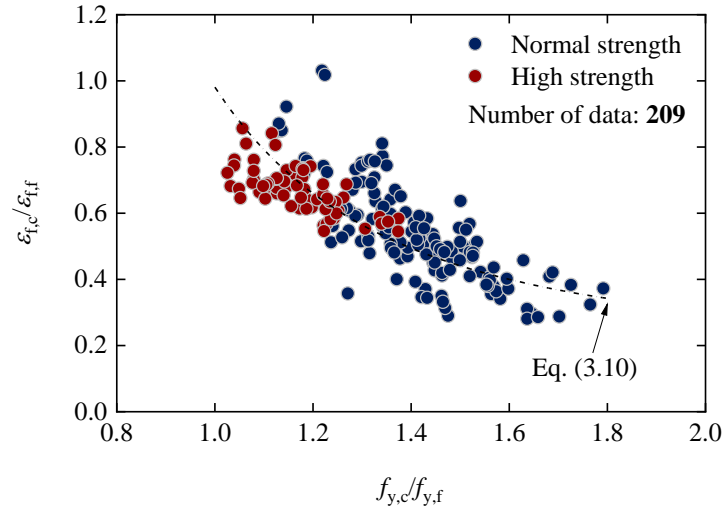


Figure 3.22 Trend between the change of elongation at fracture and strength enhancement level.

3.6 Proposed material constitutive model

The use of existing material constitutive models for cold-formed steels, such as one-stage model proposed by Ma *et al.* (2015) and modified two-stage Ramberg–Osgood model (Gardner and Yun, 2018; Mirambell and Real, 2000; Rasmussen, 2003), needs the input of basic material properties of cold-formed corners. The basic material properties of cold-formed steels, like the Young’s modulus, yield strength, and ultimate tensile strength, etc., can be determined through corner coupon tests. Without these values, these existing material models cannot be directly used to obtain the stress–strain curves.

It is known that cold work of forming alters material properties of steels with enhanced material strengths and a rounded stress–strain response with no sharply defined yield point. The enhancement of material strengths is related to material properties of parent metal and amount of plastic deformation of cold-formed corners which can be deflected by the inner or outer radius to thickness ratio of the corners, r_i/t

or r_o/t . It is of interests to develop material models that can predict the stress–strain behaviours of cold–formed steels only based on the material properties of parent metal and amount of plastic deformation, without conduction of corner coupon tests. Therefore, the focus of this section is to propose constitutive models that can accurately describe the stress–strain responses of cold–formed steels which can be used when the material properties of cold–formed corners are unavailable.

Proposed approaches, i.e., adoptions of the one–stage model proposed by Ma *et al.* (2015) and the modified two–stage Ramberg–Osgood model developed by Gardner and Yun (2018), but with predictive expressions to relate the material properties of cold–formed steels to that of parent metals and the amount of plastic deformation, for describing the material stress–strain behaviour of cold–formed steels, are summarised in this section.

3.6.1 One–stage model

The one–stage model proposed by Ma *et al.* (2015) is given by:

$$\varepsilon = \varepsilon_p + \frac{\sigma}{E} = \varepsilon_p + \frac{f_{0.2}}{E} \left(\frac{\varepsilon_p}{0.002} \right)^{\left(\frac{1}{n+K\varepsilon_p^{m_0}} \right)} \quad \text{Eq. (3.11)}$$

in which ε_p is plastic strain, n is the original strain–hardening exponent, K is a material coefficient and m is the exponent of plastic strain.

The original strain–hardening exponent n can be calculated by Eq. (3.12), the material coefficient K can be determined by Eq. (3.13), and the exponent m_0 needs to be determined by fitting the model to the tested stress–strain curve data.

$$n = \frac{\ln(20)}{\ln(f_{0.2} / f_{0.01})} \quad \text{Eq. (3.12)}$$

$$K = \frac{\log\left(\frac{f_u}{f_{0.2}}\right)\left(\frac{\varepsilon_{pu}}{0.002}\right)^{-n}}{(\varepsilon_{pu})^{m_o}} \quad \text{Eq. (3.13)}$$

in which $f_{0.2}$ and $f_{0.01}$ are the yield strength and 0.01% proof stress, respectively, f_u is the ultimate tensile strength, ε_{pu} is the plastic strain corresponding to f_u , which can be calculated by $(\varepsilon_u - f_{0.2}/E_s)$.

An implicit stress–strain curve can be determined by this one–stage model through a set of material properties, namely E , $f_{0.01}$, $f_{0.2}$, f_u , ε_u , n and m . Based on the described analyses in Section 3.5, E can be taken as $0.956E_f$ (E_f is the Young’s modulus of parent material) or the specified values in the design codes. $f_{0.01}$, $f_{0.2}$, f_u , ε_u , n can be determined from Eq. (3.4), Eq. (3.6), Eq. (3.7), Eq. (3.8) or Eq. (3.9), and Eq. (3.12), respectively, if the corner material properties are not reported. The exponent m may be determined by curve fitting as described in Ma *et al.* (2015).

Regression analysis on all tested corner coupon tests has been conducted to obtain the m values. The fitted m_o values are plotted against a parameter associated with the material properties of parent metal and $(r_i/t) \cdot \ln(f_{u,t}/f_{y,t})$ in Figure 3.23. On the basis of the least square regression analysis, the proposed predictive expression for the exponent m_o is given by Eq. (3.14). The mean predicted–to–measured value of m_o is equal to 1.02, with a COV of 0.20. The comparison between the predicted m_o values and measured m_o values is presented in Figure 3.24. With the prediction expression of the exponent m_o , all the input parameters needed for the one–stage model can be determined.

$$m_o = \exp(-0.82 \cdot (r_i / t) \ln(f_{u,t} / f_{y,t})) \quad \text{Eq. (3.14)}$$

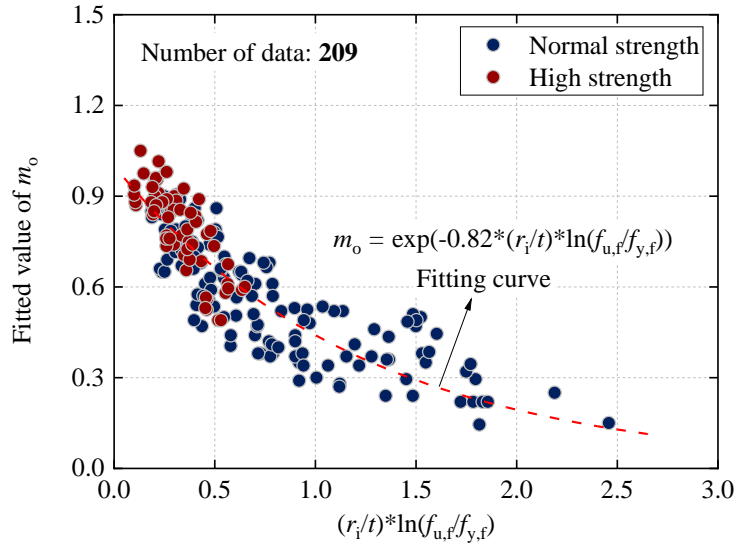


Figure 3.23 Trend between the fitted value of m_o and $(r_i/t) * \ln(f_{u,f}/f_{y,f})$.

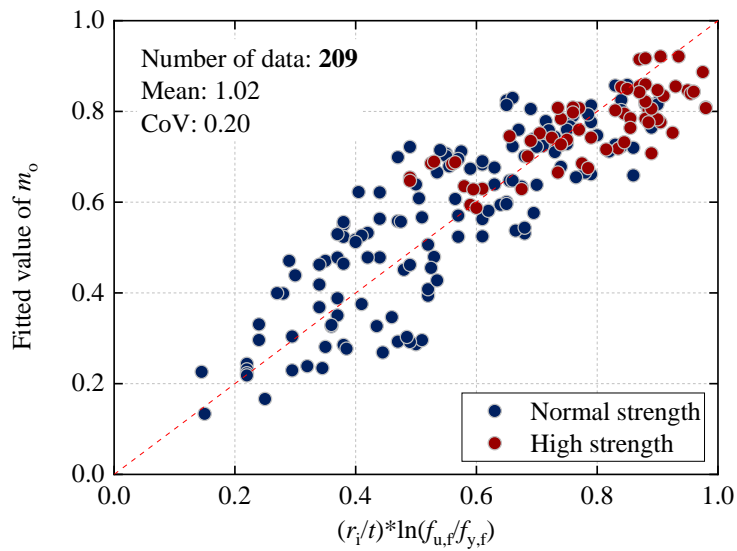


Figure 3.24 Comparison between the predicted m_o values and measured m_o values.

3.6.2 Two-stage Ramberg–Osgood model

The modified two-stage Ramberg–Osgood model proposed by Gardner and Yun (2018) is given by:

$$\varepsilon = \begin{cases} \frac{\sigma}{E} + 0.002 \left(\frac{\sigma}{f_{0.2}} \right)^n & \text{for } \sigma \leq f_{0.2} \\ \frac{\sigma - f_{0.2}}{E_{0.2}} + \left(\varepsilon_u - \varepsilon_{0.2\%} - \frac{f_u - f_{0.2}}{E_{0.2}} \right) \left(\frac{\sigma - f_{0.2}}{f_u - f_{0.2}} \right)^m + \varepsilon_{0.2\%} & \text{for } f_{0.2} < \sigma \leq f_u \end{cases} \quad \text{Eq. (3.15)}$$

in which $E_{0.2}$ is the tangent modulus of the stress–strain curve at the yield strength (0.2% proof stress), $\varepsilon_{0.2}$ is the strain corresponding to the yield strength $f_{0.2}$.

If the material properties of cold–formed steels are reported, expressions given in Gardner and Yun (2018) can be used to determine the strain–hardening exponent n , the tangent modulus at yield strength $E_{0.2}$, the ultimate strain ε_u (strain corresponding to the ultimate tensile strength f_u), the ultimate tensile strength f_u and the second strain–hardening exponent m .

If the material properties of cold–formed steels are unknown, the following approaches are recommended:

(1) The first piecewise may be determined from Eq. (3.16), and the 0.05% proof stress $f_{0.05}$ and yield strength $f_{0.2}$ may be calculated from Eq. (3.5) and Eq. (3.6), respectively.

(2) The tangent modulus $E_{0.2}$ could be taken by Eq. (3.17), while E is taken as $0.956E_f$ (E_f is the young’s modulus of parent material) or the specified values in the design codes.

(3) The strain ε_u corresponding to the ultimate tensile strength f_u can be determined by Eq. (3.8) or Eq. (3.9) developed in Section 3.5.

(4) The second strain hardening exponent m may be obtained from Eq. (3.18), where the yield strength $f_{0.2}$ and ultimate tensile strength could be calculated from Eq. (3.6) and Eq. (3.7), respectively.

$$n = \frac{\ln(4)}{\ln(f_{0.2} / f_{0.05})} \quad \text{Eq. (3.16)}$$

$$E_{0.2} = \frac{E}{1 + 0.002n \frac{E}{f_{0.2}}} \quad \text{Eq. (3.17)}$$

$$m = 1 + 3.2 \frac{f_{0.2}}{f_u} \quad \text{Eq. (3.18)}$$

By using the proposed approaches, stress–strain curves can be predicted based on the material properties of parent metal for a given corner geometry, i.e., corner radius–to–thickness ratio.

3.6.3 Evaluation of proposed models

The accuracy of the proposed models for cold–formed steels is evaluated through comparisons of typical experimental stress–strain curves from the collected database with corresponding predicted curves. A total of 6 curved coupon test results generated from this study, covering a wide nominal yield strength range of 235 MPa to 690 MPa, were used for evaluation.

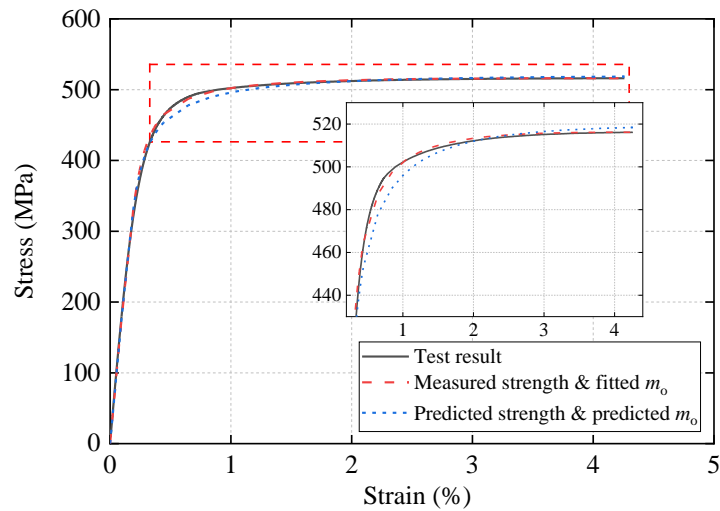
3.6.3.1 One–stage model

Representative comparisons between six experimental stress–strain curves and the corresponding predicted curves from the proposed one–stage model are depicted in Figure 3.25. In the evaluation of the one–stage model, two cases have been considered in the comparison:

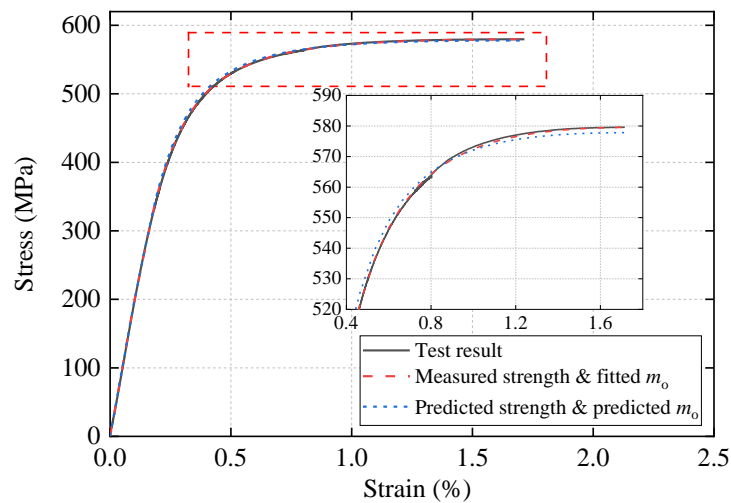
- (1) predictions using measured material strengths and predicted value of m_o ;
- (2) predictions using both predicted material strengths and value of m_o .

The measured and predicted strengths, and the fitted and predicted m_o values of the

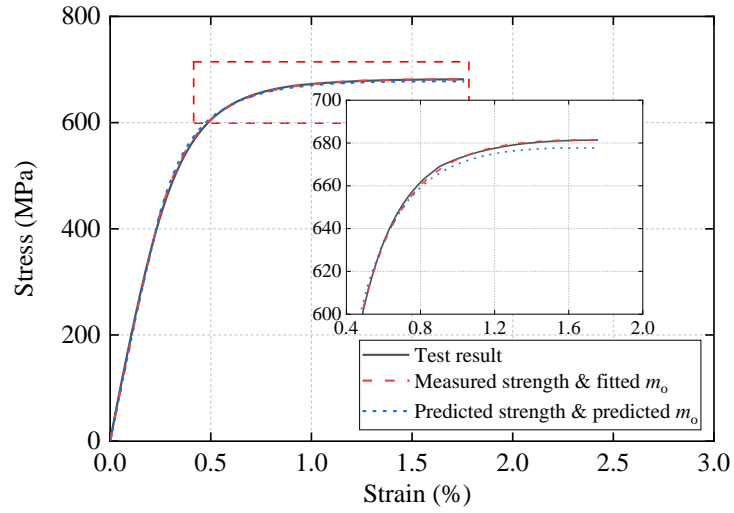
specimens used for evaluation of the proposed model are summarised in Table 3.9. The comparison of the measured and predicted parameters indicates that the expressions proposed in this Section can yield predictions with satisfactory accuracy. The predicted stress–strain curves consistently match well with the experimental stress–strain curves. Therefore, the proposed one–stage model is able to provide an accurate representation of the full range stress–strain responses of cold–formed steels.



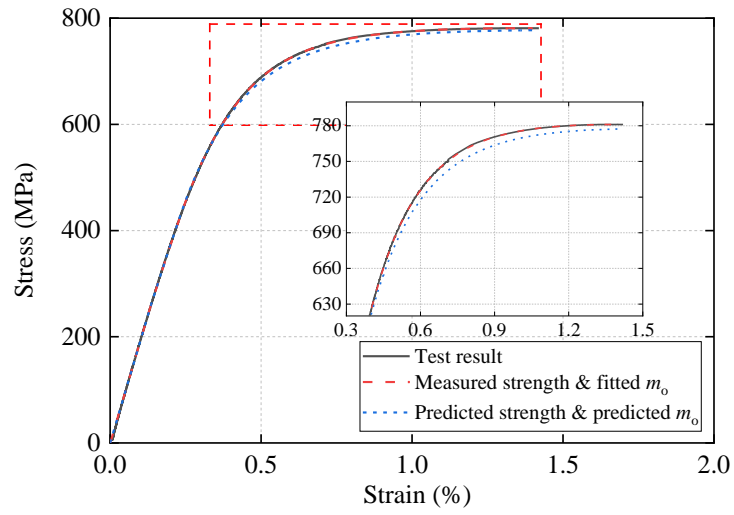
(a) 235-5-135-R5-1



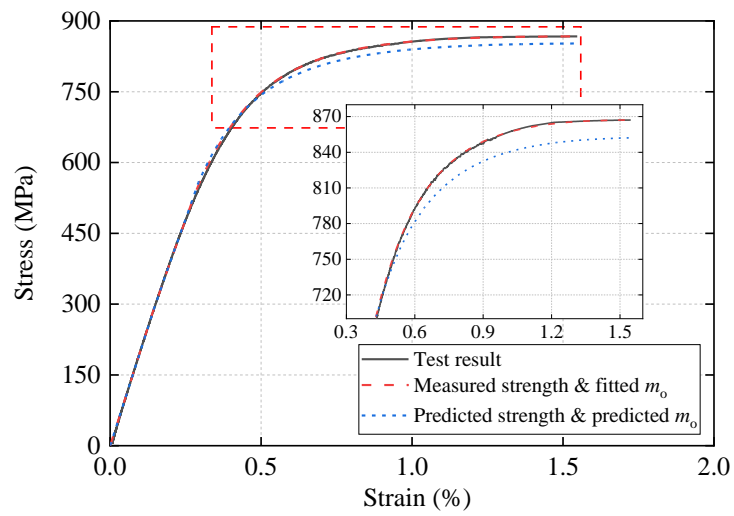
(b) 275-3-90-R3-1



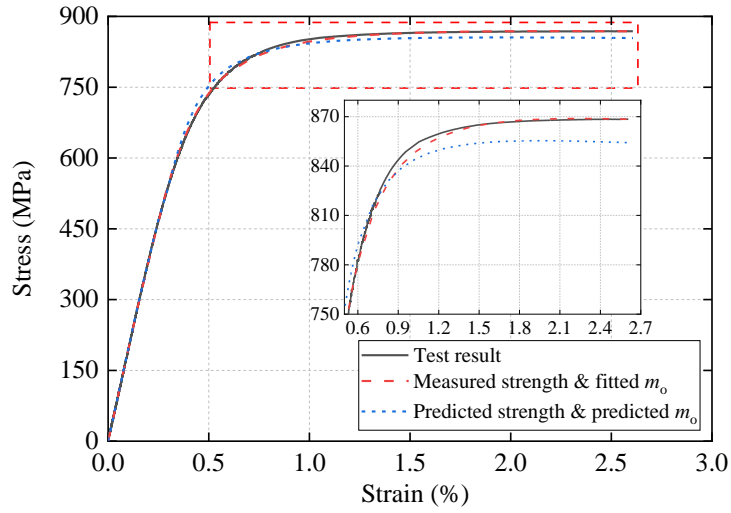
(c) 355-5cT-90-R5-2



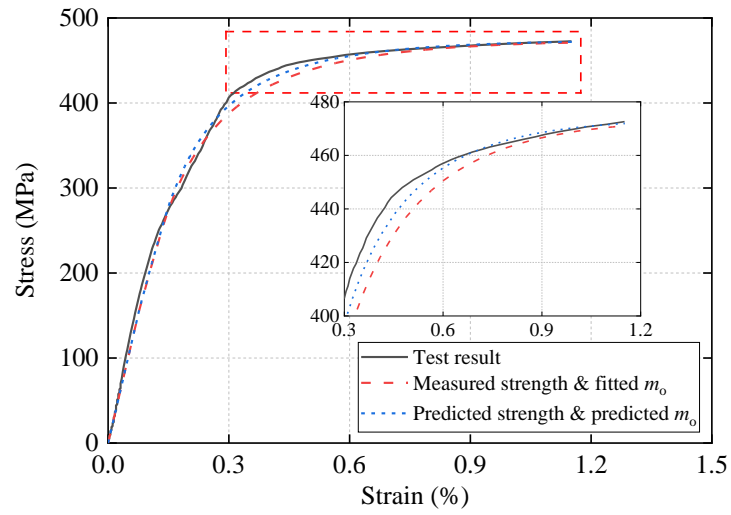
(d) 460-6-90-R5-1



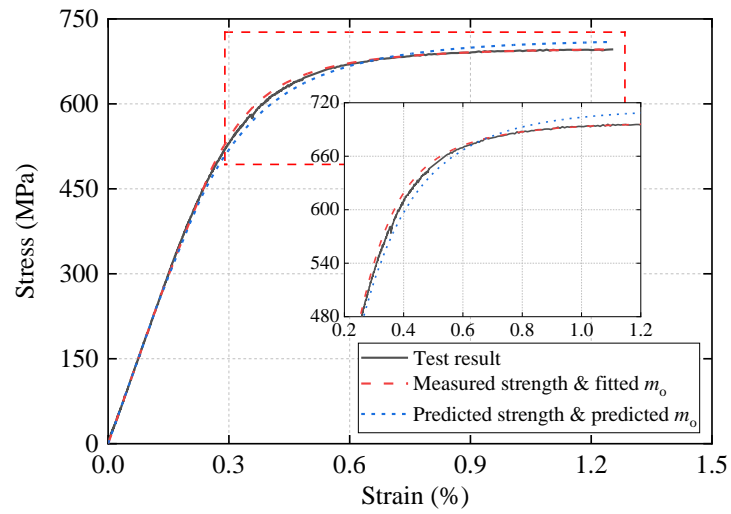
(e) 550-6-135-R10-1



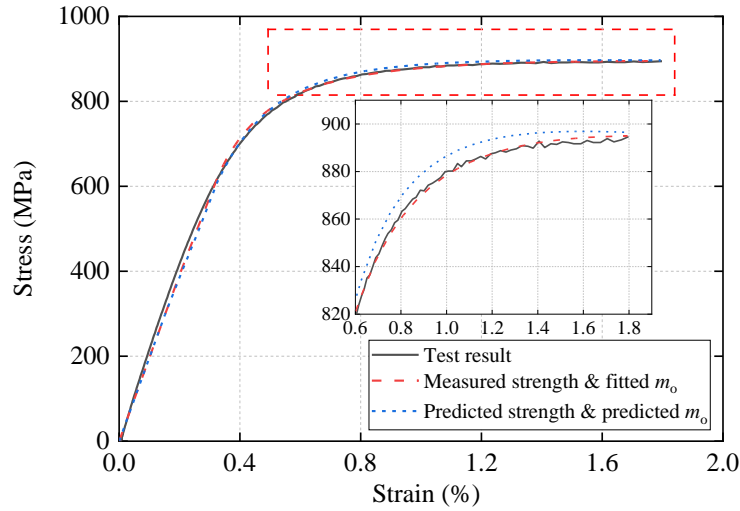
(f) 690-3-90-R15-1



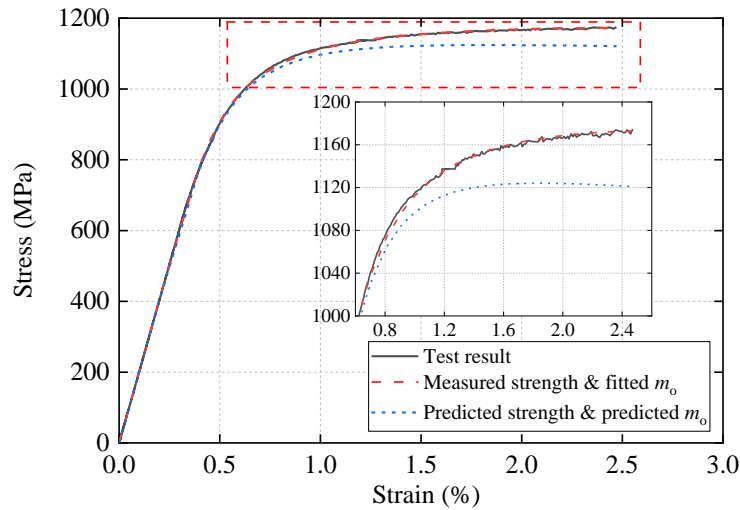
(g) S355 SHS 60×60×3 CF (Gardner *et al.*, 2010)



(h) S460 CF1 75×3-C6 (Chen *et al.*, 2020)



(i) S690 CS-A2 (Xiao *et al.*, 2022)



(j) S960 C70x40x6-C (Wang *et al.*, 2019)

Figure 3.25 Comparison of the stress–strain curves predicted from one–stage model based on measured or predicted material parameters with test stress–strain curves.

3.6.3.2 Two–stage Ramberg–Osgood model

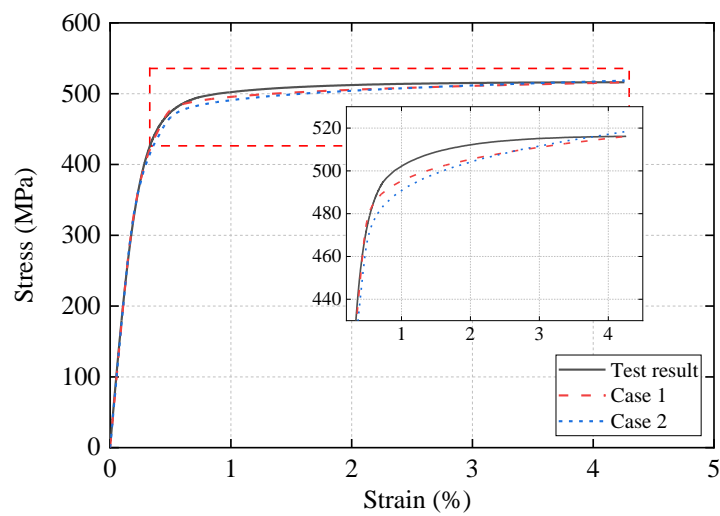
Representative comparisons between six experimental stress–strain curves and the corresponding predicted curves from the modified two–stage Ramberg–Osgood model are shown in Figure 3.26. In the evaluation of the two–stage model, two cases have been considered in the comparison as well:

- (1) predictions using measured material strengths and values of n and m obtained

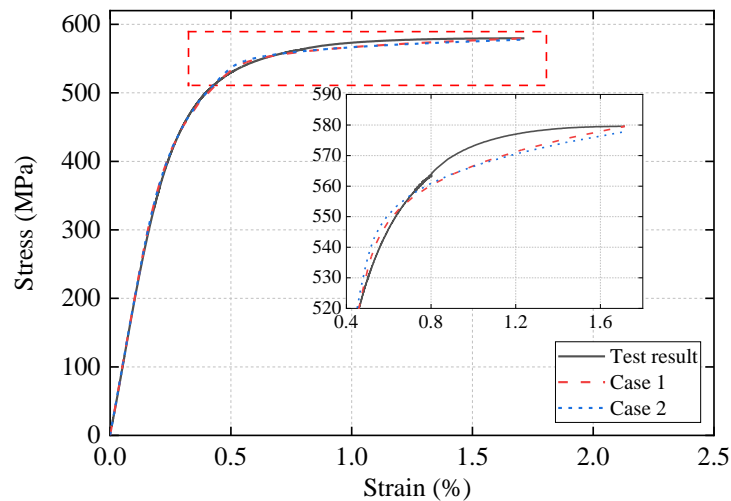
from Gardner and Yun (2018).

(2) predictions using both predicted material strengths and values of n and m .

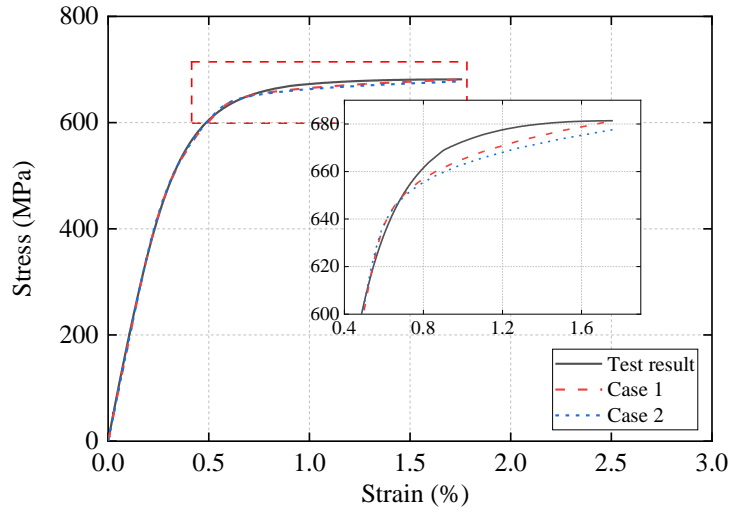
The n and m values obtained from Gardner and Yun (2018) and expressions proposed in this study of the specimens used for evaluation are summarised in Table 3.9. The comparison of the measured and predicted parameters indicates that the expressions proposed in this Section can yield predictions with satisfactory accuracy.



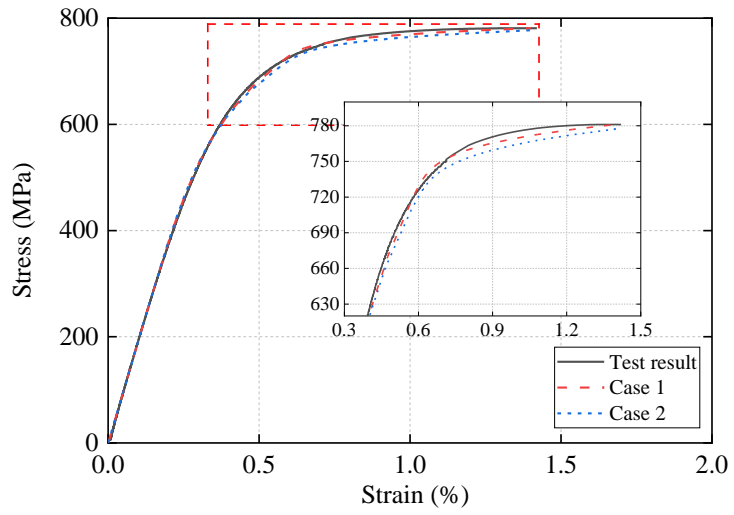
(a) 235-5-135-R5-1



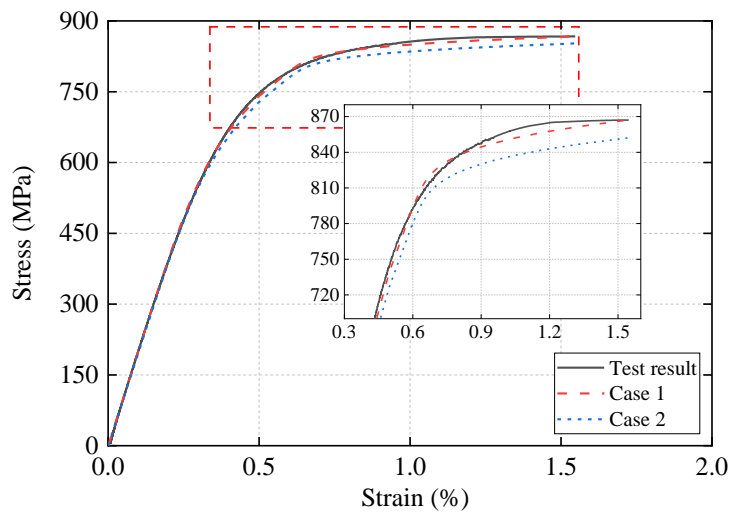
(b) 275-3-90-R3-1



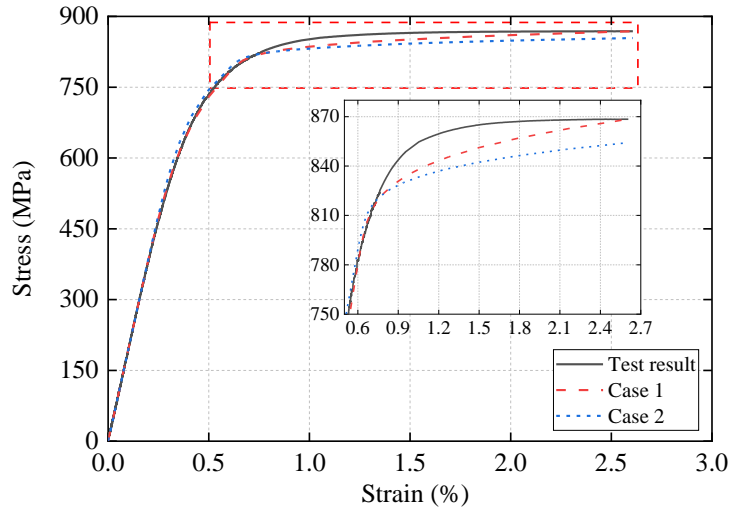
(c) 355-5cT-90-R5-2



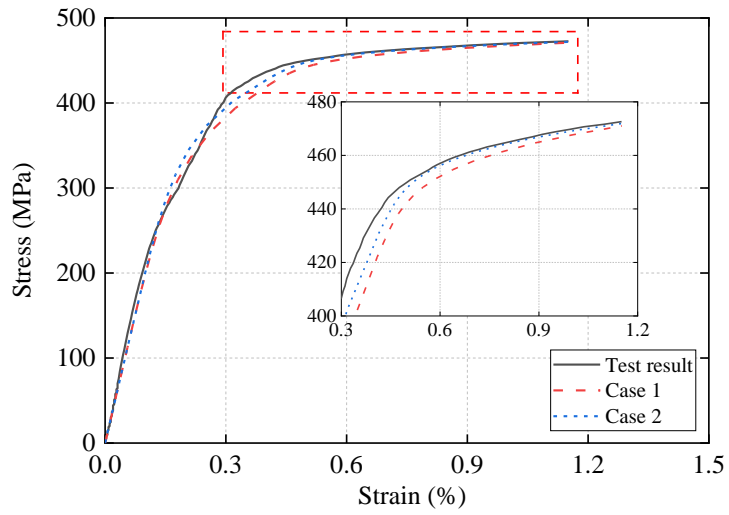
(d) 460-6-90-R5-1



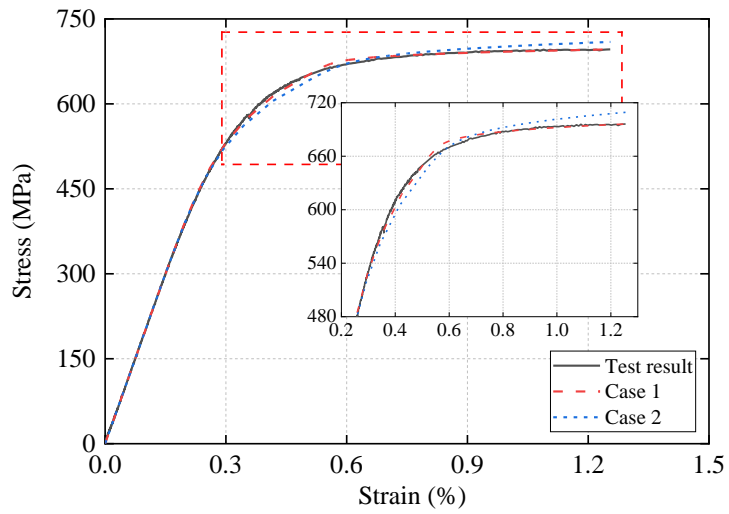
(e) 550-6-135-R10-1



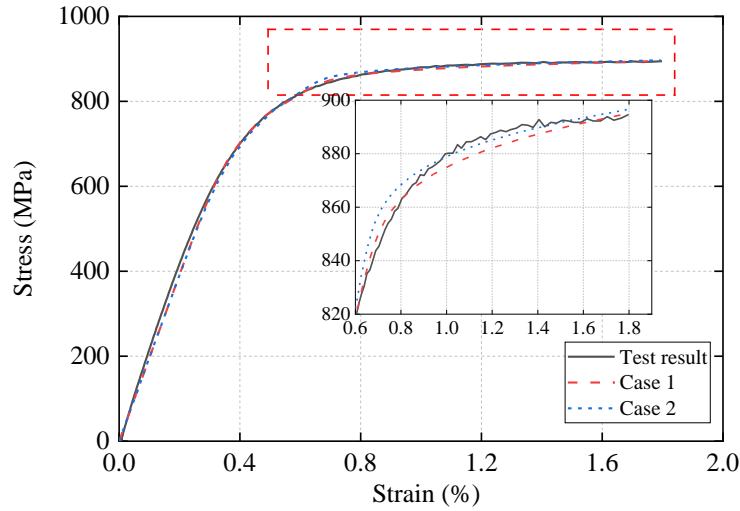
(f) 690-3-90-R15-1



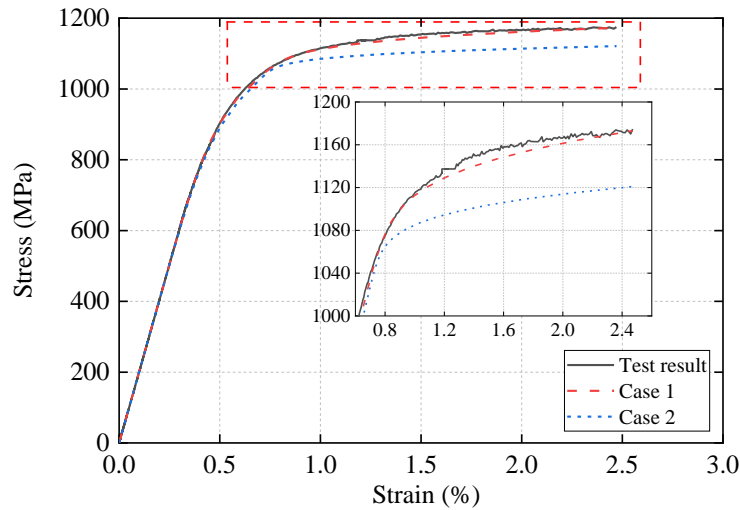
(g) S355 SHS 60×60×3 CF (Gardner *et al.*, 2010)



(h) S460 CF1 75×3-C6 (Chen *et al.*, 2020)



(i) S690 CS-A2 (Xiao *et al.*, 2022)



(j) S960 C70×40×6-C (Wang *et al.*, 2019)

Figure 3.26 Comparison of the stress–strain curves predicted from modified two–stage Ramberg–Osgood model based on measured or predicted material parameters with test stress–strain curves.

The predicted stress–strain curves consistently match well with the experimental stress–strain curves. Therefore, the modified two–stage Ramberg–Osgood with proposed expressions is able to provide an accurate representation of the full range stress–strain responses of cold–formed steels.

Table 3.9 Measured and predicted material properties of cold-formed steels used for comparison.

Specimen	Measured properties				Predicted properties				r_i/t	Fitted m_o	Predicted m_o Eq. (3.14)	Gardner & Yun (2018)		Proposed	
	$f_{0.01}$	$f_{0.05}$	$f_{0.2}$	f_u	$f_{0.01}$	$f_{0.05}$	$f_{0.2}$	f_u				n	m	n	m
					Eq. (3.4)	Eq. (3.5)	Eq. (3.6)	Eq. (3.7)							
235-5-135-R5-1	281	380	466	516	298	376	454	518	2.14	0.44	0.43	6.82	3.98	7.33	3.89
275-3-90-R3-1	311	427	522	580	318	427	526	578	1.09	0.82	0.71	6.92	3.97	6.69	4.00
355-5cT-90-R5-2	380	499	617	681	375	506	619	678	0.92	0.79	0.81	6.89	4.02	6.89	4.02
460-6-90-R5-1	426	582	718	781	436	583	708	777	0.82	0.98	0.89	6.61	4.03	7.09	4.01
550-6-135-R10-1	469	641	792	867	479	651	778	852	1.80	0.88	0.88	6.56	4.01	7.78	4.01
690-3-90-R15-1	468	640	783	869	472	677	793	854	5.60	0.61	0.63	6.91	3.97	8.71	4.07
S355 SHS 60×60×3 CF	255	340	422	471	266	359	431	472	1.37	0.84	0.89	6.42	3.96	7.64	4.01
S460 CF1-75×3-C6	427	556	661	696	398	545	649	709	2.30	0.65	0.77	7.97	4.13	7.97	4.02
S690 CS-A2	630	719	827	895	496	705	834	897	3.06	0.92	0.87	9.91	4.05	8.22	4.07
S960 C70×40×6-C	748	899	1033	1173	625	871	1034	1121	2.47	0.72	0.85	9.33	3.93	8.08	4.04

3.6.3.3 Quantitative evaluation of the prediction accuracy

Graphical comparisons of generated stress-strain curves between the proposed one-stage and two-stage Ramberg-Osgood model are shown in Figure 3.25 and Figure 3.26. Evidently, generated stress-strain curves from these two models were in good agreement with those obtained from material tests. Furthermore, to quantitatively evaluate the accuracy of these two models, the mean absolute percentage error (MAPE) between generated and measured stress-strain curves was calculated using Eq. (3.19).

$$\text{MAPE} = \frac{100\%}{n} \sum_{i=1}^n \left| \frac{\sigma_m - \sigma_p}{\sigma_m} \right| \quad \text{Eq. (3.19)}$$

in which σ_m and σ_p are measured and predicted stresses at the evaluation point, and n is the total number of the evaluation point which equals 40, representing that 40 equally spaced points in each cold-formed steel stress-strain curve were selected for the evaluation.

Table 3.10 Quantitative evaluation results between proposed material models.

Group (MPa)	Number of curves	Mean values of MAPE within sub-group	
		Proposed one-stage model	Two-stage model
$235 \leq f_{y,f} < 460$	143	0.94%	1.44%
$460 \leq f_{y,f} < 690$	65	0.61%	0.91%
$690 \leq f_{y,f}$	34	0.49%	0.72%
	Mean:	0.79%	1.20%

The MAPE of all cold-formed steel stress-strain curves in the database has been obtained, grouped, and reported in Table 3.10. The MAPEs between generated curves using the proposed one-stage Ramberg-Osgood model and measured curves are 0.94%, 0.61%, and 0.49% for each sub-group. In comparison, those of the two-stage Ramberg-Osgood model are 1.44%, 0.91%, and 0.72% for each sub-group, respectively. Generally, the mean values of MAPE are 0.79% and 1.20% for the proposed one-stage

model and two-stage model, respectively. As can be found from the quantitative evaluation results, the proposed one-stage and two-stage Ramberg-Osgood models can accurately describe the rounded stress-strain response of cold-formed steel in the corner region.

3.7 Concluding remarks

A comprehensive investigation into the cold-forming effect of normal and high strength structural carbon steel has been presented herein. An experimental investigation on normal and high strength steels was first carried out. Tensile tests were conducted on 93 flat coupons extracted from parent materials and 212 corner coupons machined from cold-formed corners. An extensive database comprising more than 900 tensile test results was developed based on the obtained test results and collected data from the global literature. Predictive expressions for the key material parameters of cold-formed steels in the corner region have been derived based on the analysis of the developed database. According to the statistical results, the predicted material parameters are shown to be in great agreement with test results. A material constitutive model was then proposed to accurately describe the stress-strain response of cold-formed steel in the corner region, while the key parameters used in this model can be determined from the abovementioned predictive expressions. Comparisons between the experimental stress-strain curves and corresponding predicted curves show that the proposed constitutive model can provide an accurate representation of the stress-strain response for cold-formed steel in the corner region. In conclusion, the proposed predictive expressions combined with the proposed constitutive model are considered to be appropriate for use in the design of cold-formed steel structures.

Chapter 4 Behaviour and design of rectangular hollow section steel columns under pure compression

4.1 Introduction

Rectangular hollow sections, one of the most widely adopted tubular section with a simple form but extraordinary structural efficiencies, for instance, offering the possibility to be infilled with concrete to obtain a larger load-bearing capacity, are the first choice for structural engineers when they design their structural components. RHS tube products can be generally classified into two sets based on their manufacturing methods, namely hot-finished tubes and cold-formed tubes. Hot-finished RHS tubes may be more favourable because of the uniform distribution of material properties and neglectable residual stresses after heat treatment. However, cold-formed RHS tubes still gain their positions in the market due to the merits of comparatively easier fabrication methods and high economic efficiencies. For the RHS tube undergoes cold-working but without post-production heat treatment during their fabrication process, they can be regarded as cold-formed RHS tubes. There are various cold-working methods to produce RHS tubes, including indirect-forming, direct-forming and a less common method by tip-to-tip welding two press-braked channel sections.

This chapter therefore presents an experimental investigation on the press-braked RHS stub columns and long columns. The material properties, residual stress distributions, and local geometric imperfections of press-braked RHS were studied. Tests were performed on a series of press-braked RHS stub columns and long columns with different steel grades, width-to-thickness H/t ratios and various non-dimensional slenderness. Finite element models were carefully developed and validated against measured test results. Following the validation, parametric studies comprising various

parameters were subsequently conducted to generate a wider spectrum of database. The experimental and numerical results are utilised to determine if current design codes can be extended to the design of press-braked RHSs under axial compression. Cross-sectional capacity and column buckling resistance predicted from existing design codes were also assessed. Modified design recommendations were provided based on the experimental results and generated numerical results. Reliability analysis was carried out to verify the applicability of current design methods and design recommendations.

4.2 Press-braked RHS stub columns

4.2.1 General

A total of 10 press-braked RHS stub columns were fabricated using structural steel plates of nominal steel grades Q355 (N series) and Q460 (H series) in this study. To form an open channel section first, steel plates were cut into steel strips with v-notches of 30 degrees on both end for full penetration weld, then the plates were subsequently press-braked. These steel plates were firstly cut into steel strips with v-notches of 30 degrees on both ends for full penetration weld, then the plates were further press-braked to form an open channel section. It is worth noting that the punch radii should be carefully selected to ensure that plastic deformations within the cold-bending corner do not exceed the limitation. EN 10219-2: 2006 (CEN, 2006b) also provides recommendations on the ratio of outer corner radius to the tube thickness, which is $2.0 \leq R_o/t \leq 3.0$ for $6 \text{ mm} < t \leq 10 \text{ mm}$. After press-braking, a careful visual inspection was conducted to check the corner cracking did not occur as the steel plates experienced large plastic deformation. Due to the length limitation of press-braking machines, the total length of specimens was shorter than those fabricated by traditional manufacturing methods.

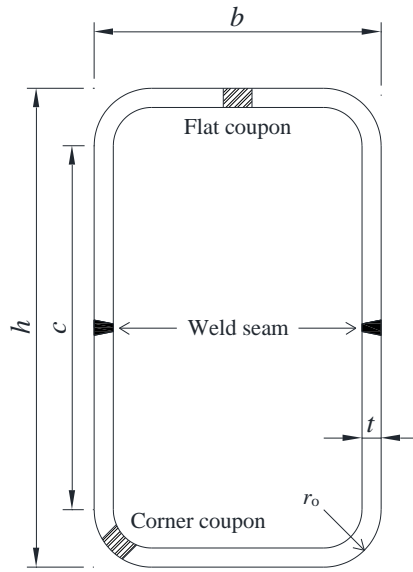


Figure 4.1 Definition of dimensions for the press-braked RHS.

It is more convenient to adopt manual gas-shield metal arc welding when tip-to-tip welding two press-braked channels together, which may introduce unexpected welding imperfection during manual welding as compared with automatic welding such as the electric resistance welding. To control the quality of welding, the welding parameters were carefully designed to ensure the input linear heat energy does not exceed 1.5kJ/mm. By doing so, the deterioration of mechanical properties around the welding seam can be regarded as have insignificant impact on the structural behaviour of columns. The welding parameters are listed in Table 4.1 and the definition of dimensions for RHS is shown in Figure 4.1.

Table 4.1 Welding parameters for the Gas-shield metal arc welding.

Nominal steel grade	Thickness	Voltage	Current	Welding speed	Line heat input
–	mm	V	A	mm/min	kJ/mm
Q355	6	24	210	200	1.21
Q355	10	30	260	240	1.56
Q460	6	24	210	200	1.21
Q460	10	30	260	240	1.56

4.2.2 Material properties

To obtain material properties of the cross-sections under investigation, tensile coupon tests were performed on 8 coupons cut from virgin plates (VP), 16 coupons cut from the flat region of RHS, and 16 coupons extracted from the corner region of the RHSs. The tensile coupons were tested using a 500kN Instron testing system, and the coupon dimensions and test procedure were conformed to the requirements of EN ISO 6892-1 (CEN, 2019). A pair of strain gauges were affixed to the centre of both sides of the coupon to record the initial axial strains, while 50mm and 25mm extensometers were mounted on the design gauge length of flat and corner coupons respectively to measure the full stress-strain response during the tensile test. Bending residual stresses were released after extracting corner coupons from the specimens, resulting in a slightly curved corner coupon after cutting. Hence, corner coupons were located and tested through a specially designed pin grip. The setup for the tensile tests on flat and corner coupons is shown in Figure 4.2.

For each tensile coupon test, the loading strain rate was controlled to follow 3 stages, a strain rate of 0.05%/min was employed from beginning of the test until a yield plateau is observed (or after 0.2% proof strength for corner coupons that have no yield plateau), then a strain rate of 0.1%/min was adopted until the ultimate strength is achieved, and finally a strain rate of 0.2%/min is performed from the ultimate strength to fracture. Stress relaxation for 100 seconds was allowed between each stage to obtain the static material properties. A similar tensile coupon test procedure was also adopted in Huang and Young (2014) and Chen *et al.* (2020).

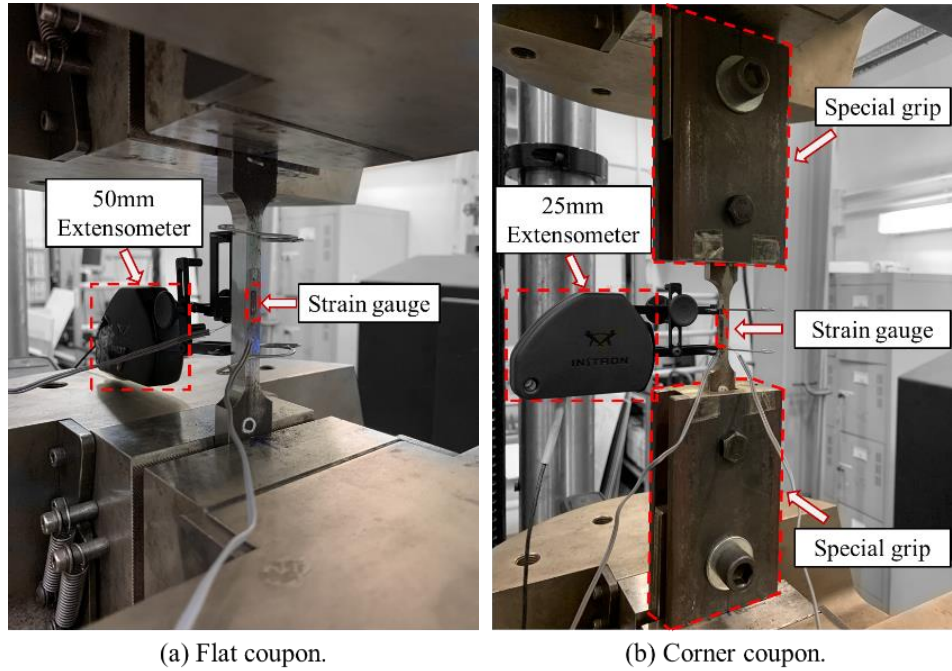


Figure 4.2 Test setup for tensile coupon tests.

Table 4.2 Measured material properties of N series press-braked RHSs.

Section	Flat coupons					Corner coupons				
	E GPa	$f_{y,f}$ MPa	$f_{u,f}$ MPa	$\epsilon_{u,f}$ %	$\epsilon_{f,f}$ %	E GPa	$f_{y,c}$ MPa	$f_{u,c}$ MPa	$\epsilon_{u,c}$ %	$\epsilon_{f,c}$ %
N6mm-VP	210	438	529	15.63	29.51	–	–	–	–	–
	209	440	533	14.44	30.67	–	–	–	–	–
N120×80×6	215	431	527	14.99	28.46	215	661	713	2.93	13.10
	212	433	526	14.32	28.74	213	657	710	2.98	13.66
N150×100×6	212	433	521	15.21	28.92	215	657	709	2.47	12.37
	211	431	526	14.48	27.71	211	655	707	2.19	11.08
N250×150×6	209	435	530	14.97	31.97	201	644	697	2.22	12.96
	212	429	527	15.85	30.76	198	650	705	1.90	11.48
N10mm-VP	213	383	531	16.99	31.54	–	–	–	–	–
	214	392	534	17.11	31.05	–	–	–	–	–
N250×150×10	202	381	540	18.36	34.91	200	626	689	3.47	12.73
	214	397	539	15.35	30.10	195	613	688	3.49	15.11

All the test results of the coupons extracted from virgin plates and different locations of RHS are tabulated in Tables 4.2 and Tables 4.3, where E_s is Young's modulus of steel, f_y is the yield strength and it is taken as lower yield stress or 0.2% proof stress $f_{0.2}$ for the coupons without a yield plateau, f_u denotes the ultimate tensile

strength, $\varepsilon_{u,f}$ denotes the corresponding strain at ultimate tensile strength, and ε_f denotes the corresponding strain at fracture, respectively. The following subscripts ‘f’ and ‘c’ were designated for distinguishing flat coupons and corner coupons.

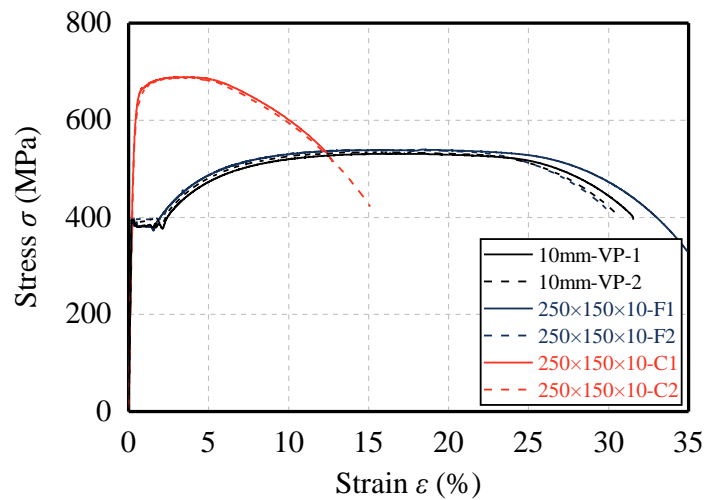
Table 4.3 Measured material properties of H series press-braked RHSs.

Section	Flat coupons					Corner coupons				
	E GPa	$f_{y,f}$ MPa	$f_{u,f}$ MPa	$\varepsilon_{u,f}$ %	$\varepsilon_{f,f}$ %	E GPa	$f_{y,c}$ MPa	$f_{u,c}$ MPa	$\varepsilon_{u,c}$ %	$\varepsilon_{f,c}$ %
H6mm-VP	201	520	597	12.73	24.24	–	–	–	–	–
	206	533	615	13.34	24.76	–	–	–	–	–
H120×80×6	212	529	604	12.74	24.18	207	767	799	1.81	4.68*
	212	523	607	13.45	18.19*	207	763	792	1.88	8.74*
H150×100×6	209	542	618	11.72	22.67	212	792	834	1.86	5.56*
	211	540	613	12.59	25.86	209	792	832	1.76	8.12*
H250×150×6	217	565	632	11.67	22.13	213	784	822	1.11	12.56
	217	554	621	12.05	25.04	216	771	822	1.60	4.71*
H10mm-VP	215	622	705	10.58	22.70	–	–	–	–	–
	218	628	704	9.47	22.59	–	–	–	–	–
H250×150×10	215	617	698	9.27	22.31	217	882	941	1.37	10.34
	215	623	697	9.59	20.62	211	878	926	1.35	10.47

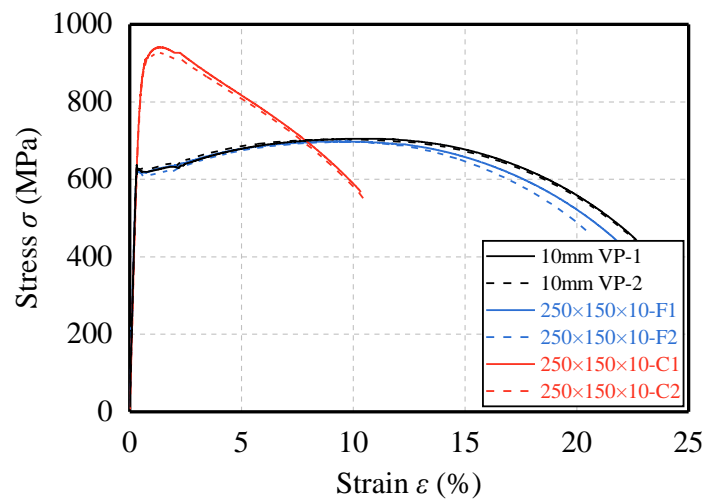
Note: * denotes for the coupon whose necking occurred out of the measuring range.

The obtained typical full range stress–strain curves of coupons are plotted in Figure 4.3. As illustrated in the figure, coupons from virgin plates and flat regions exhibit a clearly defined yield point, a yield plateau, and the following strain hardening, while the corner coupons show a more rounded and heavily strength enhanced response, which can be attributed to the cold–working effect induced by press–braking. A good agreement of stress–strain curves is observed between the virgin plates and coupons extracted from the flat region of RHSs, indicating that the manufacturing process does not affect the material properties of flat regions. However, the plastic deformation of the press–braking process results in not only the strength enhancement in corner regions but also a corresponding deterioration of the material’s ductility. Unexpected necking was occurred out of the measuring range of the extensometer on some coupons, leading

to an incorrectly recorded stress–strain relation after the tensile coupon attained their ultimate tensile strength. To distinguish those coupons, a marker “*” is plotted in the table.



(a) N250×150×10.



(b) H250×150×10.

Figure 4.3 Typical stress–strain curves obtained from coupon tests.

4.2.3 Residual stress patterns

Residual stress is an important source of material initial imperfection of structural steel members. Due to the presence of residual stresses, part of the material may yield prematurely and that may lead to instability in compression members. A destructive sectioning method was adopted to quantify the magnitude of residual stresses and to

determine the residual stress patterns of the cross-sections. 4 typical cross-sections N250×150×6, N250×150×10, H250×150×6, H250×150×6 and one repeated test H250×150×6# were selected and sectioned to investigate their residual stress distribution. As shown in Figure 4.4, the cross-sections were all in the length of 300mm and were biaxially symmetrical about the welding seam and axis of symmetry (AOS).

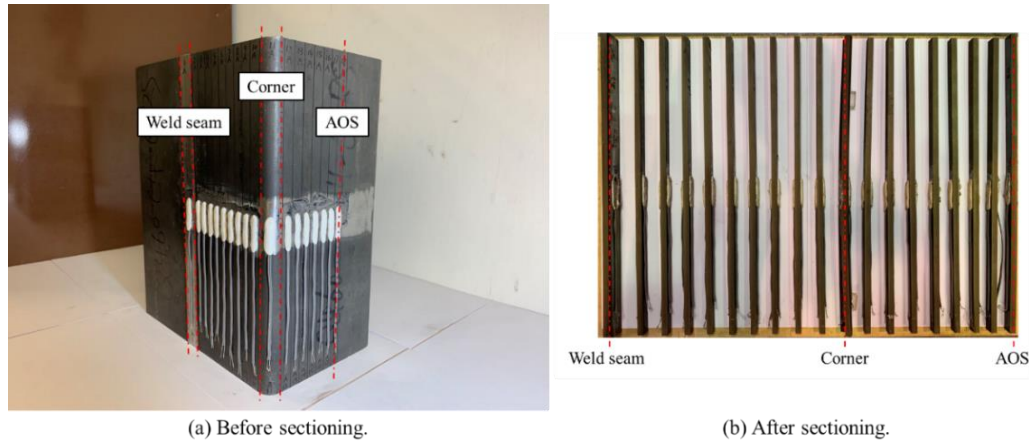


Figure 4.4 Sectioning of press-braked RHS H250×150×6.

Given the biaxially symmetrical geometry, only a quarter of the section was examined for simplicity. A pair of strain gauges were attached to the centre of the strips under the cover of waterproof glues to prevent the containment from the liquid coolant during wire cutting. The membrane residual stresses and bending residual stresses can be computed from the corresponding strain readings on the outer and inner surfaces using Eq. (4.1) and Eq. (4.2).

$$\sigma_m = -E \left(\frac{(\varepsilon_{f,out} - \varepsilon_{i,out}) + (\varepsilon_{f,in} - \varepsilon_{i,in})}{2} \right) \quad \text{Eq. (4.1)}$$

$$\sigma_b = \pm E \left(\frac{(\varepsilon_{f,out} - \varepsilon_{i,out}) - (\varepsilon_{f,in} - \varepsilon_{i,in})}{2} \right) \quad \text{Eq. (4.2)}$$

where $\varepsilon_{i,in}$ and $\varepsilon_{i,out}$ are the initial strain readings on the inner and the outer surfaces before sectioning, and $\varepsilon_{f,in}$ and $\varepsilon_{f,out}$ are the final strain readings after sectioning,

respectively.

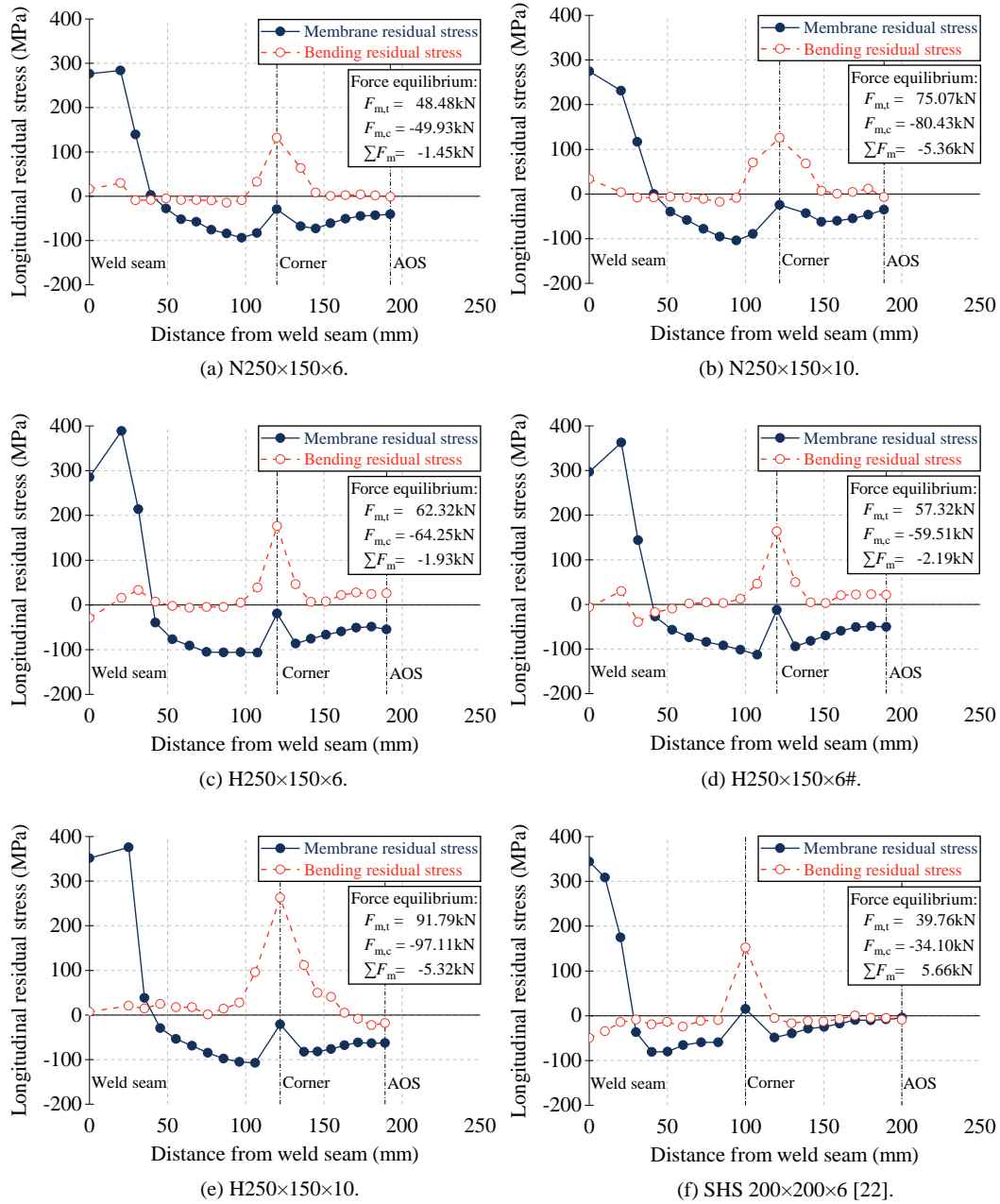


Figure 4.5 Residual stress distributions of press-braked RHSs.

The converted residual stress distributions of press-braked RHSs, together with a collected residual stress pattern of a square hollow section using the similar manufacturing process are displayed in Figure 4.5, in which the positive value of the vertical axis indicates the tensile residual stress. Relatively large tensile membrane residual stresses were discovered in the vicinity of the weld seam, mainly due to the

thermal contraction of weld metal after welding. It should be noted that the membrane residual stresses are self-equilibrating within the cross-section. Force equilibriums of membrane residual force within the section are given for each investigated RHSs in Figure 4.5, where $F_{m,t}$ and $F_{m,c}$ indicate the tensile and the compressive member residual forces, respectively.

Bending residual stresses are primarily associated with plastic deformation during the manufacturing process. Those stresses are anticipated to be locked in the RHSs until they have been sectioned. Conforming to the illustrated bending residual stress patterns, most of the steel strips after sectioning remained flat except for the strips located in the corner region, which further confirm that the bending residual stresses mainly exist among the corner regions. Based on the sectioning results and the measured residual stress distributions, a simplified predictive residual stress pattern was subsequently proposed for the press-braked RHSs, as depicted in Figure 4.6. It should be noted that the membrane residual stress is independent of the yield strength of steel, while the bending residual stress is related to the yield strength due to plastic deformation, and it fulfils self-equilibrium throughout the thickness of the section.

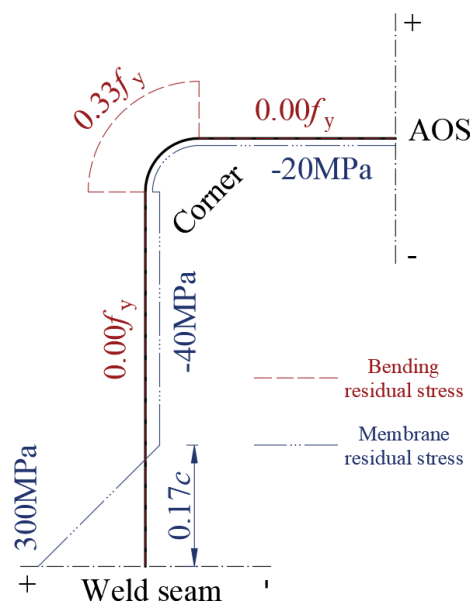


Figure 4.6 The simplified predictive residual stress pattern of press-braked RHS.

4.2.4 Local imperfection measurement

Local imperfection measurements were employed on all stub columns prior to the test. Figure 4.7 shows the instrumentation of the local imperfection measurement. The specimen was placed on a milling machine with 3 linear variable displacement transducers (LVDTs, accuracy of 0.01mm) fixed above. To eliminate the potential imperfection caused by the cold sawing at both ends of the specimen, the measurements were started and finished 50mm away from each end of the specimens. During the measurement, the readings of 3 LVDTs, δ_1 , δ_2 , and δ_3 , was recorded by a data logger, and the local imperfection amplitude δ can be subsequently obtained, while the value δ is equal to $(\delta_1 + \delta_3)/2 - \delta_2$. A typical profile of the measured local imperfection of Section H250×150×6 was shown in Figure 4.8. The maximum local imperfection amplitude, δ , measured from each section were also reported in Table 4.4. It is worth noting that all disclosed geometric defects fulfil the requirements on the tolerance of cold-formed structural hollow sections EN 10219-2 (CEN, 2006b).



Figure 4.7 Instrumentation of the local imperfection measurement.

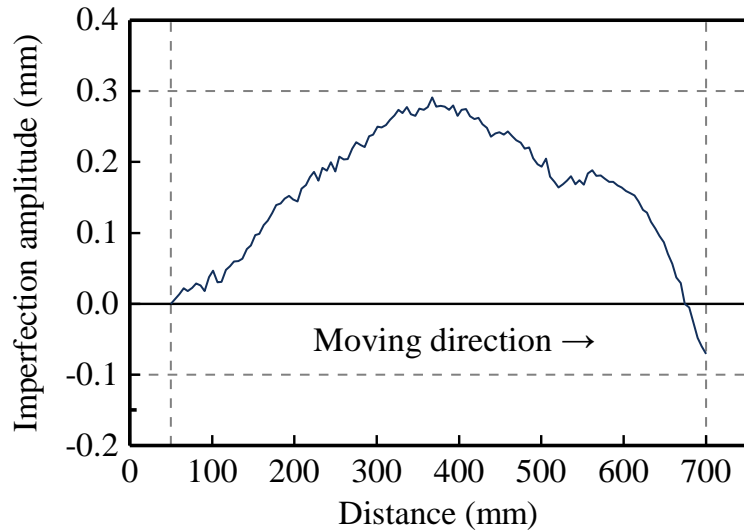


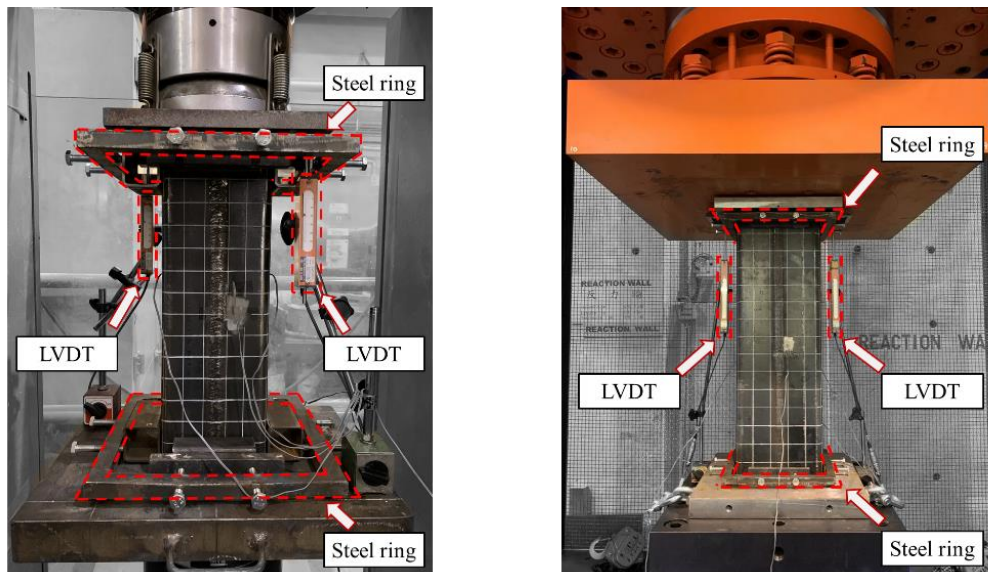
Figure 4.8 The local imperfection profile of specimen H250×150×6.

4.2.5 Stub column tests

4.2.5.1 Instrumentation

To investigate the stub column behaviour of press-braked RHSs, fix-ended pure compression tests were performed on 10 stub columns. The stub columns were tested using a 4,600kN MTS compression machine and a 25,000kN POPWILL servo hydraulic testing system, on the basis of the predicted load-bearing capacity of each specimen. Figure 4.9 presents the experimental setups for stub column tests for different compression machines. To avoid premature end failure and ensure uniform compression, each end of the stub column was preliminarily milled to be flat before the test and they were restrained by steel rings during the test, and the columns were subsequently positioned between 2 parallel hardened steel plates. A total of 4 strain gauges were mounted at each face of the column at mid-height to record the initial strain history and act as a monitor to adjust the specimen's location during the pre-loading phase. Meanwhile, 2 LVDTs were placed in the diagonal position to measure the axial shortening, Δ . The initial strain readings and obtained axial shortening readings for each specimen were almost the same as their counterparts in the early stage

of the compression test, indicating that the stub columns were compressed uniformly during the experiment. The initial strain history was used to modify the early stage of axial load–end shortening curve up to 40% of the measured peak load, eliminating potential effects of any gaps that existed between the specimen and test rig or among the testing machine itself.



(a) 4600kN MTS hydraulic compression machine. (b) 25000kN Popwill universal compression machine.

Figure 4.9 Press-braked RHS stub column test setups.

The specimens were tested under displacement control with a loading rate of $0.05\% \times L/\text{min}$, which was the same as the loading rate employed for the tensile coupon tests. To consistently compare the stub column behaviour with the obtained static material properties, 100s stress relaxation was also conducted when specimens attained their peak loads, to obtain the static ultimate loading–bearing capacities.

4.2.5.2 Test results

All tested stub columns exhibited expected local buckling failure modes, as shown in Figure 4.10. Once the onset of the local buckling occurred, the bearing–load of columns reached their maximum values and tended to decrease with the development

of the local buckling. The key parameters and results of the stub column tests are summarised in Table 4.4, where b , h , t , r_o are defined in Figure 4.1, δ represents the measured maximum local imperfection amplitude, L denotes the specimen length, f_y is the measured yield strength, and N_{Test} denotes the ultimate load-bearing capacity.

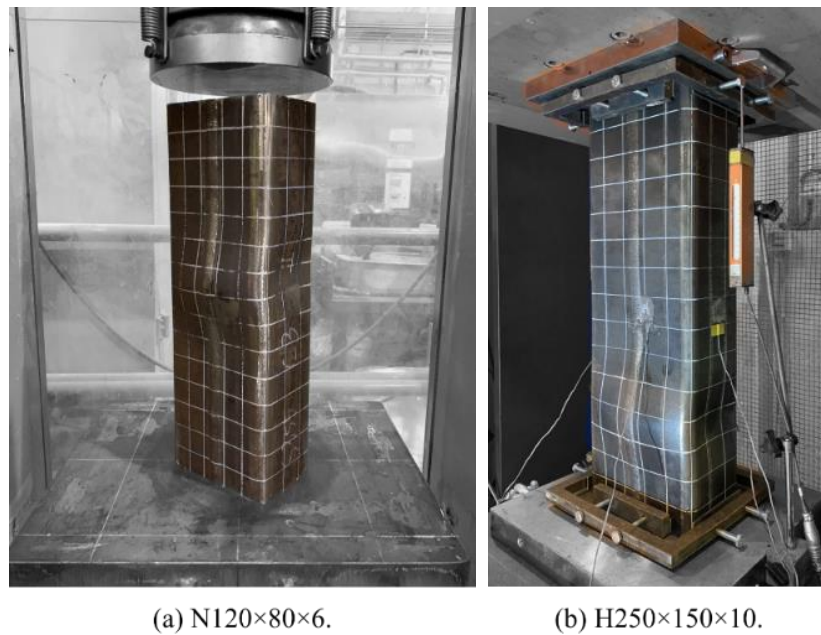


Figure 4.10 Typical failure modes of press-braked RHS stub columns.

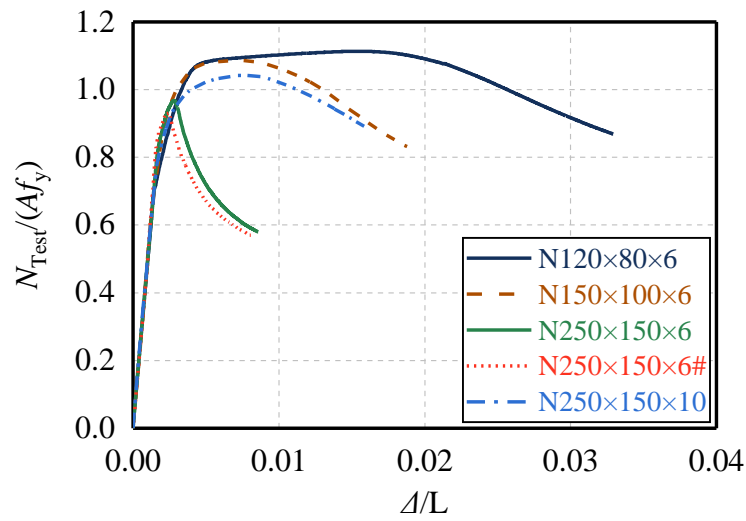
Table 4.4 Key parameters and results of press-braked RHS stub column tests.

Specimen	b	h	t	r_o	δ	L	Af_y	N_{Test}	N_{Test}/Af_y
–	mm	mm	mm	mm	mm	mm	kN	kN	–
N120×80×6	80.34	119.83	6.18	14.0	0.13	360	1036	1153	1.11
N150×100×6	99.30	149.28	6.12	13.5	0.39	445	1276	1386	1.09
N250×150×6	149.55	249.28	6.05	13.5	0.65	748	2050	1983	0.97
N250×150×6#	149.80	249.75	6.09	13.5	1.14	750	2066	1921	0.93
N250×150×10	149.06	249.55	9.79	21.5	0.21	749	2946	3071	1.04
H120×80×6	79.91	119.02	5.85	11.0	0.24	360	1110	1300	1.17
H150×100×6	99.70	149.29	5.90	11.0	0.26	445	1470	1605	1.09
H250×150×6	148.62	249.98	5.81	11.0	0.29	748	2467	2244	0.91
H250×150×6#	149.54	249.60	5.80	10.5	0.56	749	2471	2042	0.83
H250×150×10	148.62	249.80	9.89	19.0	1.10	750	4494	4694	1.04

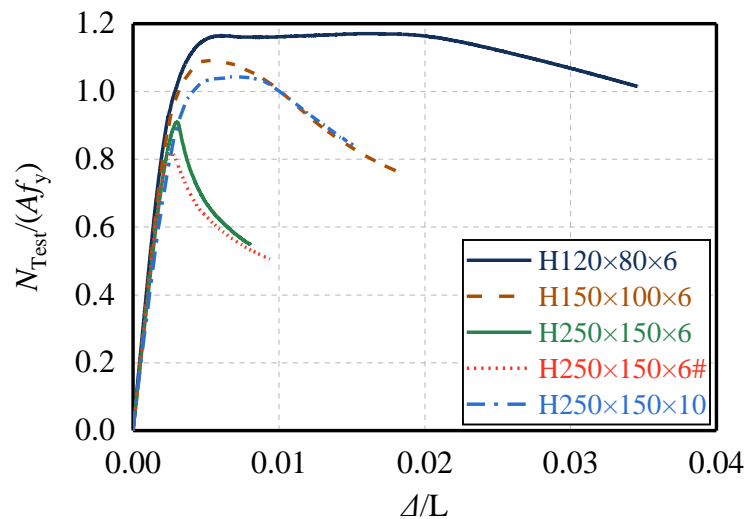
Note: # denotes for the repeated test.

The obtained axial loads, N_{Test} are further normalised by the squash loads, Af_y , and they are plotted against the normalised axial shortenings (measured end shortenings

divided by the column length, Δ/L) in Fig 4.11.



(a) N series.



(b) H series.

Figure 4.11 Normalised axial strength versus axial strain curves of press-braked RHS stub columns.

Clear post-peak trends are observed between different specimens, as the load-bearing capacity of the stockiest cross-section can be maintained for a long plateau, whereas the slenderer cross-section exhibits a rapid deterioration of load-bearing capacity after reaching the peak load. It should be noted that for Sections N250x150x6 and H250x150x6, the repeated test showed a relatively lower load-bearing capacity,

and its location of local buckling was more approached to the end of the specimen. It was anticipated that the larger local imperfection (presented in Table 4.4, $\delta = 0.29$ for Section H250×150×6 and $\delta = 0.56$ for Section H250×150×6#) may prematurely trigger local plate buckling in such a slender cross-section, directly leading to a reduction in the load-bearing capacity.

4.2.6 Finite element modelling and parametric study

4.2.6.1 Developed finite element model

In addition to the experimental investigation, finite element modelling on the press-braked RHSs is conducted using commercial software package Abaqus (ABAQUS). The FE modelling aims for replicating the test results on press-braked RHSs and conducting parametric studies to obtain an extended database over a wide range of parameters.

As demonstrated in many studies (Liu *et al.*, 2021; Ma *et al.*, 2016b; Yun *et al.*, 2020), the structural behaviour of hollow structural steel sections under compression, bending and combined compression and bending can be captured very well by the shell element S4R. On this basis, all FE models on press-braked RHS are established using this 4-node shell element with reduced integration based on the measured material properties, residual stress distributions and geometric dimensions. As shown in Figure 4.12, a prior mesh convergence study on specimen N150×100×6 was performed to ensure the accuracy of prediction without losing computational efficiency. When a uniform mesh size of the tube thickness t is employed along the flat region, and three elements were employed for the corner region, the numerical results were found to agree with the test results satisfactorily and can maximise the efficiency simultaneously. The measured material properties of flat and corner coupons from corresponding cross-

sections were converted into true stress versus log plastic strain curves before assigning material responses to the flat and corner parts of the column. As part of the flat region near the corner region may be also strengthened due to the cold working effects, the corner material properties were assigned beyond the corner region to the flat region in the prior study to distinguish what level of the strength enhancement in the flat region is.

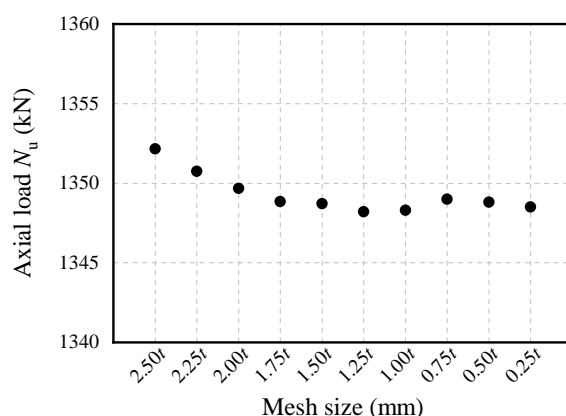


Figure 4.12 Mesh convergence study of specimen N150×100×6.

For press-braked RHSs, their bending residual stresses were directly introduced during the forming process of corners and mainly existed in the corner regions, as illustrated in Figure 4.5. However, the effect of bending residual stress is considered to be inherently included in the results of corner coupon tests since the corner coupon was firstly straightened from the state of bend, recovering the bending residual stresses which were released during sectioning. And the membrane residual stresses caused by the thermal contraction arising from the uneven cooling speeds between the molten weld metal and the adjacent parent metal, were explicitly incorporated into the FE models through the ABAQUS ‘Initial condition’ command to study the effects of membrane residual stress distribution onto the structural behaviour of press-braked RHSs under axial compression. Figure 4.13 presents the magnitudes and distributions of the input membrane residual stresses for stub column of Section H250×150×6. For other columns whose residual stress pattern has not been measured, their membrane

residual stress distribution was modelled using the predictive model as shown in Figure 4.6. To reflect the real boundary conditions during the test, both ends of the column was fully restrained against all degrees of freedom except for the loaded end which allows axial translations. The influence of local geometric imperfections on stub columns were also considered through superposing the lowest elastic buckling mode which was generated from the linear elastic buckling analysis.

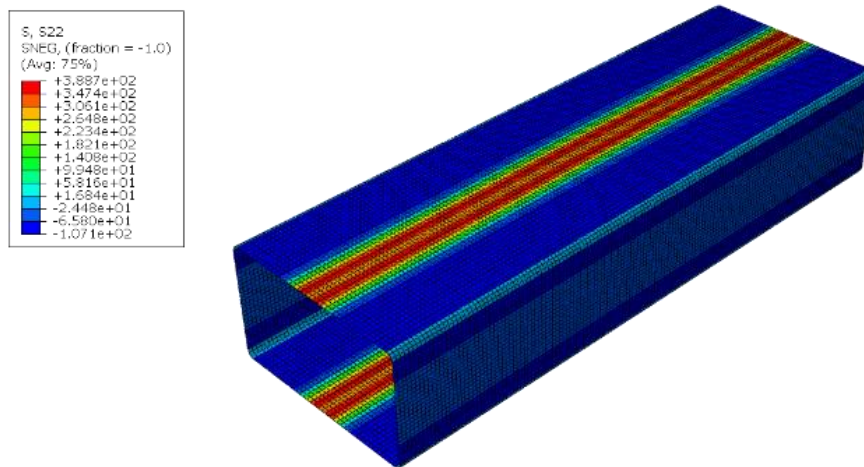


Figure 4.13 Input membrane residual stress distribution for H250×150×6 FE model.

4.2.6.2 Validation

To evaluate the accuracy of the developed press-braked RHSs FE models, the obtained maximum axial loads and axial load versus end shortening responses from numerical models under various combinations of corner strength enhancement, the existence of residual stresses and amplitudes of local geometric imperfections, were compared with those measured results. As presented in Table 4.5, the numerical models incorporating corner strength enhancement of 1 time the tube thickness, residual stress distribution and measured local geometric imperfections can well capture the ultimate bearing load during the test.

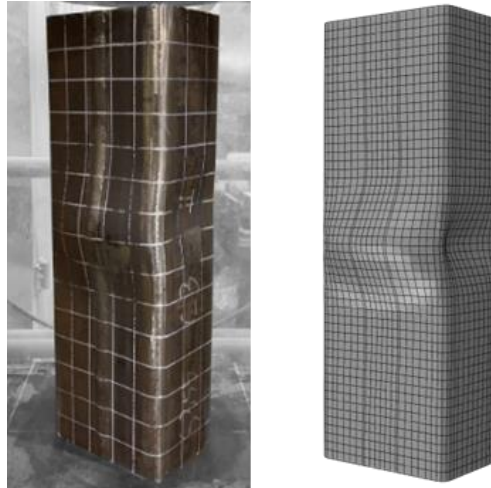
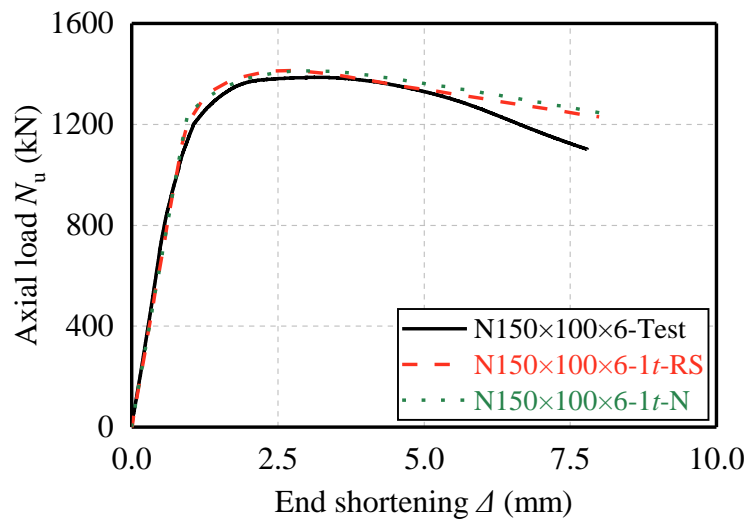


Figure 4.14 Comparisons of local buckling failure modes obtained from the experiment and numerical model.

The local buckling failure modes of specimen N120×80×6 obtained from the experiment and numerical model are compared in Figure 4.14. The obtained axial load versus end shortening responses of columns N150×100×6 and H150×100×6 from both experimental and numerical studies are depicted in Figure 4.15 for comparison. It can be found that the simulated $N_u - \Delta$ responses yielded satisfactory agreement with those obtained from the experiments.



(a) N150×100×6.

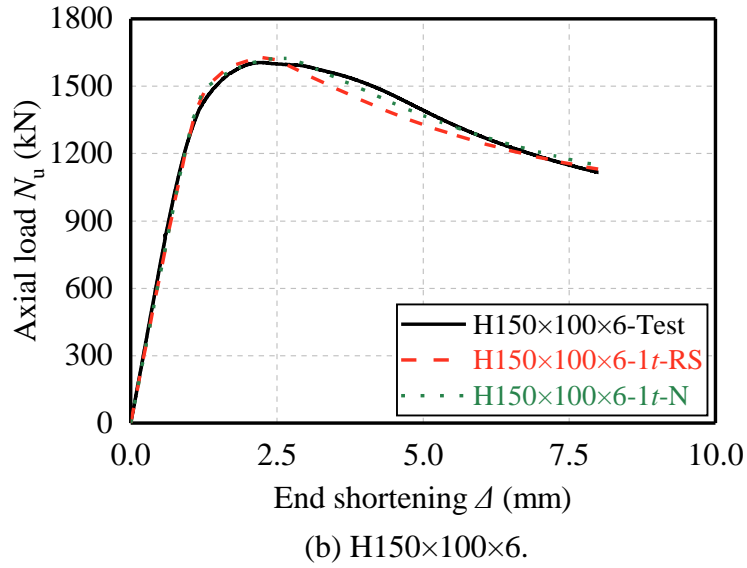


Figure 4.15 Comparisons of axial load versus end shortening curves between experimental and numerical results.

Table 4.5 Comparisons of test results to different FE models.

Specimen	N_{FE}/N_{Test}						
	Incorporate residual stress			Without residual stress			
	0t-RS	1t-RS	2t-RS	1t-N- Measured	1t-N- 0.05t	1t-N- 0.10t	1t-N- 0.15t
N120×80×6	0.99	1.06	1.13	1.06	1.04	1.01	1.00
N150×100×6	0.97	1.02	1.07	1.02	1.02	1.00	0.98
N250×150×6	0.94	0.96	0.98	0.97	1.00	0.97	0.96
N250×150×6#	0.93	0.95	0.97	0.97	1.04	1.00	0.99
N250×150×10	1.02	1.09	1.17	1.09	1.07	1.04	1.02
H120×80×6	0.92	0.98	1.04	0.98	0.98	0.96	0.95
H150×100×6	0.97	1.01	1.06	1.01	1.01	0.98	0.97
H250×150×6	0.96	0.97	0.98	0.98	0.98	0.96	0.94
H250×150×6#	0.97	0.99	1.00	1.01	1.08	1.06	1.04
H250×150×10	0.98	1.03	1.08	1.03	1.06	1.03	1.01
Mean:	0.96	1.01	1.05	1.01	1.03	1.00	0.98
COV:	0.030	0.045	0.064	0.039	0.034	0.033	0.032

Based on this finding, the effect of membrane residual stresses and the amplitude of local geometric imperfections were further investigated using the developed FE models. The ratios of the numerical results to the experimental results tabulated in Table 4.5 demonstrate that the existence of membrane residual stresses has a negligible impact

on the load-bearing capacity of press-braked RHSs. Though the FE models which only consider the measured imperfection amplitude attain a good agreement with tests, a more accurate prediction of the ultimate loads was achieved by using $0.1t$ as the amplitude of the local geometric imperfections.

4.2.6.3 Parametric study

Upon the verification of the developed FE models, additional parametric studies were performed to supplement the test database over a wider range of cross-sectional sizes. The FE modelling technique adopted in parametric studies were in accordance with those described in previous chapter, except for some necessary modifications emphasised herein: (1) the membrane residual stresses were no longer introduced into the modelled columns due to its negligible effect, and (2) the adopted initial local imperfection amplitudes were taken as $0.1t$ for each cross-section. Table 4.6 summarises the information about geometrical cross-sectional sizes and material properties of all modelled press-braked RHSs, while the column lengths were assigned to be $3h$ for stub columns. Table 4.7 reports the material properties inputted in FE models. In summary, there are 8 types of cross-sections combined with various tube thickness and material properties, resulting in a total of 290 generated numerical results.

Table 4.6 Adopted parameters in parametric studies.

Cross-section type	Dimension	Thickness	R_o	Yield strength	Nos
–	mm	mm	mm	MPa	–
RHS	80–120, 100–150, 120–200, 150–250	4–10	$2t$	433–565	146
SHS	100–100, 140–140, 180–180, 220–220	4–10	$2t$	433–565	144

Table 4.7 Inputted material properties in parametric studies.

Steel grade	Flat materials				Corner materials			
	E_f	$f_{y,f}$	$f_{u,f}$	$\epsilon_{u,f}$	E_c	$f_{y,c}$	$f_{u,c}$	$\epsilon_{u,c}$
-	GPa	MPa	MPa	%	GPa	MPa	%	%
Q355	212	433	521	15.21	215	657	709	2.47
Q460	217	565	632	11.67	216	771	822	1.6

4.2.7 Assessment and modification of current design methods

4.2.7.1 General

Whether a rectangular hollow section can develop its plastic cross-sectional resistance is limited by the onset of local buckling. If the applied load on a cross-section achieves the squash load Af_y before the occurrence of local buckling, this cross-section is deemed as a Class 1–3 (non-slender) section in the design concept of current codes of practice, otherwise, it is classified as a Class 4 (slender) section. Eurocode 3 (CEN, 2005), ANSI/AISC 360–16 (AISC/AISC, 2022) and direct strength method (AISI, 2016) propose their slenderness limit based on their design concept to account for the local buckling effects of plated structures. However, all these design methods were proposed based on the test data on hot-finished, cold-rolled and cold-formed steel structural sections. Hence, it is necessary to re-examine their applicability on press-braked RHSs.

4.2.7.2 Eurocode 3 and ANSI/AISC 360–16

The current codes of practice Eurocode 3 and ANSI/AISC 360–16 both raise cross-section classification limits and the effective width method for the design of rectangular hollow sections. Classification of a RHS in these codes is dependent on the class of its most slender internal plate element, and this concept treats the entire sections like a collection of separate and independent plated structures. Apparently, this classification method ignores the interaction between plate elements within the cross-section, while

an adjacent relative compact plate element was considered to provide a stronger restraint to slenderer plate elements in its vicinity (Gonçalves and Camotim, 2013). Hence, as shown in Figure 4.16., rectangular hollow sections clearly show a differentiated reduced tendency as compared to square hollow sections, in which the ultimate loads, N_u from both the experimental and the numerical results are normalised by the squash loads, Af_y on the vertical axis and width-to-thickness ratios, c/t are normalised by the parameter $(f_y/E_s)^{0.5}$ on the horizontal axis. Fitting a linear regression line through the collected SHS data, a fitted classification limit of 1.19 for press-braked RHSs can be figured out between the normalised slenderness limits of Eurocode 3 and ANSI/AISC 360–16.

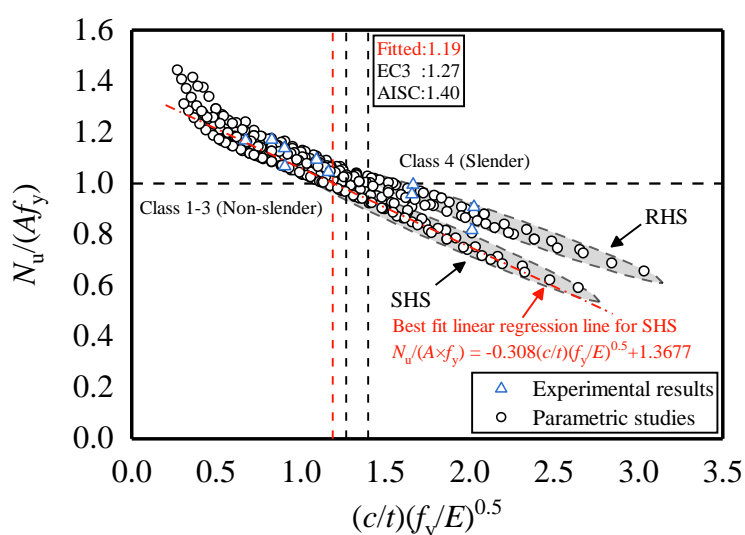


Figure 4.16 Evaluation of the cross-section classification for press-braked RHSs.

To compute the reduction in compressive resistance for Class 4 (slender) cross-sections, the effective width method is given that considers the ineffective area of plated structures which suffer from local buckling and do not bear loadings anymore (EN 1993–1–5 (CEN, 2009)). After excluding the ineffective area of a Class 4 section, the remaining area is regarded as effective enough to develop their plastic resistance, while the effective area A_{eff} can be computed by $A_{\text{eff}} = \rho \times A$, in which ρ is the reduction factor and can be calculated according to Eq. (4.3) from Eurocode 3 and ANSI/AISC 360–

16, respectively.

$$\rho_{\text{EWM}} = \begin{cases} 1 & \text{for } \bar{\lambda}_p \leq \bar{\lambda}_1 \\ (1 - K / \bar{\lambda}_p) / \bar{\lambda}_p & \text{for } \bar{\lambda}_p > \bar{\lambda}_1 \end{cases} \quad \text{Eq. (4.3)}$$

in which K is 0.22 and 0.2, and $\bar{\lambda}_1$ is taken to be 0.673 and 0.724 for Eurocode 3 and ANSI/AISC 360–16, respectively.

To precisely evaluate the design methods and to eliminate the effects of inter-element interaction within rectangular hollow sections, only the results of square hollow sections were extracted (Tayyebi and Sun, 2021) and depicted against the plate slenderness with design curves from Eurocode 3 and ANSI/AISC 360–16 in Figure 4.17.

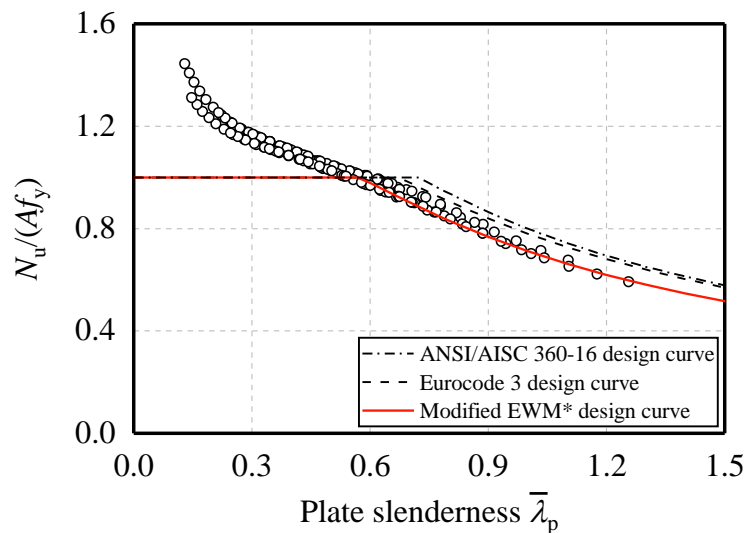


Figure 4.17 Comparison of test and FE results with effective width method–based design approaches.

Current design methods in EC3 and AISC were found to provide unconservative predictions for press-braked RHSs in section classifications as well as compressive resistances. Therefore, the effective width methods from these two codes were modified based on a newly proposed slenderness limit, $c/t = 1.19(f_y/E_s)^{0.5}$, and it is converted to an equivalent plate slenderness $\bar{\lambda}_p = 0.568$, as shown in the following equations.

$$\rho_{EWM*} = \begin{cases} 1 & \text{for } \bar{\lambda}_p \leq 0.568 \\ \left(0.899 - 0.187 / \bar{\lambda}_p\right) / \bar{\lambda}_p & \text{for } \bar{\lambda}_p > 0.568 \end{cases} \quad \text{Eq. (4.4)}$$

It should be noted that only the cross-sections that were classified as Class 4 (slender) were considered for the evaluation of Eurocode 3, ANSI/AISC 360–16 and the modified effective width method. As presented in Table 4.8, the N_u/N_{pred} ratios of these design methods were 0.97, 0.95 and 1.02, respectively, indicating that the modified effective width method is able to provide a more safe and accurate prediction for the compressive resistances of press-braked RHS stub columns.

Table 4.8 Comparisons between test and FEM results and design methods.

Specimens	Nos	N_u/N_{EC3}	N_u/N_{AISC}	N_u/N_{EWM*}	N_u/N_{DSM}	N_u/N_{DSM*}
Slender sections only	4 Tests + 107 FEM	0.97	0.95	1.02	–	–
Non-slender + slender	10 Tests + 290 FEM	–	–	–	1.06	1.02
	COV:	0.048	0.053	0.035	0.100	0.041

4.2.7.3 Direct strength method (DSM)

The direct strength method was originally proposed for the design of thin-walled cold-formed sections such as angles, channels, and Σ sections, and it is currently adopted in AISI S100–16. Compared with the effective width method which computes the section resistance based on the c/t ratio of individual plate elements, DSM regards the whole cross-section as an entirety to consider the inter-element interaction between each plate. Hence, this characteristic makes DSM a more straightforward design method, since it does not involve the complex calculation process of effective areas, effective moduli and shifted centroids. The design formulae of DSM are presented in Eq. (4.5), in which $\bar{\lambda}_o$ is the overall section slenderness and can be determined from Eq. (4.6).

$$N_{\text{DSM}} = \begin{cases} Af_y & \text{for } \bar{\lambda}_o \leq 0.776 \\ \left[1 - 0.15 \left(\frac{1}{\bar{\lambda}_o} \right)^{0.8} \right] \left(\frac{1}{\bar{\lambda}_o} \right)^{0.8} \times Af_y & \text{for } \bar{\lambda}_o > 0.776 \end{cases} \quad \text{Eq. (4.5)}$$

$$\bar{\lambda}_o = \sqrt{\frac{f_y}{f_{\text{cr}}}} \quad \text{Eq. (4.6)}$$

According to DSM, the elastic buckling stress f_{cr} of the cross-section is obtained by an elastic buckling analysis using the finite-element analysis software ABAQUS. Therefore, the DSM design curve was consequently obtained and depicted in Figure 4.18. DSM also provides rather unconservative predictions for press-braked RHSs not only in the limit between non-slender and slender sections, but also compressive resistances. To further improve the prediction performance of DSM, the original DSM design formulae are modified as Eq. (4.7) and plotted in Figure 4.18, in which the original slenderness limit is taken as 0.68 based on the regression analysis and the design formula in the range of non-slender sections is proposed to provide a better prediction on section resistances.

$$N_{\text{DSM}^*} = \begin{cases} 1.2 \times Af_y & \text{for } \bar{\lambda}_o \leq 0.367 \\ \left\{ 2 - \left[1 - 0.204 \left(\frac{1}{\bar{\lambda}_{o,1}} \right)^{0.88} \right] \left(\frac{1}{\bar{\lambda}_{o,1}} \right)^{0.88} \right\} \times Af_y & \text{for } \bar{\lambda}_o \leq 0.677, \bar{\lambda}_{o,1} = 1.354 - \bar{\lambda}_o \\ \left[1 - 0.204 \left(\frac{1}{\bar{\lambda}_o} \right)^{0.88} \right] \left(\frac{1}{\bar{\lambda}_o} \right)^{0.88} \times Af_y & \text{for } \bar{\lambda}_o > 0.677 \end{cases} \quad \text{Eq. (4.7)}$$

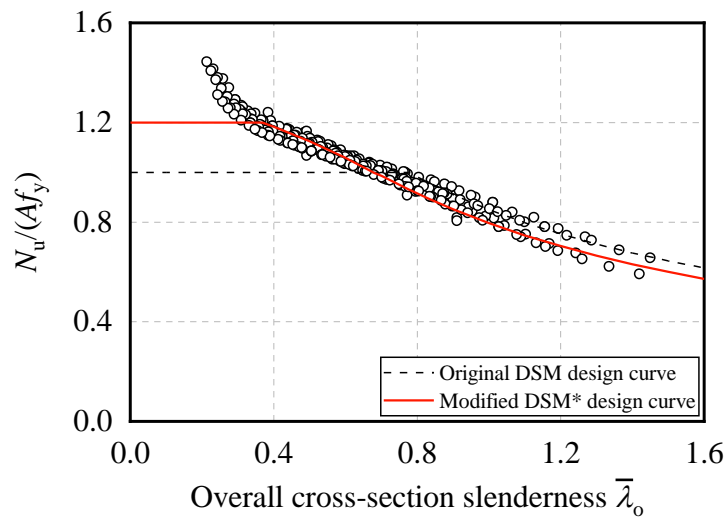


Figure 4.18 Comparison of test and FE results with original and modified direct strength methods.

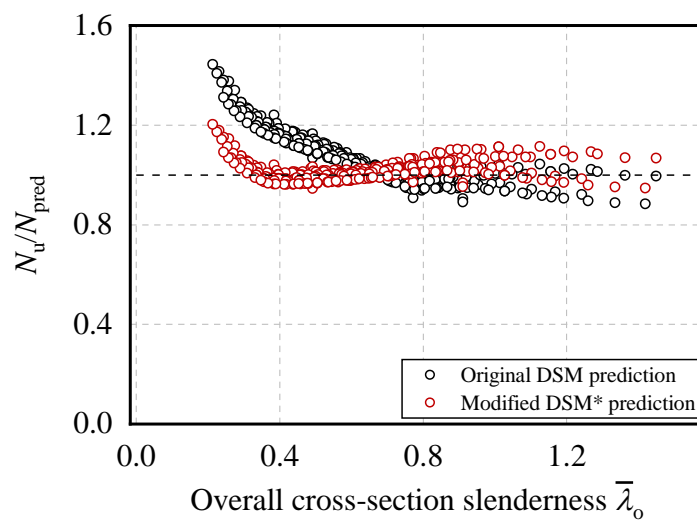


Figure 4.19 Comparison of test and FE results normalised by original and modified direct strength methods.

The compressive resistance of press-braked RHSs computed using the original and modified DSM design method were normalised to the experimental and numerical results and depicted in Figure 4.19. As clearly illustrated in the figure, the proposed modified DSM (DSM*) design method is found to improve the prediction capability of compressive resistances of non-slender sections and provide a more accurate prediction for slender cross-sections. In parallel with the graphical evaluation, quantitative

assessment results are presented in Table 4.7. The corresponding N_u/N_{pred} ratios of the original and the modified DSM design method are found to be 1.06 and 1.02, with the coefficient of variation being greatly improved from 0.100 to 0.041, indicating that the modified direct strength method offers a more consistent and accurate compressive resistance prediction for press-braked RHS stub columns.

4.3 Press-braked RHS long columns

4.3.1 General

The long column specimens were fabricated using the same Q460 steel and manufacturing method described in the stub column session. Both ends of long column were milled flat and welded to endplates. The corresponding material properties and local imperfections of the press-braked RHS long columns have been measured on the stub column specimens and reported in Chapter 4.2. Prior to the long column test, the global imperfection of the specimens was carefully measured. The global imperfection amplitude was defined as the measured maximum deviations from the reference line, while the deviations at 4 interval points of the column were measured by a digital calliper, following the similar procedure described in Wang *et al.* (2014).

4.3.2 Long column tests

4.3.2.1 Instrumentation

A total of 7 long column specimens were tested to study their flexural buckling behaviours under concentric compression. The long column test setup is depicted in Figure 4.20.

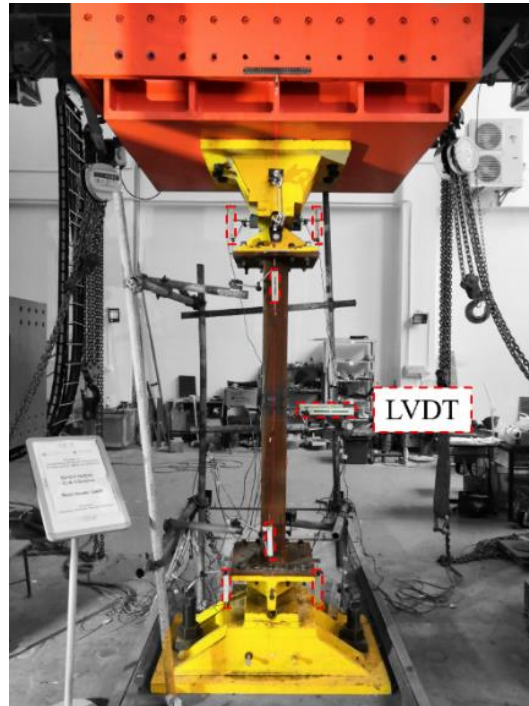


Figure 4.20 Instrumentation of long column test.

All long column tests were performed on the 10,000kN Popwill universal compression machine, while a pair of knife edges were mounted to both ends of the specimen to achieve a pin-ended support boundary condition. The effective length L_e for each specimen is equal to the specimen length plus the additional length of 210mm for each knife edge. To eliminate any gaps caused by the out-of-flatness of specimen's endplates, thin steel sheets were inserted in the proper position between the endplate and the plate of the knife edge. 4 strain gauges were attached at the mid-height of the 4 faces of the columns to measure the strain development at these locations. 6 LVDTs were vertically installed at the bottom and top endplates to capture axial shortenings and end rotations, while 2 LVDTs were horizontally pointed to the mid-height of the column to measure the lateral deflections.

During the long column test, the loading displacement was applied on the specimen with a loading rate of 0.2 mm/min. Also, a stress relaxation for 100 seconds was performed after the specimen obtained their maximum load-bearing capacities, same

as the procedure done in stub column tests to obtain the static ultimate flexural buckling resistance. It is worth noting that all long columns were anticipated and designed to fail regarding their minor principal axis, hence the non-dimensional slenderness of each column can be computed from Eq. (4.8), where I_{minor} is the moment of inertia of the minor principal axis.

$$\bar{\lambda} = \sqrt{\frac{Af_y L_e^2}{\pi^2 EI_{\text{minor}}}} \quad \text{Eq. (4.8)}$$

4.3.2.2 Test results

Table 4.9 summarises the geometric dimensions, effective length and maximum global imperfection amplitude for each specimen. The corresponding failure modes for each specimen were shown in Figure 4.21, in the order of the increasing specimen's effective lengths. All tested specimens buckled at their minor principal axis, with global buckling and global–local interactive buckling failure modes being observed.

Table 4.9 Key parameters and results of press-braked RHS long column test.

Specimens	b	h	t	r_o	ω_g	L_e	$\bar{\lambda}$	N_{Test}
–	mm	mm	mm	mm	mm	mm	–	kN
L250×150×10–a	148.66	248.54	9.89	19	0.05	1120	0.33	4546
L250×150×10–b	148.62	247.88	9.89	19	0.1	1520	0.45	4708
L250×150×10–c	148.48	248.19	9.89	19	0.07	1820	0.53	4315
L250×150×10–d	148.42	246.76	9.89	19	0.05	2220	0.65	3905
L250×150×10–e	145.97	247.7	9.89	19	0.04	2520	0.74	4048
L250×150×10–f	147.94	247.88	9.89	19	–0.02	2820	0.83	3716
L250×150×10–f #	147.87	247.92	9.89	19	0.12	2820	0.83	3356

Notes: # denotes the repeated specimen.

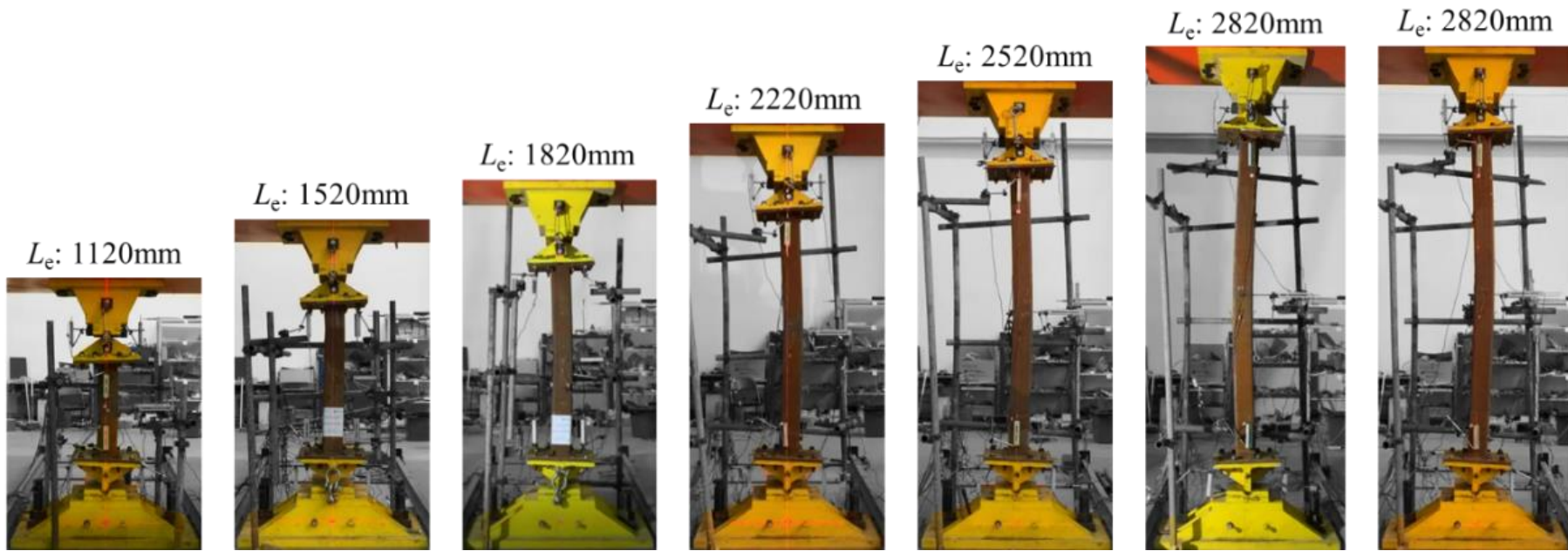


Figure 4.21 Failure modes of long column specimens.

The axial load–mid deflection responses of press–braked RHSs columns are displayed in Figure 4.22.

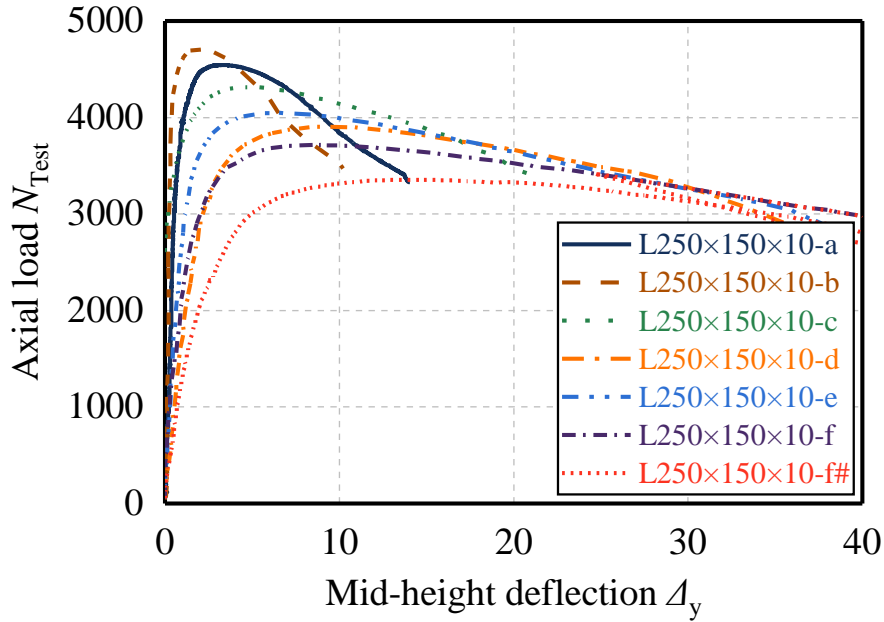


Figure 4.22 Axial load versus mid–height deflection curves of long column tests.

For the relatively stockier specimens L250×150×10–a and L250×150×10–b, it is found that local buckling gradually formed after specimens attained their ultimate flexural buckling resistances, and the development of mid–height lateral deflections was still in a slow–growth manner after the ultimate load. The ultimate flexural buckling resistances of these two specimens were closed to those of the stub column counterpart, even though the local buckling failure mode was somewhat not the same due to the different boundary conditions. It can be reasonably considered that the length effect has little impact on the flexural buckling resistances of press–braked RHS columns in such a range of member slenderness. With regard to the rest of the specimens, the failure mode was dominated by overall flexural buckling about their minor principal axis, except for the repeated specimen L250×150×10–f# which was found that showed an interaction of overall flexural buckling and local buckling failure mode. The unexpectedly mixed failure mode may be triggered by different local

geometric imperfections on different columns and may explain the reason why the repeated test obtained a lower ultimate flexural buckling resistance as compared to its counterpart. Note also that the lateral deflections were rapidly developed after specimens attained their ultimate load, unlike the slow-growth behaviours exhibited on specimens LC250×150×10-a and LC250×150×10-b. For instance, the lateral deflection of the specimen L250×150×10-e dramatically increased from 8mm to 30mm in 3 seconds, indicating that this specimen was in a severely unstable condition under compressive loading.

4.3.3 Finite element modelling and parametric study

4.3.3.1 Validation

The basic finite element modelling technique for press-braked RHS long column was similar with that adopted for stub columns. The corner strength enhancement in press-braked RHS long column was also considered in the finite element models through assigning the corner material properties into the extended corner regions with the length of t . Membrane residual stresses were not introduced into the FEM because of the negligible impact on the load-bearing capacity of press-braked RHSs. The bending residual stress were considered to be released when the coupons were extracted from the cold-formed corner, and reintroduced into the coupon when conducting tensile tests. Therefore, the effect of bending residual stress can be regarded as being implicitly incorporated into the measured stress-strain response of corner materials. Therefore, the introduction of residual stresses in the FEM is unnecessary.

For long column specimens, to mimic the pin-ended boundary conditions adopted in experiments, two reference points were coupled with both ends of the column through kinematic coupling. The rotation of the bending axis was set free at the coupled

reference points, while the axial displacement was restrained except for the loading point. It should be noted that the reference points were longitudinally offset by 210 mm from each end of column. Axial displacement was applied to the top reference point in a General, static analysis step. The geometrically and materially nonlinear imperfect analysis was enabled during the analysis.

The structural behaviour of hollow section column was susceptible to the local and global imperfections. To consider the effects of initial geometric imperfection, both local and global imperfection profiles obtained from the eigenvalue buckling analysis were applied in the FEM. The scaled factors of these imperfection profiles using in the FEM validation process were taken as the measured values reported in Table 4.4 and 4.9, respectively. To further study the effects of global imperfection, different values of global imperfection of $L/500$, $L/1000$, and $L/1500$ were also adopted in the FEM.

Table 4.10 Comparisons between different adopted values of global imperfection.

Specimens	N_{Test} kN	Measured	N_{FEM}/N_{Test}		
			$L/500$	$L/1000$	$L/1500$
L250×150×10–a	4546	1.08	0.97	1.02	1.05
L250×150×10–b	4708	1.05	0.94	0.99	1.02
L250×150×10–c	4315	1.04	0.93	0.98	1.01
L250×150×10–d	3905	1.09	0.98	1.03	1.06
L250×150×10–e	4048	1.03	0.92	0.97	1.00
L250×150×10–f	3716	1.08	0.97	1.02	1.05
L250×150×10–f#	3356	1.20	1.09	1.14	1.17
	Mean:	1.08	0.97	1.02	1.05

The obtained numerical results of these FEMs using measured values, $L/500$, $L/1000$, and $L/1500$ as the magnitudes of the global imperfection were reported in Table 4.10. The mean N_{FEM}/N_{Test} value of $L/1000$ were found to be the closest to the unity, indicating that the FEM adopting $L/1000$ as the magnitude of the global imperfection can satisfactorily replicate the structural behaviour of pin-ended press-braked RHS

columns.

Typical comparisons of the axial load–lateral displacement curves and axial load–end rotation curves for specimen L250×150×10–f–R are presented in Figure 4.23 and Figure 4.24.

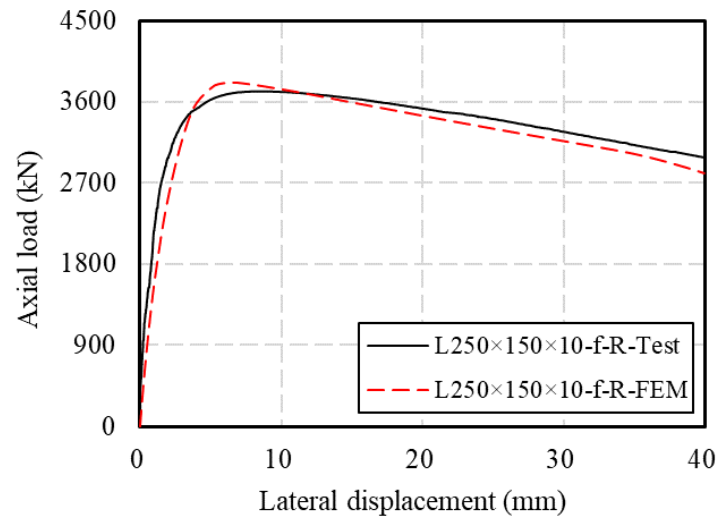


Figure 4.23 Comparisons of the axial load–lateral displacement curves for specimen L250×150×10–f–R.

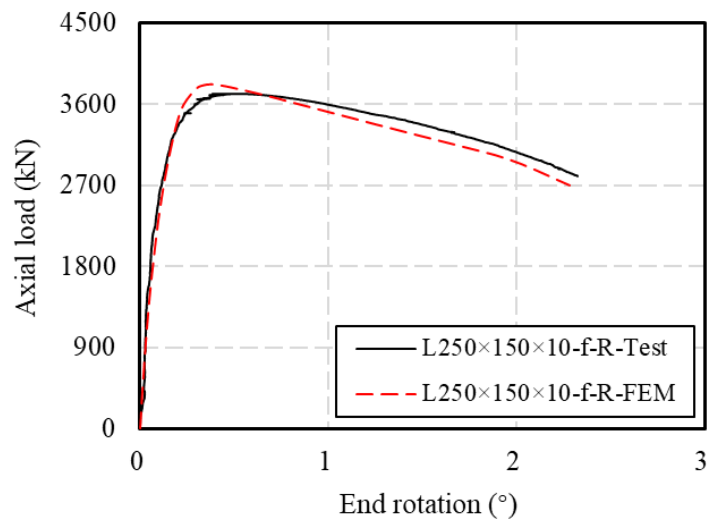


Figure 4.24 Comparisons of the axial load–end rotation curves for specimen L250×150×10–f–R.

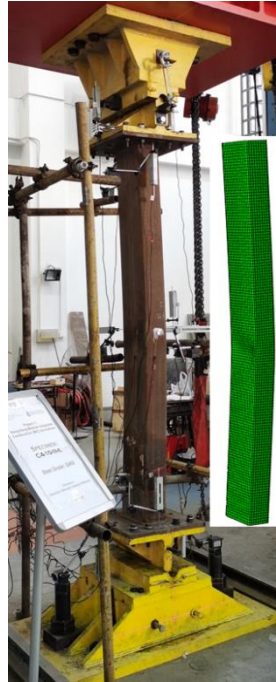


Figure 4.25 Comparisons of the failure modes for specimen L250×150×10–d.

The comparison of the failure mode for specimen L250×150×10–d is also shown in Figure 4.25. Overall, the proposed FEM can satisfactorily replicate the structural performance of pin–ended press–braked RHS columns, regarding their ultimate capacities, axial load–lateral displacement and end rotation responses, and the failure modes.

4.3.3.2 Parametric study

Following the validation of the proposed FEM methodology, a series of parametric studies on press–braked RHS long columns was performed, aiming at expanding the test results database.

In the parametric study, a total of 5 different steel grades from normal to high strengths including 275 MPa, 355 MPa, 460 MPa, 550 MPa, and 690 MPa were covered. Since the manufacturing process does not affect the material properties of flat regions, the stress–strain responses of flat materials in flat regions were considered to behave in a hot–rolled steel type. Hence, the nominal values of Young’s modulus $E_{s,f}$, yield

strength $f_{y,f}$, and ultimate strength $f_{u,f}$ from EN 1993-1-1:2022 (2022) were adopted as the key material parameters of flat materials. The material constitutive model developed for hot-rolled steels by Yun and Gardner (2017) was adopted to describe the stress-strain response and generate the stress-strain curves for corresponding flat materials, while the other input parameters such as the strain hardening strain $\epsilon_{sh,f}$ and the ultimate strain $\epsilon_{u,f}$ are reported in Table 4.11. For the material properties within the cold-formed corner region, predictive expressions developed in Chapter 3 were used to determine the Young's moduli $E_{s,c}$, 0.05% proof strengths $f_{0.05\%,c}$, enhanced yield strengths $f_{y,c}$, enhanced ultimate strengths $f_{u,c}$ and the ultimate strains of cold-formed steels. Based on the experimental finding, an average r_i/t ratio of 1.0 were selected to reflect the average strength enhancement level of press-braked RHSs. Then, on the basis of determined key material parameters as listed in Table 4.11, the material constitutive model for cold-formed steels proposed in Chapter 3 was adopted to generate the corresponding stress-strain curves for corner materials which were assigned in the cold-formed corner region.

Table 4.11 Input material properties adopted in the parametric study.

Steel grade MPa	Flat materials					Corner materials				
	E_f GPa	$f_{y,f}$ MPa	$f_{u,f}$ MPa	$\epsilon_{sh,f}$ %	$\epsilon_{u,f}$ %	E_c GPa	$f_{0.05\%,c}$ MPa	$f_{y,c}$ MPa	$f_{u,c}$ %	$\epsilon_{u,c}$ %
275 MPa	210	275	390	1.55	17.69	198	351	431	472	1.61
355 MPa	210	355	490	1.74	16.53	198	445	545	597	1.62
460 MPa	210	460	540	3.00	8.89	198	496	600	659	1.65
550 MPa	210	550	600	3.00	6.00	198	543	653	718	1.67
690 MPa	210	690	770	3.00	6.23	198	701	845	928	1.66

Five sets of non-slender press-braked rectangular cross-section profiles, $150 \times 150 \times 6$, $150 \times 150 \times 10$, $150 \times 100 \times 6$, $150 \times 100 \times 10$, and $200 \times 100 \times 10$, were examined, regarding their structural behaviours of major and minor axes buckling. The modelled effective column lengths were ranged from 1130 mm to 14130 mm to achieve

a range of non-dimensional slenderness values $\bar{\lambda}$ from 0.20 to 2.70. In total, 345 numerical results on press-braked RHS columns, covering normal to high strength steel grades and various geometric dimensions, were generated. The generated numerical results were captured and combined with the experimental results for further study.

4.3.4 Assessment and modification of current design methods

4.3.4.1 General

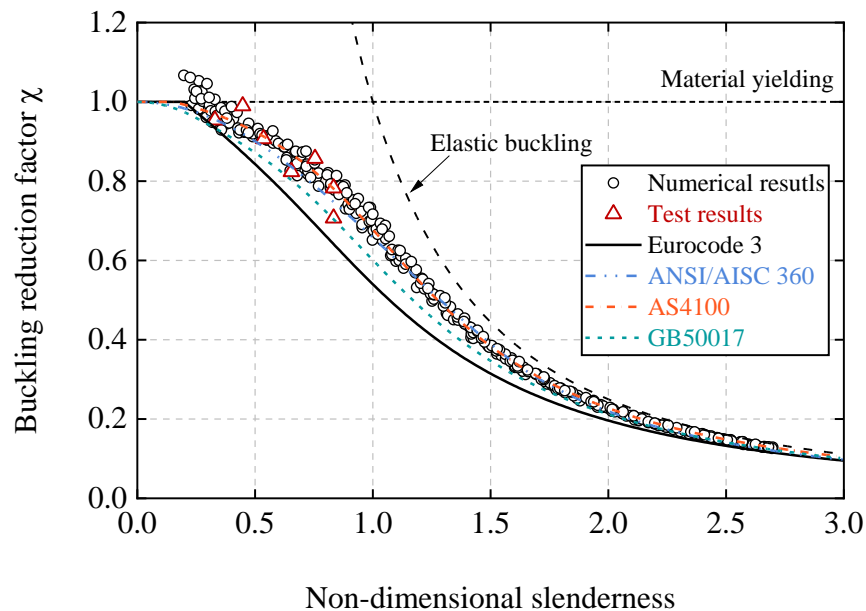


Figure 4.26 Comparisons of Test and numerical results with codified design curves.

The experimental and numerical results described from the previous section were used for evaluating the applicability of current design methods to the press-braked RHS columns. The regional design guides for steel structures, including European standard EN 1993-1-1: 2022 (CEN, 2022), Chinese standard GB 50017-2017 (MOHURD, 2017), American specification ANSI/AISC 360-16 (AISC/AISC, 2022), and Australian standard AS 4100:2020 (Australia, 2020), were examined and discussed. The obtained maximum capacities from experimental and numerical results are normalised and

plotted against the non-dimensional slenderness in Figure 4.26, while the design curves from different standards are also depicted in the same figure for comparison. The assessment results and design recommendation were presented in the following sections.

4.3.4.2 Eurocode 3 design method

Eurocode 3 adopts a multi-column buckling curve concept and uses the Ayrton–Perry formula for the design of steel columns. The selection of column buckling curve is depended on the cross-section types, fabrication routes, buckling axes and material strength grades. For cold-formed RHSs, buckling curve c with an imperfection factor α of 0.49 should be chosen as specified in EN 1993–1–1 and EN 1993–1–12. As recommended in Eurocode 3, the load-bearing capacity of steel columns should be computed by

$$N_{EC3} = \frac{\chi_{EC3} A f_y}{\gamma_{M1}} \quad \text{Eq. (4.9)}$$

$$\chi_{EC3} = \frac{1}{\Phi + \sqrt{\Phi^2 - \bar{\lambda}^2}} \quad \text{Eq. (4.10)}$$

$$\Phi = 0.5 \left[1 + \eta + \bar{\lambda}^2 \right] \quad \text{Eq. (4.11)}$$

$$\eta = \alpha(\bar{\lambda} - 0.2) \quad \text{Eq. (4.12)}$$

$$\bar{\lambda} = \sqrt{\frac{A f_y}{N_{cr}}} \quad \text{Eq. (4.13)}$$

where A represents the gross cross-sectional area for non-slender sections, f_y is the average yield strength (weighted by area) equals $(f_{y,t} A_f + f_{y,c} A_c) / (A_f + A_c)$, taking into account the corner yield strength with strength enhancements, χ is the reduction factor, $\bar{\lambda}$ indicates the non-dimensional slenderness, α denotes the imperfection factor, and

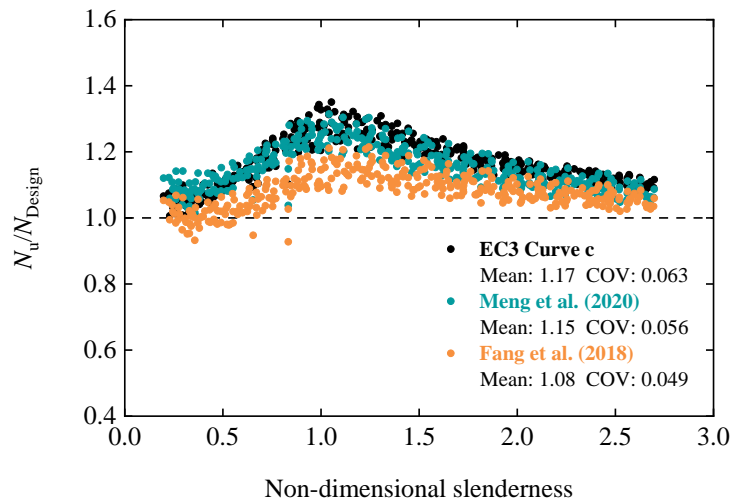
N_{cr} is the elastic critical buckling load.

The imperfection item η that adopted in the Ayrton–Perry formula implicitly incorporated the detrimental effects of residual stresses and global geometric imperfections. The magnitudes of residual stresses are almost constant independent of steel grades, and the disadvantage effect of residual stress has shown to be reduced with the increase of steel grades. To consider the influence of yield strength in designing the column strengths, Fang *et al.* (2018b) and Meng and Gardner (2020a) both proposed respective modifications to the calculation of imperfection item η . The proposed expressions for imperfection factor η are given in Eq. (4.14) and Eq. (4.15), respectively.

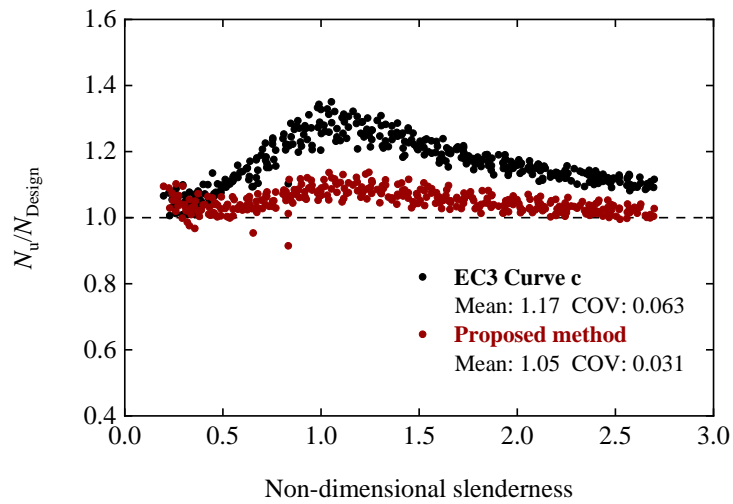
$$\eta_{\text{Meng}} = 0.56\sqrt{235 / f_y} (\bar{\lambda} - 0.1) \quad \text{Eq. (4.14)}$$

$$\eta_{\text{Fang}} = 0.49(\bar{\lambda}\sqrt{235 / f_y} - 0.2) \quad \text{Eq. (4.15)}$$

The ultimate strengths N_u from experimental and numerical tests were derived and compared to the design values calculated based on the original Eurocode 3 method and modified Eurocode 3 methods proposed by Fang *et al.* (2018b) and Meng and Gardner (2020a). The normalised N_u to N_{Design} values are plotted in Figure 4.27 (a), and the comparison results are reported in Table 4.12, with mean N_u/N_{Design} ratios equal to 1.17, 1.15, and 1.08, respectively. The corresponding COV are 0.063, 0.056, and 0.049, respectively.



(a) EC3 and modified EC3 methods



(b) EC3 and proposed method

Figure 4.27 Comparisons of test and numerical results with the design values calculated from different design methods.

To further improve the design accuracy of Eurocode 3, a modification was proposed for the imperfection item η , while the modified expression for η is shown in Eq. (4.16). In this expression, the column buckling curve ‘b’ is recommended to be adopted and a shorter plateau of 0.1 is suggested. The normalised N_u to N_{Design} values for the proposed methods are also plotted in Figure 4.27 (b), while the mean values and COV of N_u/N_{Design} are 1.05 and 0.031, respectively. Based on the proposed modification to imperfection item η , the prediction accuracy for press-braked RHS columns was

improved by around 10%, and less scattered of data was achieved.

$$\eta_{\text{mod}} = 0.34(\bar{\lambda}\sqrt{235/f_y} - 0.1) \quad \text{Eq. (4.16)}$$

Table 4.12 Comparison of experimental and numerical results with design values.

Design methods	N_u/N_{Design}	COV
–	–	–
EC3 curve c	1.17	0.063
Proposed method	1.05	0.031
GB 50017–2017 curve b	1.08	0.039
GB 50017–2017 curve a	1.00	0.025
ANSI/AISC 360–16	1.03	0.030
AS 4100:2020	1.02	0.023

4.3.4.3 Chinese standards GB 50017–2017

GB 50017–2017 adopts a two–phase relationship to predict the buckling reduction factor χ , as shown in Eq. (4.17) and Eq. (4.18).

$$N_{\text{GB 50017}} = \chi_{\text{GB 50017}} A f_y \quad \text{Eq. (4.17)}$$

$$\chi_{\text{GB 50017}} = \begin{cases} 1 - \alpha_1 \bar{\lambda}^2 & \text{for } \bar{\lambda} \leq 0.215 \\ \frac{1}{2\bar{\lambda}^2} \left[\left(\alpha_2 + \alpha_3 \bar{\lambda} + \bar{\lambda}^2 \right) - \sqrt{\left(\alpha_2 + \alpha_3 \bar{\lambda} + \bar{\lambda}^2 \right)^2 - 4\bar{\lambda}^2} \right] & \text{for } \bar{\lambda} > 0.215 \end{cases} \quad \text{Eq. (4.18)}$$

where the non–dimensional slenderness $\bar{\lambda}$ is defined in the same manner as in Eurocode 3, and the imperfection factors α_1 , α_2 , and α_3 are depended on the selected buckling curve. For rolled and welded RHSs, the buckling curve ‘b’ is specified with $\alpha_1 = 0.650$, $\alpha_2 = 0.965$, and $\alpha_3 = 0.300$.

To assess the applicability of GB 50017–2017 on press–braked RHS columns, the ultimate strengths N_u from experimental and numerical tests were derived and compared to the design values calculated based on GB buckling curve ‘b’ and ‘a’ ($\alpha_1 = 0.410$, $\alpha_2 = 0.986$, and $\alpha_3 = 0.152$). The normalised N_u to N_{Design} values are plotted in

Figure 4.28, and the comparison results are reported in Table 4.12, with mean N_u/N_{Design} ratios equal to 1.08 and 1.00, and COV equal to 0.039 and 0.025 for curve ‘b’ and curve ‘a’, respectively. The comparison results show that the selection of curve ‘a’ can provide the most accurate prediction accuracy for press-braked RHS columns. Hence, the buckling curve ‘a’ with $\alpha_1 = 0.410$, $\alpha_2 = 0.986$, and $\alpha_3 = 0.152$ in GB 50017–2017 is suggested to be adopted for the buckling resistance prediction of press-braked RHS columns.

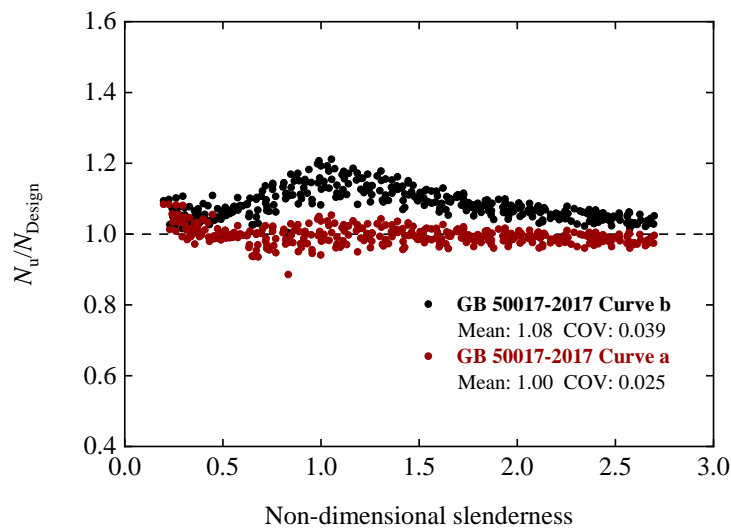


Figure 4.28 Comparisons of results with the design values calculated from GB 50017.

4.3.4.3 American specification ANSI/AISC 360–16

ANSI/AISC 360–16 also adopts a two-phase relationship to predict the buckling reduction factor χ , but with only one column curve being considered, which means a fixed value of imperfection factor was considered in the design of columns, whatever the steel grade and cross-sections are. The column curve codified in ANSI/AISC 360–16 is given in Eq. (4.19) and Eq. (4.20).

$$N_{ANSI/AISC\ 360} = \chi_{ANSI/AISC\ 360} A f_y \quad \text{Eq. (4.19)}$$

$$\chi_{ANSI/AISC\ 360} = \begin{cases} 0.658\bar{\lambda}^2 & \text{for } \bar{\lambda} \leq 1.5 \\ \frac{0.877}{\bar{\lambda}^2} & \text{for } \bar{\lambda} > 1.5 \end{cases} \quad \text{Eq. (4.20)}$$

in which an exponential expression for the buckling reduction factor χ is adopted in the inelastic range ($\bar{\lambda} \leq 1.5$) to consider the effect of residual stresses, and a reduced Euler equation is used in the elastic range ($\bar{\lambda} > 1.5$) where the effect of residual stress is deemed as minimum in this range.

To assess the applicability of ANSI/AISC 360–16 on press-braked RHS columns, the ultimate strengths N_u from experimental and numerical tests were derived and compared to the design values. The normalised N_u to N_{Design} values are plotted in Figure 4.29, and the comparison results are reported in Table 4.12, with mean N_u/N_{Design} ratio equals to 1.03, and COV equals to 0.030. As can be found from the comparison result, the ANSI/AISC 360–16 design curve gives slightly conservative but reasonably accurate predictions for the design of press-braked RHS columns.

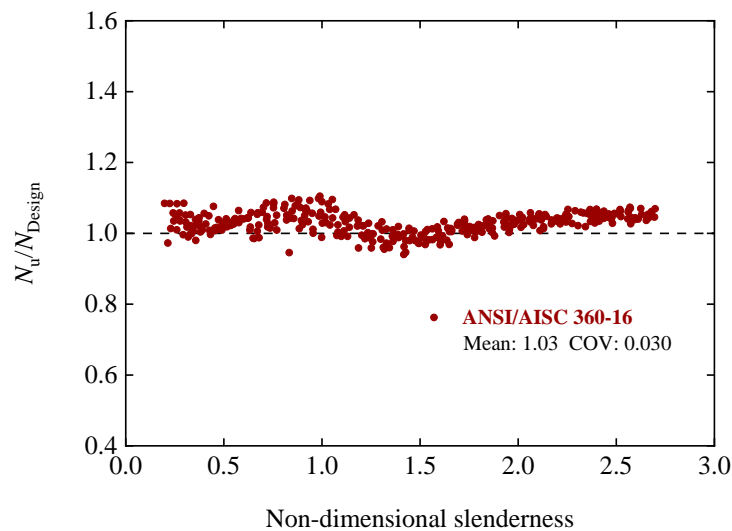


Figure 4.29 Comparison of results with the design values from ANSI/AISC 360–16.

4.3.4.4 Australian standards AS 4100:2020

The non-dimensional slenderness of AS 4100:2020 $\bar{\lambda}_{AS\ 4100}$ is slightly different

from that adopted in the abovementioned design methods, and it equals to $\bar{\lambda}$ multiplied by a factor of $\pi(E_s/250)^{1/2}$, as given in Eq. (4.21). The buckling reduction factor χ in AS 4100:2020 is expressed through Eq. (4.22) to Eq. (4.25).

$$\bar{\lambda}_{AS\ 4100} = \bar{\lambda} \left(\pi \sqrt{\frac{E_s}{250}} \right) \quad \text{Eq. (4.21)}$$

$$N_{AS\ 4100} = \chi_{AS\ 4100} A f_y \quad \text{Eq. (4.22)}$$

$$\chi_{AS\ 4100} = \zeta \left(1 - \sqrt{1 - \left[\frac{90}{\zeta (\bar{\lambda}_{AS\ 4100} + \alpha_a \alpha_b)} \right]} \right) \quad \text{Eq. (4.23)}$$

$$\alpha_a = \frac{2100 (\bar{\lambda}_{AS\ 4100} - 13.5)}{\bar{\lambda}_{AS\ 4100}^2 - 15.3 \bar{\lambda}_{AS\ 4100} + 2050} \quad \text{Eq. (4.24)}$$

$$\zeta = \frac{\left[(\bar{\lambda}_{AS\ 4100} + \alpha_a \alpha_b) / 90 \right]^2 + 1 + 0.00326 (\bar{\lambda}_{AS\ 4100} + \alpha_a \alpha_b - 13.5)}{2 \left[(\bar{\lambda}_{AS\ 4100} + \alpha_a \alpha_b) / 90 \right]^2} \quad \text{Eq. (4.25)}$$

in which α_a is the non-dimensional slenderness modifier, and α_b is the imperfection factor taken as -0.5 for cold-formed (non-stress relieved) RHS and CHS.

To assess the applicability of AS 4100:2020 on press-braked RHS columns, the ultimate strengths N_u from experimental and numerical tests were derived and compared to the design values. The normalised N_u to N_{Design} values are plotted in Figure 4.30, and the comparison results are reported in Table 4.12, with mean N_u/N_{Design} ratio equals to 1.02, and COV equals to 0.023. As can be found from the comparison result, the AS 4100:2020 design curve gives slightly more accurate than the resistance predicted from ANSI/AISC 360-16 for the design of press-braked RHS columns.

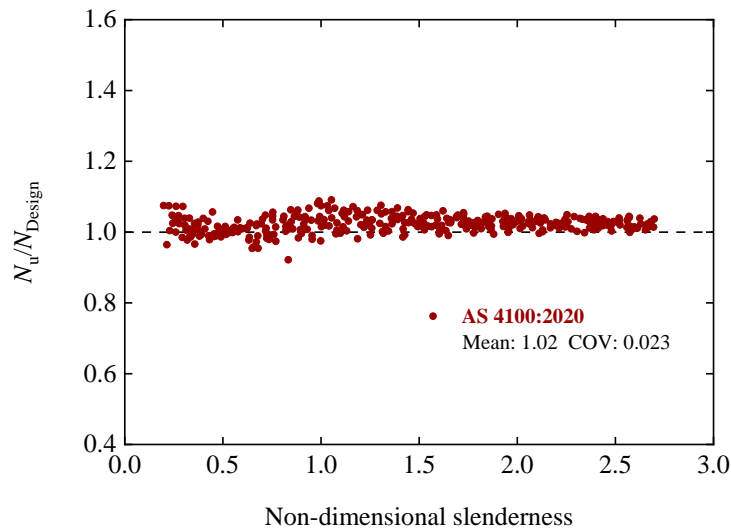


Figure 4.30 Comparison of test and numerical results with the design values calculated from AS 4100:2020.

4.3.5 Reliability analysis

The reliability of different design methods for press-braked RHS columns under concentric compression was evaluated in line with the requirements and procedures stipulated in EN 1990 (CEN, 2002) and AISI S100–16 (AISI, 2016), respectively. Different statistical parameters adopted in the reliability analysis were described in the following sections.

4.3.5.1 EN 1990 method

A partial factor $\gamma_{M1} = 1.00$ was applied to the column buckling strength design formulas of Eurocode 3 to achieve the specified safety level. The basic parameters – Young’s modulus E , yield strength f_y , cross-sectional area A in the theoretical resistance model were varied and their variations can be taken into account through COV, V_E , V_{f_y} , and V_A , respectively. The ratio of the mean yield strength value $f_{y,m}$ to the nominal yield strength value $f_{y,n}$, COV of the yield strength V_{f_y} , COV of the area V_A , and COV of the Young’s modulus V_E are reported in Table 4.13, following the recommendations in EN

1993–1–1:2022 (CEN, 2022).

Table 4.13 Summary of statistical parameters in reliability analysis.

Design methods	Steel grade	$f_{y,m}/f_{y,n}$	V_{f_y}	V_A	V_E
EN 1993–1–1:2022	275	1.25	0.055	0.026	0.030
	355	1.20	0.050	0.026	0.030
	460	1.15	0.045	0.026	0.030
	550	1.10	0.035	0.026	0.030
	690	1.10	0.035	0.026	0.030
ANSI/AISC 360–16	All	1.10	0.100	–	0.050

The column buckling strength design formula was converted as Eq. (4.26) to separate the dependency of basic variables E , f_y , and A (Law, 2010; Meng and Gardner, 2020a). The combined COV of the materials and geometric dimensions can thus be obtained through Eq. (4.27). For the case of a large number of tests ($n \geq 100$), the design resistance value r_d utilised to determine the partial factor γ_M may be obtained by Eq. (4.28). Finally, the partial factors γ_M^* of overall design model can be subsequently acquired by the least-squares best fit to each pair of r_n and r_d , as expressed in Eq. (4.29).

$$N_{b,R} = g_{rt} = KE_a^{k_1} f_y^{k_2} A^{k_3} \quad \text{Eq. (4.26)}$$

$$V_{rt} = \sqrt{(k_1 V_{E_a})^2 + (k_2 V_{f_y})^2 + (k_3 V_A)^2} \quad \text{Eq. (4.27)}$$

$$r_d = b g_{rt}(\underline{X}_m) \exp(-k_{d,\infty} Q - 0.5 Q^2) \quad \text{Eq. (4.28)}$$

$$\gamma_M^* = \frac{\sum_{i=1}^n r_{n,i}^2}{\sum_{i=1}^n r_{n,i} r_{d,i}} \quad \text{Eq. (4.29)}$$

in which K is a constant, independent of the basic variables, and k_1 , k_2 , and k_3 are the coefficients computed for each specimen, varying with the member slenderness.

The results of the reliability analysis are summarised in Table 4.14. As can be found

from the table, γ_M^* for the original Eurocode 3 and proposed design method are 0.955 and 1.060, respectively.

Table 4.14 Results of reliability analysis for different design methods.

Design methods	Press-braked RHS long column	
	γ_M^*	β
EC3 curve c	0.955	–
Proposed method	1.060	–
GB 50017–2017 curve b	–	2.890
GB 50017–2017 curve a	–	2.525
ANSI/AISC 360–16	–	2.827
AS 4100:2020	–	2.578

4.3.5.2 AISI S100 method

For the design methods of GB 50017–2017, ANSI/AISC 360–16, and AS 4100:2020, the reliability analysis procedures conforming to the suggestions in AISI S100–16 (AISI, 2016) were employed to evaluate their reliability. A resistance factor $\phi = 0.9$ is specified in ANSI/AISC 360–16, ASCE/SEI 48–19 and AS 4100:2020 design methods. While for GB 50017–2017, it is worth noting that the resistance factor is implicitly incorporated in the design yield strength ($f_{y,d} = f_{y,n}/\gamma_M$, and $\gamma_M = 1.1$), hence the resistance factor ϕ of GB 50017–2017 can be obtained as $1/1.1 \approx 0.91$.

Under various loading situations, a basic dead load (DL) and live load (LL) combination of $1.35 \times DL + 1.5 \times LL$ for GB 50017–2017 (MOHURD, 2012), $1.2 \times DL + 1.6 \times LL$ for ANSI/AISC 360–16, $1.2 \times DL + 1.5 \times LL$ for AS 4100:2020, and a live load over dead load ratio of 3 were adopted from the practical perspective. The reliability index β was computed using Eq. (4.30) and the design methods were deemed to be reliable if the reliability index β was greater than 2.5 (AISI, 2016).

$$\beta = \frac{\ln\left(\frac{R_n(P_m M_m F_m)}{Q_m}\right)}{\sqrt{V_P^2 + V_M^2 + V_F^2 + V_Q^2}} \quad \text{Eq. (4.30)}$$

where R_n/Q_m is the nominal resistance to the average load effect ratio, P_m and V_P are the mean value and COV of the experimental/predicted strength ratios, M_m and V_M are the mean value and COV of the material properties variable, and F_m and V_F are the mean value and COV of the cross-section geometries variable.

Key parameters and results of reliability analyses are listed in Table 4.13 and Table 4.14. Of the results investigated, the reliability index β for GB 50017–2017, ANSI/AISC 360–16, and AS 4100:2020 design methods were all greater than 2.5, implying that satisfied reliability level was acquired for these design methods.

4.4 Concluding remarks

A comprehensive test programme was conducted on press-braked rectangular hollow section columns to investigate the characteristics of these sections including material properties distribution, residual stress pattern, local geometric imperfection, global geometric imperfection, cross-sectional compressive resistance, and global flexural buckling resistance. A simplified predictive residual stress pattern was proposed on the basis of the sectioning results and collected data. Finite element models for press-braked RHS stub and long columns were developed and validated against the experimental results. Parametric studies were conducted to expand the test database over a wider spectrum of parameters.

The experimental results combined with generated numerical results were utilised to evaluate the applicability of different design codes for press-braked RHSs. In terms of cross-section level, modified effective width method and modified direct strength

method were proposed in this chapter and these methods were found to yield more accurate prediction results than original methods. In terms of structural member level, codified column design curves were firstly evaluated. A modified Eurocode 3 design method was subsequently proposed to provide more accurate prediction results. It is found that using curve ‘a’ in GB 50017–2017 can achieve the most accurate prediction accuracy, and ANSI/AISC 360–16 and AS 4100:2020 can also provide relatively accurate prediction results for press-braked RHS columns. Corresponding reliability analyses haven been performed to evaluate the reliability of current and proposed design methods.

Chapter 5 Structural behaviour and design of pin-ended octagonal hollow section columns

5.1 Introduction

Previous investigations on polygonal hollow sections mainly focused on the issues in material and cross-section levels. For instance, the distribution of material properties around cross-sections, magnitudes of residual stresses, and cross-section classification limit. Although the behaviour of polygonal hollow section stub columns has been systematically investigated, limited attention has been paid to the polygonal hollow section column members that may experience the global buckling effect considered for their use in lighting poles and transmission towers. Up to date, the investigation on the polygonal hollow section at member level is scarce. Hence, in order to generate safe structural designs, the structural performance of polygonal hollow section columns needs to be clearly understood.

This chapter therefore firstly presents an experimental investigation on the structural behaviour of regular and irregular octagonal hollow section (OctHS) long columns. The regular and irregular OctHS specimens were made of high strength steels with nominal steel grades of 460 MPa and 690 MPa. The irregular OctHS specimens were tested under two buckling axes (major and minor). The test instrumentation, loading procedure, and test results were presented. Finite element models were carefully developed and validated against measured test results. Following the validation, parametric studies comprising various parameters were subsequently conducted to generate a wider spectrum of database. The experimental and numerical results were utilised to determine if current design codes can be extended to the design of cold-formed OctHS long columns. Assessment results and modifications to the

current design standards were provided. Reliability analysis was performed for the current design standards and the proposed method.

5.2 Experimental investigation of OctHS columns

5.2.1 Specimen details of OctHS columns



Figure 5.1 Half section of irregular octagonal hollow section ($H/W = 2$).

Cold-formed octagonal hollow section columns were fabricated through press-braking and welding in this study. The steel plates were firstly cut into designed dimensions with their edges being v-notched. Then the press-braking process was performed to form half sections, as shown in Figure 5.1. Since the specimens were fabricated from thin gauge Q460 and Q690 steel plates with nominal thicknesses of 3 mm and 6 mm, to control the welding quality, gas-shield metal arc welding was adopted and the welding parameters were well designed, as reported in Table 5.1. By doing so, the deterioration of mechanical properties around the welding seam can be regarded as have insignificant impact on the structural behaviour of columns. Except for the controlled welding parameters, spot welds were performed to connect two half sections, and ceramic backing plates to prevent welding defects were also attached behind the position of welding, as illustrated in Figure 5.2. After welding, both ends of the column

were milled flat and two 20 mm thick steel end plates were welded to both ends.

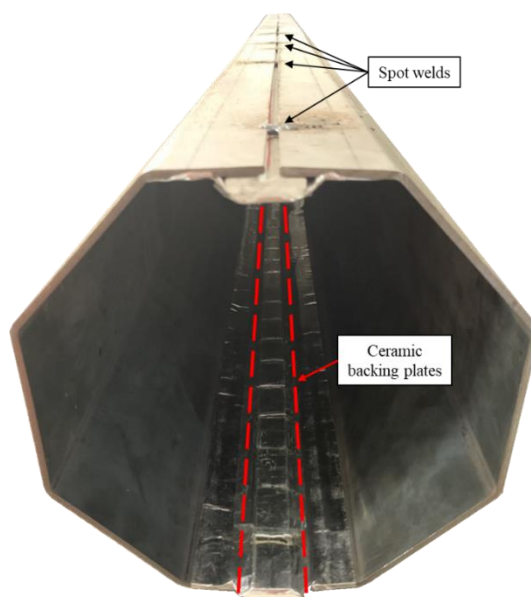


Figure 5.2 Arrangement of spot welds and ceramic backing plates of specimen.

Table 5.1 Welding parameters for the Gas–shield metal arc welding.

Steel grade	Thickness	Voltage	Current	Welding speed
–	mm	V	A	mm/min
Q460	3	20	170	350
Q460	6	24	170	350
Q690	3	20	170	350
Q690	6	24	170	350

The regular OctHS column specimens consist of four types of cross–sections – 4O–140×3, 4O–170×3, 6O–120×3, and 6O–140×3, which were labelled following their nominal steel grade, nominal height H , and nominal plate thickness t , while the definitions of symbols were provided in Figure 5.3. It should be noted that all regular OctHSs investigated in this study were classified into non–slender cross sections. In total, 10 regular OctHS specimens with different cross–sections and various lengths were tested in the experimental programme. The irregular OctHS columns specimens consist of four types of cross–sections – 4O1.5–140×6, 4O2.0–140×6, 6O1.5–120×6, and 6O2.0–120×6, which were labelled following their nominal steel grade, aspect ratio (H/W), nominal width W , and nominal plate thickness t , while the definitions of

symbols were provided in Figure 5.4. It should be noted that irregular OctHSs investigated in this study can be classified into both non-slender and slender cross-sections. In total, 12 irregular OctHS specimens with different cross-sections and various lengths were tested in the experimental programme.

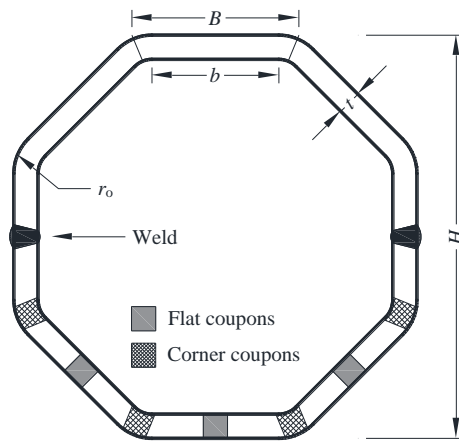


Figure 5.3 Definition of symbols and locations of tensile coupons for the regular octagonal hollow section.

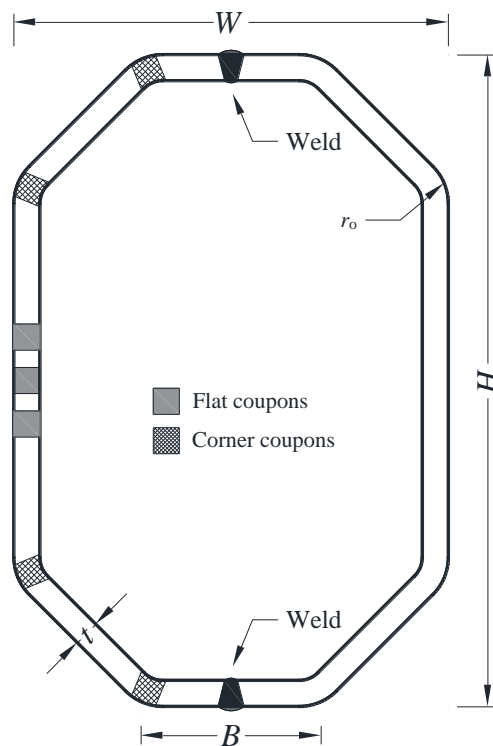
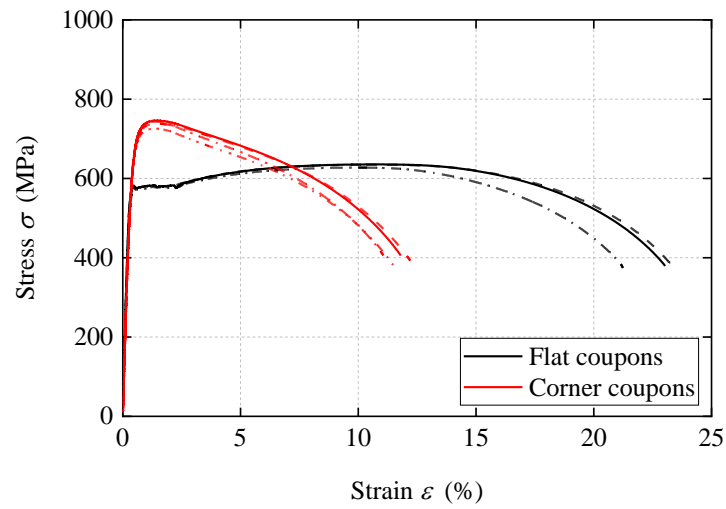
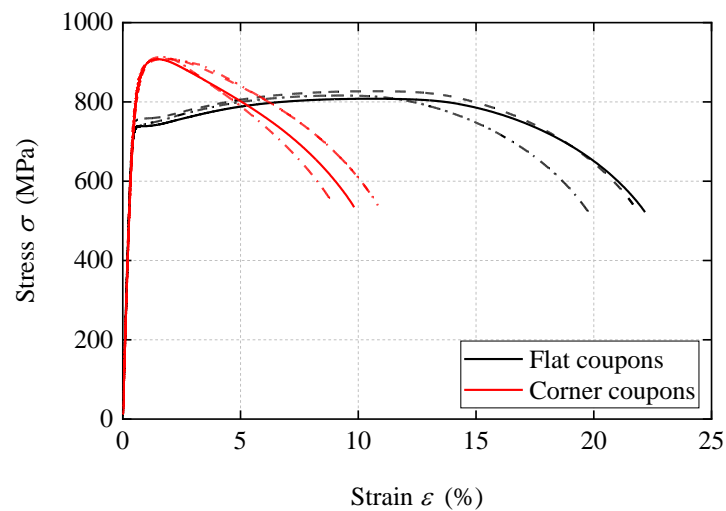


Figure 5.4 Definition of symbols and locations of tensile coupons for the irregular octagonal hollow section.

5.2.2 Material properties



(a) Q460 - 3 mm

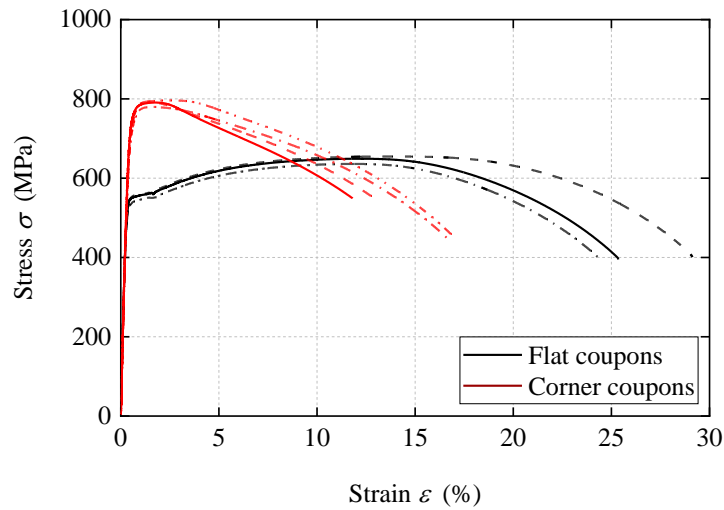


(b) Q690 - 3 mm

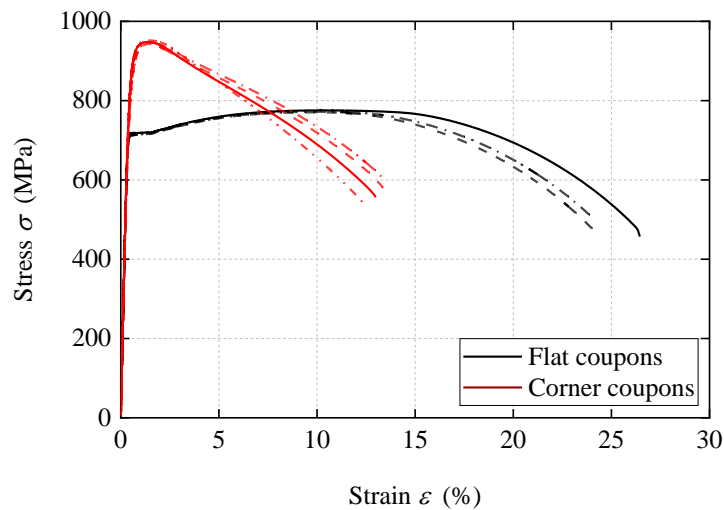
Figure 5.5 Measured stress–strain curves of Q460 – 3 mm and Q690 – 3 mm flat and corner coupons.

To determine the material properties of investigated OctHSs, tensile coupon tests were performed. Figure 5.3 and Figure 5.4 show the locations from where the flat tensile coupons and corner tensile coupons were extracted. Three flat tensile coupons and four corner tensile coupons were extracted from each cross-section. The dimensions of the tensile coupons were designed in line with the requirements of EN

ISO 6892–1: 2019 (CEN, 2019), and were identical to those described in Chapter 3. The tensile test procedures including test setup, arrangements of strain gauges and the extensometer, and loading protocol that similar with those described in Chapter 3 were also adopted.



(a) Q460 - 6 mm



(b) Q690 - 6 mm

Figure 5.6 Measured stress–strain curves of Q460 – 6 mm and Q690 – 6 mm flat and corner coupons.

All the material test results are tabulated in Tables 5.2 and Tables 5.3 for Q460 and Q690 steel plates, respectively. The obtained typical full range stress–strain curves of

coupons are plotted in Figure 5.5 and Figure 5.6, in which stress–strain curves of flat coupons are shown in black lines, and curves of corner coupons are depicted in red lines.

Table 5.2 Obtained material properties of Q460 steel plates.

Steel plate	Specimen	E GPa	$f_{0.2}$ MPa	f_u MPa	ϵ_u %	$\epsilon_f, 25\text{mm}$ %
Q460 – 3 mm	Flat–1	202	581	636	10.62	23.03
	Flat–2	203	579	635	10.53	23.38
	Flat–3	204	571	627	9.59	21.24
	Mean:	203	577	632	10.25	22.55
	Corner–1	193	686	746	1.39	11.80
	Corner–2	199	673	738	1.43	12.21
	Corner–3	202	669	726	1.36	11.53
	Corner–4	199	684	743	1.36	11.06
	Mean:	200	678	738	1.39	11.65
	Q460 – 6 mm	Flat–1	199	555	649	12.26
Flat–2		199	559	655	13.62	29.13
Flat–3		200	541	636	11.72	24.42
Mean:		199	552	647	12.53	26.30
Corner–1		193	749	791	1.76	11.81
Corner–2		193	733	793	1.40	13.00
Corner–3		196	717	780	1.58	16.65
Corner–4		199	747	796	2.46	16.91
Mean		196	737	790	1.80	14.59

Table 5.3 Obtained material properties of Q690 steel plates.

Steel plate	Specimen	E GPa	$f_{0.2}$ MPa	f_u MPa	ϵ_u %	$\epsilon_f, 25\text{mm}$ %
Q690 – 3 mm	Flat–1	200	734	808	10.42	22.17
	Flat–2	203	753	827	10.52	21.67
	Flat–3	207	733	816	9.18	19.80
	Mean:	203	740	817	10.04	21.21
	Corner–1	194	832	908	1.49	9.82
	Corner–2	193	817	909	1.77	10.70
	Corner–3	200	825	913	1.61	8.86
	Corner–4	208	836	909	1.68	10.87
	Mean:	200	828	910	1.64	10.06
Q690 – 6 mm	Flat–1	218	717	775	10.34	26.45
	Flat–2	219	711	771	9.66	24.24

Flat-3	218	712	772	10.11	23.89
Mean:	218	714	773	10.04	24.86
Corner-1	216	894	948	1.37	12.99
Corner-2	213	861	943	1.43	13.62
Corner-3	209	864	946	1.47	13.45
Corner-4	219	900	952	1.40	12.33
Mean:	214	880	947	1.42	13.10

5.2.3 Initial global geometric imperfection

Prior to the long column tests, the initial global imperfection of cold-formed OctHS columns were determined. Through a Leica total station, measurements were taken on the locations at mid height and near both ends of the columns to determine the deviation value of bow shape. Then, obtained global imperfection magnitudes were utilised to determine the loading eccentricities in the following section.

5.2.4 Test set-up and loading eccentricity

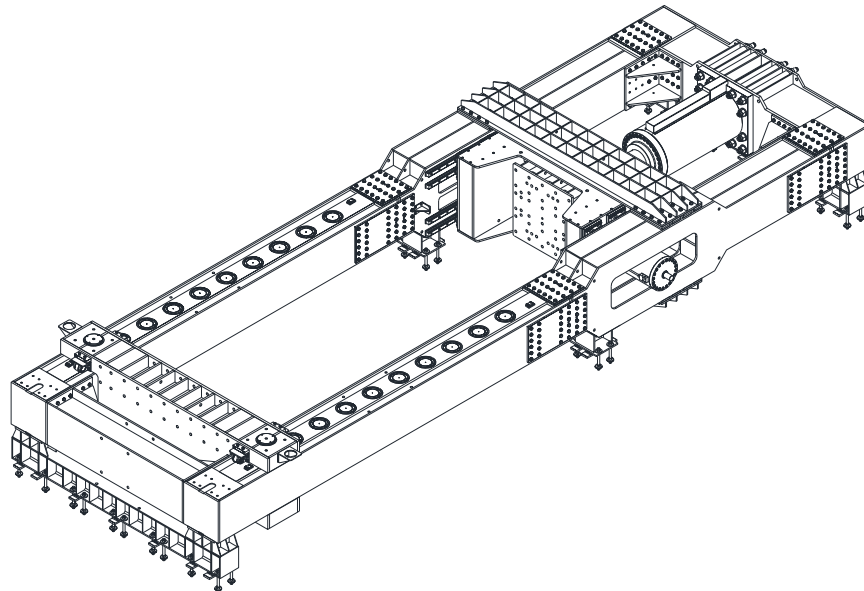


Figure 5.7 Isometric view of testing machine.

A total of 22 OctHS long columns, including 10 regular OctHS column specimens and 12 irregular OctHS column specimens, were tested under the Popwil 5000 kN universal compression machine in Shanghai University. The isometric view of the

testing machine is shown in Figure 5.7, and the detailed test setup is shown in Figure 5.8. The OctHS column specimens were placed between a pair of knife edges to mimic the rotation free pin-ended boundary conditions regarding their target bending axis. The effective length of specimen was determined by the original length of specimen L plus the additional height of knife edges which is equal to 65 mm at both ends ($L_{\text{eff}} = L + 130 \text{ mm}$). A total of four LVDTs were set for different purposes, while LVDT 1 was used to record the mid-height lateral deflection Δ_y , LVDT 2–3 were used to record the axial shortenings of top end which can be further converted to the end rotation, and LVDT 4 aimed to monitor the out-of-plane displacement. To record the axial strain development histories and determine the loading eccentricities, two strain gauges were affixed on the central of both faces in the bending plane at the mid-height of each column.

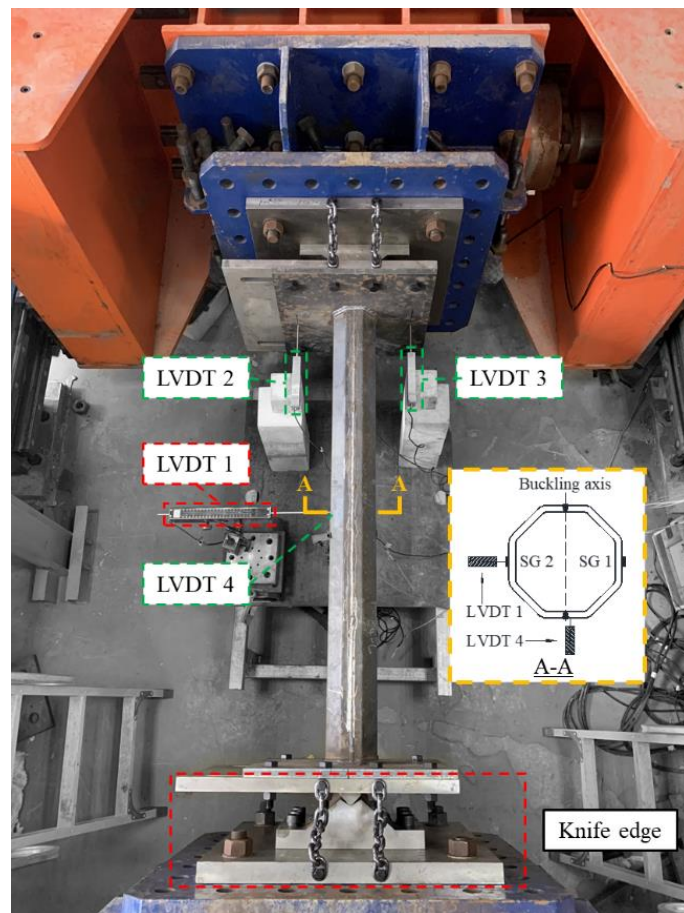


Figure 5.8 Flexural buckling test setup of OctHS columns.

The readings of strain gauges combined with the readings of applied axial load and mid–height lateral deflection Δ_y were utilised to determine the loading eccentricities e . The loading eccentricities e can then be obtained using the following equation:

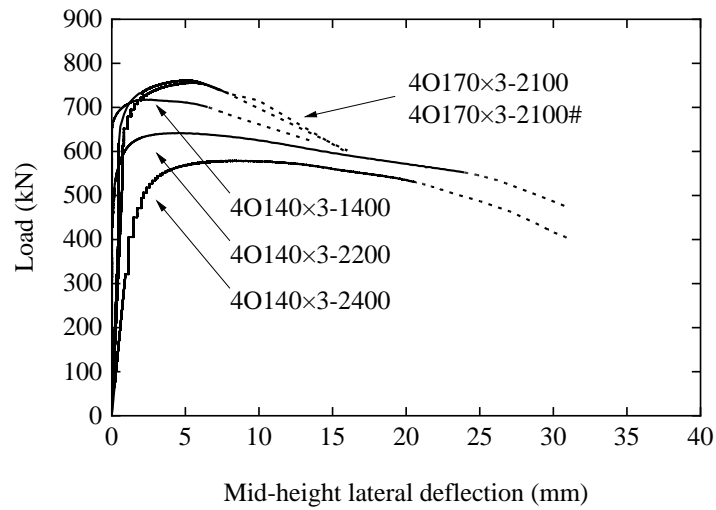
$$e = \frac{E_s I (\varepsilon_{\max} - \varepsilon_{\min})}{sN} - \omega_g - \Delta_y \quad \text{Eq. (5.1)}$$

in which $E_s I$ is the flexural rigidity of the cross–section about the buckling axis, ε_{\max} and ε_{\min} are the strain gauges readings on the concave and convex sides, s is the distance between strain gauges, N is the applied load, ω_g is the initial global imperfection, and Δ_y is the mid–height lateral deflection. Similar approaches were also adopted in Chen and Young (2019), and Meng and Gardner (2020a). It should be noted that the magnitude of initial global geometric imperfection in Eq. (5.1) was always positive because the convex side of bow shape for each column was always placed at the left side when the column specimen being placed into the machine.

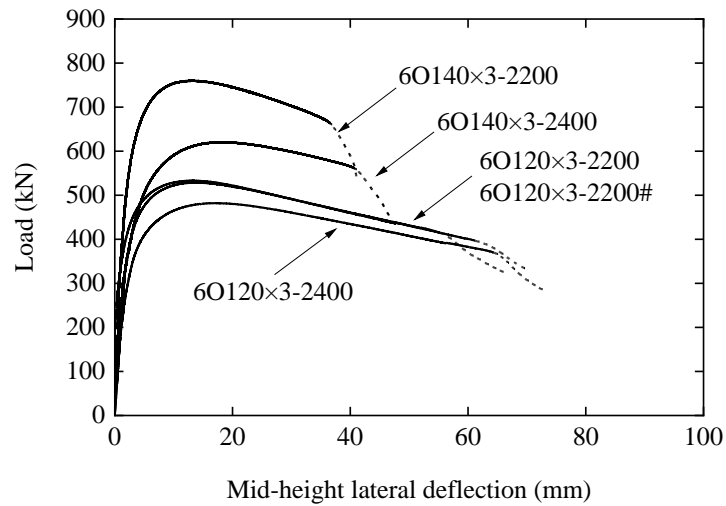
Displacement controlled loading method with a uniform loading speed of 0.2 mm/min was adopted during the test for each specimen. The applied load, readings from LVDTs and strain gauges were recorded at one second intervals by a data acquisition system.

5.2.5 Column test results

The obtained geometric dimensions and key test results are tabulated in Table 5.4 and Table 5.5 for regular and irregular OctHS column specimens, respectively. The axial load versus mid–height lateral deflection curves for each OctHS column specimen are shown in Figure 5.9 and Figure 5.10. All tested columns buckled in the direction where the convex side of global buckling was, except for specimen 4O140×3–2200 which has an unanticipated buckling direction.

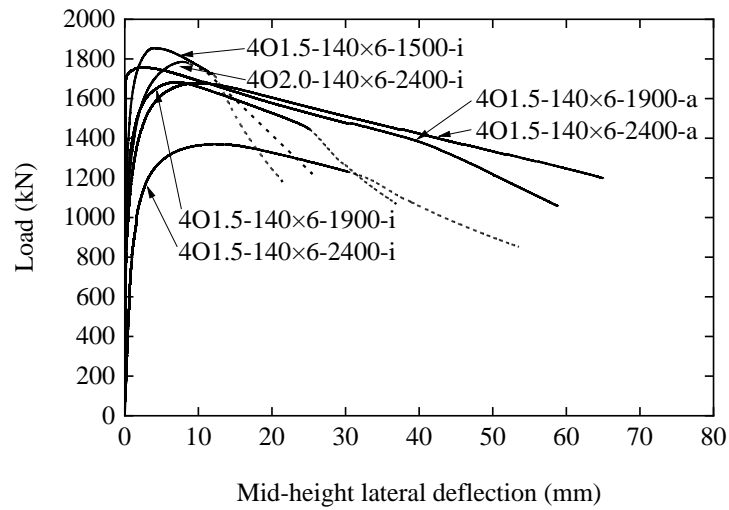


(a) Q460 regular OctHS columns

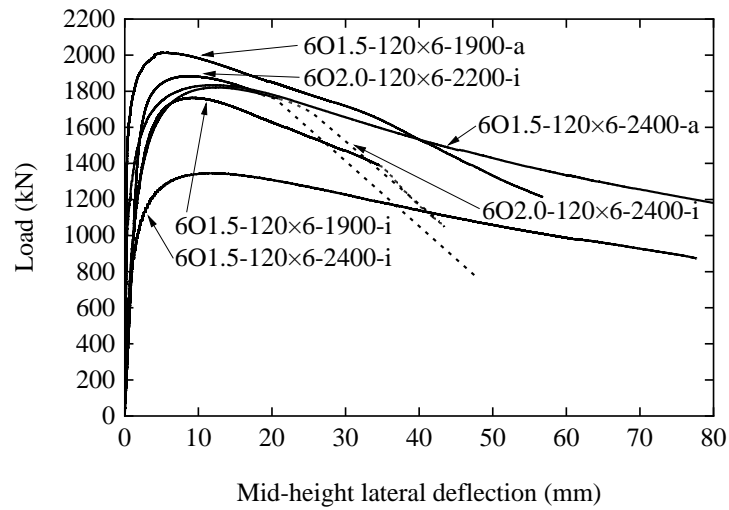


(b) Q690 regular OctHS columns

Figure 5.9 Axial load–mid–height lateral deflection curves of regular OctHS column specimens.



(a) Q460 irregular OctHS columns



(b) Q690 irregular OctHS columns

Figure 5.10 Axial load–mid–height lateral deflection curves of irregular OctHS column specimens.

Table 5.4 Dimensions and test results of regular OctHS columns.

Specimen	H mm	t mm	r_o mm	r_i mm	I $\times 10^3 \text{ mm}^4$	L mm	$\bar{\lambda}$ –	ω_g mm	$e+\omega_g$ mm	$(e+\omega_g)/L$ –	N_{Test} kN
4O140×3–1400	136.81	3.00	10.29	5.15	3111.4	1397	0.54	0.54	0.69	1/2024	718
4O140×3–2200	138.52	3.00	10.29	5.15	3232.7	2196	0.81	0.32	0.43	1/5115	642
4O140×3–2400	138.78	3.00	10.29	5.15	3251.4	2396	0.88	1.81	1.99	1/1206	579
4O170×3–2100	168.05	3.00	10.29	5.15	5851.9	2095	0.64	0.65	2.25	1/931	761
4O170×3–2100#	167.64	3.00	10.29	5.15	5808.5	2093	0.64	0.58	2.49	1/840	756
6O120×3–2200	120.49	2.91	10.09	4.90	2044.1	2193	1.05	1.20	2.39	1/916	529
6O120×3–2200#	119.29	2.91	10.09	4.90	1981.5	2194	1.07	0.95	2.05	1/1072	534
6O120×3–2400	118.50	2.91	10.09	4.90	1941.5	2395	1.17	0.85	2.31	1/1037	482
6O140×3–2200	138.05	2.91	10.09	4.90	3109.0	2190	0.91	0.77	1.25	1/1752	760
6O140×3–2400	138.10	2.91	10.09	4.90	3112.4	2396	1.00	1.20	1.81	1/1324	620

Table 5.5 Dimensions and test results of irregular OctHS columns.

Specimen	H	W	t	r_o	r_i	I	L	$\bar{\lambda}$	ω_g	$e+\omega_g$	$(e+\omega_g)/L$	N_{Test}
–	mm	mm	mm	mm	mm	$\times 10^3 \text{ mm}^4$	mm	–	mm	mm	–	kN
4O1.5–140×6–1500–i	205.67	135.43	5.78	17.96	8.66	8825.3	1497	0.54	0.60	0.35	1/4277	1854
4O1.5–140×6–1900–i	204.58	136.81	5.78	17.96	8.66	8951.5	1896	0.66	1.35	0.75	1/2522	1684
4O1.5–140×6–2400–i	206.19	134.70	5.78	17.96	8.66	8755.2	2392	0.84	0.90	2.29	1/1044	1370
4O1.5–140×6–1900–a	203.71	137.03	5.78	17.96	8.66	15722.7	1897	0.50	0.90	1.14	1/1664	1757
4O1.5–140×6–2400–a	206.41	134.99	5.78	17.96	8.66	16150.2	2397	0.62	0.50	1.97	1/1217	1678
4O2.0–140×6–2400–i	274.63	135.69	5.78	17.96	8.66	12224.8	2397	0.74	1.50	1.13	1/2121	1785
6O1.5–120×6–1900–i	175.41	117.69	6.00	19.59	10.76	5736.1	1893	0.85	1.05	1.53	1/1237	1764
6O1.5–120×6–2400–i	179.36	115.20	6.00	19.59	10.76	5636.2	2395	1.08	1.40	2.22	1/1078	1346
6O1.5–120×6–1900–a	176.68	116.60	6.00	19.59	10.76	10305.3	1895	0.64	0.25	0.98	1/1933	2014
6O1.5–120×6–2400–a	177.44	114.33	6.00	19.59	10.76	10318.6	2398	0.79	0.95	1.84	1/1303	1834
6O2.0–120×6–2200–i	238.03	116.80	6.00	19.59	10.76	7958.5	2196	0.90	1.85	2.62	1/838	1884
6O2.0–120×6–2400–i	237.03	114.13	6.00	19.59	10.76	7555.9	2397	0.99	0.50	1.74	1/1378	1821

Notes: –a indicates major axis bending and –i indicates minor axis bending.

For all specimens, global buckling was gradually formed from the beginning of test until the specimen obtained the ultimate strength. However, different post-peak behaviours were found between regular and irregular OctHS columns. For regular OctHS columns, the ultimate load was maintained for a while and started to gradually decrease, then local deformation abruptly occurred accompanying with a loud thump. At the same time, the axial load applied at specimens dramatically dropped to a relatively lower level, and a sudden jump in the lateral deflection can also be found. The sudden drop in axial load and jump in lateral deflection were plotted in dashed lines in Figure 5.9 for a better illustration. For part of irregular OctHS columns which were designed to buckle about the major axis, local deformations were gradually formed in a moderate manner after the obtainment of ultimate load, and the applied loads dropped smoothly. But for those specimens anticipated to buckle about their minor bending axis, they also experienced similar phenomena described for regular OctHS specimens (also shown by dashed lines in Figure 5.10), except for the specimen 6O1.5-120×6-2400-i, which shows a gradually deteriorated post-peak behaviour due to its relatively large member slenderness.

The development histories of axial load versus axial strain of all columns are shown in Figure 5.11 and Figure 5.12 for regular and irregular OctHS columns, respectively. The readings from two strain gauges no doubt were found to be in compression and coincided with each other well at the initial stage. However, with the increase of lateral deflection, these two curves began to separate and even reverse. Readings from SG1 in the concave side still increased with the increase of applied load, while readings from SG2 in the convex side started to decrease, indicating that the convex side of the column gradually suffered from tension due to the increasing second-order bending moment caused by the lateral deflection. As the applied loads increase to the ultimate load, all the readings of SG1 exceeded the value of the yield strain ($\varepsilon_y = f_y/E_s$), representing that

the steel yielding occurs, and all OctHS specimens failed in an elasto–plastic manner. The sudden occurrence of local deformations was also highlighted in dotted lines in Figure 5.11 and Figure 5.12. It is worth noting that the SG1 strain readings from concave side of specimens which have gradual forming of local deformations can eventually develop to a quite large value, as compared with other specimens. The overview of failure mode for each specimen can be found in Figure 5.13 and Figure 5.14 for regular and irregular OctHS columns, respectively.

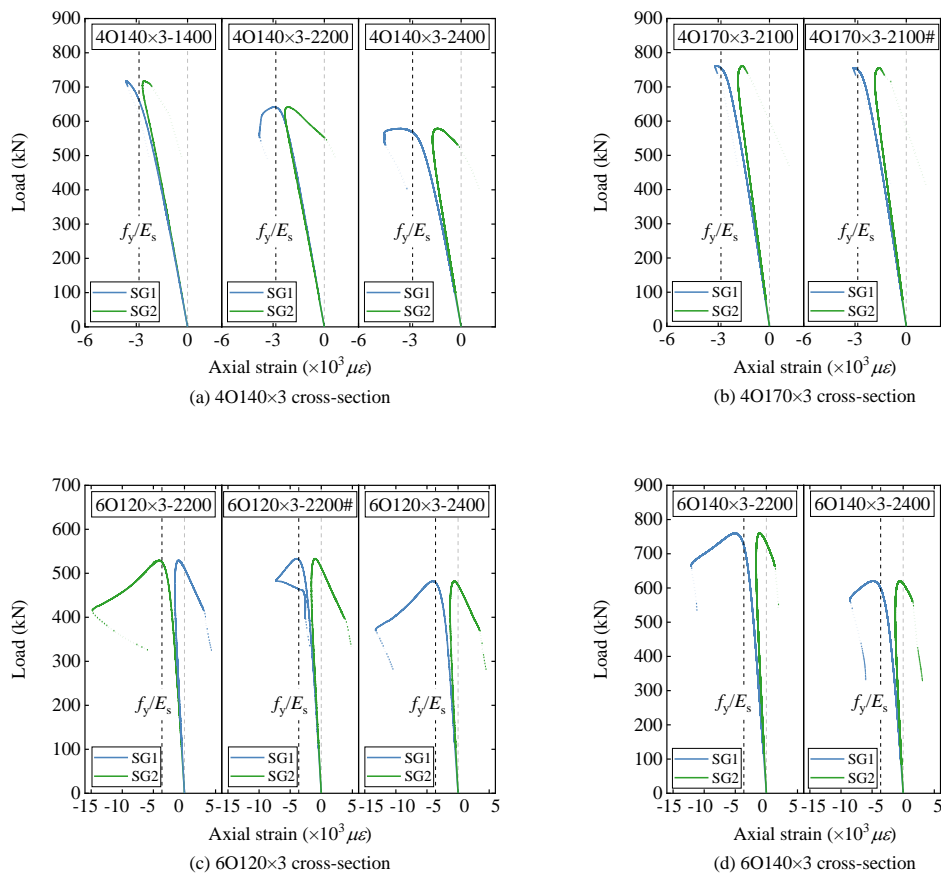


Figure 5.11 Axial load–axial strain curves of regular OctHS specimens.

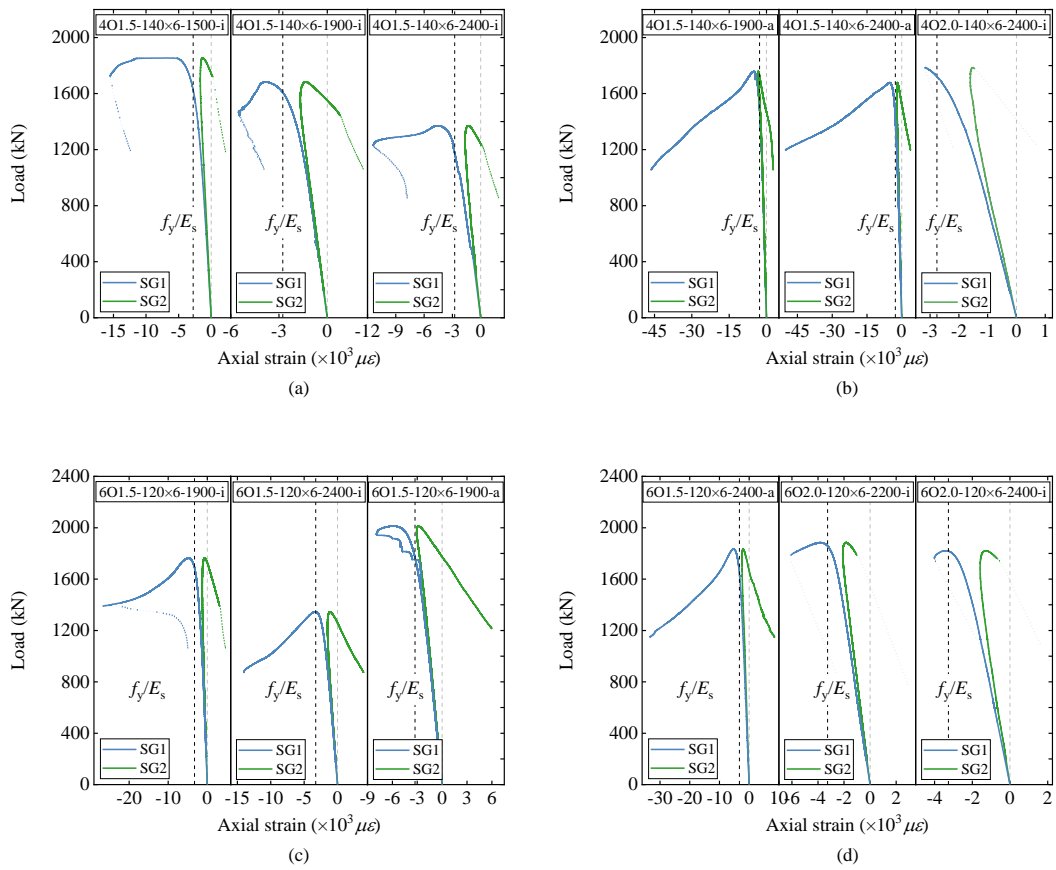
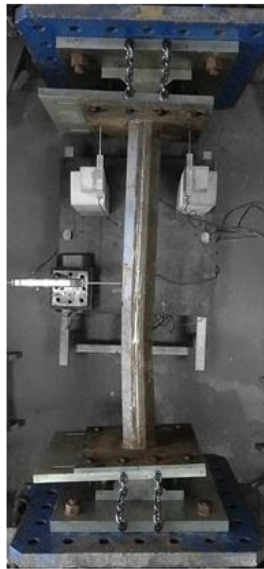
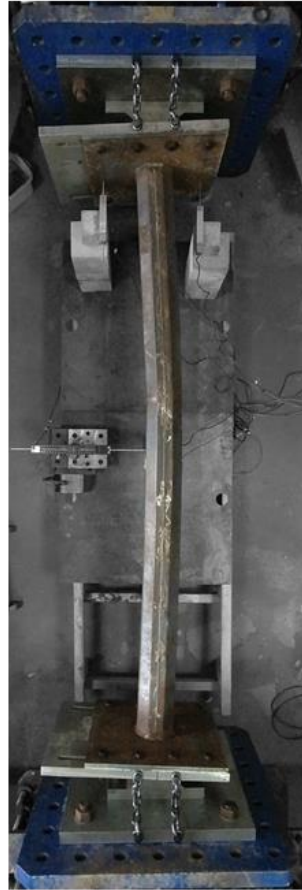


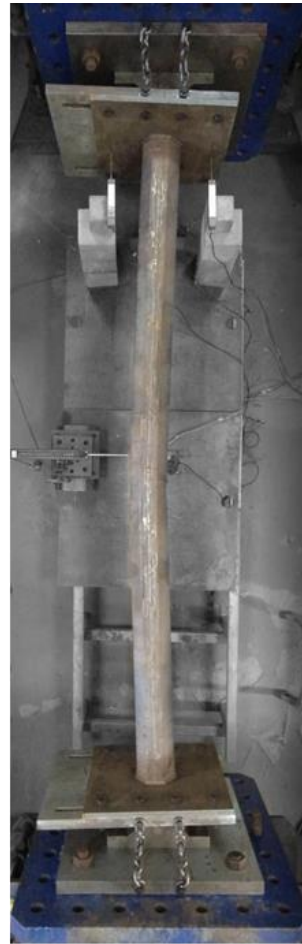
Figure 5.12 Axial load–axial strain curves of irregular OctHS specimens.



(a) 4O-140×3-1400



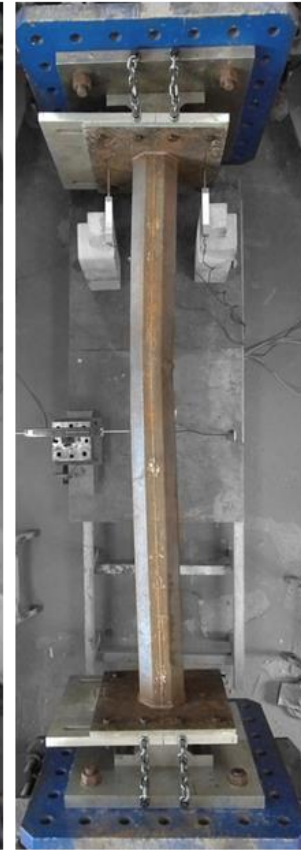
(b) 4O-140×3-2200



(c) 4O-140×3-2400



(d) 4O-170×3-2100



(e) 4O-170×3-2100#



(f) 60-120×3-2200

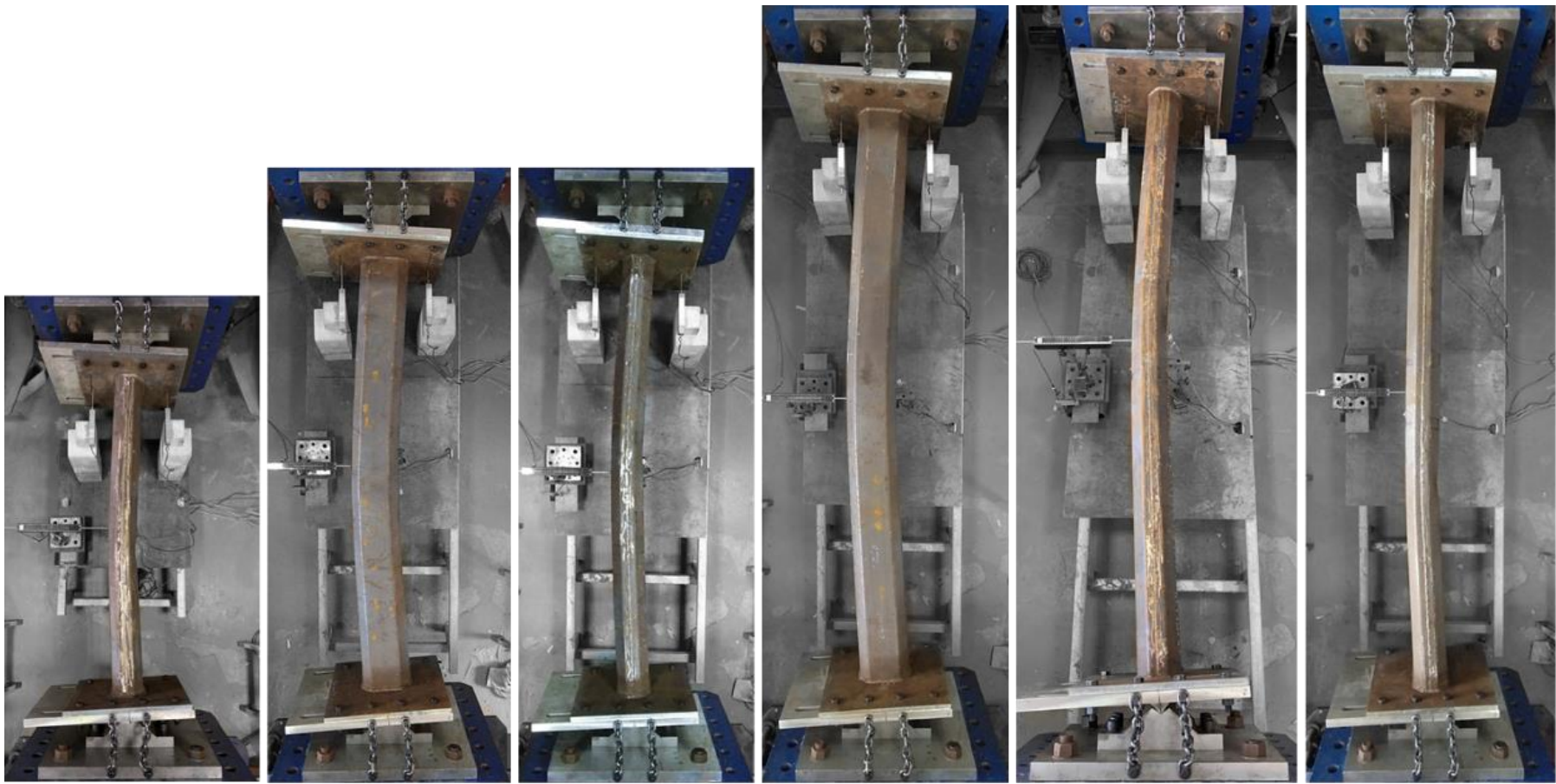
(g) 60-120×3-2200#

(h) 60-120×3-2400

(i) 60-140×3-2200

(j) 60-140×3-2400

Figure 5.13 Failure modes of regular OctHS columns.



(a) 4O1.5-140×6-1500-i

(b) 4O1.5-140×6-1900-a

(c) 4O1.5-140×6-1900-i

(d) 4O1.5-140×6-2400-a

(e) 4O1.5-140×6-2400-i

(f) 4O2.0-140×6-2400-i



(g) 6O1.5-120×6-1900-a (h) 6O1.5-120×6-1900-i (i) 6O1.5-120×6-2400-a (j) 6O1.5-120×6-2400-i (k) 6O2.0-120×6-2200-i (l) 6O2.0-120×6-2400-i

Figure 5.14 Failure modes of irregular OctHS columns.

5.3 Numerical investigations and parametric study

5.3.1 Finite element modelling validation

Finite element modelling (FEM) was developed for the numerical modelling on the structural behaviour of cold-formed OctHS long columns through Geometrically and Materially Nonlinear Imperfect Analysis (GMNIA) using the finite element analysis software ABAQUS. S4R shell element is selected from the element library for modelling the OctHS specimens in this study, as it was proved to have appropriate computational accuracy and efficiency for simulating tubular structures. Based on a prior investigation on the mesh convergency, a uniform mesh size of $B/10$ was selected to mesh flat regions of the cross-section, and three elements were adopted to uniformly discretise the corner regions. Since the cold-forming effect caused in the manufacturing process not only affect the materials within the corner region but also its vicinity, the extension of the strength enhancement region for OctHS was determined as $1t$, which was derived based on the comparisons between the test and numerical results from Chen *et al.* (2021). For the modelling of flat and corner materials, the engineering stress-strain responses of corresponding materials were transformed into the true stress-plastic strain responses using Eq. (5.2) and Eq. (5.3), in which σ_{eng} and ε_{eng} is the engineering stress and strain, respectively, σ_{true} is the obtained true stress, and $\varepsilon_{\text{plastic}}$ is the converted logarithmic plastic strain.

$$\sigma_{\text{true}} = \sigma_{\text{eng}} (1 + \varepsilon_{\text{eng}}) \quad \text{Eq. (5.2)}$$

$$\varepsilon_{\text{p}} = \ln(1 + \varepsilon_{\text{eng}}) - \frac{\sigma_{\text{true}}}{E_{\text{a}}} \quad \text{Eq. (5.3)}$$

To mimic the rotation free pin-ended boundary conditions, both ends of the specimen were coupled to a reference point through kinematic coupling, while the

reference points were longitudinal offset 65 mm away from the centre of corresponding end surfaces. The reference points were only allowed to rotate about the bending axis, whilst the top reference point has an additional longitudinal translation as compared to the bottom counterpart. Regarding the introduction of initial geometric imperfections, the initial local imperfection magnitude of $0.1t$ was selected based on the suggestions from Zhu *et al.* (2019) and Chen *et al.* (2021), since the manufacturing process adopted to fabricate OctHSs was similar, and the distribution and magnitude of initial local imperfection were thus deemed similar. To further study the effects of global imperfection, different values of global imperfection of measured values ($e + \omega_g$), $L/500$, $L/1000$, and $L/1500$ were separately incorporated in the FEM.

Residual stresses that existed in the cold-formed hollow sections can be attributed to the mechanical fabrication and uneven cooling process after welding. The residual stresses may cause reductions in resistance (Chen *et al.*, 2020; Fang *et al.*, 2018a; Su *et al.*, 2020), and their effect on the structural performance of cold-formed hollow section structures has been investigated (Cruise and Gardner, 2008; Fang *et al.*, 2018b; Ma *et al.*, 2016b). The bending residual stresses were considered to be released when the coupons were extracted from the cold-formed hollow section structures, and made the coupon slightly curved. However, during the subsequent tensile coupon test, the bending residual stresses were reintroduced, and the coupon returned to its flat state under the tensile load. Therefore, the effect of bending residual stress can be regarded as being inherently incorporated into the measured stress-strain relationships of the materials (Rasmussen KJR, 1993).

Although the effect of longitudinal membrane residual stresses on the cold-formed SHS, RHS and CHS long columns were verified as negligible, their effect on the cold-formed OctHS long columns still needs to be re-examined. It is noteworthy that the

residual stress patterns are directly dependent on the fabrication routes. Hence, a longitudinal membrane residual stresses distribution obtained from Zhu *et al.* (2019) for the S355 cold-formed OctHS column was explicitly assigned into the separate FEM to examine its effect on the structural performance of OctHS long columns. The assigned residual stress distribution on the modelled specimens is shown in Figure 5.15, where the portion in red denotes the tensile residual stress caused by the cooling of the welding seam.

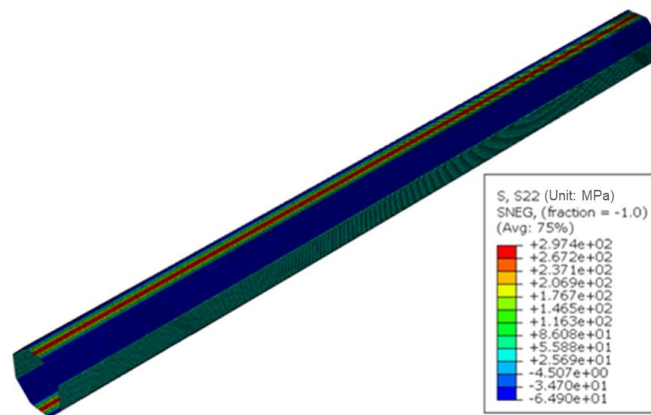


Figure 5.15 The assigned residual stress distribution on the modelled specimen.

It is worth noting that the column lengths were varied to study the effect of longitudinal membrane residual stress on columns with different member slenderness. The comparison between the maximum loads obtained from the models with longitudinal membrane residual stresses incorporated N_{RS} and without considering those residual stresses $N_{W/ORS}$ is presented in Figure 5.16. The differences were all less than 1%, revealing the negligible effect of longitudinal membrane residual stresses on cold-formed OctHS columns.

Typical axial load versus mid-height lateral deflection curves obtained from experiments and FEM are compared in Figure 5.17 and Figure 5.18. The N_{FEM} to N_{Test} ratios are listed in Table 5.6 and Table 5.7, in which numerical results of FEM adopted different global imperfection values are also presented.

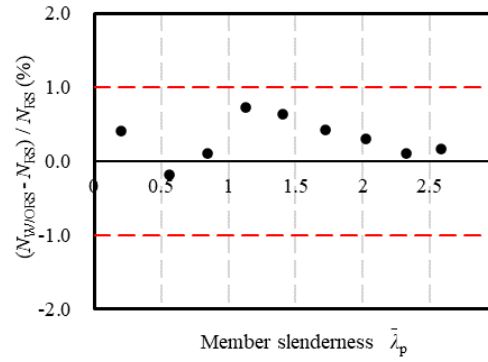
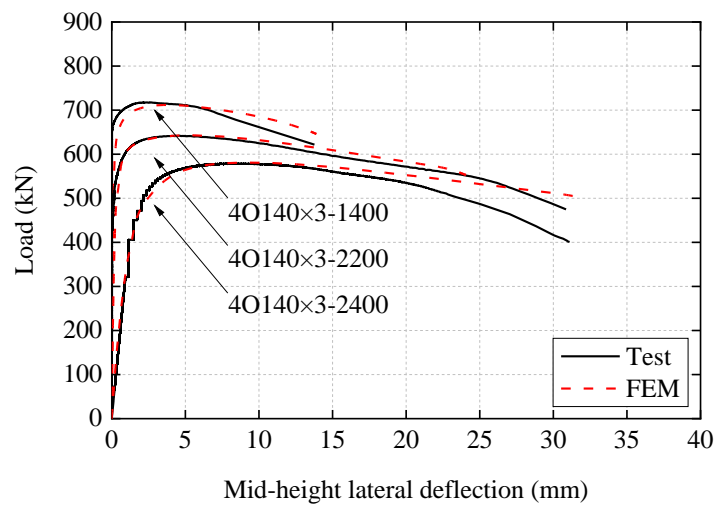
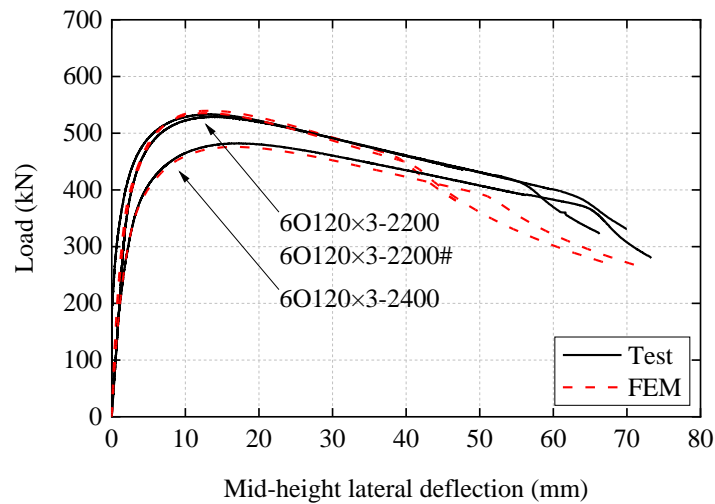


Figure 5.16 The effect of membrane residual stress on the load-bearing capacities.

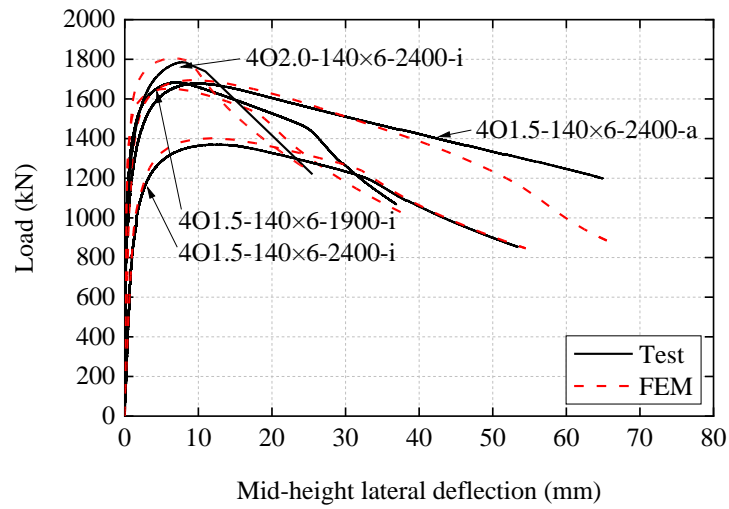


(a) 4O140×3 cross-section

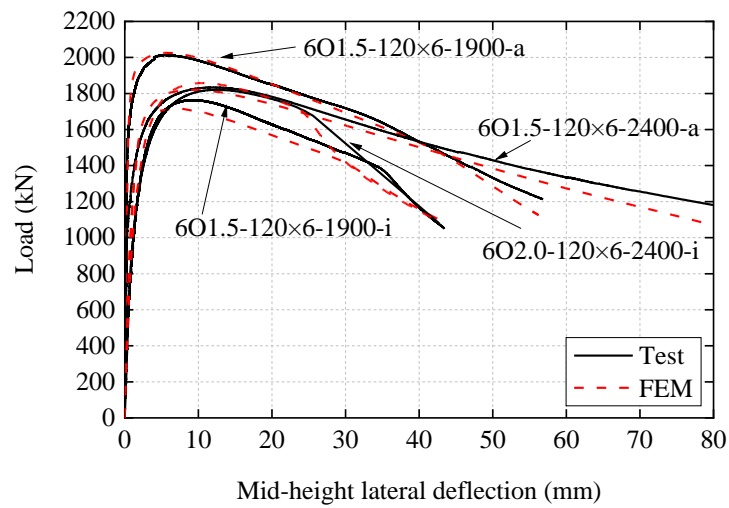


(b) 6O120×3 cross-section

Figure 5.17 Comparisons of experimental and numerical load–mid–height lateral deflection curves of regular OctHS specimens.



(a) Q460 irregular OctHS columns



(b) Q690 irregular OctHS columns

Figure 5.18 Comparisons of experimental and numerical load–mid–height lateral deflection curves of irregular OctHS specimens.

Table 5.6 Comparisons between different global imperfection for regular OctHSs.

Specimens	N_{Test}	N_{FEM}/N_{Test}			
	kN	Measured	$L/500$	$L/1000$	$L/1500$
4O140×3–1400	718	0.99	0.94	0.97	0.98
4O140×3–2200	642	1.00	0.88	0.94	0.96
4O140×3–2400	579	1.00	0.92	0.99	1.01
4O170×3–2100	761	1.05	1.01	1.06	1.07
4O170×3–2100#	756	1.05	1.01	1.06	1.08
6O120×3–2200	529	1.02	0.95	1.03	1.06
6O120×3–2200#	534	1.00	0.92	1.00	1.03
6O120×3–2400	482	0.99	0.91	0.98	1.01
6O140×3–2200	760	0.97	0.86	0.93	0.95
6O140×3–2400	620	1.09	0.98	1.06	1.09
	Mean:	1.02	0.94	1.00	1.02

Table 5.7 Comparisons between different global imperfection for irregular OctHSs.

Specimens	N_{Test}	N_{FEM}/N_{Test}			
	kN	Measured	$L/500$	$L/1000$	$L/1500$
4O1.5–140×6–1500–i	1854	0.97	0.87	0.93	1.0
4O1.5–140×6–1900–i	1684	0.98	0.88	0.94	1.0
4O1.5–140×6–2400–i	1370	1.02	0.96	1.02	1.1
4O1.5–140×6–1900–a	1757	1.03	0.96	1.02	1.0
4O1.5–140×6–2400–a	1678	1.01	0.94	1.00	1.0
4O2.0–140×6–2400–i	1785	1.01	0.91	0.97	1.0
6O1.5–120×6–1900–i	1764	0.97	0.90	0.96	1.0
6O1.5–120×6–2400–i	1346	1.05	0.98	1.04	1.1
6O1.5–120×6–1900–a	2014	1.01	0.93	0.99	1.0
6O1.5–120×6–2400–a	1834	0.99	0.92	0.98	1.0
6O2.0–120×6–2200–i	1884	1.05	1.01	1.07	1.1
6O2.0–120×6–2400–i	1821	1.02	0.93	0.99	1.0
	Mean:	1.01	0.93	0.99	1.02

The comparisons of the typical failure modes for global buckling and local deformation are shown in Figure 5.19, Figure 5.20, Figure 5.21, and Figure 5.22 for regular and irregular OctHS columns, respectively. As can be found from these figures and tables, the proposed FEM can satisfactorily replicate the structural behaviour of cold-formed OctHS long columns, regarding their ultimate capacities, axial load–lateral deflection relationships, and failure modes.

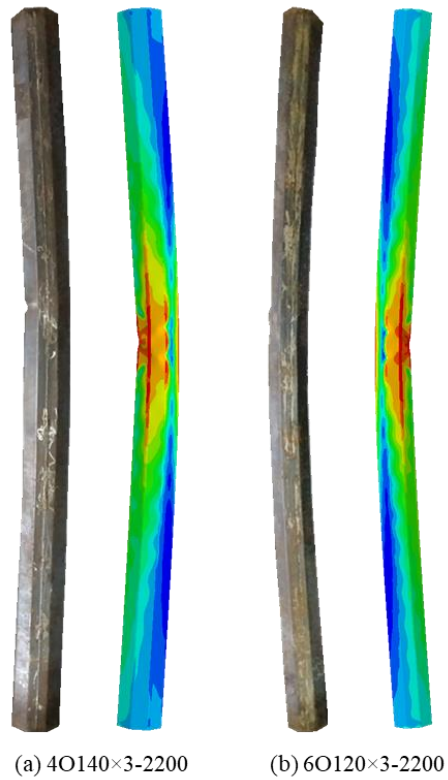


Figure 5.19 Comparisons of global flexural buckling failure mode of regular OctHS column specimens.

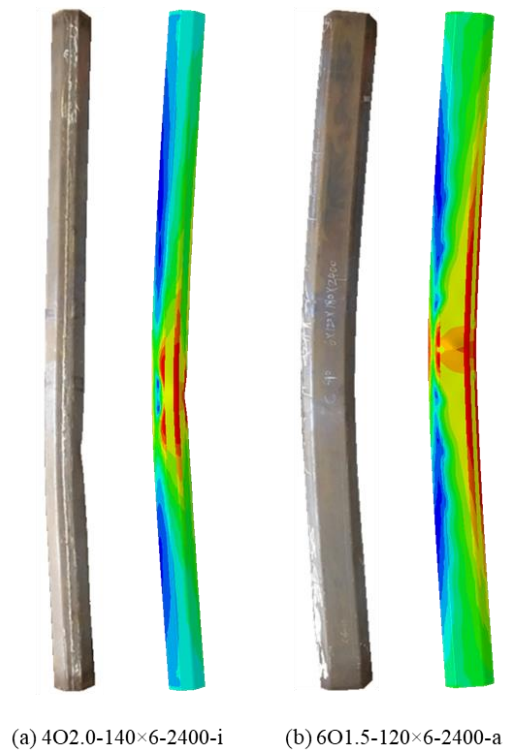


Figure 5.20 Comparisons of global flexural buckling failure mode of irregular OctHS column specimens.

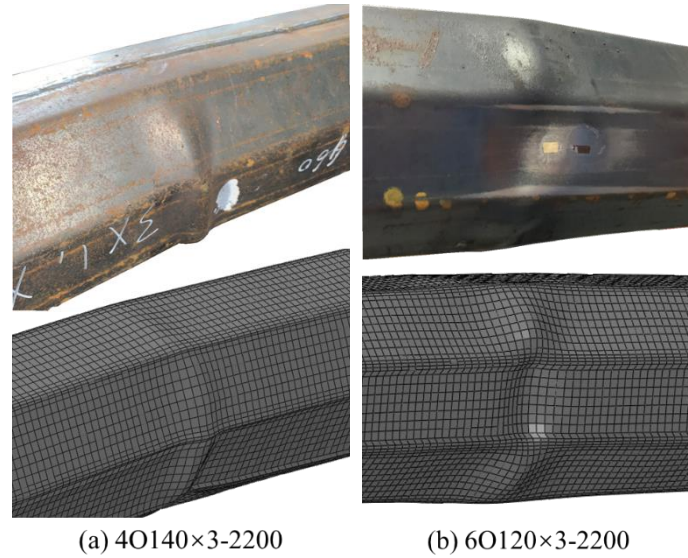


Figure 5.21 Comparison of local deformation failure mode for regular OctHS columns.

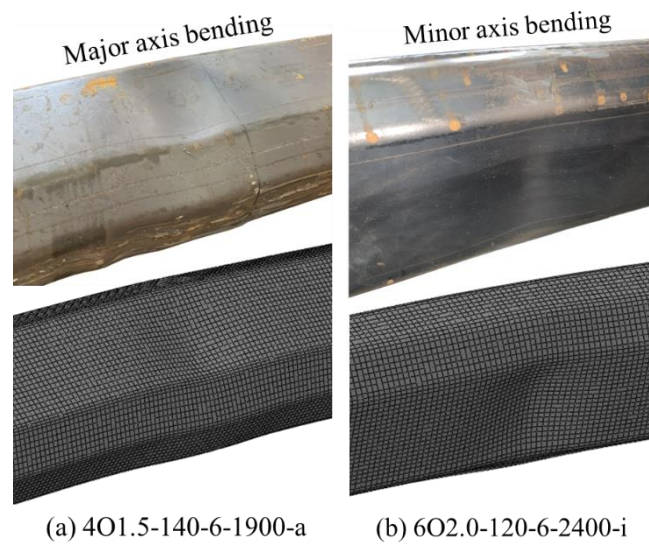


Figure 5.22 Comparison of local deformation failure mode for irregular OctHS columns.

5.3.2 Parametric study

Having proved the suitability of the proposed FEM and to investigate the structural behaviour of cold-formed OctHS columns under concentric compression, parametric studies were performed on the structures with a wider range of steel grades, cross-

sectional sizes, and non-dimensional slenderness. In total, additional 608 numerical models for regular OctHS columns and 539 numerical models for irregular OctHS columns were established.

In the parametric study, a total of 5 different steel grades from normal to high strengths including 275 MPa, 355 MPa, 460 MPa, 550 MPa, and 690 MPa were covered. The stress–strain responses of flat materials in flat regions were the same as those adopted in Chapter 4.3.3.2, while the material properties within the cold–formed corner region were slightly different, since different average r_i/t ratio of 1.7 was found for cold–formed OctHS as compared with the 1.0 value for RHS. Hence, the stress–strain responses of corner materials were regenerated based on the r_i/t ratio of 1.7. The determined key material parameters are listed in Table 5.8, and the representative stress–strain curves of 275 MPa, 460 MPa, and 690 MPa grade steels are shown in Figure 5.23.

Table 5.8 Input material properties adopted in the parametric study.

Steel grade MPa	Flat materials					Corner materials				
	E_t GPa	$f_{y,f}$ MPa	$f_{u,f}$ MPa	$\varepsilon_{sh,f}$ %	$\varepsilon_{u,f}$ %	E_c GPa	$f_{0.05,c}$ MPa	$f_{y,c}$ MPa	$f_{u,c}$ %	$\varepsilon_{u,c}$ %
275	210	275	390	1.55	17.69	198	335	405	454	1.94
355	210	355	490	1.74	16.53	198	425	514	573	1.89
460	210	460	540	3.00	8.89	198	480	574	631	1.65
550	210	550	600	3.00	6.00	198	528	630	687	1.56
690	210	690	770	3.00	6.23	198	680	813	888	1.59

For regular OctHS columns, four types of non-slender cross-section profiles – 160×3 , 160×5 , 250×6 , and 250×10 , were examined in the parametric study. In terms of irregular OctHS columns, the section width W and thickness t were fixed as 120 mm and 6 mm, but the aspect ratios (H/W) were varied from 1.25 to 2.00 (1.25, 1.50, 1.75, and 2.00). With the steel grades varied to achieve a range of cross-sectional slenderness, cross-sections of irregular OctHS columns considered in the parametric study can be

classified as non-slender and slender cross-sections. An outer corner radius R_o of $3t$ was adopted based on the statistical evaluation of the cold-formed OctHS specimens in this study. The column lengths L investigated herein were varied to obtain non-dimensional slenderness $\bar{\lambda}$ ranging from 0.12 to 2.77. The obtained numerical results combined with experimental results were used for further analysis in the following section.

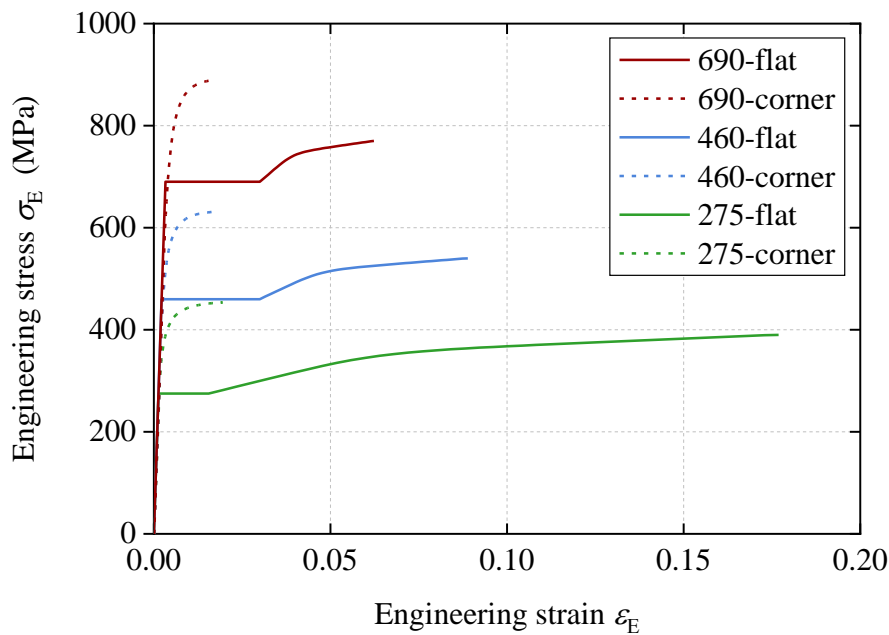


Figure 5.23 Representative stress–strain curves of input materials.

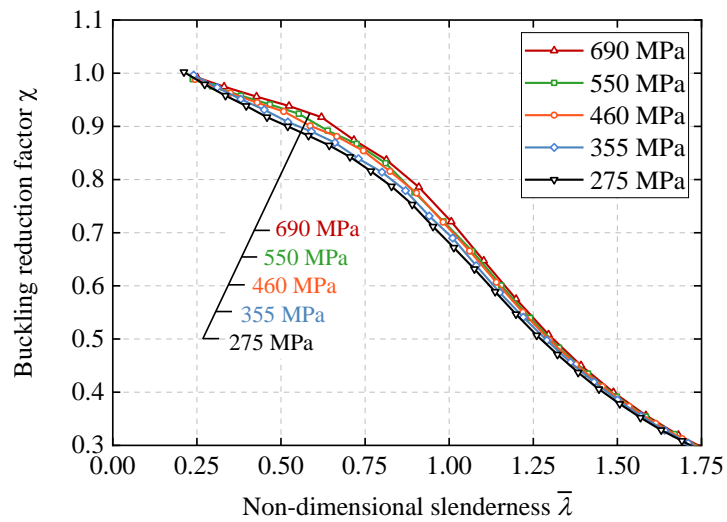
5.4 Analysis of results and design of OctHS long columns

5.4.1 Analysis of numerical results

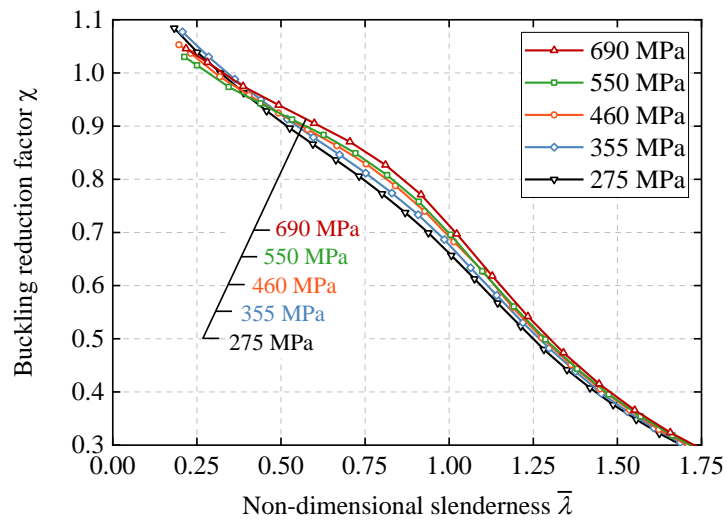
5.4.1.1 Effect of the steel grade

The effect of input material properties on the column buckling strengths of OctHS columns was studied in this section. For regular OctHS columns, the modelled columns which extruded from cross-sections 160×3 and 250×10 were selected for comparison. In terms of irregular OctHS columns, the modelled columns which extruded from

cross-section $O1.5-120 \times 6$ bending about their major and minor axes were also selected for comparison. For these selected columns, their ultimate strengths were normalised by the cross-section resistance and were further plotted against the non-dimensional slenderness in Figure 5.24 and Figure 5.25.



(a) 160×3 cross-section



(b) 250×10 cross-section

Figure 5.24 Effects of steel grades on the strengths of regular OctHS columns.

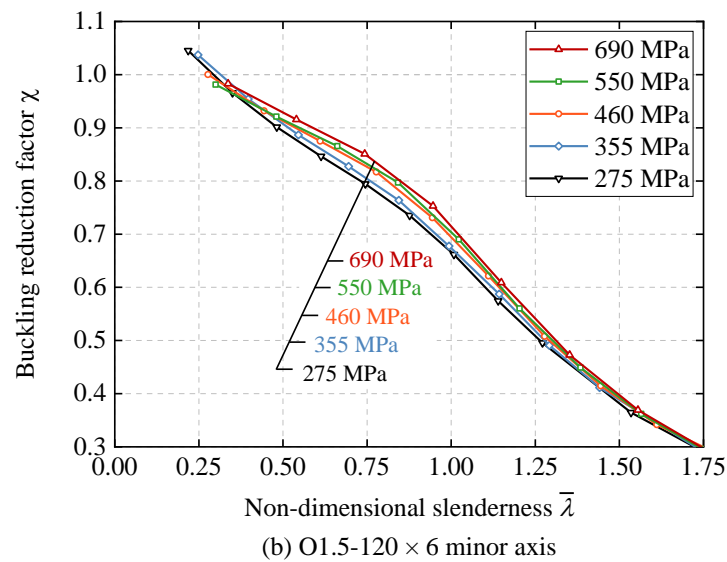
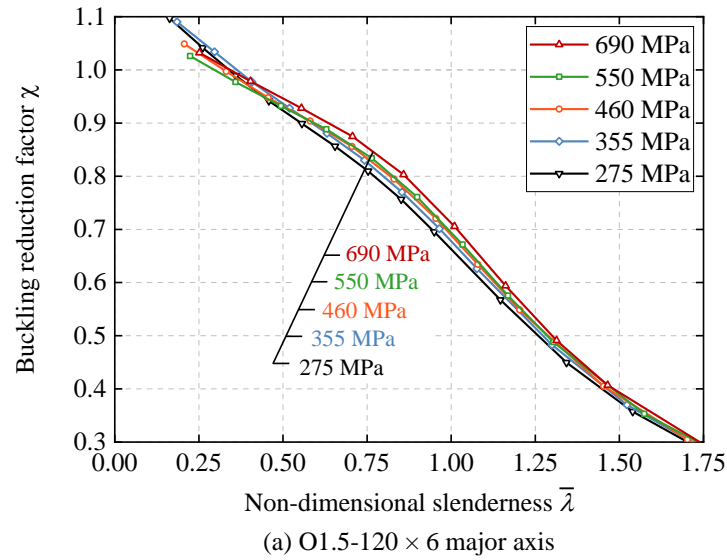
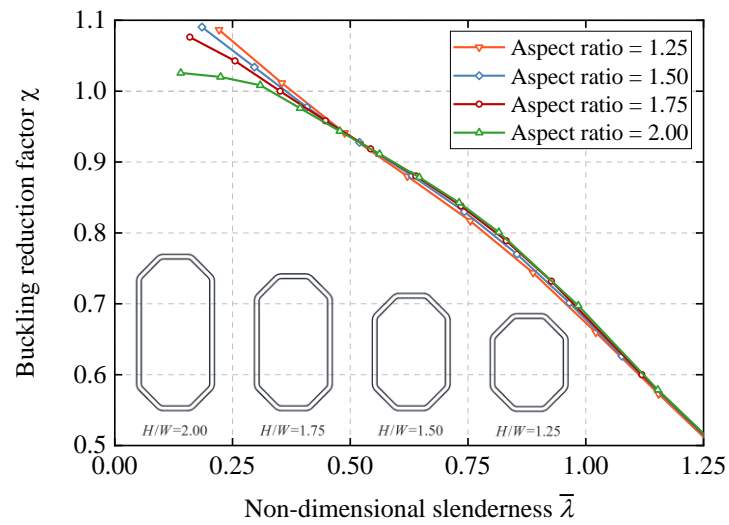


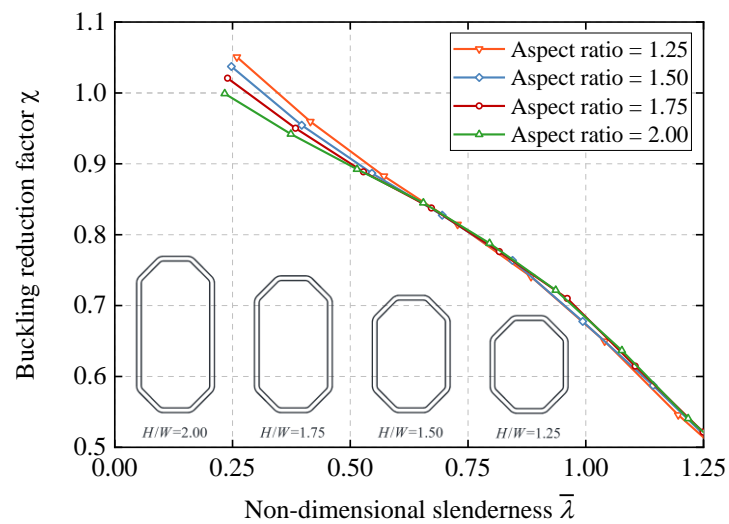
Figure 5.25 Effects of steel grades on the strengths of irregular OctHS columns.

In these figures, it can be clearly found that the buckling reduction factors χ increase with the increase of steel grade under the same non-dimensional slenderness. The increment of buckling reduction factor χ is somewhat related to the non-dimensional slenderness, and the increment is higher for the modelled columns with the non-dimensional slenderness between 0.5 to 1.0, similar to the findings observed in Fang *et al.* (2018b) and Meng *et al.* (2020a) for RHSs and CHSs.

5.4.1.2 Effect of the aspect ratio



(a) 355 MPa - major axis



(b) 355 MPa - minor axis

Figure 5.26 Effects of aspect ratios (H/W) on the strengths of irregular OctHS columns.

The effect of cross-section aspect ratio (H/W) on the column buckling strengths of irregular OctHS columns was investigated in this section. For this purpose, part of the modelled irregular OctHS columns with steel grade of 355 MPa was selected. The section width and thickness of these columns were fixed as 120 mm and 6 mm, with the section height varying with the change of aspect ratio. Also, the obtained ultimate

strengths of these columns were normalised by corresponding cross-section resistances and plotted against the non-dimensional slenderness in Figure 5.26.

As can be found from the figure, the effect of aspect ratio is similar for modelled columns bending about their major and minor axes. In the range of low slenderness between 0.2 to 0.5, higher normalised column strengths can be acquired with smaller aspect ratios, which may be attributed to the facts that the local buckling behaviour is not that severer in a shorter plate element (smaller aspect ratio) than that in a longer plate element (higher aspect ratio), and the column strengths are more dependent on the strain hardening effect of materials in the low member slenderness. When member slenderness increasing from 0.5 to a higher value, the effect of aspect ratio is not obvious.

5.4.2 Cross-section classifications of the OctHS

Cross-section classification is a crucial step in the design of structural members under compression. Local buckling occurred in the plate elements may deteriorate the overall cross-sectional resistance. To compute the reduction in compressive resistance for slender cross-sections, the effective width method is given that considers the ineffective area of plated structures which suffer from local buckling and do not bear loadings anymore. After excluding the ineffective area of a Class 4 section, the remaining area is regarded as effective enough to develop their plastic resistance, while the effective area A_{eff} can be computed by $A_{\text{eff}} = \rho \times A$, in which ρ is the reduction factor and can be calculated according to Eq. (5.4) to Eq. (5.6) from Eurocode 3 and ANSI/AISC 360-16, respectively.

$$\rho_{\text{EWM}} = \begin{cases} 1 & \text{for } \bar{\lambda}_p \leq 0.673 \\ (1 - 0.22 / \bar{\lambda}_p) / \lambda_p & \text{for } \bar{\lambda}_p > 0.673 \end{cases}$$

Eq. (5.4)

$$\bar{\lambda}_p = \sqrt{f_y / f_{cr}} \quad \text{Eq. (5.5)}$$

$$f_{cr} = k \frac{\pi^2 E_s}{12(1-\nu^2)} \left(\frac{t}{b} \right)^2 \quad \text{Eq. (5.6)}$$

However, this cross-section classification limit was originally designed for RHSs and SHSs, and it was observed from Zhu *et al.* (2017), Fang *et al.* (2019), and Chen *et al.* (2020) that this cross-section classification limit was not suitable for the design of OctHSs. Hence, Chen *et al.* (2021) proposed a new cross-section classification limit for OctHSs based on collected experimental results and generated numerical results. The new plate slenderness was tightened from 0.673 to 0.585, since the 135° corners existed in OctHS tend to provide weaker restraint to their adjacent plate elements as compared with the restraint provided by 90° angles. The original effective width method was subsequently modified in line with the new proposed plate slenderness limit, as expressed in Eq. (5.7).

$$\rho_{EWM, \text{OctHS}} = \begin{cases} 1 & \text{for } \bar{\lambda}_p \leq 0.585 \\ \left(1.05 - 0.272 / \bar{\lambda}_p\right) / \bar{\lambda}_p & \text{for } \bar{\lambda}_p > 0.585 \end{cases} \quad \text{Eq. (5.7)}$$

It is worth noting that Eq. (5.7) was eventually adopted in the effective design of OctHS members with slender cross-sections in the following session.

5.4.3 Column buckling strengths of the OctHS

The column buckling strengths of OctHS members were assessed through the same design methods described in Chapter 4.3.4, but with one additional design codes ASCE/SEI 48–19 (2019) being evaluated, in which provides a design expression for regular OctHSs. For this purpose, the obtained ultimate strengths from experimental and numerical results are normalised and plotted against the non-dimensional

slenderness in Figure 5.27 and Figure 5.28, while the column buckling curves from different standards are also depicted in the same figure for comparison. The assessment results and design recommendations were presented in the following sections.

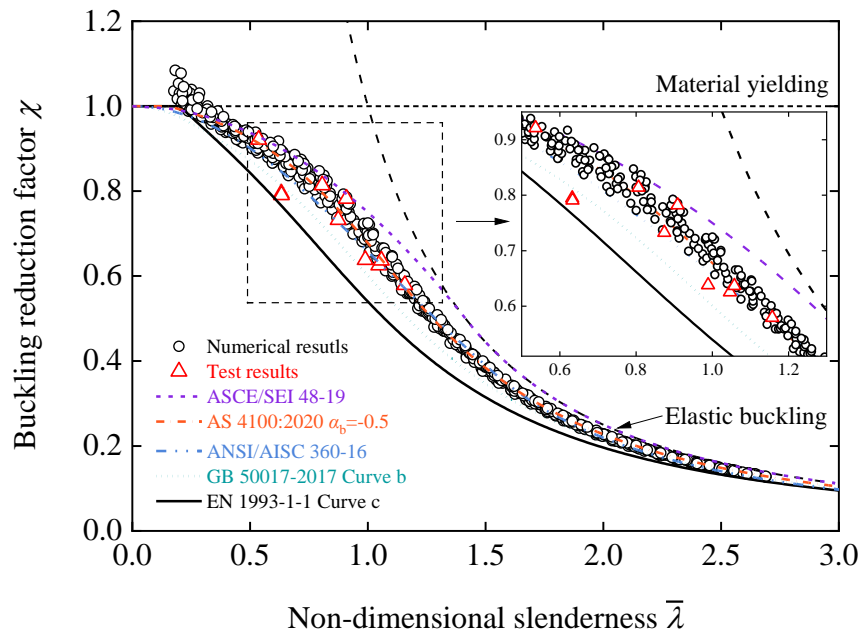


Figure 5.27 Comparisons of experimental and numerical results with codified design curves for regular OctHS columns.

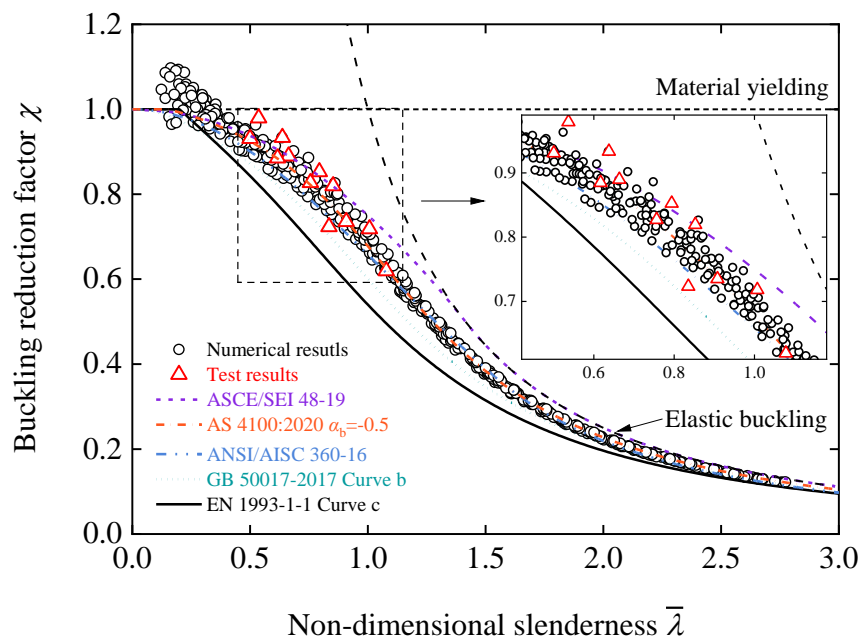


Figure 5.28 Comparisons of experimental and numerical results with codified design curves for irregular OctHS columns.

5.4.3.1 Eurocode 3 design method

Eurocode 3 adopts multi-column buckling curves for the flexural buckling design of non-slender cross-section columns, while for their slender counterparts prone to the global-local interactive buckling, special attention should be paid to adopt the effective cross-sectional geometric properties in the design process. The gross cross-sectional area A should be replaced by the effective cross-sectional area A_{eff} , which can be obtained through the modified effective width method (Eq. (5.7)) for OctHSs. It is worth noting that since OctHS is a biaxially symmetric cross-section, the neutral axis of the effective cross-section is coincided with that of the full cross-section. Therefore, no additional consideration needs to be paid to account for effects caused by the shift of neutral axis. For the flexural buckling design of OctHS columns in Eurocode 3, the design column flexural buckling capacity can be computed by the following expressions:

$$N_{\text{EC3}} = \begin{cases} \chi_{\text{EC3}} A f_y & \text{for non-slender cross-sections} \\ \chi_{\text{EC3}} A_{\text{eff}} f_y & \text{for slender cross-sections} \end{cases} \quad \text{Eq. (5.8)}$$

$$\chi_{\text{EC3}} = \frac{1}{\Phi + \sqrt{\Phi^2 - \bar{\lambda}^2}} \quad \text{Eq. (5.9)}$$

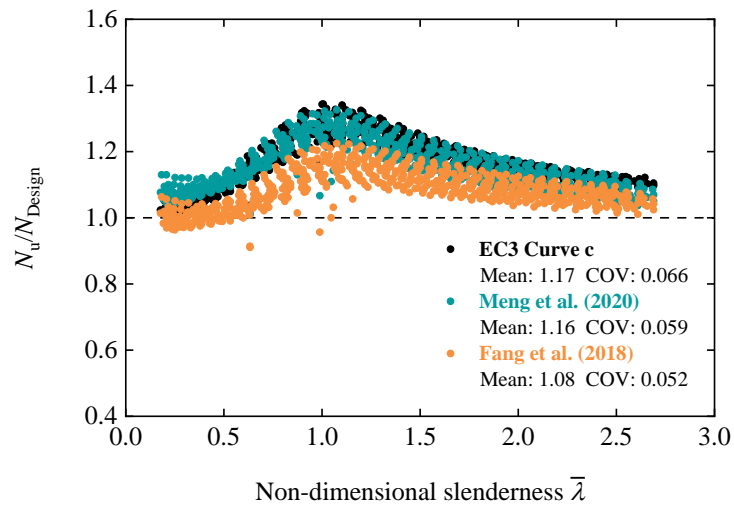
$$\Phi = 0.5 \left[1 + \eta + \bar{\lambda}^2 \right] \quad \text{Eq. (5.10)}$$

$$\eta = \alpha(\bar{\lambda} - 0.2) \quad \text{Eq. (5.11)}$$

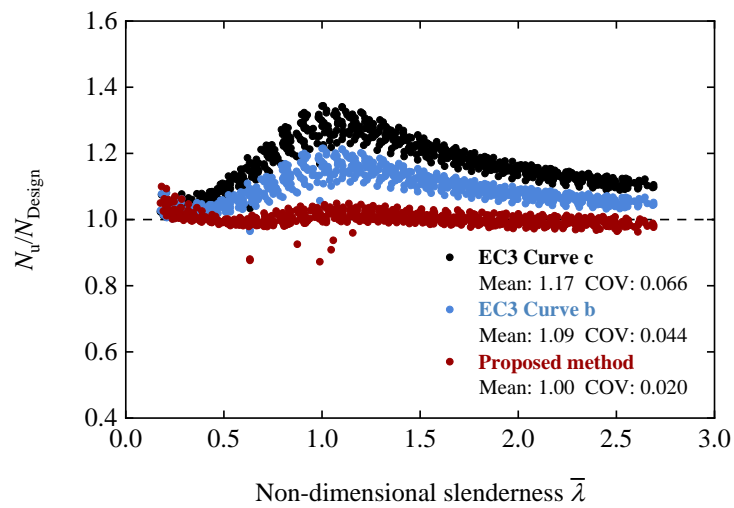
$$\bar{\lambda} = \begin{cases} \sqrt{\frac{A f_y}{N_{\text{cr}}}} & \text{for non-slender cross-sections} \\ \sqrt{\frac{A_{\text{eff}} f_y}{N_{\text{cr}}}} & \text{for slender cross-sections} \end{cases} \quad \text{Eq. (5.12)}$$

where A and A_{eff} represent the gross cross-sectional area for non-slender sections and

the effective cross-sectional area for slender sections, respectively.



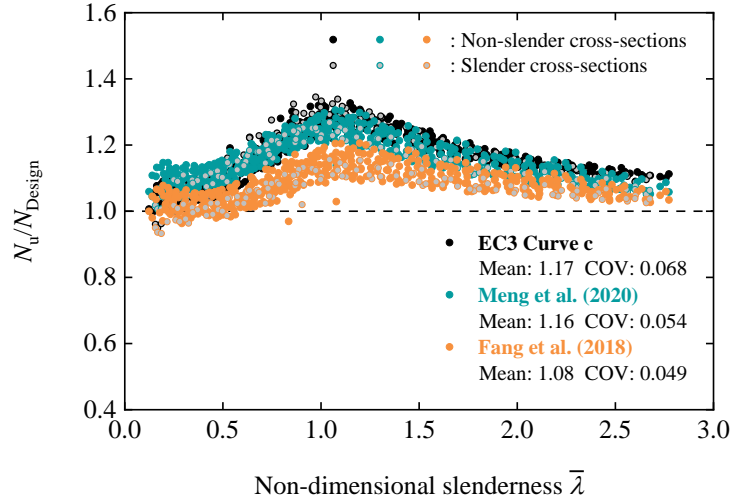
(a) EC3 and modified EC3 methods



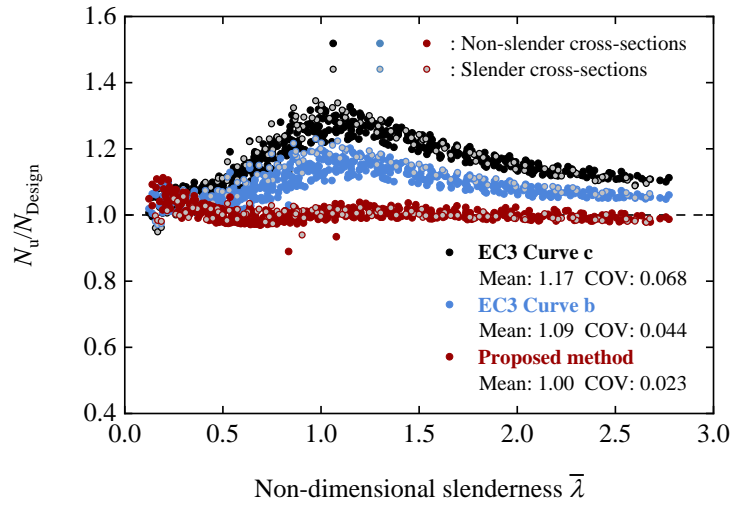
(b) EC3 and proposed method

Figure 5.29 Comparisons of experimental and numerical results with design values from different methods for regular OctHS columns.

The ultimate strengths N_u from experimental and numerical tests were derived and compared to the design values calculated based on the original Eurocode 3 method and modified Eurocode 3 methods proposed by Fang *et al.* (2018b) and Meng and Gardner (2020a). The normalised N_u to design values from different design methods N_{Design} are plotted in Figure 5.29 and Figure 5.30, and the assessment results of different design methods are reported in Table 5.9.



(a) EC3 and modified EC3 methods



(b) EC3 and proposed method

Figure 5.30 Comparisons of experimental and numerical results with design values from different methods for irregular OctHS columns.

To further improve the design accuracy of Eurocode 3, a modification was proposed for the imperfection item η , while the modified expression for η is shown in Eq. (5.13).

$$\eta_{\text{mod}} = 0.23(\bar{\lambda}\sqrt{235/f_y} - 0.1) \quad \text{Eq. (5.13)}$$

in which a smaller imperfection factor α is recommended to be adopted and a shorter plateau of 0.1 is suggested. The normalised N_u to N_{Design} values for the proposed

methods are also plotted in Figure 5.29 and Figure 5.30, while the mean values and COV of N_u/N_{Design} are 1.00 and 1.00, and 0.020 and 0.023 for regular and irregular OctHS columns, respectively. Based on the proposed modification to imperfection item η , the flexural buckling capacity of OctHS columns can be accurately predicted with satisfied consistency.

Table 5.9 Assessments of different design methods.

Design methods	Regular OctHSs		Irregular OctHSs	
	N_u/N_{Design}	COV	N_u/N_{Design}	COV
EC3 curve c	1.17	0.066	1.17	0.068
EC3 curve b	1.09	0.044	1.09	0.044
Meng <i>et al.</i> (2020)	1.16	0.059	1.16	0.054
Fang <i>et al.</i> (2018)	1.08	0.052	1.08	0.049
Proposed method	1.00	0.020	1.00	0.023
GB 50017–2017 curve b	1.09	0.040	1.09	0.038
GB 50017–2017 curve a	1.00	0.023	1.00	0.028
ANSI/AISC 360–16	1.03	0.028	1.03	0.030
ASCE/SEI 48–19	0.92	0.057	0.93	0.066
AS 4100:2020	1.02	0.022	1.03	0.025

5.4.3.2 Chinese standards GB 50017–2017

Differently, for the design of flexural buckling of columns with the slender cross-section, GB 50017–2017 does not consider the effective cross-sectional area in the determination of non-dimensional slenderness. The flexural buckling capacity of columns can be computed by the following expressions:

$$N_{GB\ 50017} = \begin{cases} \chi_{GB\ 50017} A f_y & \text{for non-slender cross-sections} \\ \chi_{GB\ 50017} A_{eff} f_y & \text{for slender cross-sections} \end{cases} \quad \text{Eq. (5.14)}$$

$$\chi_{GB\ 50017} = \begin{cases} 1 - \alpha_1 \bar{\lambda}^2 & \text{for } \bar{\lambda} \leq 0.215 \\ \frac{1}{2\bar{\lambda}^2} \left[\left(\alpha_2 + \alpha_3 \bar{\lambda} + \bar{\lambda}^2 \right) - \sqrt{\left(\alpha_2 + \alpha_3 \bar{\lambda} + \bar{\lambda}^2 \right)^2 - 4\bar{\lambda}^2} \right] & \text{for } \bar{\lambda} > 0.215 \end{cases} \quad \text{Eq. (5.15)}$$

$$\bar{\lambda} = \sqrt{\frac{Af_y}{N_{cr}}} \text{ for non-slender and slender cross-sections} \quad \text{Eq. (5.16)}$$

To assess the applicability of GB 50017–2017 on OctHS columns, the ultimate strengths N_u from experimental and numerical tests were derived and compared to the design values calculated based on GB buckling curve ‘b’ ($\alpha_1 = 0.650$, $\alpha_2 = 0.965$, and $\alpha_3 = 0.300$) and ‘a’ ($\alpha_1 = 0.410$, $\alpha_2 = 0.986$, and $\alpha_3 = 0.152$). The normalised N_u/N_{Design} values are plotted in Figure 5.31 and Figure 5.32, and the comparison results are reported in Table 5.9. The comparison results show that the selection of curve ‘a’ can provide the most accurate prediction accuracy for OctHS columns. Hence, the buckling curve ‘a’ with $\alpha_1 = 0.410$, $\alpha_2 = 0.986$, and $\alpha_3 = 0.152$ in GB 50017–2017 is suggested to be adopted for the prediction of flexural buckling strength of OctHS columns.

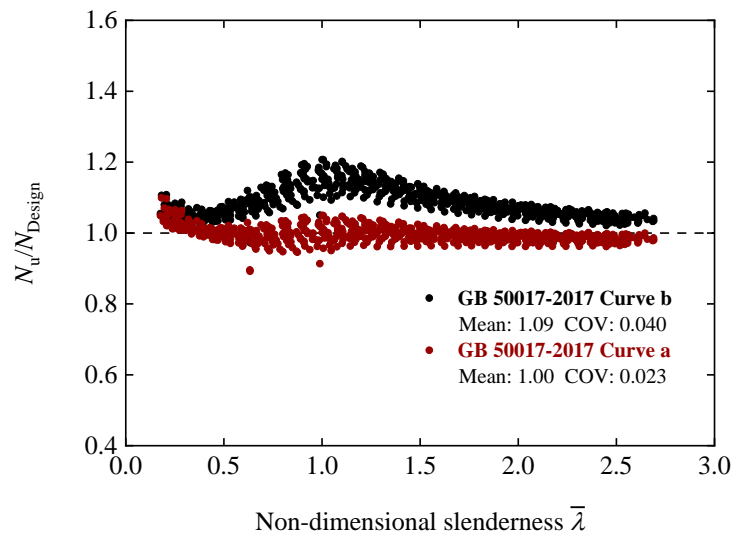


Figure 5.31 Comparisons of experimental and numerical results with design values from GB 50017–2017 for regular OctHS.

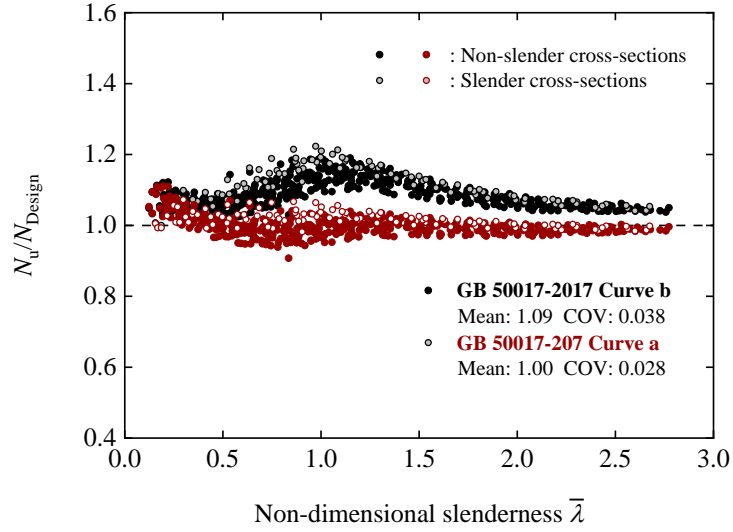


Figure 5.32 Comparisons of experimental and numerical results with design values from GB 50017–2017 for irregular OctHS columns.

5.4.3.3 American specifications

In ANSI/AISC 360–16, the flexural buckling capacity of non–slender cross–sections can be obtained through Eq. (5.17) to Eq. (5.19). When the cross–section contains slender plate elements, a unified effective width method is adopted to account for the potential reduction in flexural buckling capacity due to global–local interactive buckling. The effective width method generalised for global–local interactive buckling proposed by Peköz (1986) was modified in this thesis based on the modified effective width method for OctHSs (Eq. (5.7)), as expressed in Eq. (5.19).

$$N_{ANSI/AISC\ 360} = \begin{cases} \chi_{ANSI/AISC\ 360} A f_y & \text{for non-slender cross-sections} \\ \chi_{ANSI/AISC\ 360} A_{eff} f_y & \text{for slender cross-sections} \end{cases} \quad \text{Eq. (5.17)}$$

$$\chi_{ANSI/AISC\ 360} = \begin{cases} 0.658 \bar{\lambda}^2 & \text{for } \bar{\lambda} \leq 1.5 \\ \frac{0.877}{\bar{\lambda}^2} & \text{for } \bar{\lambda} > 1.5 \end{cases} \quad \text{Eq. (5.18)}$$

$$\rho = \begin{cases} 1 & \text{for } \bar{\lambda}_p \leq 0.585 \sqrt{\frac{1}{\chi_{\text{ANSI/AISC 360}}}} \\ \frac{1.05}{\bar{\lambda}_p \sqrt{\chi_{\text{ANSI/AISC 360}}}} - \frac{0.272}{\left(\bar{\lambda}_p \sqrt{\chi_{\text{ANSI/AISC 360}}}\right)^2} & \text{for } \bar{\lambda}_p > 0.585 \sqrt{\frac{1}{\chi_{\text{ANSI/AISC 360}}}} \end{cases} \quad \text{Eq. (5.19)}$$

This indicates that columns which contain slender plate elements may not necessarily need to have any reduction in column strength due to the local buckling, and the point at which the slender plate element begins to influence column strength is determined by a continuous function (Eq. (5.19)) of the cross-section slenderness and member slenderness. In other words, the effect of plate local buckling decreases with the increase of column slenderness, and vice versa.

ASCE/SEI 48–19 column strength prediction expression adopts a similar design concept to that in ANSI/AISC 360–16. To make a direct comparison, the design expressions of ASCE/SEI 48–19 were generalised and expressed as Eq. (5.20) to Eq. (5.21), conforming to the format of ANSI/AISC 360–16. It should be noted that the reduction of cross-section resistances due to local buckling in ASCE/SEI 48–19 was also determined in accordance with Eq. (5.19).

$$N_{\text{ASCE/SEI 48}} = \begin{cases} \chi_{\text{ASCE/SEI 48}} A f_y & \text{for non-slender cross-sections} \\ \chi_{\text{ASCE/SEI 48}} A_{\text{eff}} f_y & \text{for slender cross-sections} \end{cases} \quad \text{Eq. (5.20)}$$

$$\chi_{\text{ASCE/SEI 48}} = \begin{cases} 1 - \frac{\bar{\lambda}^2}{4} & \text{for } \bar{\lambda} \leq \sqrt{2} \\ \frac{1}{\bar{\lambda}^2} & \text{for } \bar{\lambda} > \sqrt{2} \end{cases} \quad \text{Eq. (5.21)}$$

The ultimate strengths N_u from experimental and numerical tests were derived and compared to the design values calculated based on ANSI/AISC 360–16 design method and ASCE/SEI 48–19 design method. The normalised N_u/N_{Design} values for regular and irregular OctHS columns are respectively plotted in Figure 5.33 and Figure 5.34, and

the comparison results are reported in Table 5.9.

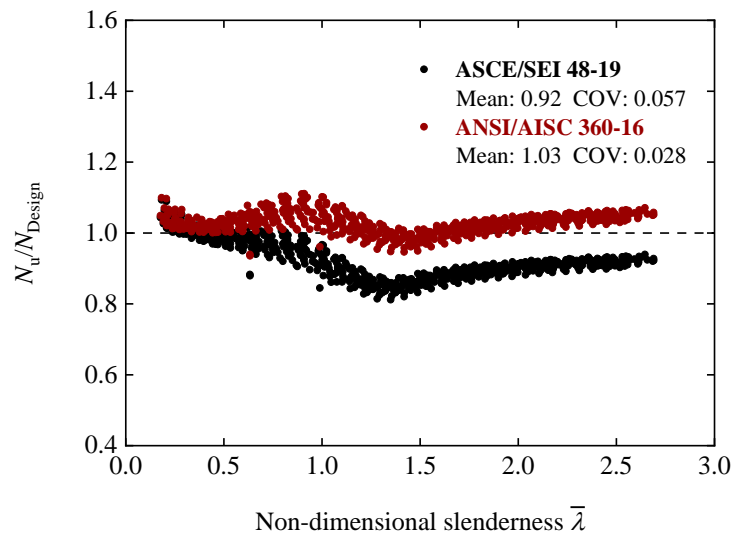


Figure 5.33 Comparisons of experimental and numerical results with design values from American specifications for regular OctHS columns.

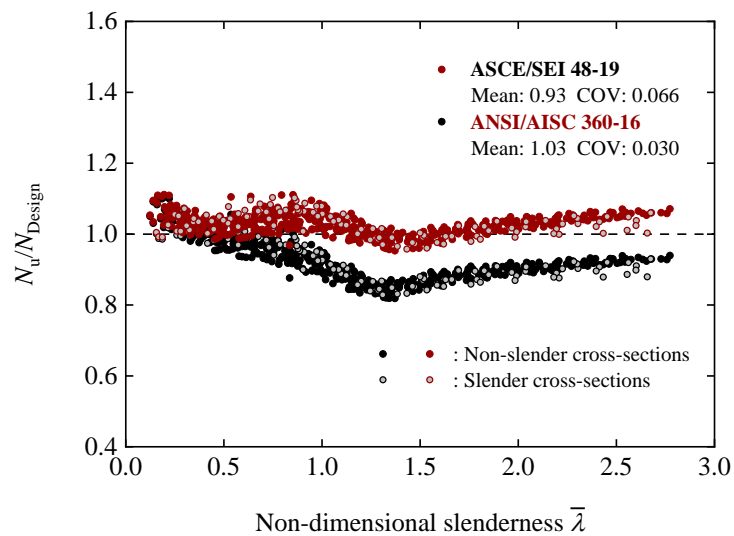


Figure 5.34 Comparisons of experimental and numerical results with design values from American specifications for irregular OctHS columns.

As can be observed in figures, ASCE/SEI 48–19 design method overestimates the strength for the majority of OctHS columns. It can be concluded that ANSI/AISC 360–16 design method can provide more accurate prediction results for both regular and irregular OctHS columns. And a design recommendation is suggested to correct the

overestimate problem of ASCE/SEI 48–19 design method by adopting the same design expressions from ANSI/AISC 360–16.

5.4.3.4 Australian standards AS 4100:2020

The member slenderness of AS 4100:2020 $\bar{\lambda}_{AS\ 4100}$ is slightly different from that adopted in the abovementioned design methods, and it equals to $\bar{\lambda}$ multiplied by a factor of $\pi(E_s/250)^{1/2}$, as given in Eq. (5.22). The design flexural buckling strength in AS 4100:2020 can be obtained through Eq. (5.23) to Eq. (5.26).

$$\bar{\lambda}_{AS\ 4100} = \begin{cases} \bar{\lambda} \left(\pi \sqrt{\frac{E_s}{250}} \right) & \text{for non-slender cross-sections} \\ \bar{\lambda} \left(\sqrt{\frac{A_{\text{eff}}}{A}} \pi \sqrt{\frac{E_s}{250}} \right) & \text{for slender cross-sections} \end{cases} \quad \text{Eq. (5.22)}$$

$$N_{AS\ 4100} = \begin{cases} \chi_{AS\ 4100} A f_y & \text{for non-slender cross-sections} \\ \chi_{AS\ 4100} A_{\text{eff}} f_y & \text{for slender cross-sections} \end{cases} \quad \text{Eq. (5.23)}$$

$$\chi_{AS\ 4100} = \zeta \left(1 - \sqrt{1 - \left[\frac{90}{\zeta (\bar{\lambda}_{AS\ 4100} + \alpha_a \alpha_b)} \right]^2} \right) \quad \text{Eq. (5.24)}$$

$$\alpha_a = \frac{2100 (\bar{\lambda}_{AS\ 4100} - 13.5)}{\bar{\lambda}_{AS\ 4100}^2 - 15.3 \bar{\lambda}_{AS\ 4100} + 2050} \quad \text{Eq. (5.25)}$$

$$\zeta = \frac{\left[(\bar{\lambda}_{AS\ 4100} + \alpha_a \alpha_b) / 90 \right]^2 + 1 + 0.00326 (\bar{\lambda}_{AS\ 4100} + \alpha_a \alpha_b - 13.5)}{2 \left[(\bar{\lambda}_{AS\ 4100} + \alpha_a \alpha_b) / 90 \right]^2} \quad \text{Eq. (5.26)}$$

in which α_a is the non-dimensional slenderness modifier, and α_b is the imperfection factor taken as -0.5 for cold-formed (non-stress relieved) RHSs and CHSs.

To assess the applicability of AS 4100:2020 on OctHS columns, the ultimate strengths N_u from experimental and numerical tests were derived and compared to the design values. The normalised N_u/N_{Design} values are plotted in Figure 5.35 and Figure

5.36, and the comparison results are reported in Table 5.9, while the mean values and COV of N_u/N_{Design} are 1.02 and 1.03, and 0.022 and 0.025 for regular and irregular OctHS columns, respectively. As can be found from the comparison result, the AS 4100:2020 design method gives slightly conservative but reasonably accurate predictions for the design of OctHS columns.

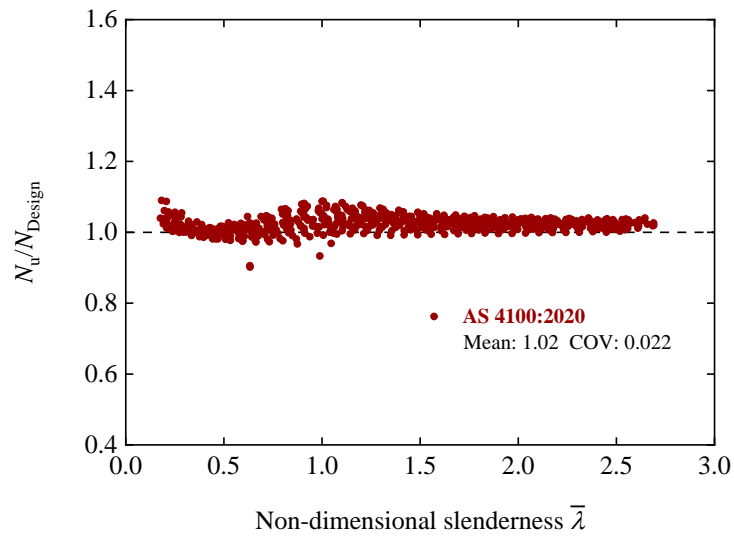


Figure 5.35 Comparisons of experimental and numerical results with design values from AS 4100:2020 for regular OctHS columns.

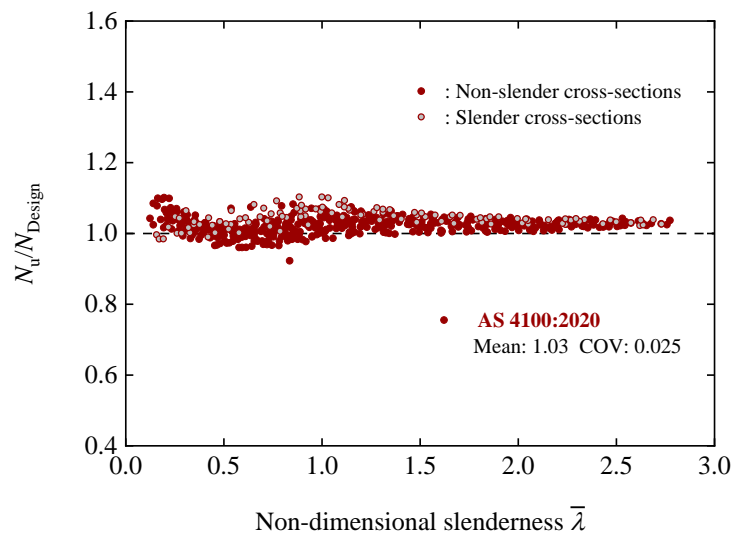


Figure 5.36 Comparisons of experimental and numerical results with design values from AS 4100:2020 for irregular OctHS columns.

5.5 Reliability analysis

The reliability of different design methods for OctHS columns under concentric compression was evaluated in line with the requirements stipulated in EN 1990 (CEN, 2002) and AISI S100–16 (AISI, 2016), following the similar procedures for press-braked RHS long column. Different statistical parameters adopted in the reliability analysis were described in the following sections.

5.5.1 EN 1990 method

A partial factor $\gamma_{M1} = 1.00$ was applied to the column buckling strength design formulas of Eurocode 3 to achieve the specified safety level. The basic parameters – Young’s modulus E , yield strength f_y , cross-sectional area A in the theoretical resistance model were varied and their variations can be taken into account through COV, V_E , V_{f_y} , and V_A , in accordance with the EN 1993–1–1:2022, as summarised in Table 4.13.

The column buckling strength design formula was converted as Eq. (5.27) to separate the dependency of basic variables E , f_y , and A (Law, 2010; Meng and Gardner, 2020a). The combined COV of the materials and geometric dimensions can thus be obtained through Eq. (5.28). For the case of a large number of tests ($n \geq 100$), the design resistance value r_d utilised to determine the partial factor γ_M may be obtained by Eq. (5.29). Finally, the partial factors γ_M^* of overall design model can be subsequently acquired by the least-squares best fit to each pair of r_n and r_d , as expressed in Eq. (5.30).

$$N_{b,R} = g_{rt} = KE_a^{k_1} f_y^{k_2} A^{k_3} \quad \text{Eq. (5.27)}$$

$$V_{rt} = \sqrt{(k_1 V_{E_a})^2 + (k_2 V_{f_y})^2 + (k_3 V_A)^2} \quad \text{Eq. (5.28)}$$

$$r_d = b g_{rt} (\underline{X}_m) \exp(-k_{d,\infty} Q - 0.5Q^2) \quad \text{Eq. (5.29)}$$

$$\gamma_M^* = \frac{\sum_{i=1}^n r_{n,i}^2}{\sum_{i=1}^n r_{n,i} r_{d,i}} \quad \text{Eq. (5.30)}$$

in which K is a constant, independent of the basic variables, and k_1 , k_2 , and k_3 are the coefficients computed for each specimen, varying with the member slenderness, as plotted in Figure 5.37 and Figure 5.38.

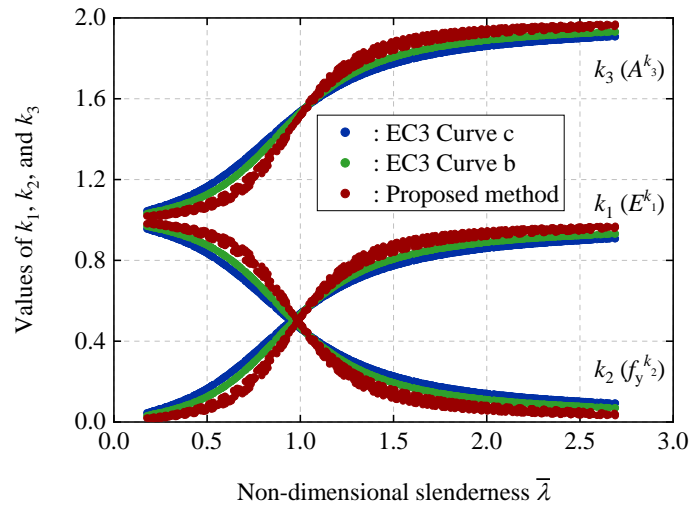


Figure 5.37 Values of $k_1 - k_3$ adopted in EN 1990 method for regular OctHS columns.

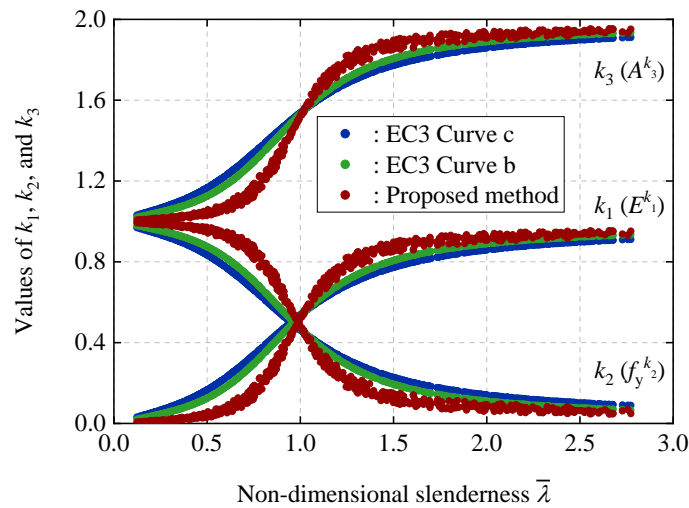


Figure 5.38 Values of $k_1 - k_3$ adopted in EN 1990 method for irregular OctHS columns.

The results of the reliability analysis are summarised in Table 5.10. γ_M^* for regular and irregular OctHS columns were estimated as close to the unity when adopting curve

‘b’ in the column buckling design, indicating that the current partial factor γ_{M1} of 1.00 can be safely incorporated into the theoretical resistance model if curve ‘b’ is adopted for the design of OctHS columns. However, according to the assessment results, a larger γ_M^* value of 1.10 is recommended to acquire the required level of safety if the proposed modified EC3 method incorporating Eq. (5.13) is adopted.

Table 5.10 Results of reliability analysis for different design methods.

Design methods	Regular OctHSs		Irregular OctHSs	
	γ_M^*	β	γ_M^*	β
EC3 curve c	0.954	–	0.955	–
EC3 curve b	1.023	–	1.020	–
Proposed method	1.110	–	1.104	–
GB 50017–2017 curve b	–	2.897	–	2.927
GB 50017–2017 curve a	–	2.532	–	2.553
ANSI/AISC 360–16	–	2.828	–	2.831
ASCE/SEI 48–19	–	2.279	–	2.305
AS 4100:2020	–	2.582	–	2.592

5.5.2 AISI S100 method

For the design methods of GB 50017–2017, ANSI/AISC 360–16, ASCE/SEI 48–19 and AS 4100:2020, the reliability analysis procedures conforming to the suggestions in AISI S100–16 (AISI, 2016) was employed to evaluate their reliability. A resistance factor $\phi = 0.9$ is specified in ANSI/AISC 360–16, ASCE/SEI 48–19 and AS 4100:2020 design methods. While for GB 50017–2017, it is worth noting that the resistance factor is implicitly incorporated in the design yield strength ($f_{y,d} = f_{y,n}/\gamma_M$, and $\gamma_M = 1.1$), hence the resistance factor ϕ of GB 50017–2017 can be obtained as $1/1.1 \approx 0.91$.

Under various loading situations, a basic load combination of $1.35 \times DL + 1.5 \times LL$ for GB 50017–2017 (MOHURD, 2012), $1.2 \times DL + 1.6 \times LL$ for ANSI/AISC 360–16 and ASCE/SEI 48–19, $1.2 \times DL + 1.5 \times LL$ for AS 4100:2020, and a live load over dead load ratio of 3 were adopted from the practical view. The reliability index β was

computed using Eq. (5.31) and the design methods were deemed to be reliable if the reliability index β was greater than 2.5 (AISI, 2016).

$$\beta = \frac{\ln\left(\frac{R_n(P_m M_m F_m)}{Q_m}\right)}{\sqrt{V_P^2 + V_M^2 + V_F^2 + V_Q^2}} \quad \text{Eq. (5.31)}$$

where R_n/Q_m is the nominal resistance to the average load effect ratio, and $P_m, M_m, F_m, V_P, V_M, V_F,$ and V_Q represent the mean values and COVs of the variables related to the uncertainties in materials, geometric dimensions, and load effects, respectively.

Key parameters and results of reliability analyses are listed in Table 5.10. Of the results investigated, the reliability index β for GB 50017–2017 (curve ‘a’), ANSI/AISC 360–16, and AS 4100:2020 design methods were all greater than 2.5, implying that satisfied reliability level was acquired for these design methods.

5.6 Concluding remarks

The experimental and numerical investigations on the structural behaviour of pin-ended cold-formed OctHS columns are presented in this chapter. Specimen design details, material properties, measurement of initial global imperfection, pin-ended column test setup, and test results are reported. Finite element modelling was developed and validated against the experimental results. Parametric studies were conducted to expand the test database over a wider spectrum of parameters. The experimental results combined with generated numerical results were utilised to evaluate the applicability of different design methods for the flexural buckling design of OctHS columns. Based on the assessment and reliability analysis results, it can be concluded that column buckling curve ‘b’ in Eurocode 3 can be safely applied in the design of OctHS columns with the original partial factor $\gamma_M = 1.00$, and a larger γ_M^* value of 1.10 is recommended

to achieve the required level of safety for the proposed modified EC3 method. It is also found that using curve 'a' in GB 50017–2017 can achieve the most accurate prediction accuracy, and ANSI/AISC 360–16 and AS 4100:2020 can also provide relatively accurate prediction results for the design of OctHS columns. ASCE/SEI 48–19 design method overestimates the column strength for the majority of OctHS columns, and a design recommendation is suggested to correct the overestimate problem of ASCE/SEI 48–19 design method by adopting the same design expressions from ANSI/AISC 360–16. Hence, the codified design methods from Eurocode 3 (curve 'b'), GB 50017–2017 (curve 'a'), ANSI/AISC 360–16, and AS 4100:2020 are recommended for the flexural buckling design of OctHS columns since it is accurate and reliable.

Chapter 6 Conclusions and future works

6.1 Introduction

This thesis aims to investigate the material characteristics of cold-formed steel and structural behaviour and design of cold-formed polygonal hollow section columns. The specimens used for material characterisation were manufactured from structural steel plates with nominal yield strengths of 235 MPa, 275 MPa, 355 MPa, 460 MPa, 550 MPa, and 690 MPa. For polygonal hollow sections, steel plates with nominal steel grades of 355 MPa, 460 MPa, and 690 MPa were adopted to fabricate polygonal hollow section columns. Assessments on the current design codes were made and corresponding design recommendations were proposed. The following sessions highlight the major findings of this thesis. Recommendations on future research works are also presented.

6.2 Material characterisation of cold-formed steels

Comprehensive experimental investigations into effects of cold-forming on structural steels were conducted. The nominal steel grades of the tensile coupons used in the material tests were 235 MPa, 275 MPa, 355 MPa, 460 MPa, 550 MPa, and 690 MPa. To derive the key material parameters for cold-formed steels, a total of 93 flat coupons extracted from the parent steel plates and 212 corner coupons machined from cold-formed corners were tested in accordance with EN ISO 6892-1:2019. It can be found that there is no difference in the developing mechanism of changes in material properties, and there is no clear boundary between normal and high strength steel. The strength enhancement behaviour is only affected by the $f_{u,t}/f_{y,t}$ ratio of parent materials and the indicator of plastic deformation, r_i/t ratio, after cold-forming. A substantial test database was developed, including test results of 341 flat coupons and 613 corner

coupons with nominal steel grades from 235 MPa to 960 MPa. A series of semi-empirical models to predict the material properties of cold-formed steel were then proposed based on the developed database. To describe the stress-strain responses of cold-formed steel, constitutive models available from the literature were adopted to represent the stress-strain curves. The key parameters adopted in these models were further calibrated against measured data, and predictive expressions were proposed for those parameters which cannot be directly obtained. The stress-strain curves generated from the modified constitutive models are shown to be more accurate than existing material models and they agree very well with the experimental results of both cold-formed normal strength and high strength steel.

6.3 Behaviour and design of rectangular hollow section steel columns under pure compression

Material properties, residual stress distributions, and structural behaviour of press-braked RHS columns were comprehensively studied. Measured yield strengths of the flat coupons were from 381 to 628 MPa, while those of the corner coupons were from 613 to 882 MPa. A total of 54 strips were sectioned from five different RHSs to obtain the membrane and the bending residual stress distributions in the cross-sections. Based on the observed consistent pattern of residual stress distributions in press-braked RHSs, a simplified residual stress predictive pattern was subsequently proposed.

Cross-sectional resistances of press-braked RHSs were investigated through a total of 10 stub column tests. For the structural behaviour of long columns, a total of 7 long columns with various member slenderness were tested. Corresponding finite element models were then developed and validated against the experimental results. Satisfactory agreement was yield between the obtained test results and the generated numerical results. Subsequently, additional 290 FEMs for stub columns and 345 FEMs

for long columns were established for comprehensive parametric studies.

The applicability of current codes of practice for press-braked RHSs was assessed against the obtained experimental and numerical results, and corresponding design recommendations were given. For cross-sectional resistances, it can be concluded that: (1) Both the existing effective width method and the direct strength method tend to overestimate the resistance of press-braked RHSs; and (2) Improved design expressions based on these methods are proposed to achieve a more accurate and less scattered prediction on cross-sectional resistances of press-braked RHSs. For the flexural buckling strength, it can be summarised that: (1) EN 1993-1-1 provides a conservative prediction on column strengths when column buckling curve 'c' was adopted. A modified expression of the imperfection factor incorporating the influence of steel grades is proposed. Improved prediction accuracy has been achieved by utilising this modified expression; (2) In GB 50017-2017, the adoption of column buckling curve 'a' gives the most accurate prediction for column strengths, as compared with column buckling curve 'b' recommended for hollow sections; (3) ANSI/AISC 360-16 offers satisfactory column strength predictions; and (4) AS 4100:2020 achieves relatively better performance, in terms of column strength prediction, than ANSI/AISC 360-16.

6.4 Structural behaviour and design of pin-ended octagonal hollow section columns

The structural behaviour of cold-formed OctHS long columns was experimentally investigated. Regular OctHSs and irregular OctHSs with different aspect ratios were designed and fabricated using four types of steel plates – Q460 3mm, Q460 6 mm, Q690 3mm, and Q690 6 mm. The measured yield strengths of flat coupons were from 541 to 753 MPa, while those for corner coupons were from 669 to 900 MPa. The initial

global geometric imperfection for each column was measured, and the corresponding loading eccentricities were determined during long column tests. Key results of the column tests including axial load versus mid-height lateral deflection curves, axial load versus axial strain curves, and failure modes are reported.

Numerical investigations into cold-formed OctHS columns were performed. The effect of residual stresses on OctHS columns under quasi-static loading is found to be negligible, but it needs to be further investigated under dynamic loading. Developed finite element models for regular and irregular OctHS columns were carefully validated against the test results. Following the validation of the developed FEM, comprehensive parametric studies were conducted on OctHS columns. In total, additional 608 numerical models for regular OctHS columns and 539 numerical models for irregular OctHS columns were established. Effects of steel grades, cross-sections, aspect ratios and member slenderness were investigated and presented.

The cross-section classification rule for the OctHS proposed by Chen *et al.* (2021) was adopted in the member buckling design. The applicability of current design methods for OctHS long columns were then assessed, and corresponding modifications were proposed. Reliability analyses in accordance with EN 1990 and AISI S100-16 methods were performed to verify the safety level of these design methods and design recommendations. Based on the results obtained from the assessments and the reliability analyses, the following conclusions are drawn: (1) Column buckling curve 'b' in Eurocode 3 can be safely applied in the design of OctHS columns with the original partial factor $\gamma_M = 1.00$, and a modified value of $\gamma_M^* = 1.10$ is recommended to achieve the required level of safety for the proposed modified EC3 method; (2) Incorporating the material safety factor $\gamma_M = 1.10$, GB 50017-2017 can accurately and reliably predict the flexural buckling strength of OctHS columns using column curve 'a'; (3)

ANSI/AISC 360–16 and AS 4100:2020 both provide slightly conservative but still precise strength predictions for OctHS columns if a resistance factor $\phi = 0.9$ was adopted; and (4) ASCE SEI 48–19 generally overestimates the flexural buckling strength of OctHS columns, and it is recommended to adopt the same design expressions in ANSI/AISC 360–16 to improve its prediction accuracy.

6.5 Future works

The current experimental investigations focus on the material properties of cold-formed steel at ambient temperature. In the design process of cold-formed steel structures, fire resistance design is an important and essential procedure to ensure structural safety, as steel is sensitive to elevated temperatures, which means fire may dramatically deteriorate the capacity of steel members. Therefore, the structural behaviour of cold-formed steel under fire and after fire exposure needs to be investigated to achieve a safe structure design.

Structural behaviour and design of polygonal hollow section columns under eccentric loadings should be conducted to supplement the design rules of polygonal tubular structures. To develop an accurate interaction curve under combined compression and bending, the behaviour of polygonal tubular structures under pure bending needs to be investigated first. Then, tests on beam–columns of polygonal tubular sections should be conducted.

Since OctHS is different from RHS and CHS in confinement effectiveness to the concrete core, resulting in their different structural behaviour. The confinement effect of OctHS needs to be investigated. Hence, research on structural behaviour and design of concrete–filled OctHS members is necessary.

References

- ABAQUS. Dassault Systems. *Waltham, MA, USA, 2020.*
- Abdel-Rahman, N., and Sivakumaran, K. (1997). Material properties models for analysis of cold-formed steel members. *Journal of Structural Engineering*, 123(9), 1135-1143.
- Afshan, S., Rossi, B., and Gardner, L. (2013). Strength enhancements in cold-formed structural sections — Part I: Material testing. *Journal of Constructional Steel Research*, 83, 177-188.
- AISC/AISC. (2022). ANSI/AISC 360-22. Specification for structural steel buildings. In. Chicago: American Institute of Steel Construction.
- AISI. (2016). AISI S100-16. North American Specification for the Design of Cold-Formed Steel Structural Members. In. The United States: American Iron and Steel Institute.
- Arrayago, I., Real, E., and Gardner, L. (2015). Description of stress–strain curves for stainless steel alloys. *Materials & Design*, 87, 540-552.
- AS/NZS. (2018). AS/ NZS 4600:2018, Cold-formed steel structures. In. Australia: Standards Australia limited.
- ASCE. (2019). ASCE/SEI 48-19. Design of steel transmission pole structures. In. Reston, Virginia: American Society of Civil Engineers (ASCE).
- Ashraf, M., Gardner, L., and Nethercot, D. (2005). Strength enhancement of the corner regions of stainless steel cross-sections. *Journal of Constructional Steel Research*, 61(1), 37-52.
- Australia, S. (2020). AS 4100-2020: Steel structures. In. Homebush, NSW, Australia: Standards Australia.
- Ayough, P., Ibrahim, Z., Sulong, N. R., and Hsiao, P.-C. (2021). The effects of cross-sectional shapes on the axial performance of concrete-filled steel tube columns. *Journal of Constructional Steel Research*, 176, 106424.
- Britvec, S., Chajes, A., Warren, K., Uribe, J., and Winter, G. (1970). Effects of cold work in cold-formed steel structural members.
- Buchanan, C., Gardner, L., and Liew, A. (2016). The continuous strength method for the design of circular hollow sections. *Journal of Constructional Steel Research*, 118, 207-216.

- CEN. (2002). EN 1990:2002. Eurocode - Basis of structural design. In. Brussels: European Committee for Standardization.
- CEN. (2005). EN 1993-1-1. Eurocode 3: Design of steel structures - Part 1-1: General rules and rules for buildings. In. Brussels: European Committee for Standardization.
- CEN. (2006a). EN 1993-1-4. Eurocode 3 - Design of steel structures - Part 1-4: General rules - Supplementary rules for stainless steels. In. Brussels: European Committee for Standardization.
- CEN. (2006b). EN 10219-2: 2006. Cold formed welded structural hollow sections of non-alloy and fine grain steels - Part 2: Tolerances, dimensions and sectional properties. In. Brussels: European Committee for Standardization.
- CEN. (2006c). Eurocode 3 - Design of steel structures - Part 1-3: General rules - Supplementary rules for cold-formed members and sheeting. In. Brussels: European Committee for Standardization.
- CEN. (2007). Eurocode 3: Design of steel structures -Part 1-12: additional rules for the extension of EN 1993 up to steel grades S700. In. Brussels: European Committee for Standardization.
- CEN. (2009). EN 1993-1-5:2006. Eurocode 3: Design of steel structures -Part 1-5: Plated structural elements. In. Brussels: European Committee for Standardization.
- CEN. (2019). EN ISO 6892-1:2019. Metallic materials — Tensile testing Part 1: Method of test at room temperature. In. Brussels: European Committee for Standardization.
- CEN. (2022). EN 1993-1-1:2022. Eurocode 3: Design of steel structures -Part 1-1: General rules and rules for buildings. In. Brussels: European Committee for Standardization.
- CENELEC. (2012). EN 50341-1:2012. Overhead Electrical Lines Exceeding AC 45 kV – Part 1: General Requirements - Common Specifications. In. Brussels: European Committee for Electrotechnical Standardization.
- Chajes, A., Britvec, S., and Winter, G. (1963). Effects of cold-straining on structural sheet steels. *Journal of the Structural Division*, 89(2), 1-32.
- Chen, J., and Chan, T.-M. (2019). Experimental assessment of the flexural behaviour of concrete-filled steel tubular beams with octagonal sections. *Engineering Structures*, 199, 109604.

- Chen, J., Chan, T.-M., Su, R. K. L., and Castro, J. M. (2019). Experimental assessment of the cyclic behaviour of concrete-filled steel tubular beam-columns with octagonal sections. *Engineering Structures*, 180, 544-560.
- Chen, J., Fang, H., and Chan, T.-M. (2021). Design of fixed-ended octagonal shaped steel hollow sections in compression. *Engineering Structures*, 228, 111520.
- Chen, J., Liu, H., and Chan, T.-M. (2020). Material properties and residual stresses of cold-formed octagonal hollow sections. *Journal of Constructional Steel Research*, 170, 106078.
- Chen, J., Zhu, J.-Y., and Chan, T.-M. (2020). Experimental and numerical investigation on stub column behaviour of cold-formed octagonal hollow sections. *Engineering Structures*, 214, 110669.
- Chen, M.-T., and Young, B. (2019). Structural performance of cold-formed steel elliptical hollow section pin-ended columns. *Thin-Walled Structures*, 136, 267-279.
- Coetsee, J., Van der Merwe, P., and van den Berg, G. (1990). *The effect of workhardening and residual stresses due to cold work of forming on the strength of cold-formed stainless steel lipped channel sections* Tenth International Speciality Conference on Cold-Formed Steel Structures, St. Louis, Missouri, USA.
- Cruise, R. B., and Gardner, L. (2008). Residual stress analysis of structural stainless steel sections. *Journal of Constructional Steel Research*, 64(3), 352-366.
- Dalia, Z. M., Bhowmick, A. K., and Grondin, G. Y. (2021). Local buckling of multi-sided steel tube sections under axial compression and bending. *Journal of Constructional Steel Research*, 186, 106909.
- Ding, F.-x., Li, Z., Cheng, S., and Yu, Z.-w. (2016). Composite action of octagonal concrete-filled steel tubular stub columns under axial loading. *Thin-Walled Structures*, 107, 453-461.
- ECCS. (1986). Recommended testing procedure for assessing the behaviour of structural steel elements under cyclic loads. In. Brussels, Belgium: European Convention for Constructional Steelwork.
- Fang, H., Chan, T.-M., and Young, B. (2018a). Material properties and residual stresses of octagonal high strength steel hollow sections. *Journal of Constructional Steel Research*, 148, 479-490.
- Fang, H., Chan, T.-M., and Young, B. (2018b). Structural performance of cold-formed

- high strength steel tubular columns. *Engineering Structures*, 177, 473-488.
- Fang, H., Chan, T.-M., and Young, B. (2019). Behavior of Octagonal High-Strength Steel Tubular Stub Columns. *Journal of Structural Engineering*, 145(12), 04019150.
- Fang, H., Chan, T.-M., and Young, B. (2021a). Experimental and Numerical Investigations of Octagonal High-Strength Steel Tubular Stub Columns under Combined Compression and Bending. *Journal of Structural Engineering*, 147(1), 04020282.
- Fang, H., Chan, T.-M., and Young, B. (2021b). Structural performance of concrete-filled cold-formed high-strength steel octagonal tubular stub columns. *Engineering Structures*, 239.
- Fang, H., Li, Q.-Y., Chan, T.-M., and Young, B. (2023). Behaviour and design of high-strength octagonal CFST short columns subjected to combined compression and bending. *Journal of Constructional Steel Research*, 200, 107679.
- Gardner, L., and Nethercot, D. A. (2004). Experiments on stainless steel hollow sections—Part 1: Material and cross-sectional behaviour. *Journal of Constructional Steel Research*, 60(9), 1291-1318.
- Gardner, L., Saari, N., and Wang, F. (2010). Comparative experimental study of hot-rolled and cold-formed rectangular hollow sections. *Thin-Walled Structures*, 48(7), 495-507.
- Gardner, L., and Yun, X. (2018). Description of stress-strain curves for cold-formed steels. *Construction and Building Materials*, 189, 527-538.
- Godat, A., Legeron, F., and Bazonga, D. (2012). Stability investigation of local buckling behavior of tubular polygon columns under concentric compression. *Thin-Walled Structures*, 53, 131-140.
- Gonçalves, R., and Camotim, D. (2013). Elastic buckling of uniformly compressed thin-walled regular polygonal tubes. *Thin-Walled Structures*, 71, 35-45.
- Guo, Y.-J., Zhu, A.-Z., Pi, Y.-L., and Tin-Loi, F. (2007). Experimental study on compressive strengths of thick-walled cold-formed sections. *Journal of Constructional Steel Research*, 63(5), 718-723.
- Hayeck, M. (2016). *Development of a new design method for steel hollow section members resistance* Université de Liège, Liège, Belgique].

- Hill, H. (1944). *Determination of stress-strain relations from "offset" yield strength values*.
- Holmquist, J., and Nadai, A. (1939). A theoretical and experimental approach to the problem of collapse of deep-well casing. *Drilling and Production Practice*,
- Hosford, W. F. (2012). *Iron and Steel*. Cambridge: Cambridge University Press.
- Hradil, P., Talja, A., Real, E., Mirambell, E., and Rossi, B. (2013). Generalized multistage mechanical model for nonlinear metallic materials. *Thin-Walled Structures*, 63, 63-69.
- Huang, Y., and Young, B. (2014). The art of coupon tests. *Journal of Constructional Steel Research*, 96, 159-175.
- Hui, C. (2014). *Moment redistribution in cold-formed steel purlin systems* Imperial College London London].
- Jiang, K., and Zhao, O. (2022a). Net Section Failure of S690 High-Strength Steel Angle-to-Plate Connections. *Journal of Structural Engineering*, 148(4), 04022021.
- Jiang, K., and Zhao, O. (2022b). Testing, numerical modelling and design of S690 high strength steel channel-to-plate connections. *Thin-Walled Structures*, 179.
- Kalaga, S., and Yenumula, P. (2016). *Design of electrical transmission lines: structures and foundations*. CRC Press.
- Karren, K. W. (1965). *EFFECTS OF COLD-FORMING ON LIGHT-GAGE STEEL* Cornell University].
- Karren, K. W. (1967). Corner properties of cold-formed steel shapes. *Journal of the Structural Division*, 93(1), 401-432.
- Kettler, M. (2008). *Elastic-plastic cross-sectional resistance of semi-compact H-and hollow sections* Graz University of Technology].
- Key, P. W., Hasan, S. W., and Hancock, G. J. (1988). Column behavior of cold-formed hollow sections. *Journal of Structural Engineering*, 114(2), 390-407.
- Kim, H., Kim, C., Barlat, F., Pavlina, E., and Lee, M.-G. (2013). Nonlinear elastic behaviors of low and high strength steels in unloading and reloading. *Materials Science and Engineering: A*, 562, 161-171.
- Kyvelou, P., Gardner, L., and Nethercot, D. A. (2017). Testing and Analysis of Composite Cold-Formed Steel and Wood-Based Flooring Systems. *Journal of*

Structural Engineering, 143(11), 04017146.

Law, K. H. (2010). *Instabilities in Structural Steel Elliptical Hollow Section Members*

Li, Q.-Y., and Young, B. (2022). Experimental and numerical investigation on cold-formed steel built-up section pin-ended columns. *Thin-Walled Structures*, 170.

Lind, N., and Schroff, D. (1971). Utilization of cold work in light gage steel.

Liu, H.-X., Fang, H., Zhu, J.-Y., and Chan, T.-M. (2021). Numerical investigation on the structural performance of octagonal hollow section columns. *Structures*,

Liu, H., Jiang, H., Hu, Y.-F., Chan, T.-M., and Chung, K.-F. (2022). Structural behaviour of Q355 and Q460 press-braked rectangular hollow section stub columns. *Journal of Constructional Steel Research*, 197, 107497.

Liu, J.-z., Fang, H., and Chan, T.-M. (2022a). Experimental and numerical investigations on stub column behaviour of cold-formed high strength steel irregular octagonal hollow sections. *Thin-Walled Structures*, 180.

Liu, J.-z., Fang, H., and Chan, T.-M. (2022b). Experimental investigations on material properties and stub column behaviour of high strength steel irregular hexagonal hollow sections. *Journal of Constructional Steel Research*, 196.

Liu, J.-z., Fang, H., and Chan, T.-M. (2022c). Structural behaviour of high strength steel hexagonal hollow section stub columns under axial compression. *Engineering Structures*, 268, 114653.

Liu, J.-z., Fang, H., Chen, S., and Chan, T.-M. (2022). Material properties and residual stresses of high strength steel hexagonal hollow sections. *Journal of Constructional Steel Research*, 190.

Lu, Q., and Zhao, C. (2022). Numerical analysis of seismic behavior of octagonal multi cavity steel composite columns. *Journal of Constructional Steel Research*, 191, 107171.

Ma, J.-L., Chan, T.-M., and Young, B. (2015). Material properties and residual stresses of cold-formed high strength steel hollow sections. *Journal of Constructional Steel Research*, 109, 152-165.

Ma, J.-L., Chan, T.-M., and Young, B. (2016a). Experimental investigation of cold-formed high strength steel tubular beams. *Engineering Structures*, 126, 200-209.

Ma, J.-L., Chan, T.-M., and Young, B. (2016b). Experimental investigation on stub-column behavior of cold-formed high-strength steel tubular sections. *Journal*

- of Structural Engineering*, 142(5), 04015174.
- Ma, J.-L., Chan, T.-M., and Young, B. (2019). Cold-Formed High-Strength Steel Rectangular and Square Hollow Sections under Combined Compression and Bending. *Journal of Structural Engineering*, 145(12).
- Ma, J.-L., Chan, T.-M., and Young, B. (2021). Cold-formed high strength steel tubular beam-columns. *Engineering Structures*, 230, 111618.
- Mander, J. B. (1983). Seismic design of bridge piers.
- Meng, X., and Gardner, L. (2020a). Behavior and Design of Normal- and High-Strength Steel SHS and RHS Columns. *Journal of Structural Engineering*, 146(11), 04020227.
- Meng, X., and Gardner, L. (2020b). Behavior and Design of Normal- and High-Strength Steel SHS and RHS Columns. *Journal of Structural Engineering*, 146(11), 04020227.
- Mirambell, E., and Real, E. (2000). On the calculation of deflections in structural stainless steel beams: an experimental and numerical investigation. *Journal of Constructional Steel Research*, 54(1), 109-133.
- MOHURD. (2012). Load code for the design of building structures (GB 50009-2012). In.
- MOHURD. (2017). GB 50017-2017: Code for design of steel structures. In. Beijing, China: MOHURD (Ministry of Housing and Urban-Rural Development of the People's Republic of China).
- Naohiro, W., Kikuo, I., Tadayoshi, O., and Yosuke, K. (2017). 05.11: Local buckling behavior of octagonal hollow cross-section member under axial compression or bending shear. *ce/papers*, 1(2-3), 1116-1122.
- Olsson, A. (2001). *Stainless steel plasticity: material modelling and structural applications* Luleå tekniska universitet].
- Pandey, M., and Young, B. (2019). Tests of cold-formed high strength steel tubular T-joints. *Thin-Walled Structures*, 143.
- Peköz, T. (1986). Development of a unified approach to the design of cold-formed steel members.
- Pham, C. H., Trinh, H. N., and Proust, G. (2021). Effect of manufacturing process on microstructures and mechanical properties, and design of cold-formed G450 steel channels. *Thin-Walled Structures*, 162.

- Quach, W., Teng, J. G., and Chung, K. F. (2008). Three-stage full-range stress-strain model for stainless steels. *Journal of Structural Engineering*, 134(9), 1518-1527.
- Quach, W. M., and Huang, J. F. (2011). Stress-Strain Models for Light Gauge Steels. *Procedia engineering*, 14, 288-296.
- Ramberg, W., and Osgood, W. R. (1943). *Description of stress-strain curves by three parameters*.
- Rasmussen, K., and Hancock, G. (1993). Design of cold-formed stainless steel tubular members. II: Beams. *Journal of Structural Engineering*, 119(8), 2368-2386.
- Rasmussen, K. J. (2003). Full-range stress–strain curves for stainless steel alloys. *Journal of Constructional Steel Research*, 59(1), 47-61.
- Rasmussen KJR, H. G. (1993). Design of cold-formed stainless steel tubular members. I:columns. *Journal of Structural Engineering*, 119(8), 2349–2367.
- Rossi, B., Afshan, S., and Gardner, L. (2013). Strength enhancements in cold-formed structural sections — Part II: Predictive models. *Journal of Constructional Steel Research*, 83, 189-196.
- Singh, T. G., and Singh, K. D. (2018). Experimental investigation on performance of perforated cold–formed steel tubular stub columns. *Thin-Walled Structures*, 131, 107-121.
- Slocum, R. (2015). Considerations in the design and fabrication of tubular steel transmission structures. Proceedings of the fifteenth international symposium on tubular structures–ISTS,
- Somodi, B., and Kövesdi, B. (2017). Flexural buckling resistance of cold-formed HSS hollow section members. *Journal of Constructional Steel Research*, 128, 179-192.
- Sun, M., and Packer, J. A. (2014). Direct-formed and continuous-formed rectangular hollow sections — Comparison of static properties. *Journal of Constructional Steel Research*, 92, 67-78.
- Tayyebi, K., and Sun, M. (2020). Stub column behaviour of heat-treated and galvanized RHS manufactured by different methods. *Journal of Constructional Steel Research*, 166, 105910.
- Tayyebi, K., and Sun, M. (2021). Design of direct-formed square and rectangular hollow section stub columns. *Journal of Constructional Steel Research*, 178.

- Tayyebi, K., Sun, M., and Karimi, K. (2020). Residual stresses of heat-treated and hot-dip galvanized RHS cold-formed by different methods. *Journal of Constructional Steel Research*, 169.
- Tran, A. T., Veljkovic, M., Rebelo, C., and da Silva, L. S. (2016). Resistance of cold-formed high strength steel circular and polygonal sections — Part 1: Experimental investigations. *Journal of Constructional Steel Research*, 120, 245-257.
- Van den Berg, G., and Van der Merwe, P. (1992). *Prediction of corner mechanical properties for stainless steels due to cold forming* Eleventh International Speciality Conference on Cold-Formed Steel Structures, St. Louise, Missouri, USA.
- Wang, F., Zhao, O., and Young, B. (2019). Flexural behaviour and strengths of press-braked S960 ultra-high strength steel channel section beams. *Engineering Structures*, 200.
- Wang, F., Zhao, O., and Young, B. (2020). Testing and numerical modelling of S960 ultra-high strength steel angle and channel section stub columns. *Engineering Structures*, 204.
- Wang, J., Afshan, S., Schillo, N., Theofanous, M., Feldmann, M., and Gardner, L. (2017). Material properties and compressive local buckling response of high strength steel square and rectangular hollow sections. *Engineering Structures*, 130, 297-315.
- Wang, Y.-B., Li, G.-Q., Chen, S.-W., and Sun, F.-F. (2014). Experimental and numerical study on the behavior of axially compressed high strength steel box-columns. *Engineering Structures*, 58, 79-91.
- Wilkinson, T., and Hancock, G. J. (1998). Tests to examine compact web slenderness of cold-formed RHS. *Journal of Structural Engineering*, 124(10), 1166-1174.
- Xiao, M., Hu, Y. F., Shen, M. H., Chung, K. F., and Nethercot, D. A. (2022). Compression tests on stocky and slender columns of high strength S690 cold-formed square tubes. *Engineering Structures*, 273.
- Xu, F., Cai, Y., Chan, T.-M., and Young, B. (2023). Tube wall deformation behaviour of tensile-loaded blind-bolted connections in octagonal hollow section tubes. *Thin-Walled Structures*, 184, 110447.
- Yang, L., Yin, F., Wang, J., Bilal, A., Ahmed, A. H., and Lin, M. (2022). Local buckling resistances of cold-formed high-strength steel SHS and RHS with varying corner radius. *Thin-Walled Structures*, 172.

- Yang, M., Akiyama, Y., and Sasaki, T. (2004). Evaluation of change in material properties due to plastic deformation. *Journal of Materials Processing Technology*, 151(1-3), 232-236.
- Yang, Y., Zhang, B., Wang, Y., Jiang, Z., and Li, K. (2022). Mechanical behaviors and constitutive model of structural steel influenced by strain aging. *Journal of Constructional Steel Research*, 192, 107211.
- Yun, X., and Gardner, L. (2017). Stress-strain curves for hot-rolled steels. *Journal of Constructional Steel Research*, 133, 36-46.
- Yun, X., Gardner, L., and Boissonnade, N. (2018). The continuous strength method for the design of hot-rolled steel cross-sections. *Engineering Structures*, 157, 179-191.
- Yun, X., Wang, Z., and Gardner, L. (2020). Structural performance and design of hot-rolled steel SHS and RHS under combined axial compression and bending. *Structures*, 27, 1289-1298.
- Zhang, L., Wang, F., Liang, Y., and Zhao, O. (2019). Press-braked S690 high strength steel equal-leg angle and plain channel section stub columns: Testing, numerical simulation and design. *Engineering Structures*, 201.
- Zhang, L., Wang, F., Liang, Y., and Zhao, O. (2020). Experimental and numerical studies of press-braked S690 high strength steel channel section beams. *Thin-Walled Structures*, 148.
- Zhang, T., Ding, F.-x., Wang, L., Liu, X.-m., and Jiang, G.-s. (2018). Behavior of polygonal concrete-filled steel tubular stub columns under axial loading. *Steel and Composite Structures, An International Journal*, 28(5), 573-588.
- Zhang, X., Liu, S., Zhao, M., and Chiew, S.-P. (2016). Residual stress of cold-formed thick-walled steel rectangular hollow sections. *Steel and Composite Structures*, 22(4), 837-853.
- Zhong, Y., Sun, Y., Hai Tan, K., and Zhao, O. (2021). Testing, modelling and design of high strength concrete-filled high strength steel tube (HCFHST) stub columns under combined compression and bending. *Engineering Structures*, 241.
- Zhu, J.-Y., and Chan, T.-M. (2018). Experimental investigation on octagonal concrete filled steel stub columns under uniaxial compression. *Journal of Constructional Steel Research*, 147, 457-467.
- Zhu, J.-Y., and Chan, T.-M. (2019). Experimental investigation on steel-tube-

confined-concrete stub column with different cross-section shapes under uniaxial-compression. *Journal of Constructional Steel Research*, 162.

Zhu, J.-Y., Chan, T.-M., and Young, B. (2019). Cross-sectional capacity of octagonal tubular steel stub columns under uniaxial compression. *Engineering Structures*, 184, 480-494.